

Generation of Homogeneous Wave Fields in Phase Resolving Wave Propagation Models

Panagiotis Vasarmidis

Doctoral dissertation submitted to obtain the academic degree of
Doctor of Civil Engineering

Supervisors

Prof. Peter Troch, PhD - Vicky Stratigaki, PhD

Department of Civil Engineering
Faculty of Engineering and Architecture, Ghent University

October 2021



**Generation of Homogeneous Wave Fields in Phase Resolving Wave
Propagation Models**

Panagiotis Vasarmidis

Doctoral dissertation submitted to obtain the academic degree of
Doctor of Civil Engineering

Supervisors

Prof. Peter Troch, PhD - Vicky Stratigaki, PhD

Department of Civil Engineering
Faculty of Engineering and Architecture, Ghent University

October 2021

ISBN 978-94-6355-541-8

NUR 956, 950

Wettelijk depot: D/2021/10.500/89

Members of the Examination Board

Chair

Prof. Patrick De Baets, PhD, Ghent University

Other members entitled to vote

Prof. Joris Degroote, PhD, Ghent University

Georgios Klonaris, PhD, Ghent University

Prof. Ad Reniers, PhD, Technische Universiteit Delft, the Netherlands

Prof. Eugen Rusu, PhD, "Dunarea de Jos" University of Galati, Romania

Tomohiro Suzuki, PhD, Flanders Hydraulics Research

Supervisors

Prof. Peter Troch, PhD, Ghent University

Vicky Stratigaki, PhD, Ghent University

A word of thanks

Being at the final stage of the journey that is called PhD has led me to think of all these moments that make up this unique experience. A challenging procedure that forms you as a person, that makes you wonder whether or not you will come out of it unscathed, that tries out your limits, that offers you great opportunities to travel, meet wise people and cultivate your mind. A journey with ups and downs, with moments of excitement and disappointment, with highly motivated creative ideas and moments of extensive criticism of your work. Luckily, in all these you are not alone. There are people accompanying you, that help you overcome any obstacles, make you feel stronger and wiser. This section is a great opportunity to thank all these people, with the help of whom this research has reached its current mature state.

First of all my gratitude goes to my PhD supervisors, prof. Peter Troch and dr. Vicky Stratigaki. I would like to thank them for giving me the opportunity to join the Coastal Engineering Research Group of UGent, for convincing me that pursuing a PhD was the right career step for me and for giving me all the freedom to work on what I enjoy the most. Thank you for the constant trust, support and motivation that you gave me through all the years of my PhD, for making me feel at home in the department and for giving me the chance to continue my research in a Post-Doctoral position.

Thank you to the members of my examination board for critically reviewing my dissertation and providing valuable feedback on my research and the manuscript itself. Thanks to your constructive remarks and suggestions my dissertation has improved and reached its final status. My special thanks go to prof. Marcel Zijlema (TUDelft) for our fruitful discussions and his encouragement that gave me confidence to continue my research related to SWASH. Thank you to dr. Tomohiro Suzuki and dr. Giorgos Klonaris for the scientific discussions and guidance that helped me go one step further.

Additionally, I would like to thank all my colleagues in UGent. Lien and Ellen: for always being there to support me with all administrative issues that arose until the last days before my final presentation; Tom, Herman and Dave: for being the soul of the physical modeling group of the department and for your willingness to transfer your knowledge and experience during experiments. Further, my special thanks to my friends and colleagues David, Max and Gael: Thank you for welcoming me in the coastal engineering research group, sharing your PhD experience with

me and giving me useful advice on how to keep a work-life balance while doing a PhD. Of course I cannot but mention our Film Fest Gent tradition, which has always been an event to wait for at the beginning of each academic year. My buddy Joe: for realizing from the first moment that we have so much in common and for his constant encouragement. Thank you to Nicolas: for translating my summary to Dutch; Minghao: for the authentic Chinese tea; Carlos: for sharing his enthusiasm on fluid dynamics; Timothy: for making my day with his jokes; Brecht: for introducing me in the world of HPC; Tim: for proving that presenting your results in a nice way is as important as the results themselves; Philip: for being a special office mate; Vincent: for helping me with the PhD submission process; Corrado: for the best walking tour in Ghent; Ine: for the authentic speculoos recipe; Peter Devriese: for the ride to COB; Efrain: for the excellent Mexican tequila; the new batch of PhD students Maria, Rafael and Paulino: for reminding me how it is to be an enthusiastic young researcher that is about to start a PhD.

Furthermore, I would like to thank all my friends: Vasilis, Alexandros, Nikos D., Tasos, Christos, Ioanna, Marios, Kostas, Elena, Nikos S., Giorgos, Petros, Apos, Natasa, Katerina. Thank you for helping me disconnect from the PhD in my free time, for the memorable nights out, the weekends and holidays that we spent together, the Skype talks and most importantly for providing your support when I needed it from all the corners of the world: Greece, The Netherlands, Belgium... Special thanks to Nikos D. and Tasos with whom we share not only the same interests but also the passion for Coastal Engineering. We supported each other through all the years of our common studies and this support continued during my PhD, through constructive brainstorming and long discussions that helped me in critical points of my research.

At this point I would like to thank my family. A big thanks goes to my parents that have been continuously supporting me during all phases of my life. They always encouraged me to follow my dreams and supported any decision that I made, even when that meant that I would live 2000 km away from them. Thank you to my brother Nikos and his partner Areti for always believing in me and being there to hear my thoughts and concerns. Our conversations helped me see things from a different perspective and reevaluate my goals. Before closing this thank you section, I would like express my most sincere thanks to the person that supported me the most during this period, my partner, Myrsini. Thank you for continuously encouraging me to pursue this PhD, for standing by me during the easy and difficult moments of my research, for your practical support that included proof-reading and listening of my ideas and finally for your positive and always optimistic energy that calmed my stress and anxiety. None of this would have been possible without you, I feel lucky to have you by my side.

Panagiotis Vasarmidis
October 2021

Funding Acknowledgement

This research was funded by Research Foundation - Flanders (FWO). The author is a PhD fellow (fellowship 11D9618N) of the FWO (Fonds Wetenschappelijk Onderzoek - Research Foundation Flanders), Belgium.

Contents

A word of thanks	v
Funding Acknowledgement	vii
Nomenclature	xxiii
Samenvatting	xxvii
Summary	xxx
1 Introduction	1
1.1 Background	1
1.2 Knowledge gaps	4
1.3 Objectives and Methodology	5
1.4 Outline	6
2 Theoretical Background	9
2.1 Water wave theories	9
2.1.1 Linear wave theory	9
2.1.2 Second and Third order Stokes wave theory	13
2.1.3 Second order Superharmonics and Subharmonics	14
2.2 Numerical wave models	16
2.2.1 Phase-averaged models	17
2.2.2 Phase-resolving models	17
2.3 Mild-slope wave propagation model MILDwave	20
2.4 Non-hydrostatic wave propagation model SWASH	23
3 Development of periodic boundaries in MILDwave model	27
3.1 Introduction	28
3.2 Wave generation layouts in MILDwave	30
3.2.1 L-shaped wave generator	30
3.2.2 Arc-shaped wave generator	31
3.2.3 Wave generation line combined with periodic boundaries	32
3.3 Validation with analytical solutions	35
3.3.1 Generation of regular waves	35

3.3.2	Generation of irregular long-crested waves	39
3.3.3	Generation of irregular short-crested waves	42
3.4	Numerical validation using the Vincent and Briggs shoal experiment	47
3.5	Application to wave energy converter farms	51
3.6	Conclusions	54
4	Linear and nonlinear properties of SWASH Model	55
4.1	Introduction	55
4.2	Governing equations	57
4.3	Derivation of linear properties	61
4.4	Derivation of nonlinear properties	63
4.4.1	Second order equations and solutions	64
4.4.2	Third order solutions	67
4.4.3	Transfer functions for subharmonics and superharmonics .	70
4.5	Sensitivity analysis on advection terms of vertical momentum equation	78
4.6	Conclusions	80
5	Development of internal wave generation in SWASH model	83
5.1	Introduction	84
5.2	Weakly reflective wave generation boundary	87
5.3	Internal wave generation	89
5.3.1	Energy Velocity	89
5.3.2	Source term addition method	93
5.3.3	Spatially distributed source function	93
5.4	Validation with analytical solutions	95
5.4.1	Generation of regular waves	95
5.4.2	Reflected dispersive waves	99
5.4.3	Irregular long-crested waves in a numerical basin with constant depth	102
5.4.4	Oblique waves in a numerical basin with constant depth .	104
5.4.5	Irregular short-crested waves in a numerical basin with constant depth	107
5.5	Validation with experimental data	110
5.5.1	Numerical validation using the Berkhoff shoal experiment .	110
5.5.2	Numerical validation using the Vincent and Briggs shoal experiment	114
5.5.3	Wave diffraction around a vertical wall	119
5.6	Conclusions	127
6	Conclusions and Further Work	129
6.1	Summary of the key findings	129
6.2	Recommendations for future research	132

Appendices	135
A Comparison of different wave generation layouts in MILDwave	135
B Analysis of SWASH equations using Wolfram Mathematica	145
B.1 Stokes-type Fourier analysis for two layers	146
B.2 Second order solutions	157
B.3 Third order solutions	159
B.4 Subharmonic transfer functions	163
B.5 Superharmonic transfer functions	171
C Source code of the implemented internal wave generation method in SWASH	180
C.1 New subroutine SwashIntWavgen.ftn90	180
C.2 Extension of subroutine SwashUpdateData.ftn90	187
References	191

List of Figures

Figure 1.1	Estimation of the human population living near the coast in 2060 (Neumann et al., 2015).	2
Figure 1.2	(a) The rise in global mean sea level from 1900 and (b) projections of global mean sea level until 2100 for three different emission cases (from Copernicus Marine Environment Monitoring Service, Intergovernmental Panel on Climate Change).	3
Figure 1.3	Flowchart containing the main knowledge gaps, the objectives and the methodology of the present dissertation.	7
Figure 2.1	The diagram of Le Mehaute presenting the validity region of each wave theory.	10
Figure 2.2	Definition sketch of wave parameters.	11
Figure 2.3	(a) Superharmonic and (b) subharmonic transfer functions, $G_{\eta}^{m \pm n} d / \eta_{01m} \eta_{01n}$, as a function of the dimensionless depths $k_m d$ and $k_n d$	16
Figure 2.4	Finite difference scheme implemented in MILDwave for (a) Equation 2.33 and (b) Equation 2.34.	22
Figure 3.1	Water surface elevation, η , for regular incident waves with a wave height of $H = 1$ m, wave period of $T = 12$ s, and wave propagation angle of $\theta = 45^\circ$ affected by diffraction patterns due to the intersection of the two wave generation lines and the interaction with the lateral sponge layers.	29
Figure 3.2	Definition sketch of L-shaped wave generator.	31
Figure 3.3	Definition sketch of arc-shaped wave generator.	32
Figure 3.4	Definition sketch of wave generation line combined with periodic boundaries.	33
Figure 3.5	Definition sketch of computational domain with periodic boundaries.	34
Figure 3.6	Definition sketch of three wave generation layouts: (a) L-shaped, (b) arc-shaped, (c) line-shaped with periodic lateral boundaries. Dimensions are expressed in the number of wave lengths, $L_w = 100$ m, which corresponds to a wave period, $T = 12$ s, and water depth, $d = 7.5$ m.	36

Figure 3.7	Disturbance coefficient, k_d , and water surface elevation, η , in the inner computational domain at $t = 80T$ for regular incident waves with $H = 1$ m, $T = 12$ s, and $\theta = 30^\circ$ generated by an L-shaped wave generation layout (a,b), an arc-shaped wave generation layout (c,d), and by the use of periodic boundaries (e,f).	37
Figure 3.8	(a) Mean (E_{mean}) and (b) maximum (E_{max}) value of the absolute errors calculated using Equation 3.11 for each wave generation layout for a range of different incident wave angles, θ	38
Figure 3.9	Disturbance coefficient, k_d , and water surface elevation, η , in the inner computational domain at $t = 7000$ s for irregular long-crested waves with $H_s = 1$ m, $T_p = 12$ s, and (a,b) $\theta = 0^\circ$ and (c,d) $\theta = 15^\circ$	40
Figure 3.10	Disturbance coefficient, k_d , and water surface elevation, η , in the inner computational domain at $t = 7000$ s for irregular long-crested waves with $H_s = 1$ m, $T_p = 12$ s, and (a,b) $\theta = 30^\circ$ and (c,d) $\theta = 45^\circ$	41
Figure 3.11	Comparison between the frequency spectra, S_0 and S_{45} , resulting from MILDwave simulations for different incident wave angles ($\theta = 0^\circ$ and $\theta = 45^\circ$, respectively), and the target frequency spectrum, S_t , for irregular waves with $H_s = 1$ m, $T_p = 12$ s, and $\gamma = 3.3$	42
Figure 3.12	Relation between the directional spreading parameter, s_1 , and the spreading standard deviation, σ_θ	44
Figure 3.13	Comparison between the normalised spreading function distributions, D_n , calculated in MILDwave with the Miles and the Sand and Mynett wave synthesis methods and the target distribution, $D_{n,t}$, for irregular short-crested waves with a spreading standard deviation, σ_θ , of (a) 10° and (b) 30°	45
Figure 3.14	Disturbance coefficient, k_d , and water surface elevation, η , in the inner computational domain at $t = 7000$ s for irregular short-crested waves with $H_s = 1$ m, $T_p = 12$ s, $\theta = 0^\circ$, and $\sigma_\theta = 10^\circ$ synthesized by using the Miles method (a,b) and the Sand and Mynett method (c,d).	46
Figure 3.15	Disturbance coefficient, k_d , and water surface elevation, η , in the inner computational domain at $t = 7000$ s for irregular short-crested waves with $H_s = 1$ m, $T_p = 12$ s, $\theta = 0^\circ$, and $\sigma_\theta = 30^\circ$ synthesized by using the Miles method (a,b) and the Sand and Mynett method (c,d).	47
Figure 3.16	Bottom levels of the experimental setup used by Vincent and Briggs, as it is implemented in the numerical domain in MILDwave.	48
Figure 3.17	Comparison between the frequency spectra simulated in MILDwave and the target frequency spectrum for irregular waves with $H_s = 2.54$ cm, $T_p = 1.3$ s, $\sigma_\theta = 0^\circ$, and (a) $\gamma = 2$ and (b) $\gamma = 20$	49

Figure 3.18 Comparison of normalised wave heights, H/H_0 , between numerical model results (blue solid lines) and experimental data (red circles) along the measurement transect of Figure 3.16 for the test cases of non-breaking waves of Table 3.1.	51
Figure 3.19 Disturbance coefficient, k_d , for a nine Heaving Cylindrical Wave Energy Converter (HCWEC) array under the effect of irregular short-crested waves with $H_s = 2.0$ m, $T_p = 6.0$ s and $\sigma_\theta = 10^\circ$. Figure adopted from Verao Fernandez (2019).	52
Figure 3.20 Disturbance coefficient, k_d , along two cross-sections S1 (up) and S2 (bottom) as indicated in Figure 3.19 for a nine Heaving Cylindrical Wave Energy Converter (HCWEC) array under the effect of irregular short-crested waves with $H_s = 2.0$ m, $T_p = 6.0$ s and $\sigma_\theta = 10^\circ$. Figure adopted from Verao Fernandez (2019).	53
Figure 3.21 Absolute value of the complex wave amplitude $ \eta $ for the regular wave of $H = 2$ m, $T = 10$ s and $\theta = -24^\circ$ for a 10 WEC 2-array farm. Figure adopted from Balitsky et al. (2019).	53
Figure 4.1 Arrangement of the unknowns in a staggered grid: (a) Central differences scheme and (b) Keller Box scheme. Figure adopted from Zijlema and Stelling (2008).	58
Figure 4.2 Definition sketch for the case of two vertical layers and positioning of flow parameters with respect to z-axis.	59
Figure 4.3 (a) Ratio $\omega_{SWASH}/\omega_{Airy}$ and (b) the corresponding relative error for one, two, three and four vertical layers as a function of the dimensionless depth kd	63
Figure 4.4 Comparison of (a) normalised second order amplitude of the surface elevation, $\eta_{02,SWASH}/\eta_{02,St}$, and (b) the corresponding relative error for one, two, three and four vertical layers as a function of the dimensionless depth kd	66
Figure 4.5 Comparison of (a) normalised amplitude dispersion, $\omega_{13,SWASH}/\omega_{13,St}$, and (b) the corresponding relative error for one, two, three and four vertical layers as a function of the dimensionless depth kd	69
Figure 4.6 Comparison of (a) normalised third order amplitude of the surface elevation, $\eta_{03,SWASH}/\eta_{03,St}$, and (b) the corresponding relative error for one, two, three and four vertical layers as a function of the dimensionless depth kd	69
Figure 4.7 Normalised subharmonic transfer function $G_{SWASH}^{m-n}/G_{theor}^{m-n}$ for one, two, three and four vertical layers as a function of the dimensionless depths $k_m d$ and $k_n d$	74
Figure 4.8 Relative error in the normalised subharmonic transfer function $G_{SWASH}^{m-n}/G_{theor}^{m-n}$ for one, two, three and four vertical layers as a function of the dimensionless depths $k_m d$ and $k_n d$	74
Figure 4.9 Comparison of normalised subharmonic transfer function $G_{SWASH}^{m-n}/G_{theor}^{m-n}$ for the case that $k_n d \rightarrow k_m d$, $k_n d = 0.5k_m d$ and $k_n d = 1.5k_m d$	75

Figure 4.10 Normalised superharmonic transfer function $G_{SWASH}^{m+n}/G_{theor}^{m+n}$ for one, two, three and four vertical layers as a function of the dimensionless depths $k_m d$ and $k_n d$	76
Figure 4.11 Relative error in the normalised superharmonic transfer function $G_{SWASH}^{m+n}/G_{theor}^{m+n}$ for one, two, three and four vertical layers as a function of the dimensionless depths $k_m d$ and $k_n d$	76
Figure 4.12 Comparison of normalised superharmonic transfer function $G_{SWASH}^{m+n} / G_{theor}^{m+n}$ for the case that $k_n d = k_m d$, $k_n d = 0.5k_m d$ and $k_n d = 1.5k_m d$	77
Figure 4.13 Comparison of normalised second order amplitude of the surface elevation, $\eta_{02,SWASH}/\eta_{02,St}$, for two and four vertical layers for the cases that: a) both advection terms are included (blue line), b) only horizontal advection term is included (orange line) and c) both advection terms are excluded (yellow line).	79
Figure 5.1 Definition sketches of the three main methods to generate waves in numerical models; a) Method 1: weakly reflective wave generation, b) Method 2: moving boundary wave generation and c) Method 3: Internal wave generation.	85
Figure 5.2 Absolute reflection coefficient as a function of the incident wave angle θ and the dimensionless depth kd for the case that $c_0 = \sqrt{gd}$ and $\alpha = 0^\circ$	89
Figure 5.3 (a) The normalised energy velocities C_e/C_{gAiry} and (b) the corresponding relative error for one, two and three vertical layers as a function of the dimensionless depth kd	93
Figure 5.4 Source term addition method definition in a 2D vertical domain.	94
Figure 5.5 Spatially distributed source function definition in a 2D vertical domain.	94
Figure 5.6 Definition sketch of the implemented numerical set-up for the study of regular waves.	96
Figure 5.7 Comparison between computed (dashed lines) and target (solid lines) normalised water surface elevation η/η_0 for the case of linear waves with dimensionless depth (a,b) $kd = \pi/6$ (one layer) and (c,d) $kd = \pi$ (two equidistant layers).	97
Figure 5.8 Comparison between computed (markers) and target (solid lines) maximum (a) horizontal and (b) vertical velocity profiles using two internal wave generation methods for the case of deep water linear waves ($H = 0.02$ m, $T = 3.0$ s, $d = 10$ m, ten equidistant layers).	97
Figure 5.9 Snapshots of normalised water surface elevation η/η_0 at $t = 50T$ using the spatially distributed source function wave generation method for (a) $H/d = 0.01$ (linear), (b) $H/d = 0.1$, (c) $H/d = 0.2$ and (d) $H/d = 0.3$	98
Figure 5.10 Definition sketch of the implemented numerical set-up for the study of reflected dispersive waves using a) weakly reflective wave generation and b) internal wave generation.	99

Figure 5.11 Snapshot of normalised water surface elevation η/η_0 at $t = 50T$ using two internal wave generation methods and the analytical solution (black markers) for the case of deep water linear waves ($H = 0.02$ m, $T = 3.0$ s, $d = 10$ m, two equidistant layers) with a sponge layer at the left boundary and a fully reflective wall at the right boundary.	100
Figure 5.12 Snapshots of normalised water surface elevations η/η_0 at (a) $t = 28T$ and (b) $t = 100T$ using internal wave generation (method 3, red solid line) and weakly reflective wave generation (method 1, blue dashed line) compared with the analytical solution (black circles) for the case of dispersive waves.	101
Figure 5.13 Snapshots of normalised water surface elevations η/η_0 at $t = 100T$ using internal wave generation for three different sponge layer positions, $x_{sponge} \leq -3L$ (red solid line), $x_{sponge} \leq -2L$ (blue dash-dot line) and $x_{sponge} \leq -1L$ (black dashed line). . . .	102
Figure 5.14 Comparison between the frequency spectra resulting from using two internal wave generation methods and the target frequency spectrum S_t for irregular waves with $H_s = 0.5$ m, $d = 10$ m (a) $T_p = 12$ s (one layer) and (b) $T_p = 8$ s (two equidistant layers). . .	103
Figure 5.15 Definition sketch for the case of one internal wave generators at $x = 0$ m.	104
Figure 5.16 Comparison between (a) computed and (b) target normalised water surface elevation η/η_0 at $t = 40T$ for the case of oblique linear waves ($H = 0.01$ m, $T = 4.0$ s, $d = 1.0$ m and $\theta = 15^\circ$) with a sponge layer at the left and right boundaries and periodic boundaries at y -direction.	105
Figure 5.17 Comparison between computed (dashed line) and target (solid line) normalised water surface elevation η/η_0 at $t = 40T$ for the case of oblique linear waves ($H = 0.01$ m, $T = 4.0$ s, $d = 1.0$ m and $\theta = 15^\circ$): (a) cross section at $y = 45$ m, (b) cross section at $x = 0$ m.	105
Figure 5.18 Definition sketch for the case of two internal wave generators at $x = 0$ m and $x = 60$ m.	106
Figure 5.19 Comparison between (a) computed and (b) analytical normalised water surface elevation η/η_0 at $t = 30T$ for $\theta_1 = 15^\circ$, $\theta_2 = 195^\circ$:(c) cross section at $y = 35$ m (d) cross section at $x = 18$ m.	106
Figure 5.20 Comparison between (a) computed and (b) analytical normalised water surface elevation η/η_0 at $t = 30T$ for $\theta_1 = 15^\circ$, $\theta_2 = 165^\circ$:(c) cross section at $y = 35$ m (d) cross section at $x = 18$ m.	107
Figure 5.21 Definition sketch of the implemented numerical set-up for the study of short-crested waves.	108

Figure 5.22 The frequency spectra (top panels) and the normalised spreading function distributions (bottom panels) resulting from the use of method 3 (red dashed line), compared with the analytical solution (black solid line) for irregular short-crested waves with spreading standard deviation σ_θ of (a,c) 10° and (b,d) 30°	109
Figure 5.23 (a) The experimental setup as introduced in the numerical domain in SWASH, (b) Normalised wave height H/H_0 in the whole computational domain for the experiment of Berkhoff et al. (1982).	111
Figure 5.24 Comparison of normalised wave heights H/H_0 between numerical model results (red solid lines) and experimental data (black circles) along different measurement transects.	112
Figure 5.25 3D visualisation of regular waves propagating over the Berkhoff shoal.	113
Figure 5.26 Bottom levels of the experimental setup of Vincent and Briggs (1989) experiment as introduced in the numerical domain in SWASH.	114
Figure 5.27 Comparison of normalised wave heights H/H_0 between numerical model results (red solid lines) and experimental data (black circles) along different measurement transects for test case M1.	116
Figure 5.28 Comparison of normalised wave heights H/H_0 between numerical model results (red solid lines) and experimental data (black circles) along transect 4 for non-breaking irregular waves.	117
Figure 5.29 Normalised wave heights H/H_0 along transect 4 and wave-induced currents for breaking irregular waves.	117
Figure 5.30 3D visualisation of short-crested waves propagating over the shoal of Vincent and Briggs (1989) experiment (test case N3).	118
Figure 5.31 Experimental setup of Briggs et al. (1995) as introduced in the numerical domain in SWASH.	119
Figure 5.32 Comparison of diffraction coefficients between numerical model results (red plus signs) and experimental data (black circles) for test case M1.	121
Figure 5.33 Comparison of diffraction coefficients between numerical model results (red plus signs) and experimental data (black circles) for test case M4.	121
Figure 5.34 Comparison of diffraction coefficients between numerical model results (red plus signs) and experimental data (black circles) for test case N1.	122
Figure 5.35 Comparison of diffraction coefficients between numerical model results (red plus signs) and experimental data (black circles) for test case N2.	122
Figure 5.36 Comparison of diffraction coefficients between numerical model results (red plus signs) and experimental data (black circles) for test case B1.	123
Figure 5.37 Comparison of diffraction coefficients between numerical model results (red plus signs) and experimental data (black circles) for test case B2.	123

Figure 5.38 Comparison between the performance of the internal wave generation (method 3, red plus signs) and the weakly reflective generation (method 1, blue circles) for predicting the diffraction coefficients observed by Briggs et al. (1995) experiment. Black solid lines represent perfect agreement, while red solid line and the blue dashed line are the fitting lines for method 3 and method 1, respectively.	125
Figure 5.39 3D visualisation of short-crested waves diffracting around the vertical wall of Briggs et al. (1995) experiment (test case N1). . .	126
Figure A.1 Disturbance coefficient, k_d , and water surface elevation, η , in the inner computational domain at $t = 80T$ for regular incident waves with $H = 1$ m, $T = 12$ s, and $\theta = 0^\circ$ generated by an L-shaped wave generation layout (a,b), an arc-shaped wave generation layout (c,d), and by the use of periodic boundaries (e,f).	136
Figure A.2 Disturbance coefficient, k_d , and water surface elevation, η , in the inner computational domain at $t = 80T$ for regular incident waves with $H = 1$ m, $T = 12$ s, and $\theta = 5^\circ$ generated by an L-shaped wave generation layout (a,b), an arc-shaped wave generation layout (c,d), and by the use of periodic boundaries (e,f).	137
Figure A.3 Disturbance coefficient, k_d , and water surface elevation, η , in the inner computational domain at $t = 80T$ for regular incident waves with $H = 1$ m, $T = 12$ s, and $\theta = 10^\circ$ generated by an L-shaped wave generation layout (a,b), an arc-shaped wave generation layout (c,d), and by the use of periodic boundaries (e,f).	138
Figure A.4 Disturbance coefficient, k_d , and water surface elevation, η , in the inner computational domain at $t = 80T$ for regular incident waves with $H = 1$ m, $T = 12$ s, and $\theta = 15^\circ$ generated by an L-shaped wave generation layout (a,b), an arc-shaped wave generation layout (c,d), and by the use of periodic boundaries (e,f).	139
Figure A.5 Disturbance coefficient, k_d , and water surface elevation, η , in the inner computational domain at $t = 80T$ for regular incident waves with $H = 1$ m, $T = 12$ s, and $\theta = 20^\circ$ generated by an L-shaped wave generation layout (a,b), an arc-shaped wave generation layout (c,d), and by the use of periodic boundaries (e,f).	140
Figure A.6 Disturbance coefficient, k_d , and water surface elevation, η , in the inner computational domain at $t = 80T$ for regular incident waves with $H = 1$ m, $T = 12$ s, and $\theta = 25^\circ$ generated by an L-shaped wave generation layout (a,b), an arc-shaped wave generation layout (c,d), and by the use of periodic boundaries (e,f).	141
Figure A.7 Disturbance coefficient, k_d , and water surface elevation, η , in the inner computational domain at $t = 80T$ for regular incident waves with $H = 1$ m, $T = 12$ s, and $\theta = 35^\circ$ generated by an L-shaped wave generation layout (a,b), an arc-shaped wave generation layout (c,d), and by the use of periodic boundaries (e,f).	142

Figure A.8	Disturbance coefficient, k_d , and water surface elevation, η , in the inner computational domain at $t = 80T$ for regular incident waves with $H = 1$ m, $T = 12$ s, and $\theta = 40^\circ$ generated by an L-shaped wave generation layout (a,b), an arc-shaped wave generation layout (c,d), and by the use of periodic boundaries (e,f).	143
Figure A.9	Disturbance coefficient, k_d , and water surface elevation, η , in the inner computational domain at $t = 80T$ for regular incident waves with $H = 1$ m, $T = 12$ s, and $\theta = 45^\circ$ generated by an L-shaped wave generation layout (a,b), an arc-shaped wave generation layout (c,d), and by the use of periodic boundaries (e,f).	144

List of Tables

Table 2.1 Degree of capability of each type of model to describe different wave processes.	20
Table 3.1 Numerical input wave conditions for non-breaking waves based on the Vincent and Briggs (1989) experimental wave conditions. . .	49
Table 3.2 Root mean square error (RMSE) and skill factor of the normalised wave heights.	50
Table 4.1 Range of dimensionless depth kd as a function of the number of vertical layers and the corresponding relative error in the dispersion relation.	63
Table 4.2 Range of dimensionless depth kd as a function of the number of vertical layers and the corresponding relative error in the second order amplitude of the surface elevation.	67
Table 4.3 Range of dimensionless depth kd as a function of the number of vertical layers and the corresponding relative error in the amplitude dispersion.	70
Table 4.4 Range of dimensionless depth kd as a function of the number of vertical layers and the corresponding relative error in the third order amplitude of the surface elevation.	70
Table 4.5 Index of agreement of the second order subharmonic and superharmonic transfer functions of SWASH model.	78
Table 4.6 Range of dimensionless depth kd over which the relative error in the second order amplitude of the surface elevation, stays below 10%.	80
Table 5.1 Range of dimensionless depth kd as a function of the number of vertical layers and the corresponding relative error in the normalised energy velocities C_e/C_{gAiry}	93
Table 5.2 Wave conditions of the examined linear regular waves.	96
Table 5.3 Wave conditions of the examined nonlinear regular waves.	98
Table 5.4 Wave conditions of the examined irregular long-crested waves.	102
Table 5.5 Wave conditions of the examined irregular short-crested waves.	108

Table 5.6	Root mean square error (RMSE) and Skill factor of the normalised wave heights for each section.	112
Table 5.7	Numerical input wave conditions based on the Vincent and Briggs (1989) experimental wave conditions.	115
Table 5.8	Root mean square error (RMSE) and Skill factor of the normalised wave heights for each test case.	116
Table 5.9	Numerical input wave conditions based on the Briggs et al. (1995) experimental wave conditions.	120

Nomenclature

Latin symbols (I)

a	wave amplitude	m
B	sponge layer width	—
C	wave celerity or phase velocity	m/s
C_g	wave group velocity	m/s
C_e	wave energy velocity	m/s
c_0	linear wave speed for absorption	m/s
c_f	dimensionless friction coefficient	—
D	amplitude of the source function	m/s
$D(\theta)$	directional spreading function	—
d	still water depth	m
E	absolute error	—
	spectral density	m^2/Hz
f	wave frequency	Hz
f_p	peak wave frequency	Hz
\hat{f}	carrier wave frequency	Hz
G	transfer function	—
g	gravitational acceleration	m/s^2
$g(x)$	shape function of the source area	—
H	wave height	m
H_0	wave height at the wave generation boundary	m
H_s	significant wave height	m
h	total water depth	m
I	an integral for source function	$1/m$
K	number of layers	—
k	wave number	rad/m
kd	dimensionless water depth	—
k_d	disturbance coefficient	—
L	wavelength	m
L_w	wavelength	m
L_{per}	periodicity length	m
M	number of wave direction components	—
N	number of frequency components	—

Latin symbols (II)

N_x	number of cells in the x-direction	—
N_y	number of cells in the y-direction	—
N_{tot}	total number of wave components	—
q	non-hydrostatic pressure	N/m^2
R	reflection coefficient	—
$S(b)$	absorption function	—
$S(f)$	frequency spectrum	—
s_1	directional spreading parameter	—
T	wave period	s
T_p	peak wave period	s
t	time	s
U	depth averaged velocity in x-direction	m/s
u	horizontal velocity component in x-direction	m/s
\hat{u}	inter-layer velocity variations	m/s
v	horizontal velocity component in y-direction	m/s
W	width of the wave generation source area	m
w	vertical velocity component in z-direction	m/s
w_{rel}	relative velocity at the layer interface	m/s
x	horizontal Cartesian coordinate	—
y	second horizontal Cartesian coordinate	—
z	vertical Cartesian coordinate	—

Greek symbols (I)

α	Phillips constant	—
	wave propagation angle for absorption	°
β	angle related to arc-shaped wave generation	°
γ	peak enhancement factor	—
Δf	frequency interval	Hz
Δt	time step	s
Δx	grid spacing in x-direction	m
Δy	grid spacing in y-direction	m
$\Delta\theta$	wave propagation angle interval	°
$\delta(x)$	Dirac delta function	$1/m$
δ	auxiliary coefficient for source area	—
ϵ	wave steepness	—
	random phase	—
η	surface elevation	m
η^*	additional surface elevation	m
η_i	instantaneous surface elevation	m
θ	wave propagation angle	°
κ	dimensionless water depth	—
Λ	source function applied to a single point	m^2/s
ρ_0	density	kg/m^3

Greek symbols (II)

σ	spectral width parameter	—
σ_θ	spreading standard deviation	°
τ_b	bottom stress	m^2/s^2
τ_{ij}	turbulent stresses	m^2/s^2
ϕ	velocity potential	m^2/s
	frequency dependent factor	—
ω	angular frequency	rad/s
ω_{13}	amplitude dispersion	—
$\bar{\omega}$	carrier angular frequency	rad/s

Symbols

$^\circ$	angle	degrees
∂	partial derivative	
d	total derivative	
∇	vector differential operator	
Γ	Gamma function	
Σ	sum	

Subscripts

01	first order amplitude	
02	second order amplitude	
03	third order amplitude	
12	layer interface between first and second layer	
13	third order correction to the first order	
b	bottom	
e	evanescent mode	
GB	generation boundary	
k	k-th layer	
$k1$	first vertical layer (bottom)	
$k2$	second vertical layer	
m	wave component m	
max	maximum value	
$mean$	mean value	
min	minimum value	
n	normalised	
	wave component n	
O	observed value	
P	predicted value	
p	progressive mode	
St	Stokes	
s	surface	
t	target	

Superscripts

(1)	first order solution
(2)	second order solution
(3)	third order solution
$2m$	self interacting superharmonic
$2n$	self interacting superharmonic
$m + n$	superharmonic
$m - n$	subharmonic
I	incident wave

Abbreviations

1D	one-dimensional
2D	two-dimensional
2DV	two-dimensional vertical domain
3D	three-dimensional
BE	Boussinesq equations
CFL	Courant-Friedrichs-Lewy criterion
CPU	Central Processing Unit
GABC	Generating Absorbing Boundary Condition
HCWEC	Heaving Cylindrical Wave Energy Converter
HPC	High Performance Computing
IA	Index of Agreement
JONSWAP	Joint North Sea Wave Observation Project
MSE	Mild-slope equations
NEOWAVE	Non-hydrostatic Evolution of Ocean WAVES
NHE	Non-hydrostatic equations
NHWAVE	Non-Hydrostatic WAVE Model
NSE	Navier-Stokes equations
OSWEC	Oscillating Surging Wave Energy Converter
RANS	Reynolds-Averaged Navier-Stokes equations
RMSE	Root Mean Square Error
SPH	Smoothed Particle Hydrodynamics
SWAN	Simulating WAVes Nearshore
SWASH	Simulating WAVes till SHore
SWL	Still Water Level
TMA	Texel, Marsen, Arsloe
VOF	Volume Of Fluid
WAM	WAVE Modelling
WEC	Wave Energy Converter
WG	Wave Gauge

Samenvatting

Dutch summary

De kustzone is altijd een hoeksteen geweest in de ontwikkeling van de mens, wat betreft sociale, culturele en economische evolutie. Tegenwoordig komt een groot deel van de globale economische activiteit uit kustzones via maritime transport, met een continu stijgende vraag naar havenfaciliteiten. Daarbovenop maken de recreatieve opportuniteiten aangeboden door kustzones, samen met hun unieke landschap, deze zones zeer aantrekkelijk voor de ontwikkeling van eigendom en toeristische en commerciële activiteiten. Als resultaat is een groot deel van de menselijke bevolking geconcentreerd in deze zones, wat de kustsystemen consequent onder druk heeft geplaatst. Terzelfertijd zijn de opwarming van de aarde en de klimaatverandering deze kustzones direct aan het beïnvloeden, waardoor deze zones steeds vatbaarder worden.

Een van de uitdagingen waarmee de ingenieurswereld geconfronteerd wordt is de studie van kustomgevingen, om hun kwetsbaarheid veroorzaakt door het stijgende zeeniveau en de resulterende verhoging in golfhoogtes te beoordelen. Met het oog op dit doel vormen numerieke modellen een waardevol middel voor coastal engineers. In de laatste jaren worden fase-oplossende golfmodellen steeds meer gebruikt om een realistische en nauwkeurige voorstelling van de golven en hun transformatie in tijd en ruimte te verkrijgen.

In deze thesis beschouwen we ontwikkelingen in twee fase-oplossende modellen, het milde-helling golfmodel MILDwave en het non-hydrostatische golfmodel SWASH. Het hoofddoel is het verbeteren van de homogeniteit van de opgewekte golfvelden in deze golfmodellen middels het opvoeren van hun vermogen om de beoogde golfcondities accuraat te genereren en terzelfdertijd het minimaliseren van de verstoring van het opgewekte golfveld door ongewenste golfdiffractie- en reflectiepatronen dankzij de opgelegde numerieke grenzen.

Initieel worden periodische grenzen ontwikkeld in MILDwave en wordt een nieuwe golfgeneratie layout voorgesteld die bestaat uit een enkele golfgeneratie lijn binnen een computationeel domein gecombineerd met periodische laterale grenzen. Deze golfgeneratie layout is voorgesteld als een alternatief voor de L-vormige en boogvormige golfgeneratie layouts. De eerder in literatuur voorgestelde golfgeneratie layouts leiden tot golfdiffractiepatronen binnen het computationeel domein als een resultaat van de kruising van twee golfgeneratie lijnen en de interactie met de laterale dempingslaag. Daartegenover, met de periodische grenzen techniek,

komt de informatie die een zijde van het numerieke domein verlaat binnen in de tegenovergestelde zijde en dus zijn geen laterale dempingslagen nodig. Als resultaat verbetert de voorgestelde generatie layout significant de homogeniteit van het gegenereerde golfveld en bijgevolg verhoogt de nauwkeurigheid van de simulaties in het geval van schuine regelmatige golven. Daarbovenop is de prestatie van de periodieke grenzen geëvalueerd voor twee verschillende golfsynthese methoden voor de generatie van kortkruinige golven. De resultaten tonen dat het model capabel is om zowel een homogeen golfveld als het beoogde frequentie- en directionele spectrum te reproduceren. De generatielayout gebruikmakend van periodische laterale grenzen maakt het milde-helling golfmodel MILDwave een essentieel middel om kustzones te bestuderen met 3D lineaire golfcondities, dankzij zijn significante kleine computationele kost en zijn hoge numerieke stabiliteit en robuustheid.

Alhoewel milde-helling golfmodellen redelijk goede resultaten produceren in diep en intermediair water, zijn ze niet zo nauwkeurig in ondiep water waar de nonlineariteit sterk wordt en dus niet verwaarloosbaar is. In gevallen waar nonlineaire processen zoals golfbreking, golf-golfinteractie of harmonische generatie belangrijk zijn, zijn modellen gebaseerd op de niet-hydrostatische aanpak een aantrekkelijk alternatief. Een representatief model van deze categorie is het niet-hydrostatische golfmodel SWASH. In de huidige thesis worden de geldende vergelijkingen van het niet-hydrostatisch golfmodel, SWASH, geanalyseerd om de lineaire en niet-lineaire eigenschappen van het model te bestuderen. Preciezer, een Stokes-type Fourier analyse op een vlakke bodem is uitgevoerd om zo de lineaire, tweede en derde orde geldende vergelijkingen van SWASH te definiëren. Door het stelsel van deze vergelijkingen analytisch op te lossen worden de eerste, tweede en derde orde vergelijkingen van SWASH afgeleid voor de gevallen waar een, twee, drie en vier equidistante verticale lagen toegepast zijn. De vergelijking van de afgeleide uitdrukkingen met de exacte oplossingen gegeven door Stokes golftheorie laat de identificatie van dieptebereiken toe waarover het model de beoogde nauwkeurigheid bereikt afhankelijk van het aantal gebruikte lagen. Deze dieptebereiken zijn samengevat in tabellen waaruit SWASH gebruikers kunnen beslissen hoeveel verticale lagen te gebruiken, rekening houdend met de acceptabele fout op de lineaire en nonlineaire eigenschappen van elk specifiek geval. Los van het bovenstaande kunnen de afgeleide oplossingen gebruikt worden om hogere ordes randvoorwaarden te formuleren voor regelmatige en onregelmatige golven. Gebruik maken van de exacte oplossingen van de geldende vergelijkingen als input aan de golfgeneratiegrens verzekert dat de vorm van de golf behouden blijft doorheen het ganse testoppervlak en dus blijft het gegenereerde golfveld homogeen.

Uiteindelijk werden twee golfgeneratie methodes ontwikkeld in het golfmodel SWASH. Een bron term toevoegingsmethode waar additionele oppervlakteverhoging is toegevoegd aan het berekende wateroppervlak in een specifieke locatie in het domein en een ruimtelijk verdeelde bronfunctie waar een ruimtelijk verdeelde massa toegevoegd is in de vrije oppervlak vergelijking. Interne golfgeneratie is voorgesteld als een alternatief voor de traditionele laagreflectieve golfgeneratie volgens dewelke de horizontale snelheidscomponenten van de beoogde inkomende golven worden opgelegd aan de grens van het computationele domein over de verticale richting. De totale snelheid is een lineaire superpositie van de snelheid van de beoogde golven en

de snelheid van de golven die zich voortplanten naar de grens. Deze methode maakt gebruik van de veronderstelling dat de golven die naar de rand van het computationele domein propageren ondiepe water golven zijn met kleine amplitudes en een richting loodrecht op de domeinsgrens en dus wordt deze methode ook als laagreflectief gezien wanneer dispersieve en directionele golven onderzocht worden. Een vergelijking tussen de interne en de laagreflectieve golfgeneratie methodes toont aan dat de eerstvernoemde voordelig is over de laatstvernoemde. De voorgestelde methode maakt het mogelijk om nauwkeuriger de beoogde golfkarakteristieken te genereren zelf in het geval van hoogdispersieve en directionele golven en terzelve tijd wordt elke reflectie door de aanwezigheid van de laagreflectieve golfgenerator vermeden. Daarbovenop is het bewezen dat het algemene prestatievermogen van de ruimtelijk verdeelde bronfunctie beter is dan de bronterm toevoegingsmethode aangezien de laatstvernoemde onstabiel wordt voor grote golfhoogtes en hoge frequentie ruis kan veroorzaken. Het ontwikkelde model met de toevoeging van de interne golfgeneratie methode is ook gevalideerd met drie benchmark experimentele testen. In deze vergelijking is een zeer goede overeenkomst geobserveerd tussen het numerieke model en de experimentele resultaten.

In dit werk is fundamenteel onderzoek verricht om het vermogen van fase-oplossende modellen voor het genereren van homogene golfvelden te verbeteren, en op deze manier zijn de huidige kennishiaten aangepakt. De nieuwe ontwikkelingen en implementaties zijn grondig gevalideerd met analytische oplossingen en experimentele data. De observaties maken duidelijk dat de nieuwe methodes ontwikkeld in MILDwave en SWASH succesvol gebruikt kunnen worden om lang bestaande ingenieursproblemen, zoals de studie van kunstmatige structuren (e.g. golfbrekers, artificiële riffen) en golfenergieconvector (GEC) parken op een nauwkeurigere manier te bestuderen met realistische driedimensionale golfcondities.

Summary

The coast has always formed a cornerstone of human development, in terms of social, cultural and economic evolution. Nowadays, a big proportion of the global economic activity comes from the coastal zones through maritime transport, with the demands for harbor and port facilities to be continuously increasing. Additionally, the recreation opportunities offered by the coastal zones together with the unique landscapes, make these areas very attractive for property development and touristic and commercial activities. As a result a big part of the human population is concentrated in such areas, which consequently has put coastal systems under high pressure. At the same time, global warming and climate change are directly influencing these coastal areas, which are consequently becoming more and more susceptible.

One of the challenges that the engineering world has to face is the study of coastal environments, in order to assess their vulnerability due to the rising of the sea-level and the resulting increase of the wave heights. Towards this goal, numerical models constitute a valuable tool for coastal engineers. In recent years, phase-resolving wave models are used more and more often in order to get a realistic and accurate representation of the waves in the field and their transformation over time and space.

In this dissertation, developments are considered in two phase-resolving models, the mild-slope wave model MILDwave and the non-hydrostatic wave model SWASH. The core aim is to improve the homogeneity of the generated wave fields in these wave models by enhancing their capability of accurately generating the target wave conditions and at the same time by minimising the disturbance of the generated wave field by unwanted wave diffraction and reflection patterns due to the imposed numerical boundaries.

Initially, periodic boundaries are developed in the MILDwave model and a new wave generation layout is proposed which consists of a single wave generation line inside the computational domain combined with periodic lateral boundaries. This wave generation layout is proposed as an alternative to the L-shaped and arc-shaped wave generation layouts. These previously proposed from literature wave generation layouts lead to wave diffraction patterns inside the computational domain as a result of the intersection of the two wave generation lines and the interaction with the lateral sponge layers. By contrast, with the periodic boundaries technique, the information leaving one end of the numerical domain enters the

opposite end and thus no lateral sponges are required. As a result, the proposed generation layout improves significantly the homogeneity of the generated wave field and consequently increases the accuracy of the simulations in case of oblique regular waves. In addition, the performance of the periodic boundaries is evaluated for two different wave synthesis methods for the generation of short-crested waves. The results show that the model is capable of reproducing a homogeneous wave field as well as the target frequency spectrum and the target directional spectrum. The developed generation layout using periodic lateral boundaries makes the mild-slope wave model, MILDwave, an essential tool to study coastal areas under 3D linear wave conditions, due to its significantly small computational cost and its high numerical stability and robustness.

Although mild-slope wave models produce reasonably good results in deep and intermediate water, they are not as accurate in shallow water where nonlinearity is becoming strong and thus not negligible. In cases that nonlinear processes such as wave breaking, wave-wave interaction or harmonic generation are important, models based on the non-hydrostatic approach are an attractive alternative. A representative model of this category is the non-hydrostatic model SWASH. In the present dissertation, the governing equations of the non-hydrostatic wave model, SWASH, are analysed in order to examine the linear and nonlinear properties of the model. More precisely, a Stokes-type Fourier analysis on a flat bottom is performed in order to define the linear, second and third order governing equations of SWASH. Solving analytically the system of these equations, the first, second and third order solutions are derived for the cases that one, two, three and four equidistant vertical layers are applied. The comparison of the derived expressions with the exact solutions given by Stokes wave theory allows for the identification of depth ranges over which the model achieves the target accuracy depending on the number of layers employed. These ranges have been summarised in tables from which SWASH users can decide on the number of vertical layers to be applied, taking into account the acceptable error on the linear and nonlinear properties of each specific case. Apart from the above, the derived solutions are essential to formulate higher order boundary conditions for regular and irregular waves. Using the exact solutions of the governing equations as input at the wave generation boundary ensures that the wave shapes are maintained throughout the whole test area and thus the generated wave field remains homogeneous.

Finally, two internal wave generation methods are developed in the wave model, SWASH. A source term addition method where additional surface elevation is added to the calculated surface elevation in a specific location in the domain and a spatially distributed source function where a spatially distributed mass is added in the free surface equation. Internal wave generation is proposed as an alternative to the traditional weakly reflective wave generation according to which the horizontal velocity components of the target incident waves are imposed at the boundary of the computational domain over the vertical direction. The total velocity is a linear superposition of the velocity of the target waves and the velocity of the waves propagating towards the boundary. This method is making use of the assumption that the waves propagating towards the boundary of the computational domain are shallow water waves with small amplitude and direction perpendicular to the domain

boundary and thus, this method is considered weakly reflective when dispersive and directional waves are examined. A comparison between the internal and the weakly reflective wave generation methods shows that the former method is advantageous over the latter one. The proposed method is able to generate more accurately the target wave characteristics even in case of highly dispersive and directional waves and at the same time any reflection due to the presence of the weakly reflective wave generator is avoided. Additionally, it is proved that the overall performance of the spatially distributed source function is better than the source term addition method since the latter becomes unstable for large wave heights and may cause high frequency noise. The developed model with the addition of the internal wave generation method has also been validated against three benchmark experimental tests. Through this comparison, a very good agreement is observed between the numerical model and the experimental results.

In this work, fundamental research has been performed to improve the capability of phase-resolving models of generating homogeneous wave fields and in this way the present knowledge gaps are being tackled. The new developments and implementations are thoroughly validated against analytical solutions and experimental data. The observations reveal that the new methods developed in MILDwave and SWASH can be successfully used to study long-existing engineering problems in a more accurate way, such as the study of man-made structures (e.g. breakwaters, artificial reefs, artificial islands) and wave energy converter (WEC) farms under realistic three-dimensional wave conditions.

Chapter 1

Introduction

1.1 Background

Already from the early stages of human existence and development the importance of coastal zones was revealed. Human civilization and culture were highly dependent on these areas that form borders between land and water and offer a variety of opportunities in terms of food supply, water resources, transport and recreation and thus constitute areas of high economic activity. The nature is also thriving around coastal areas thanks to the special conditions of humidity and mineral concentrations that form the ideal environment for a large number of different species of flora and fauna to live and reproduce.

Taking all the above into consideration, it comes as no surprise that urban centers have been developed in coastal areas in the ancient ages and they continue to exist and develop today. Nowadays, a big proportion of the global economic activity comes from the coastal zones through maritime transport, with the demands for harbor and port facilities to be continuously increasing. Additionally, the recreation opportunities offered by the coastal zones together with the unique landscapes that are observed there, make these areas very attractive for property development and touristic and commercial activities. As a result a big part of the human population is concentrated in such areas, where megacities have been formed especially during the beginning of the 21st century. This is a worldwide phenomenon that is still evolving and is expected to become more profound in the near future. In Figure 1.1 coastal cities with a population of more than 8 million are presented together with an estimation of the human population for the next decades living near the coast.

This high concentration of human population and the increasing economic exploitation of the coasts have put coastal systems under high pressure, making them vulnerable to damage. The intense urbanization has led to over-construction of infrastructure that can originate distortion to the natural ecosystems and can affect the resilience of coastal areas by causing coastal erosion and flooding. While coping with these challenges of socio-economic origin, coastal environments will have

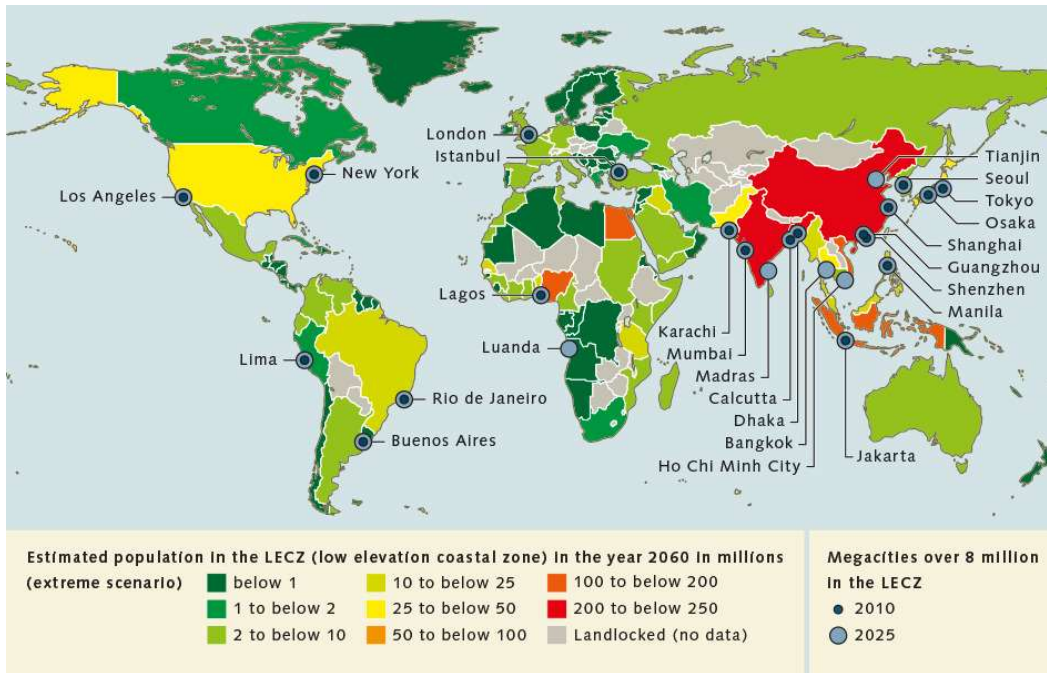


Figure 1.1: Estimation of the human population living near the coast in 2060 (Neumann et al., 2015).

to face another threat: climate change. The consequences of global warming and the climate change are becoming more and more noticeable during the last decade, including rising of the sea-level and a higher risk for extreme climate incidents, like storms, that change the wave climate. Figure 1.2 shows the rise in global mean sea level from 1900 and predictions for the mean sea level for the coming decades (Dangendorf et al., 2019). Admittedly, the impact of the climate change on coastal communities will become bigger over the years, since the extreme phenomena are expected to intensify.

Given the high population densities and the high economic and environmental importance of coastal areas, the consequences of the sea level rise will have a huge impact on the society, unless measures are taken for the protection of the coastal zones. Coastal structures, such as breakwaters, dikes etc, have been used already from the ancient years in order to protect the coast and the hinterland. The challenge, nowadays, is to reevaluate their design and to design new structures in a way that they will be able to cope with the new conditions that follow from the climate change. In that sense coastal engineers have a very important role in developing sustainable coastal zones as well as designing robust coastal defense systems for the next century. In order to achieve that they need to have a good prediction of the forces on the structures coming from the coastal hazard, and execute a risk assessment for the damage associated to the hazard. The shoreline needs to be protected from waves, flooding, extreme storm phenomena and erosion, while the appropriate conditions need to be assumed during the design phase of the coastal structures.

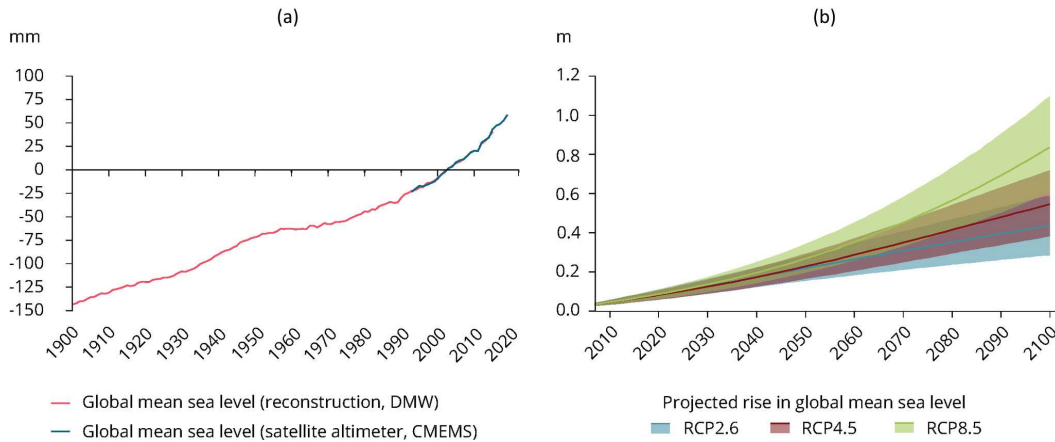


Figure 1.2: (a) The rise in global mean sea level from 1900 and (b) projections of global mean sea level until 2100 for three different emission cases (from Copernicus Marine Environment Monitoring Service, Intergovernmental Panel on Climate Change).

The correct prediction of the design data of the structures requires an accurate representation of the wave field for the conditions under examination, which is achieved through modeling and simulations. Numerical wave models are used from engineers all over the world with the aim of predicting the wave characteristics at the areas of interest. Depending on the problem under investigation and corresponding time and space scales, different models are used. For the numerical modelling, the study area is typically discretized into grid cells where the basic equations describing the governing physical processes are solved in the grid cell corner or mid nodes. The number of grid cells, the number of variables and the numerical solution technique determine the computational time that is needed for each particular case. Typically, the higher the resolution in space and time, the higher the accuracy of the results but also the higher the computational cost becomes. Therefore, a balance has to be sought between computational cost and accuracy.

Phase-resolving models are used more and more often in order to get a realistic and accurate representation of the waves in the study area and their transformation over time and space. Several phase-resolving numerical models are based on the full Reynolds-Averaged Navier-Stokes equations (Higuera et al., 2013b; Lin and Liu, 1998), which are able to resolve wave propagation and breaking processes and to provide three-dimensional velocity and pressure profiles, but at the same time add the restriction of very high computational cost. As an alternative, numerical models have been developed that are using approximated equations, typically averaged over the depth, such as mild-slope, Boussinesq-type and non-hydrostatic wave models. These models are necessary tools, especially when long duration sea states and large domains are considered.

Models based on mild-slope equations (Berkhoff, 1972; Copeland, 1985; Radder and Dingemans, 1985) are often employed to predict transformation processes of linear waves, such as wave refraction, diffraction, shoaling and reflection. On the other hand, Boussinesq-type wave models are frequently used to study wave transformation of nonlinear waves in coastal regions. They constitute the depth-

integrated equations of surface wave propagation and include perturbation expansions of the variables in order to improve their wave dispersion and nonlinear dynamics (Lynett and Liu, 2002; Shi et al., 2012; Sørensen et al., 2004). Typically, Boussinesq-type wave models are highly complicated due to e.g. high-order spatial derivatives and thus computationally expensive. An alternative to the Boussinesq-type wave models are the non-hydrostatic wave models (Bai and Cheung, 2012; Ma et al., 2012; Stelling and Zijlema, 2003) which constitute a robust tool, able to accurately describe coastal phenomena. Non-hydrostatic wave models can directly resolve the vertical and horizontal flow structure by retaining the 3D momentum equations and can improve their wave dispersion and the degree of nonlinearity by making use of a few vertical layers, while they use first order spatial derivatives. A more detailed description of the State-of-the-art of the aforementioned wave model approaches can be found in Chapter 2.

One of the most important requirements of the phase-resolving models is to be able to generate and maintain a homogeneous wave field all over the area under examination. More precisely, the generated wave field should agree to a high degree with the target one and should not be disturbed by unwanted wave diffraction and reflection patterns due to the imposed wave generation methods and the handling of the numerical boundaries. In this context, in the present dissertation developments are considered both in the mild-slope wave model MILDwave and the non-hydrostatic wave model SWASH in order to improve their efficiency to generate homogeneous wave fields. The accuracy of these models is of significant importance, since it allows for a robust design of coastal defense systems that can minimize the impact of the coastal hazards on local communities and ensure the resilience of these highly pressured but valuable areas.

1.2 Knowledge gaps

In this work, the following main knowledge gaps are identified regarding the ability of the phase-resolving models to generate homogeneous wave fields:

1. *Lack of a wave generation layout in mild-slope wave models to generate regular oblique and irregular short-crested waves;*
The previously proposed from literature L-shaped and arc-shaped wave generation layouts lead to wave diffraction patterns inside the computational domain as a result of the intersection of the two wave generation lines and the interaction with the lateral sponge layers. These diffraction patterns affect significantly the homogeneity of the generated wave field and consequently reduce the accuracy of the simulations.
2. *Absence of the exact nonlinear solutions of the governing equations of the non-hydrostatic model SWASH;*
The governing equations of the SWASH model have not been analysed before regarding their ability to describe high order nonlinear waves. Despite the fact that there are tables with dimensionless water depth ranges (kd) over which the model achieves the target linear properties depending on the number

of layers employed, there are no such tables for the nonlinear properties. Additionally, the lack of knowledge of the nonlinear expressions of the model affects the accuracy of the wave generation, since free spurious high order waves are inevitably introduced when incorrect solutions are imposed at the boundaries.

3. *Inability to handle dispersive and oblique waves at the wave generation boundary of the non-hydrostatic models.*

The most common method used to generate waves in non-hydrostatic models is the weakly reflective wave generation boundary. This method is making use of the assumption that the waves propagating towards the boundary of the computational domain are shallow water waves with small amplitude and direction perpendicular to the domain boundary and thus, this method is considered weakly reflective when dispersive and directional waves are examined. For the study of man-made structures and wave energy converter (WEC) farms, where the reflected and radiated waves cannot be estimated a priori, the weakly reflective wave generation method leads to reflections at the generation boundary which deteriorate the accuracy of the numerical results.

1.3 Objectives and Methodology

Based on the knowledge gaps identified in Section 1.2, the following main objectives and the corresponding methodology to achieve them are defined:

1. *Develop a wave generation layout for accurate and fast generation of short-crested waves in the mild-slope wave model MILDwave;*

To achieve this objective, periodic boundaries are developed in MILDwave model and a new wave generation layout is proposed which consists of a single wave generation line inside the computational domain combined with periodic lateral boundaries. This wave generation layout is compared with the L-shaped and arc-shaped wave generation layouts with respect to their efficiency to generate oblique regular waves. Moreover, the model is extended so that it can generate short-crested waves, while different wave synthesis methods are examined for the generation of short-crested waves. MILDwave with the addition of the new wave generation layout is validated against analytical solutions and experimental data.

2. *Identify linear and nonlinear properties of the non-hydrostatic wave model SWASH;*

A Stokes-type Fourier analysis on a flat bottom is performed in order to define the linear, second and third order governing equations of SWASH. Solving analytically the system of these equations, the first, second and third order solutions are derived for the cases that one, two, three and four equidistant vertical layers are applied. The comparison of the derived expressions with the exact solutions given by the Stokes wave theory, allows for the formation

of tables with water depth ranges over which the model achieves the target accuracy depending on the number of layers employed.

3. *Minimise reflections at the wave generation boundary of the SWASH model.* To achieve this objective, two internal wave generation methods are developed in the open source non-hydrostatic wave model SWASH: a source term addition method and a spatially distributed source function. In addition, the energy velocity, with which the internal wave propagates, is derived for the governing equations of SWASH in case a multi-layer layout is implemented. The developed model is validated against analytical solutions and three benchmark experimental tests. Finally, a comparison is carried out between the performance of the developed internal wave generation and the traditional weakly reflective wave generation for the case of waves that are reflected back to the numerical boundary to demonstrate the advantages of the proposed method.

In Figure 1.3, a flowchart is presented, summarising the identified knowledge gaps, the objectives to tackle them and the methodology that is followed in the present dissertation.

1.4 Outline

The structure of the thesis is as follows. First, Chapter 1 provides the background and the knowledge gaps as well as the general objectives of this thesis. In Chapter 2, the fundamentals regarding the wave theories are presented and the applied numerical wave models MILDwave and SWASH are introduced. The next chapter (Chapter 3) concerns the development of the periodic lateral boundaries in MILDwave. A wave generation layout using this development is proposed to generate directional waves. Through comparison with two other wave generation layouts as well as with experimental data we demonstrate the efficiency and accuracy of the proposed layout. Subsequently, an analysis of the governing equations of SWASH model is presented in Chapter 4 where we define the first, second and third order equations and we derive the corresponding solutions. These solutions are compared with exact solutions given in literature to determine how the model improves its linear and nonlinear properties by increasing the number of vertical layers. In Chapter 5, the SWASH model is developed further to be able to generate waves internally. This method is proposed as an alternative to the weakly reflective wave generation to study coastal areas and wave energy converter (WEC) farms even under highly dispersive and directional waves without any spurious reflection from the wave generator. Finally, the key findings of the individual chapters are summarised and recommendations for future research are provided in Chapter 6.

In chapters 3, 4 and 5 different developments and analyses, concerning the improvement of the homogeneity of the generated wave fields in phase resolving wave propagation models, are handled. Thus, a literature review together with the State-of-the-art and the novelty of the executed research are introduced in each of the above chapters individually.

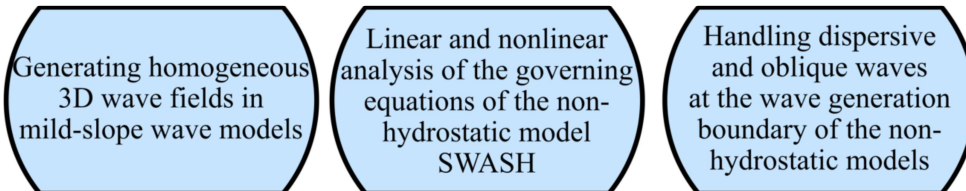
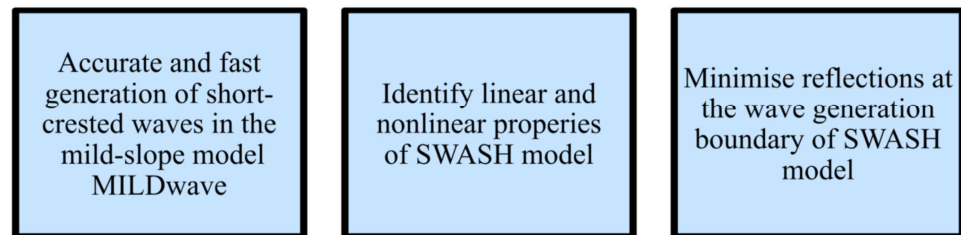
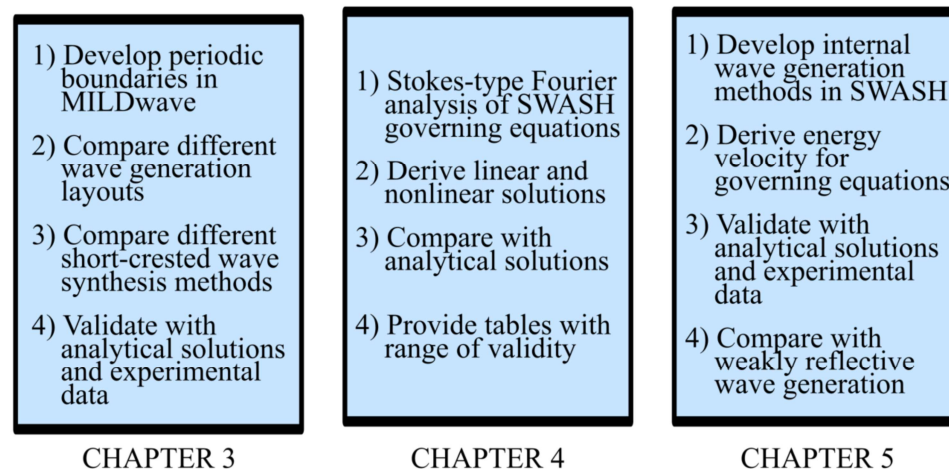
KNOWLEDGE GAPS**MAIN OBJECTIVES****METHODOLOGY**

Figure 1.3: Flowchart containing the main knowledge gaps, the objectives and the methodology of the present dissertation.

Chapter 2

Theoretical Background

This chapter is introducing information for later use in this dissertation. Firstly, it is addressed to readers who are not familiar with the theoretical background of the wave theories and the numerical models that are used in this manuscript. The exact solutions of linear and nonlinear Stokes wave theories (up to third order) are presented together with the second order transfer functions for subharmonic and superharmonic interactions. Secondly, these solutions are used in Chapter 4 as reference to define and evaluate the linear and nonlinear properties of the SWASH model. Finally, a short literature review on different types of numerical wave models with their capabilities is presented, while the MILDwave and SWASH models are introduced.

2.1 Water wave theories

2.1.1 Linear wave theory

The simplest wave theory is that of linear waves, known as Airy or small-amplitude wave theory (Airy, 1845). This theory serves as a solution of the linearised basic equations of potential flow which have been derived assuming the following:

1. The fluid is homogeneous, incompressible and inviscid;
2. The surface tension forces can be neglected;
3. The water flow is irrotational (neglect viscous and turbulent stresses);
4. The bed is horizontal, fixed and impermeable (vertical velocity is zero at the bed level);
5. The pressure along the free surface is constant;
6. The Coriolis effect can be neglected;

7. The wave amplitude is small compared to the wavelength and water depth (see Figure 2.1).

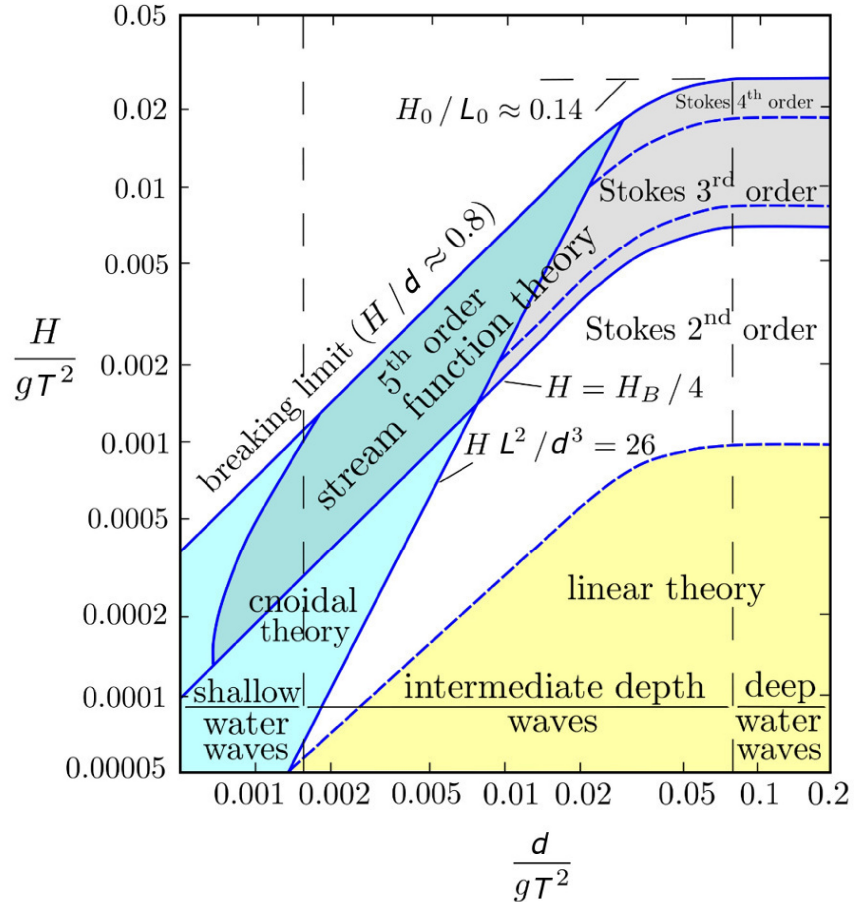


Figure 2.1: The diagram of Le Mehaute presenting the validity region of each wave theory.

In Figure 2.2 a regular wave propagating with a wave celerity (phase velocity) C on a flat bottom with water depth d is demonstrated. The main wave parameters are the wave height H , the wavelength L and the wave period T . The wave height, H , is defined as the distance between the highest (crest) and the lowest (trough) point of the wave and the wave amplitude is defined as $a = H/2$. The horizontal distance between two successive wave crests or troughs is the wavelength L , while the time interval that is required for the wave to travel a distance equal to the wavelength is defined as the wave period T . The horizontal (x -direction) and vertical (z -direction) velocity components of a water particle are u and w , respectively. Other wave parameters include the wave number $k = 2\pi/L$, the angular frequency $\omega = 2\pi/T$ and the wave celerity $C = \omega/k$.

The assumption of irrotational flow allows to define the flow in terms of velocity

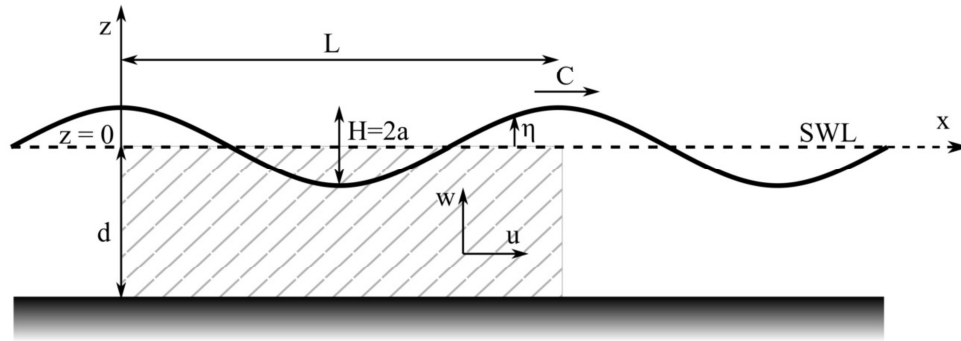


Figure 2.2: Definition sketch of wave parameters.

potential ϕ so that:

$$u = \frac{\partial \phi}{\partial x} \quad (2.1)$$

$$w = \frac{\partial \phi}{\partial z} \quad (2.2)$$

Additionally, the velocity potential must satisfy the Laplace partial differential equation:

$$\frac{\partial^2 \phi}{\partial x^2} + \frac{\partial^2 \phi}{\partial z^2} = 0 \quad -d < z < \eta(x, t) \quad (2.3)$$

The linear wave theory is derived by solving Equation 2.3 for the hatched domain presented in Figure 2.2 after defining the boundary conditions of the problem for the bottom and the free surface, while periodicity is assumed at the left and right boundaries.

Since the bottom is considered flat and impermeable, no vertical flow is present and thus the following boundary condition is extracted:

$$w = \frac{\partial \phi}{\partial z} = 0 \quad \text{at } z = -d \quad (2.4)$$

At the free surface, there are two boundary conditions. The linearised kinematic and dynamic conditions are expressed in Equations 2.5 and 2.6, respectively:

$$w = \frac{\partial \eta}{\partial t} \quad \text{at } z = 0 \quad (2.5)$$

$$g\eta + \frac{\partial \phi}{\partial t} = 0 \quad \text{at } z = 0 \quad (2.6)$$

Substituting Equations 2.4 and 2.6 in Equation 2.3 the velocity potential for the linear wave theory is obtained by solving the wave boundary value problem:

$$\phi = \frac{ag}{\omega} \frac{\cosh(k(z+d))}{\cosh(kd)} \sin(kx - \omega t) \quad (2.7)$$

Subsequently, the orbital velocity components become:

$$u = \frac{agk}{\omega} \frac{\cosh(k(z+d))}{\cosh(kd)} \cos(kx - \omega t) \quad (2.8)$$

$$w = \frac{agk}{\omega} \frac{\sinh(k(z+d))}{\cosh(kd)} \sin(kx - \omega t) \quad (2.9)$$

The initial assumption that the wave height is small compared to the wavelength ($H/L \ll 1$) allowed to define the surface boundary conditions at the still water level $z = 0$ (SWL) instead of $z = \eta$. Thus, the derived solutions of ϕ , u and w are valid up to $z = 0$.

Inserting the velocity potential from Equation 2.7 into Equation 2.6, we get the equation for the surface elevation:

$$\eta = a \cos(kx - \omega t) \quad (2.10)$$

Taking the time derivative of Equation 2.6, eliminating η using Equation 2.5 and substituting the velocity potential from Equation 2.7, the linear dispersion relation is derived:

$$\omega^2 = gk \tanh(kd) \quad (2.11)$$

It is noticed from Equations 2.7 - 2.11 that when the wave height, the period and the water depth are known, then all the wave characteristics can be determined. In addition, the linear dispersion relation indicates that the angular frequency and subsequently the wave celerity are independent of the wave amplitude.

$$C = \frac{\omega}{k} = \sqrt{\frac{g}{k} \tanh(kd)} \quad \frac{\pi}{10} < kd < \pi \text{ (transitional water)} \quad (2.12)$$

which is simplified for deep and shallow water respectively:

$$C = \sqrt{\frac{g}{k}} \quad kd \geq \pi \text{ (deep water)} \quad (2.13)$$

$$C = \sqrt{gd} \quad kd \leq \frac{\pi}{10} \text{ (shallow water)} \quad (2.14)$$

So, longer waves travel faster in deep water, while in shallow water the wave celerity depends only on the local water depth and it decreases with decreasing depth. On the other hand, the wave energy propagates with another velocity which is called the group velocity and is defined as:

$$C_g = \frac{\partial \omega}{\partial k} = \frac{1}{2} C \left(1 + \frac{2kd}{\sinh 2kd} \right) \quad (2.15)$$

Finally, the above solutions can also be derived using the linearised form of the Euler equations.

2.1.2 Second and Third order Stokes wave theory

Despite the strict assumptions presented in Section 2.1.1, the linear wave theory can be used to estimate the main wave phenomena in deep water quite reasonably. However, as the wave height increases with respect to the water depth and wavelength (see Figure 2.1) the profile of the waves is no longer symmetric as the sinusoidal one given by the linear wave theory. The waves have steeper crests and flatter troughs. In this case the nonlinear wave theories become essential, since a better approximation of the wave profile is found by adding extra harmonic waves to the primary harmonic. Here, we will focus on the 2nd and 3rd order Stokes wave theory which are valid for larger wave heights compared to the linear wave theory (deep water and a portion of intermediate water, see Figure 2.1).

Stokes (1847) developed a theory for finite amplitude waves using the perturbation expansion technique. According to this technique all the wave characteristics (surface elevation, velocity potential, velocity components, etc.) are expressed in terms of power series in successively higher orders of the wave steepness $\epsilon = ka$ so that:

$$\eta = \eta_1 + \epsilon \eta_2 \quad (2.16)$$

Solving the Laplace equation with nonlinear kinematic and dynamic surface boundary conditions and using the solutions from the linear wave theory, the water surface elevation predicted by Stokes 2nd order theory is obtained:

$$\eta = a \cos(kx - \omega t) + \frac{1}{4} ka^2 \coth(kd) (3 \coth^2(kd) - 1) \cos(2(kx - \omega t)) \quad (2.17)$$

The wave described by Equation 2.17 is called 2nd order Stokes wave. The first part of the equation is the linear wave contribution and is the same as Equation 2.10, while the second part is the second order Stokes correction which is called the second harmonic. The second harmonic propagates with the same wave celerity as the primary wave given by Equation 2.12 (the linear dispersion relation is still valid to second order) and thus it is also referred as bound second harmonic.

The 3rd order Stokes wave theory can be obtained by adding a third harmonic in Equation 2.16:

$$\eta = \eta_1 + \epsilon\eta_2 + \epsilon^2\eta_3 \quad (2.18)$$

Including the third harmonic in the Laplace equation and using the solutions from the linear and the 2nd order wave theory, the third order Stokes correction on the water surface elevation is obtained as (Skjelbreia, 1959):

$$\epsilon^2\eta_3 = \frac{3}{64}a^3k^2 \frac{1 + 8 \cosh^6(kd)}{\sinh^6(kd)} \cos(3(kx - \omega t)) \quad (2.19)$$

The linear dispersion is not valid anymore for the 3rd order Stokes wave theory and instead is given by the following expression (Skjelbreia, 1959):

$$\omega_3 = \sqrt{gk \tanh(kd)} \left(1 + \frac{1}{16} a^2 k^2 \frac{9 \tanh^4(kd) - 10 \tanh^2(kd) + 9}{\tanh^4(kd)} \right) \quad (2.20)$$

It is observed from Equation 2.20 that the third order Stokes waves are not only frequency dispersive as the linear and second order waves, but amplitude dispersive as well. This means that for a specific period, wave celerity and wavelength get larger values as the wave height increases.

2.1.3 Second order Superharmonics and Subharmonics

In coastal regions, waves with different frequencies interact with each other leading to the generation of bound subharmonics and superharmonics at the difference and sum of the frequencies of the primary waves. During this process substantial spectral energy is being transferred from the peak- to the low- and high-frequency part of the spectrum.

The superharmonics influence the wave profile, tending to steepen the wave crests and flatten the wave troughs, while during shoaling the waves are becoming more asymmetric and finally break. On the other hand, subharmonics lead to long waves over the coast that can penetrate into harbours and result in harbour resonance.

A first order wave group composed of two harmonics with frequencies ω_m and ω_n and wave numbers k_m and k_n will force a second order wave group composed of four components, one subharmonic, $\omega_m - \omega_n$, and three superharmonics, $2\omega_m$, $2\omega_n$ and $\omega_m + \omega_n$. The first and second wave group are described as follows:

$$\eta^{(1)} = \eta_{01m} \cos(k_m x - \omega_m t) + \eta_{01n} \cos(k_n x - \omega_n t) \quad (2.21)$$

$$\begin{aligned} \eta^{(2)} = & G_\eta^{m-n} \cos((k_m - k_n)x - (\omega_m - \omega_n)t) + G_\eta^{2m} \cos(2k_m x - 2\omega_m t) \\ & + G_\eta^{m+n} \cos((k_m + k_n)x - (\omega_m + \omega_n)t) + G_\eta^{2n} \cos(2k_n x - 2\omega_n t) \end{aligned} \quad (2.22)$$

where G_η^{m-n} is the subharmonic transfer function and G_η^{2m} , G_η^{2n} and G_η^{m+n} are the superharmonic transfer functions. These transfer functions are obtained from the nonlinear boundary value problem for the Laplace equation using a perturbation method, while the exact solutions derived by Schäffer (1996) for the subharmonic G_η^{m-n} and by Sand and Mansard (1986) for the superharmonic G_η^{m+n} are presented here. The self-interacting superharmonic transfer functions G_η^{2m} and G_η^{2n} are identical to the Stokes second order solution presented in Section 2.1.2.

The superharmonic transfer function G_η^{m+n} is given by the following equation (Sand and Mansard, 1986):

$$\begin{aligned}
G_\eta^{m+n} = & \frac{\eta_{01m}\eta_{01n}}{d} \left\{ \left[2(\alpha_n + \alpha_m)^2 \left(\frac{k_n k_m d^2}{\alpha_n \alpha_m} - 4\pi^2 \alpha_n \alpha_m \right) \right. \right. \\
& \left. \left. + (\alpha_n + \alpha_m) \left(\frac{k_m^2 d^2}{\alpha_m} + \frac{k_n^2 d^2}{\alpha_n} - 4\pi^2 (\alpha_m^3 + \alpha_n^3) \right) \right] / \right. \\
& \left. \left((4\pi(\alpha_m + \alpha_n)^2) - 2(k_m + k_n)d \tanh((k_m + k_n)d) \right) \right. \\
& \left. + \left[4\pi^2 \alpha_m^2 \alpha_n^2 \left(1 + \frac{\alpha_m}{\alpha_n} + \frac{\alpha_n}{\alpha_m} \right) - k_m k_n d^2 \right] / \left(4\pi \alpha_m \alpha_n \right) \right\}
\end{aligned} \tag{2.23}$$

where α_m and α_n are defined as:

$$\alpha_m = \sqrt{\left(\frac{d\omega_m^2}{2g\pi} \right)} \quad \text{and} \quad \alpha_n = \sqrt{\left(\frac{d\omega_n^2}{2g\pi} \right)} \tag{2.24}$$

Schäffer (1996) derived the subharmonic transfer function G_η^{m-n} which has the following form:

$$G_\eta^{m-n} = \frac{\eta_{01m}\eta_{01n}}{g} \left((\omega_m - \omega_n) \frac{H^{m-n}}{D^{m-n}} - L^{m-n} \right) \tag{2.25}$$

where

$$\begin{aligned}
H^{m-n} = & (\omega_m - \omega_n) \left(-\omega_m \omega_n - \frac{g^2 k_m k_n}{\omega_m \omega_n} \right) \\
& + \frac{\omega_m^3 - \omega_n^3}{2} - \frac{g^2}{2} \left(\frac{k_m^2}{\omega_m} - \frac{k_n^2}{\omega_n} \right)
\end{aligned} \tag{2.26}$$

$$D^{m-n} = g(k_m - k_n) \tanh((k_m - k_n)d) - (\omega_m - \omega_n)^2 \tag{2.27}$$

$$L^{m-n} = \frac{1}{2} \left(\frac{g^2 k_m k_n}{\omega_m \omega_n} + \omega_m \omega_n - (\omega_m^2 + \omega_n^2) \right) \tag{2.28}$$

It has to be mentioned that the above expressions are equal to the superharmonic and subharmonic transfer functions derived by Hansen (1978) and Sharma and Dean (1981). In Figure 2.3 the superharmonic and subharmonic transfer functions, $G_{\eta}^{m \pm n} d / \eta_{01m} \eta_{01n}$, of Equations 2.23 and 2.25 are presented as a function of the dimensionless depths $k_m d$ and $k_n d$. As it is observed both superharmonic and subharmonic transfer functions are getting larger values and thus are becoming more important in shallow water where the waves are longer.

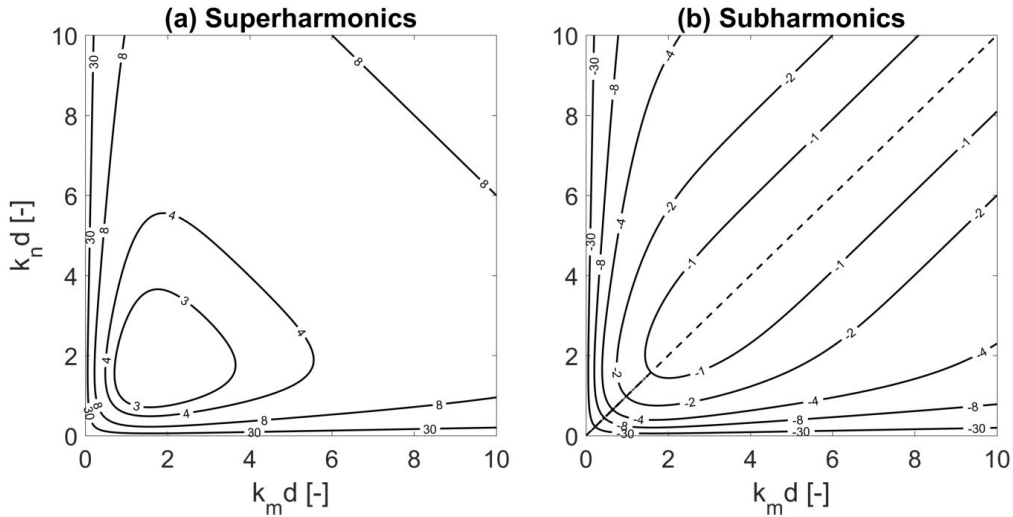


Figure 2.3: (a) Superharmonic and (b) subharmonic transfer functions, $G_{\eta}^{m \pm n} d / \eta_{01m} \eta_{01n}$, as a function of the dimensionless depths $k_m d$ and $k_n d$.

2.2 Numerical wave models

The analytical solutions of the different wave theories described in the previous sections have served as the basis to study wave shape and motion and constitute a valuable tool for coastal engineers around the world. Despite the fact that analytical models have been extensively developed and used by scientists and engineers already from the end of the 19th century, analytical methods cannot be efficiently applied when more realistic and complex cases are investigated. Such cases include, for instance, wave propagation over uneven bottoms, nonlinear wave transformation and breaking in the coastal zone and wave-structure interactions. These phenomena are described by partial differential equations which cannot be analytically solved. Fortunately, the recent advances in computing performance have brought a new horizon of research into view, where the investigation of complex phenomena can be achieved with the use of numerical methods and approximations. Numerical models have been developed to solve the governing water wave equations which can be classified in two main categories: phase-averaged (stochastic) and phase-resolving (deterministic) models.

In the present section, different types of wave propagation models are described, while the assumptions under which each model is applicable are defined. A table

is presented at the end of this section, where the degree of capability of each type of model to describe different wave processes is summarised (Table 2.1).

2.2.1 Phase-averaged models

Phase-averaged models are the most commonly employed models since they can be applied in very large domains with high computational efficiency at the same time (Reniers et al., 2010; Rusu and Guedes Soares, 2013). This capability emerges from the fact that the phase information is filtered out in their formulation and thus the computational cells can be much larger than a wavelength. The phase-averaged models are developed on the assumption that the wave field can be described as a zero-mean, quasi-homogeneous and quasi-stationary Gaussian process, which can be fully represented by means of the variance density spectrum. That is why they are often referred to in literature as spectral wave models. The governing balance equation for the mean wave energy includes various source terms corresponding to different wave processes. In deep water, the source terms take into account the wind wave generation, white capping and quadruplet wave-wave interactions, while the shallow water source terms include depth induced breaking, dissipation due to bed friction, and triad wave-wave interactions.

The most well known stochastic wave models are WAM (The Wamdi Group, 1988) and WaveWatch (Tolman, 1991) in deep water and SWAN (Booij et al., 1999) and TOMAWAC (Benoit et al., 1997) in shallow water. In general, these models can satisfactorily reproduce the bulk wave statistics such as significant wave heights and periods in oceanic regions. However, when it comes to coastal areas, where the assumption of a quasi-homogeneous and quasi-stationary Gaussian wave field is violated, these models are not as accurate.

2.2.2 Phase-resolving models

In cases where phase-related wave processes (e.g. wave diffraction) are examined or where wave nonlinearity is important, phase-resolving models are preferable over phase-averaged models. These deterministic models can resolve the evolution and transformation of each individual wave in contrast to the stochastic models that only account for wave energy spectrum evolution. Depending on the governing equations and the assumptions on their derivation, phase-resolving models can be classified in the following sub-categories: a) Navier-Stokes equations (NSE) models, b) Mild-slope equations (MSE) models, c) Boussinesq equations (BE) models and d) Non-hydrostatic equations (NHE) models.

2.2.2.1 Navier-Stokes equations models

Models based on the primitive (Reynolds-Averaged) Navier-Stokes equations are derived by applying the general laws of mass, momentum and energy conservation. They can be used for any type of fluid and can account for complex motion phenomena in the flow. These equations are able to describe water wave dynamics including wave transformation and breaking and interaction of waves with currents and structures. Several numerical models using Volume Of Fluid (VOF) methods

(Lin and Liu, 1998; Higuera et al., 2013b) or Smoothed Particle Hydrodynamics (SPH) methods (Dalrymple and Rogers, 2006; Altomare et al., 2015) have been introduced during the last decades. In virtue of the significantly fine resolution that is applied in these models, they can represent reality with high accuracy and can provide detailed three-dimensional velocity and pressure profiles. However, all these advantages come with the cost of extremely expensive computational effort. Thus, their application is still limited to the study of small temporal (a few wave periods) and spatial (a few wave lengths) scale test cases, making the study of wave transformation in coastal zones or wave penetration in harbours impossible.

2.2.2.2 Mild-slope equations models

One of the first equations that was able to consider a range of transformation processes of linear regular waves, such as wave refraction, diffraction, shoaling, and reflection and to incorporate structures was the elliptic wave equation presented by Berkhoff (1972). The governing equation was derived considering a three-dimensional irrotational flow under the assumption that the sea bottom varies gently over a wave length. Consequently, the obtained equation is known as mild-slope equation (MSE). Based on this, the parabolic model by Radder (1979) and the hyperbolic model by Copeland (1985) have been developed. In the former model, wave reflection and diffraction in the direction of wave propagation are ignored and hence the parabolic model suffers from low accuracy in cases where these phenomena are significant. On the other hand, the hyperbolic model, which takes into consideration wave reflection and diffraction in the direction of wave propagation, provides higher accuracy, but requires more computational time compared to the parabolic model. Moreover, to study the transformation of random waves, time dependent mild-slope equations have been developed. Radder and Dingemans (1985) suggested a set of canonical equations, which are based on the time dependent mild slope equations and are derived using the Hamiltonian theory of surface waves. Booij (1983), who compared the solutions of MSE with the solutions given by the Laplace equation, proved that Radder and Dingemans (1985) equations are valid for sea bottom slopes up to $1/3$. However, Suh et al. (1997) extended the latter equations by including higher order bottom effect terms proportional to the square of the bottom slope and to the bottom curvature to study wave propagation on rapidly varying topography. Models based on the MSE are fully dispersive and can produce reasonably good results in the region from a deep water to a nearshore location before wave breaking where nonlinearity is becoming strong and thus not negligible.

2.2.2.3 Boussinesq equations models

In cases that nonlinear processes such as wave breaking, wave-wave interaction or harmonic generation are important, models based on the Boussinesq equations can account for some aspects of the nonlinear wave behavior. The classical form of Boussinesq equations was derived by Peregrine (1967) and was able to describe long waves with small amplitude propagating over uneven bottoms. Thus, these equations were characterised as weakly nonlinear and weakly dispersive (nonlinear-

ity and frequency dispersion of equal order) and were applicable up to a kd value of 0.75, where k is the wave number and d is the still water depth. Since their inception, efforts have been taken place by several researchers worldwide focusing on the derivation and development of Boussinesq-type wave models with enhanced linear and nonlinear properties. Madsen et al. (1991) and Madsen and Sørensen (1992) extended the capability of the Peregrine (1967) equations to deeper water by using a Padé approximation and introducing additional third order terms in the governing equations. At the same time, Nwogu (1993) achieved similar dispersive properties by defining the horizontal velocity component at an arbitrary level with respect to the vertical axis. Later, Wei and Kirby (1995) derived a fully nonlinear Boussinesq-type wave model based on the Nwogu (1993) formulation. Since then, high-order Boussinesq-type models have been developed to further improve the linear and nonlinear effects (Klonaris et al., 2016), either through the use of higher order polynomial approximations for the vertical distribution of the flow field (Gobbi et al., 2000) or by means of the multi-layer concept of Lynett and Liu (2004b). Boussinesq-type wave models are highly complicated due to the high-order derivatives in time and space, which makes them numerically unstable and computationally expensive. A more detailed literature overview of the Boussinesq-type wave models and their application can be found in Kirby (2016) and Brocchini (2013).

2.2.2.4 Non-hydrostatic equations models

An alternative to the Boussinesq-type wave models is the non-hydrostatic wave models which constitute a numerical implementation of the Navier-Stokes equations for an incompressible fluid with a free surface and a constant density. Casulli and Stelling (1998) proposed a time-splitting integration method to solve the Reynolds-Averaged Navier-Stokes (RANS) equations, according to which at first the velocity field is predicted assuming the hydrostatic problem, and subsequently the wave field is corrected in response to the non-hydrostatic pressure correction obtained by solving a Poisson type equation. Stelling and Zijlema (2003) and Zijlema and Stelling (2005) introduced a Keller Box scheme for the discretization of the pressure over the vertical direction, while Zijlema and Stelling (2008) proved that the Keller Box scheme leads to better dispersive properties than the central differences scheme when coarse vertical resolution is applied. After these recent developments, several non-hydrostatic wave models have been developed: e.g. SWASH (Zijlema et al., 2011), NHWAVE (Ma et al., 2012) and NEOWAVE (Yamazaki et al., 2011). In contrast to the Boussinesq-type wave models, non-hydrostatic wave models can directly resolve the vertical and horizontal flow structure by retaining the 3D momentum equations and consequently can simulate rotational flows. Additionally, they can improve their wave dispersion and the degree of non-linearity by making use of a few vertical layers rather than increasing the order of derivatives of the dependent variables like Boussinesq-type wave models.

Table 2.1: Degree of capability of each type of model to describe different wave processes.

Wave Model	Diffraction	Refraction	Frequency Dispersion	Nonlinearity	Computational Efficiency
Spectral	*	*****	*****	**	*****
NSE	*****	*****	*****	*****	*
MSE	*****	*****	*****	*	*****
BE	*****	*****	*****	*****	***
NHE	*****	*****	*****	*****	***

2.3 Mild-slope wave propagation model MILDwave

MILDwave is a mild-slope equation wave propagation model developed at the Coastal Engineering Research group of Ghent University in Belgium (Troch, 1998). This particular model has previously been used to predict wave diffraction and wave penetration inside harbours (Stratigaki et al., 2011) and to study wave energy conversion applications (Beels et al., 2010; Verao Fernandez et al., 2019, 2018; Balitsky et al., 2018, 2019).

The mild-slope equations of Radder and Dingemans (1985), without including the higher order bottom effect terms of Suh et al. (1997), are the basic equations employed in the phase-resolving model, MILDwave, used to simulate wave transformation processes, such as refraction, shoaling, reflection, transmission, and diffraction, intrinsically (Troch and Stratigaki, 2016). These governing equations are given in Equations 2.29 and 2.30 and account for transformation processes of linear irregular waves with a narrow frequency band over a gently varying bathymetry (bottom slopes up to 1/3):

$$\frac{\partial \eta}{\partial t} = B\phi - \nabla(A\nabla\phi) \quad (2.29)$$

$$\frac{\partial \phi}{\partial t} = -g\eta \quad (2.30)$$

where $\eta(x, y, t)$ and $\phi(x, y, t)$ are the surface elevation and the velocity potential, respectively, at the level of still water, ∇ is the horizontal differential operator, t is the time and g is the gravitational acceleration. The coefficients A and B are calculated using Equations 2.31 and 2.32, respectively:

$$A = \frac{CC_g}{g} \quad (2.31)$$

$$B = \frac{\omega^2 - k^2CC_g}{g} \quad (2.32)$$

with C the wave celerity and C_g the group velocity for a wave with wave number, k , angular frequency, ω , wavelength, L , and frequency, f . For irregular waves, C , C_g , ω and k are replaced by the wave characteristics for the carrier frequency, \hat{f} .

A finite difference scheme, as described in Brorsen and Helm-Petersen (1998) is used to discretize and solve Equations 2.29 and 2.30. The domain is divided in grid cells with dimensions, Δx and Δy , and central differences are used both for spatial and time derivatives. Both $\eta(x, y, t)$ and $\phi(x, y, t)$ are calculated at the center of each grid cell (Figure 2.4) at different time levels, $(n + 1/2)\Delta t$ and $(n + 1)\Delta t$ as:

$$\begin{aligned} \eta_{i,j}^{n+\frac{1}{2}} &\simeq \eta_{i,j}^{n-\frac{1}{2}} + B_{i,j} \phi_{i,j}^n \Delta t \\ &\quad - \frac{A_{i+1,j} - A_{i-1,j}}{2\Delta x} \frac{\phi_{i+1,j}^n - \phi_{i-1,j}^n}{2\Delta x} \Delta t \\ &\quad - A_{i,j} \frac{\phi_{i-1,j}^n - 2\phi_{i,j}^n + \phi_{i+1,j}^n}{\Delta x^2} \Delta t \\ &\quad - \frac{A_{i,j+1} - A_{i,j-1}}{2\Delta y} \frac{\phi_{i,j+1}^n - \phi_{i,j-1}^n}{2\Delta y} \Delta t \\ &\quad - A_{i,j} \frac{\phi_{i,j-1}^n - 2\phi_{i,j}^n + \phi_{i,j+1}^n}{\Delta y^2} \Delta t \end{aligned} \quad (2.33)$$

$$\phi_{i,j}^{n+1} \simeq \phi_{i,j}^n - g\eta_{i,j}^{n+\frac{1}{2}} \Delta t \quad (2.34)$$

where A and B are given by Equations 2.31 and 2.32 and the superscripts and subscripts stand for the relevant time step and the relevant cell of the grid, respectively.

The grid cell size, $\Delta x = \Delta y$, is chosen so that $L/20 \leq \Delta x = \Delta y \leq L/10$ (for irregular waves, $L =$ shortest wavelength (maximum wave frequency)) while the time step meets the Courant-Friedrichs-Lewy criterion to ensure a stable and reliable result. Due to the coarse grid resolution and the linear nature of the equations, MILDwave is a very robust numerical model that can handle large computational domains of order $O(1 - 10 \text{ km})$ with significantly small computational cost.

In the current configuration of MILDwave, the boundary conditions are formed in such a way that one layer of ghost cells is considered at each boundary. The values at the cells closest to the boundary are copied to the ghost cells and thus the layer of the ghost cells acts as a fully reflective boundary (solid wall). However, the effect of the fully reflective domain boundaries is negligible because absorbing sponge layers are applied at the computational boundaries to dissipate the incoming wave energy.

The numerical dissipation of the incoming waves is achieved by relaxing the calculated surface elevations at each time step with an absorption function $S(b)$ that takes the value of 1 at the beginning of the sponge layer and decreases until it reaches the value 0 at the end. As a result, the reflection is minimal. Two absorption functions have been implemented in MILDwave, an elliptical ($S_1(b)$) and a sinusoidal ($S_2(b)$), given by Equations 2.35 and 2.36, respectively.

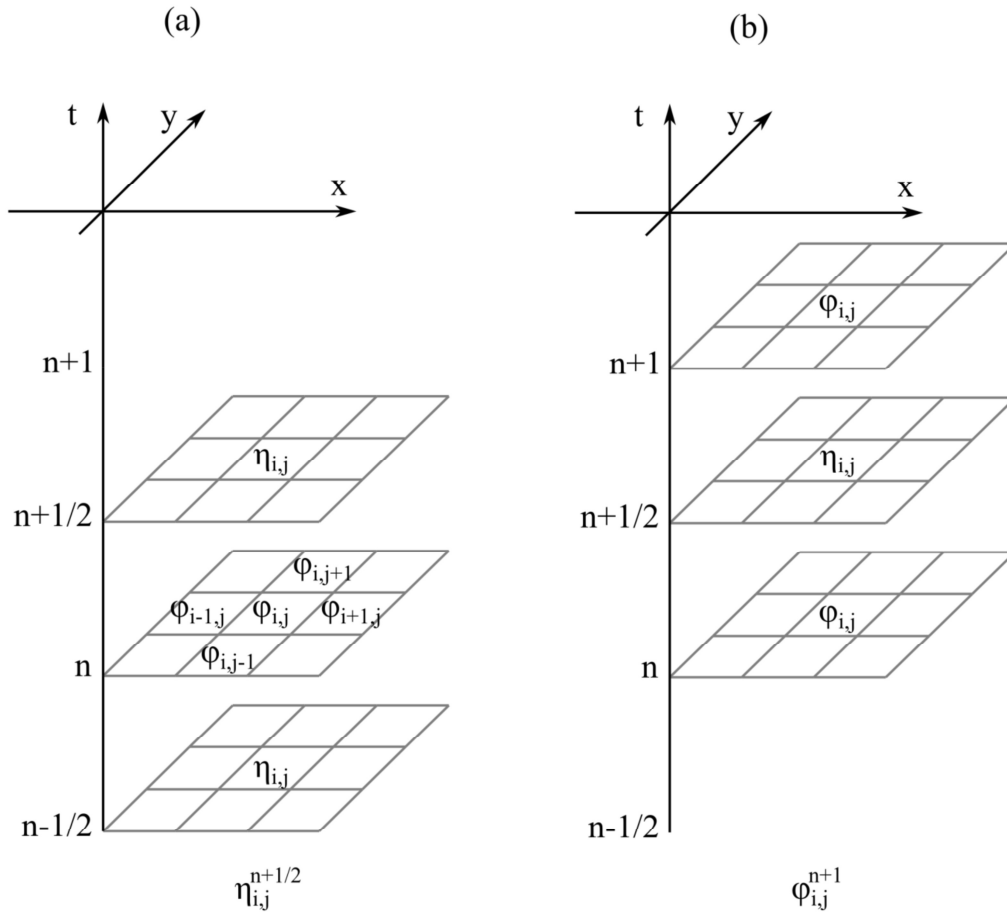


Figure 2.4: Finite difference scheme implemented in MILDwave for (a) Equation 2.33 and (b) Equation 2.34.

$$S_1(b) = \sqrt{1 - \left(\frac{b}{B_s}\right)^2} \quad (2.35)$$

$$S_2(b) = \frac{1}{2} \left(1 + \cos\left(\pi \frac{b}{B_s}\right)\right) \quad (2.36)$$

with B_s the width of the sponge layer and b the distance from the inner boundary of the sponge layer, both defined in number of computational cells.

2.4 Non-hydrostatic wave propagation model SWASH

SWASH is an open source non-hydrostatic wave model (Zijlema et al., 2011) and has admittedly reached a mature stage in the field of wave transformation in coastal environments, as it allows for the incorporation of nonlinear shallow-water effects, like bound subharmonics and superharmonics and near-resonant triad interactions (Rijnsdorp et al., 2014, 2015; Smit et al., 2014). Some recent applications of the model include wave overtopping (Suzuki et al., 2017), wave-induced currents (Rijnsdorp et al., 2017), wave runup (Nicolae Lerma et al., 2017), wave forces (Gruwez et al., 2020) and the interaction of waves with vegetation (Suzuki et al., 2019) and wave energy converters (Rijnsdorp et al., 2018).

The governing equations of the model are based on the Navier-Stokes (or Euler) equations for an incompressible fluid with a free surface η and a constant density ρ_0 . The numerical domain is bounded vertically by the free-surface $z = \eta(x, y, t)$ and the bottom $z = -d(x, y)$, where t is time, d is the still water depth and x, y and z are the Cartesian coordinates, where z is directed positive upwards. For the case of a 3D domain the governing equations are given as follows:

$$\frac{\partial u}{\partial x} + \frac{\partial v}{\partial y} + \frac{\partial w}{\partial z} = 0 \quad (2.37)$$

$$\frac{\partial u}{\partial t} + \frac{\partial uu}{\partial x} + \frac{\partial uv}{\partial y} + \frac{\partial uw}{\partial z} + g \frac{\partial \eta}{\partial x} + \frac{\partial q}{\partial x} = \frac{\partial \tau_{xx}}{\partial x} + \frac{\partial \tau_{xy}}{\partial y} + \frac{\partial \tau_{xz}}{\partial z} \quad (2.38)$$

$$\frac{\partial v}{\partial t} + \frac{\partial vu}{\partial x} + \frac{\partial vv}{\partial y} + \frac{\partial vw}{\partial z} + g \frac{\partial \eta}{\partial y} + \frac{\partial q}{\partial y} = \frac{\partial \tau_{yx}}{\partial x} + \frac{\partial \tau_{yy}}{\partial y} + \frac{\partial \tau_{yz}}{\partial z} \quad (2.39)$$

$$\frac{\partial w}{\partial t} + \frac{\partial wu}{\partial x} + \frac{\partial wv}{\partial y} + \frac{\partial ww}{\partial z} + \frac{\partial q}{\partial z} = \frac{\partial \tau_{zx}}{\partial x} + \frac{\partial \tau_{zy}}{\partial y} + \frac{\partial \tau_{zz}}{\partial z} \quad (2.40)$$

where u and v are the horizontal velocity components in x -direction and y -direction, w is the vertical velocity component in z -direction, q is the non-hydrostatic pressure, g is the gravitational acceleration and τ_{ij} represents the turbulent stresses (the i and j subscripts stand for the coordinates). Equation 2.37 is the continuity equation, while Equations 2.38 - 2.40 are the horizontal and vertical momentum equations.

The kinematic conditions at the free surface $z = \eta$ and the bottom $z = -d$ are given in Equations 2.41 and 2.42, respectively:

$$w_{z=\eta} = \frac{\partial \eta}{\partial t} + u \frac{\partial \eta}{\partial x} + v \frac{\partial \eta}{\partial y} \quad (2.41)$$

$$w_{z=-d} = -u \frac{\partial d}{\partial x} - v \frac{\partial d}{\partial y} \quad (2.42)$$

The dynamic boundary conditions at the surface are a constant pressure and no surface stresses.

The free surface equation is obtained by integrating Equation 2.37 for the entire water column $h = d + \eta$ and applying the kinematic condition at the free surface (Equation 2.41):

$$\frac{\partial \eta}{\partial t} + \frac{\partial}{\partial x} \int_{-d}^{\eta} u dz + \frac{\partial}{\partial y} \int_{-d}^{\eta} v dz = 0 \quad (2.43)$$

For the case that the number of layers in the vertical direction is K , Equation 2.43 is rewritten as:

$$\frac{\partial \eta}{\partial t} + \frac{\partial Q_{u,K}}{\partial x} + \frac{\partial Q_{v,K}}{\partial y} = 0, \text{ with } Q_{u,K} = \sum_{k=1}^K h_{u,k} u_k \text{ and } Q_{v,K} = \sum_{k=1}^K h_{v,k} v_k \quad (2.44)$$

where $h_{u,k}$, $h_{v,k}$ and u_k , v_k are the thicknesses and the layer-integrated horizontal velocities, respectively, corresponding to the k -th layer.

At the bottom boundary, a bottom stress is included based on a quadratic friction law:

$$\tau_b = c_f \frac{U|U|}{h} \quad (2.45)$$

where U is the depth averaged velocity and c_f is a dimensionless friction coefficient.

Sponge layers (relaxation zones) can be applied at the boundaries of the computational domain in order to prevent reflections back into the domain. In SWASH, the method proposed by Mayer et al. (1998) is implemented, according to which the velocity components and the free surface elevation are relaxed at each time step.

In SWASH the full process of wave breaking is not simulated but instead a breaking wave is considered analogous with a hydraulic bore. However, a high vertical resolution is needed to resolve accurately this process. Hence, Smit et al. (2013) proposed a breaking formulation which can reproduce wave breaking when a coarse vertical resolution is applied. A hydrostatic pressure distribution is assumed when $\partial \eta / \partial t > a \sqrt{gh}$, where a is the maximum wave steepness before breaking.

The numerical implementation is based on an explicit, second order finite difference method for staggered grids, where the mass and momentum are strictly conserved at a discrete level. In the horizontal direction rectilinear or orthogonal curvilinear grid can be applied, while in the vertical direction the computational domain is split into a fixed number of layers. A thorough presentation of the governing equations and the numerical methods that are implemented in SWASH can be found in Zijlema et al. (2011) and Zijlema and Stelling (2008).

For all the test cases that are examined in the present dissertation, in the horizontal direction a rectangular and uniform computational grid has been applied,

in which the grid cell resolution is determined by the condition of having at least 50 grid cells per peak wave length. Additionally, an automatic time step control is applied during the simulation based on the CFL (Courant–Friedrichs–Lewy) condition, according to which the time step is halved when the Courant number is larger than a maximum value and is doubled when the Courant number is smaller than a minimum value. In the present study a maximum and a minimum Courant number of 0.5 and 0.2 is used respectively. The fine resolution and the complexity of the governing equations make SWASH much more computationally expensive than MILDwave. However, SWASH code is parallelised which means the calculations can run in multiple processors (CPUs) and thus simulations of large computational domains of order $O(1 - 10 \text{ km})$ can be accelerated using High Performance Computing (HPC) infrastructures.

Chapter 3

Development of periodic boundaries in MILDwave model

In this chapter of the thesis, periodic lateral boundaries are developed in a time dependent mild-slope equation model, MILDwave (introduced in Section 2.3), for the accurate generation of regular waves and irregular long- and short-crested waves in any direction, tackling knowledge gap 1 (Figure 1.3). A single wave generation line inside the computational domain is combined with periodic lateral boundaries. This generation layout yields a homogeneous and thus accurate wave field in the whole domain in contrast to an L-shaped and an arc-shaped wave generation layout where wave diffraction patterns appear inside the computational domain as a result of the intersection of the two wave generation lines and the interaction with the lateral sponge layers. In addition, the performance of the periodic boundaries was evaluated for two different wave synthesis methods for short-crested waves generation, a method proposed by Miles (1989) and a method proposed by Sand and Mynett (1987). The results show that the MILDwave model with the addition of periodic boundaries and the Sand and Mynett method is capable of reproducing a homogeneous wave field as well as the target frequency spectrum and the target directional spectrum with a low computational cost. The research presented is based on the following article, with a more detailed description of the examined wave generation layouts:

originally published in Vasarmidis et al. (2019b):

Vasarmidis, P., Stratigaki, V., Troch, P., (2019b). Accurate and fast generation of irregular short crested waves by using periodic boundaries in a mild-slope wave model. *Energies* 12, 785. <https://doi.org/10.3390/en1205078>

3.1 Introduction

For numerical prediction of the wave field in a coastal area, waves are generated along the offshore boundary of the computational domain and propagate towards the coastline. However, to be able to apply a sponge layer to absorb waves reflected towards the wave generation boundary, waves should be generated inside the numerical domain and not along the boundary.

This internal wave generation technique in combination with numerical wave absorbing sponge layers was firstly proposed by Larsen and Dancy (1983) for Peregrine (1967) classical Boussinesq equations. Later, Lee and Suh (1998) achieved wave generation for the mild slope equations of Copeland (1985) and Radder and Dingemans (1985) by applying the source term addition method. The main observation was that the energy of the incident waves can be properly obtained from the viewpoint of energy transport. To generate multidirectional waves, they applied an L-shaped wave generator, which is generally composed of two wave generation lines; one parallel to the x-axis and one parallel to the y-axis of the numerical domain as well as wave absorbing sponge layers behind the two wave generation lines. However, wave diffraction patterns appear inside the computational domain as a result of the intersection of the two wave generation lines and due to the interaction with the lateral sponge layers. To deal with this problem, Lee and Yoon (2007) proposed an arc-shaped wave generation line; two parallel lines connected to a semicircle to avoid wave diffraction caused at the intersection of the previous wave generation lines. Further, Kim and Lee (2013) used an arc-shaped source band that gives smaller errors than the Lee and Yoon (2007) method, especially for a coarse grid size. Recently, Lin and Yu (2015) proposed a promising method for non-reflective boundaries in a mild-slope wave model to avoid the use of sponge layers. However, in non-reflective boundaries, the level of re-reflection strongly depends on the initial approximations since the characteristics of the reflected waves (i.e., wave angle, wave celerity) inside the numerical domain cannot be estimated a priori.

In the present research, a wave generation layout using periodic lateral boundaries is developed where a single internal wave generation line parallel to the y-axis is combined with periodic lateral boundaries at the top and bottom of the domain. With this technique, the information leaving one end of the numerical domain enters the opposite end and thus no lateral sponges are required. In this way, the wave diffraction patterns that appear inside the computational domain as a result of the intersection of the two wave generation lines and due to the interaction with the lateral sponge layers (see Figure 3.1) are avoided. In Figure 3.1, the water surface elevation, η , is presented for a regular wave field generated by an L-shaped wave generator (red dashed lines) at an angle, $\theta = 45^\circ$, from the x-axis. The absence of uniformity of the surface elevation along the crests and troughs, which is observed in the same figure, is a sign of the existence of diffraction patterns inside the numerical domain.

Periodic boundaries are implemented in a time dependent mild-slope equation model, MILDwave, developed at Ghent University (Troch, 1998) in order to accurately generate regular and irregular waves in any direction. In addition, the

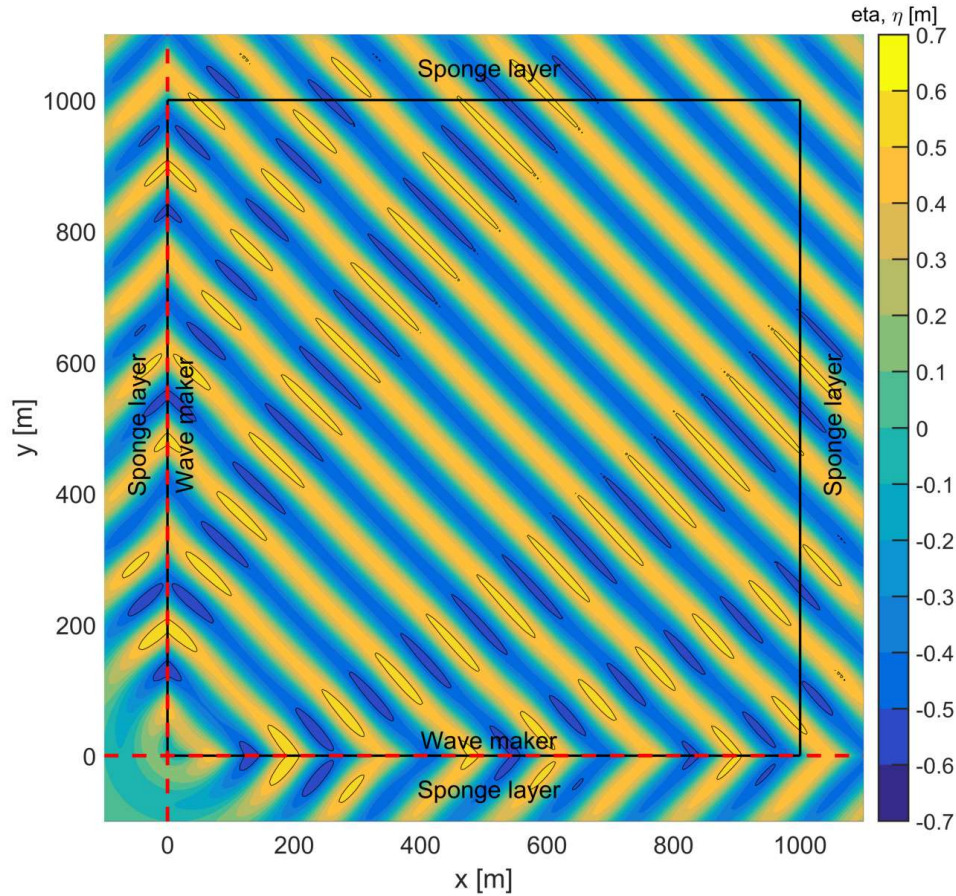


Figure 3.1: Water surface elevation, η , for regular incident waves with a wave height of $H = 1$ m, wave period of $T = 12$ s, and wave propagation angle of $\theta = 45^\circ$ affected by diffraction patterns due to the intersection of the two wave generation lines and the interaction with the lateral sponge layers.

performance of the periodic boundaries is evaluated for two different wave synthesis methods to generate short-crested waves, a method proposed by Miles (1989) and a method proposed by Sand and Mynett (1987). MILDwave has previously been used to predict wave diffraction and wave penetration inside harbours (Stratigaki et al., 2011) and to study wave energy conversion applications (Beels et al., 2010; Verao Fernandez et al., 2019, 2018; Balitsky et al., 2018, 2019). One of the challenges in the field of renewable energies is to determine the optimal geometrical layout for wave energy converter (WEC) farms, targeting the maximum possible energy production and the correct assessment of the impact of WEC farms on the wave field. To do so, accurate and detailed numerical modelling of WEC farms under realistic 3D wave conditions is considered crucial. This kind of application requires a homogeneous wave field in the whole numerical domain.

Periodic boundaries, which are commonly used in wave propagation models, such as non-hydrostatic models (Zijlema et al., 2011) and Boussinesq models (Shi

et al., 2012), have not been used before in a mild-slope wave model to study short-crested waves. So, the novelty of the present work concerns the capability of accurate and fast generation of such homogeneous wave fields with periodic boundaries in MILDwave. In engineering applications, where nonlinearities are not significant, mild-slope wave models are preferred instead of Boussinesq models or non-hydrostatic models due to their significantly smaller computational cost and their high numerical stability and robustness, and thus further development of these models should be encouraged. The implementation of periodic boundaries is important as it introduces noteworthy improvements in mild-slope models, which can then make full use of their benefits for the study of WEC farms under oblique long-crested regular and irregular waves or short-crested waves (real sea waves).

In the next section, the wave generation layouts in MILDwave and the methodology of the implemented periodic boundaries are presented. Section 3.3 provides a detailed overview of the model results for regular and irregular long- and short-crested waves. In Section 3.4, the validation results are presented where the accuracy of the developed model is compared with experimental data. Applications of the implemented method on the study of wave energy converter farms are demonstrated in Section 3.5. The last section provides conclusions and a summary discussion of the present study.

3.2 Wave generation layouts in MILDwave

In MILDwave, there are two ways to generate oblique waves, an L-shaped and an arc-shaped wave generator. This section introduces these two wave generation layouts together with the newly implemented method which consists of a wave generation line combined with periodic lateral boundaries.

3.2.1 L-shaped wave generator

The L-shaped wave generator is composed of two orthogonal lines, one parallel to the x-axis and one parallel to the y-axis of the numerical domain (Figure 3.2) as proposed by Lee and Suh (1998). The two wave generation lines intersect at a point outside the sponge layers and they extend to the computational domain boundary. The gray areas indicate the areas of the numerical domain covered by wave absorbing sponge layers. These sponge layers are necessary to absorb waves reflected by the numerical domain boundaries and by structures.

Waves are generated along the wave generation lines near the offshore boundary by applying the source term addition method proposed by Lee and Suh (1998) where the source term propagates with the energy velocity. According to this method, additional surface elevation, η^* , is added with the desired energy to the calculated surface elevation, η , along the wave generation line at each new time step and is given by Equations 3.1 and 3.2.

$$\eta^* = 2\eta^I \frac{C_e \Delta t}{\Delta x} \cos \theta \quad (3.1)$$

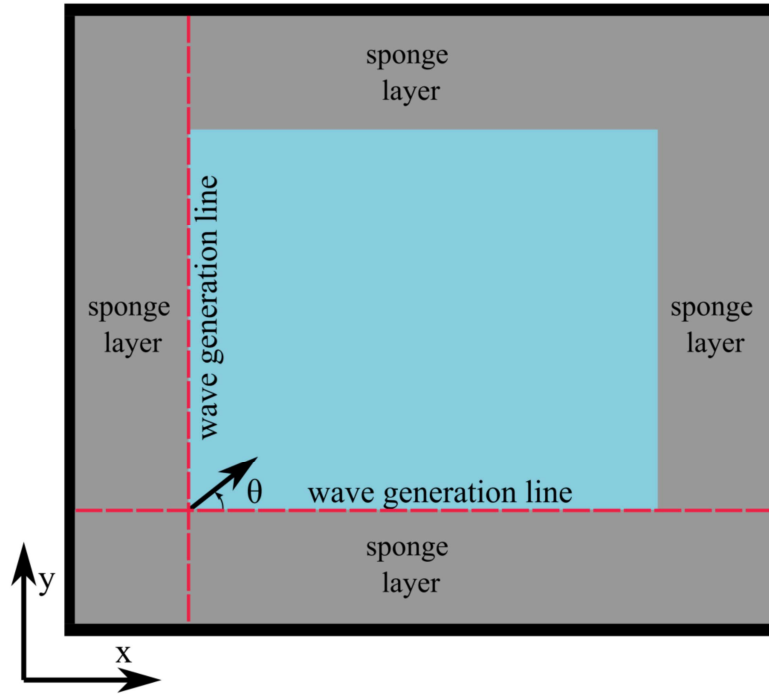


Figure 3.2: Definition sketch of L-shaped wave generator.

$$\eta^* = 2\eta^I \frac{C_e \Delta t}{\Delta y} \sin \theta \quad (3.2)$$

where Δx and Δy are the grid size in the x-axis and y-axis respectively, Δt is the time step, θ is the wave propagation angle with respect to the x-axis, η^I is the water surface elevation of incident waves, and C_e is the energy velocity of the governing mild-slope equations given by Equation 3.3.

$$C_e = \bar{C}_g \frac{\bar{\omega}}{\omega} \sqrt{1 + \frac{\bar{C}}{\bar{C}_g} \left(\left(\frac{\omega}{\bar{\omega}} \right)^2 - 1 \right)} \quad (3.3)$$

where the bar indicates that the variable is associated with the carrier angular frequency, $\bar{\omega}$.

3.2.2 Arc-shaped wave generator

As an alternative to the L-shaped wave generator, Lee and Yoon (2007) developed an arc-shape wave generation layout. In their study, several wave generation layouts have been examined and they proved that the layout composed of two parallel lines connected to a semicircle (Figure 3.3) provides the most accurate results.

The additional surface elevation, η^* , differs from those given by Equations 3.1 and 3.2 at the points located on the arc. Depending on which area of the arc your generation point is located (area A, B, C and D in Figure 3.3) the additional surface elevation is given by:

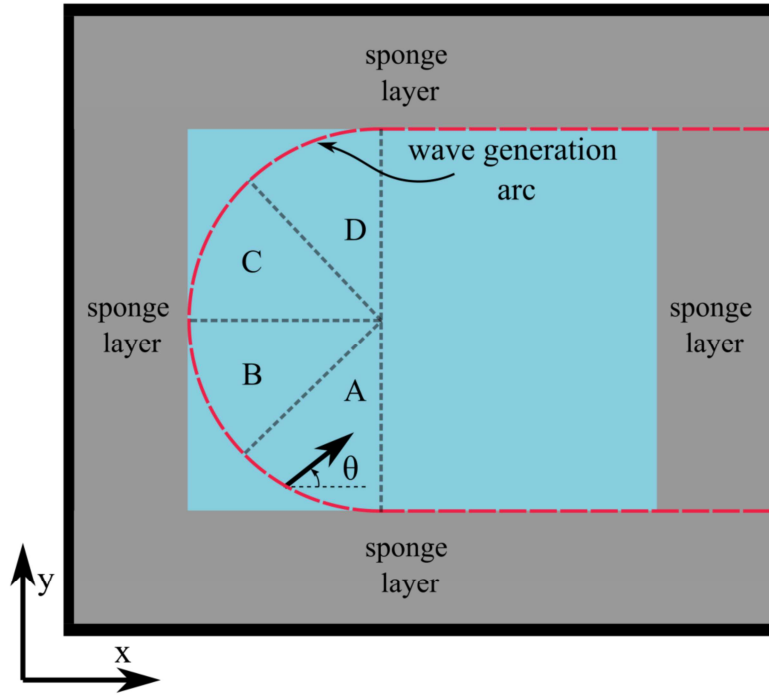


Figure 3.3: Definition sketch of arc-shaped wave generator.

$$\eta^* = 2\eta^I \frac{C_e \Delta t}{\Delta y} \frac{\sin(\beta + \theta)}{\cos\beta} \quad (\text{area A}) \quad (3.4)$$

$$\eta^* = 2\eta^I \frac{C_e \Delta t}{\Delta x} \frac{\cos(\beta - \theta)}{\cos\beta} \quad (\text{area B}) \quad (3.5)$$

$$\eta^* = 2\eta^I \frac{C_e \Delta t}{\Delta x} \frac{\cos(\beta + \theta)}{\cos\beta} \quad (\text{area C}) \quad (3.6)$$

$$\eta^* = 2\eta^I \frac{C_e \Delta t}{\Delta y} \frac{\sin(\beta - \theta)}{\cos\beta} \quad (\text{area D}) \quad (3.7)$$

where β is the angle between the line normal to the wave generation arc and x-axis for area B and C and y- axis for area A and D. It has to be mentioned that at the computational cells on the wave generation arc where the wave direction is pointing outside the curve, the additional surface elevation is zero.

3.2.3 Wave generation line combined with periodic boundaries

To create a homogeneous wave field of oblique long-crested regular and irregular waves or short-crested waves, periodic lateral boundaries have been implemented.

In the present study, a single wave generation line parallel to the y -axis is combined with periodic lateral boundaries at the top and bottom of the domain (Figure 3.4). In this way, the information leaving one end of the numerical domain enters the opposite end and thus the required model length in this direction is reduced. This technique can lead to a more homogeneous wave field than an L-shaped and an arc-shaped wave generation since no wave diffraction problems are caused by the presence of lateral sponge layers and the intersection of the two wave generation lines.

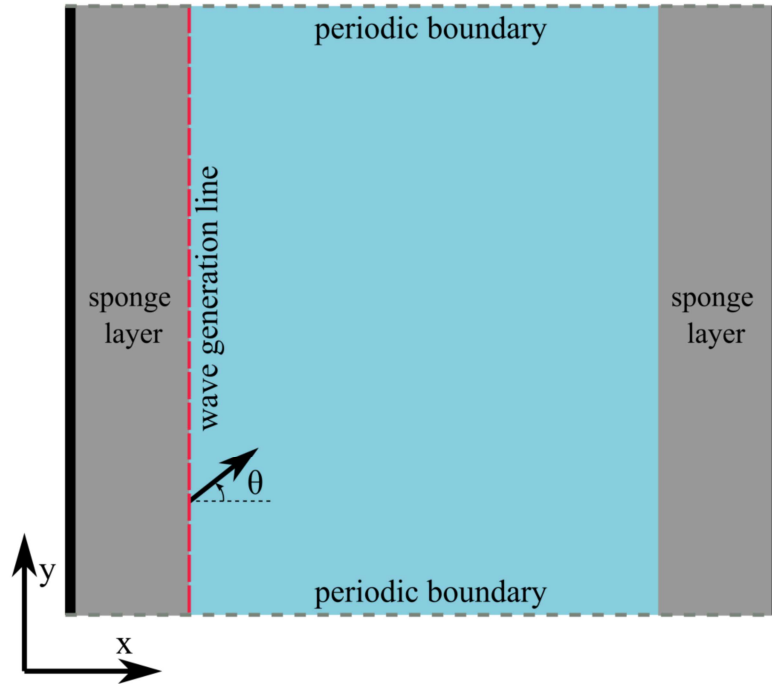


Figure 3.4: Definition sketch of wave generation line combined with periodic boundaries.

Figure 3.5 is a schematic representation of the way that the periodic boundaries are working. Firstly, the left part of the figure presents the numerical domain under investigation, with the squares representing a random number of cells where N_x and N_y is the number of cells in the x and y direction, respectively. A layer of ghost cells is present next to each vertical boundary, acting as a fully reflective wall as described in the previous section. On the other hand, the dashed lines, which are parallel to the x -axis, represent the periodic boundaries.

At the position of the periodic boundaries, the governing equation (Equation 2.33) is solved considering that the two boundaries are adjacent, as it is observed from the right part of Figure 3.5, yielding Equations 3.8 and 3.9 instead of Equation 2.33 for the bottom ($j = 1$) and top ($j = N_y$) layer of cells, respectively.

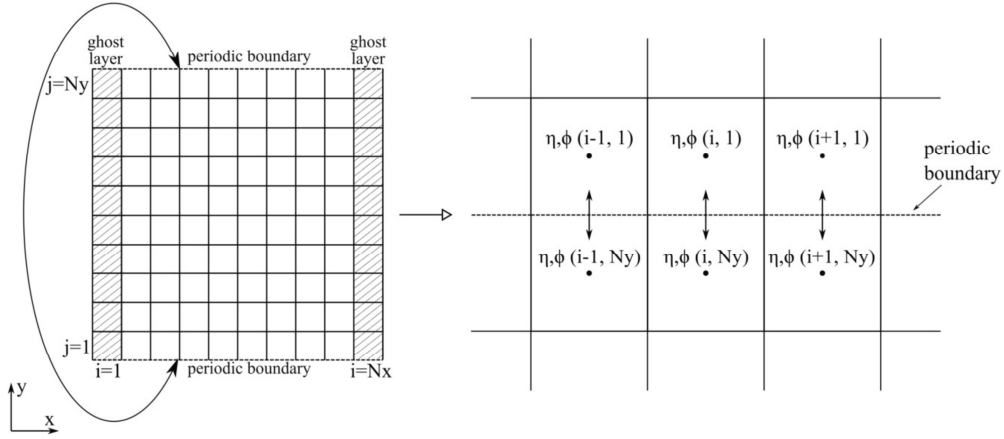


Figure 3.5: Definition sketch of computational domain with periodic boundaries.

$$\begin{aligned}
 \eta_{i,1}^{n+\frac{1}{2}} &\simeq \eta_{i,1}^{n-\frac{1}{2}} + B_{i,1} \phi_{i,1}^n \Delta t \\
 &\quad - \frac{A_{i+1,1} - A_{i-1,1}}{2\Delta x} \frac{\phi_{i+1,1}^n - \phi_{i-1,1}^n}{2\Delta x} \Delta t \\
 &\quad - A_{i,1} \frac{\phi_{i-1,1}^n - 2\phi_{i,1}^n + \phi_{i+1,1}^n}{\Delta x^2} \Delta t \\
 &\quad - \frac{A_{i,2} - A_{i,Ny}}{2\Delta y} \frac{\phi_{i,2}^n - \phi_{i,Ny}^n}{2\Delta y} \Delta t \\
 &\quad - A_{i,1} \frac{\phi_{i,Ny}^n - 2\phi_{i,1}^n + \phi_{i,2}^n}{\Delta y^2} \Delta t
 \end{aligned} \tag{3.8}$$

$$\begin{aligned}
 \eta_{i,Ny}^{n+\frac{1}{2}} &\simeq \eta_{i,Ny}^{n-\frac{1}{2}} + B_{i,Ny} \phi_{i,Ny}^n \Delta t \\
 &\quad - \frac{A_{i+1,Ny} - A_{i-1,Ny}}{2\Delta x} \frac{\phi_{i+1,Ny}^n - \phi_{i-1,Ny}^n}{2\Delta x} \Delta t \\
 &\quad - A_{i,Ny} \frac{\phi_{i-1,Ny}^n - 2\phi_{i,Ny}^n + \phi_{i+1,Ny}^n}{\Delta x^2} \Delta t \\
 &\quad - \frac{A_{i,1} - A_{i,Ny-1}}{2\Delta y} \frac{\phi_{i,1}^n - \phi_{i,Ny-1}^n}{2\Delta y} \Delta t \\
 &\quad - A_{i,Ny} \frac{\phi_{i,Ny-1}^n - 2\phi_{i,Ny}^n + \phi_{i,1}^n}{\Delta y^2} \Delta t
 \end{aligned} \tag{3.9}$$

This implementation is valid under the assumption that the bathymetry close to the lateral boundaries is uniform for the waves to pass from one boundary to the other without any distortion and thus the continuity to be satisfied. In addition, the distance between the two boundaries should be an integer multiple of the wavelength to avoid phase differences. To ensure that this requirement is valid,

the wave propagation angle, θ , of each wave component is slightly adjusted such that Equation 3.10 is satisfied (Johnson and Pattiaratchi, 2006).

$$k \sin \theta = n \frac{2\pi}{L_{per}} \quad (3.10)$$

where k is the wave number of each wave component, n is an integer, and L_{per} ($L_{per} = \Delta y Ny$) is the periodicity length.

This means that the simulated wave propagation angle slightly deviates from the input wave angle. To minimize this deviation, the periodicity length, L_{per} , of the computational domain should be carefully chosen to be larger than one periodic wave length, L_y ($L_y = L_w / \sin \theta$) (Dimakopoulos and Dimas, 2011). Hence, in the case of irregular long-crested waves, each wave component propagates in a slightly different direction than the mean value and a directional spread of the wave energy occurs. However, it has been verified that the spreading standard deviation, σ_θ , is very small ($\sigma_\theta < 2^\circ$) and the waves can be considered as uni-directional.

3.3 Validation with analytical solutions

In this section, the applicability and accuracy of periodic boundaries to propagate regular and irregular long- and short-crested waves over a flat bottom is examined. For the evaluation of the numerical simulation results, a common method is followed. The results for a series of test cases are presented in terms of a disturbance coefficient, k_d , for the entire numerical domain. For regular waves, k_d is given by the ratio, H/H_{GB} , where H is the local wave height and H_{GB} is the wave height at the wave generation boundary. In the case of irregular waves, the significant wave heights are used to calculate the k_d value (H_s/H_{sGB}). For all test cases, the numerical basin is $20L_w$ long and $20L_w$ wide (where L_w is the wave length and is equal to $L_w = 100$ m) while a uniform water depth, $d = 7.5$ m, is used. Thus, in the following numerical tests, the target wave field is a homogeneous one. A homogeneous wave field is characterised by the lack of significant fluctuations from the target, k_d , value, which is equal to $k_{dt} = 1$.

3.3.1 Generation of regular waves

Firstly, oblique regular waves are examined to compare the three different wave generation layouts presented in Section 3.2. Due to the nature of the governing equations of the numerical model, MILDwave (linear mild-slope equations), and the fact that a flat empty numerical basin is examined, the performance of the model for different wave heights and periods is similar. Thus, regular waves with a wave period of $T = 12$ s, wave height of $H = 1$ m, and wave propagation angles from $\theta = 0^\circ$ to $\theta = 45^\circ$ with respect to the x-direction are simulated.

The numerical basin consists of an inner computational domain without the sponge layers with dimensions of $10L_w \times 10L_w$ for the first two layouts and $10L_w \times 20L_w$ for the third one, as well as sponge layers with a width of $5L_w$ at the edges

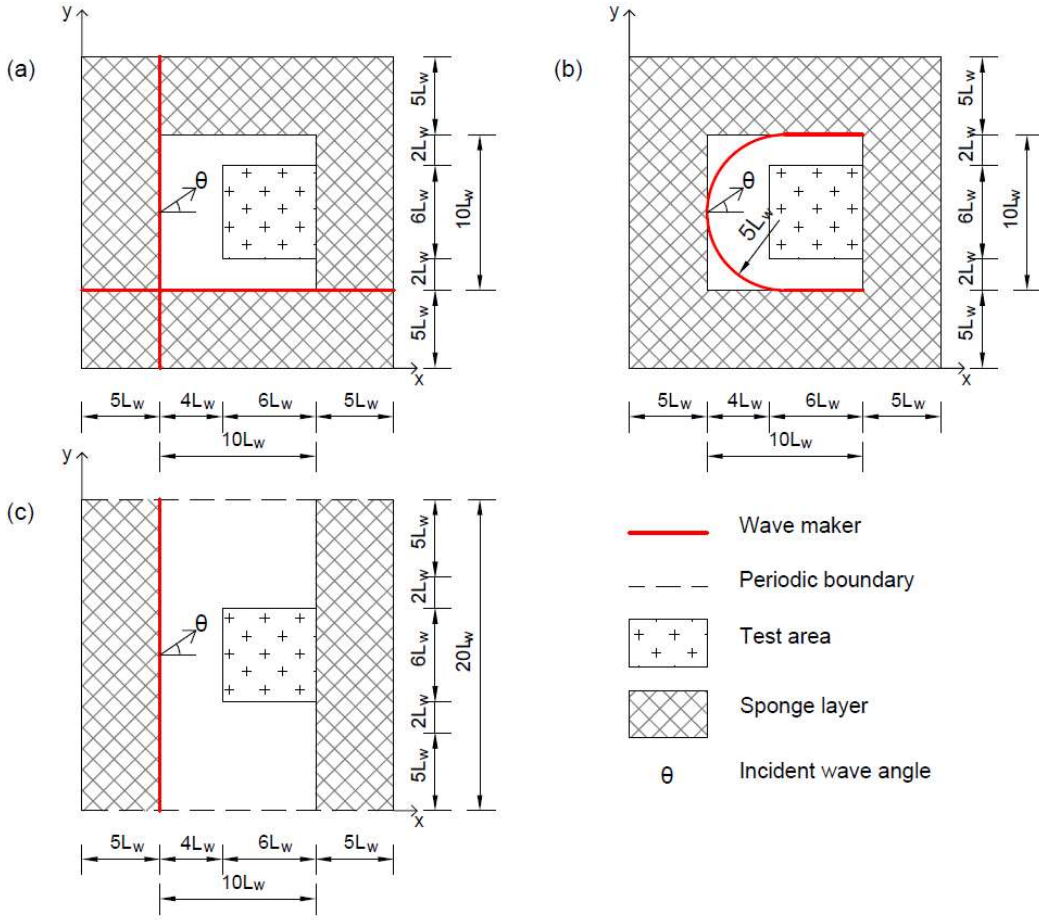


Figure 3.6: Definition sketch of three wave generation layouts: (a) L-shaped, (b) arc-shaped, (c) line-shaped with periodic lateral boundaries. Dimensions are expressed in the number of wave lengths, $L_w = 100$ m, which corresponds to a wave period, $T = 12$ s, and water depth, $d = 7.5$ m.

of the wave basin (Figure 3.6). The grid cell size is chosen so that $\Delta x = \Delta y = L_w/20 = 5$ m. To achieve a steady state wave field, the simulation duration is 1000 s with a time step of $\Delta t = 0.25$ s.

Figure 3.7 shows the plan views of the resulting disturbance coefficient, k_d , and the water surface elevation, η , in the inner computational domain at a time of $t = 80T$, where T is the wave period, for each wave generation layout for a wave propagation angle of $\theta = 30^\circ$ (see Appendix A for wave propagation angles from $\theta = 0^\circ$ to $\theta = 45^\circ$). The black solid contour lines indicate the region where the surface elevation is out of the target range ($\eta > 0.5$ m, $\eta < -0.5$ m). It is observed that the third wave generation layout with the periodic lateral boundaries yields a more homogeneous wave field across the whole domain, which is not disturbed by unwanted wave diffraction patterns in contrast to the other two wave generation layouts. These wave diffraction disturbances are caused by the lateral sponge layers and the intersection of the two wave generation lines, and thus the k_d values fluctuate around the target value ($k_{d_t} = 1$).

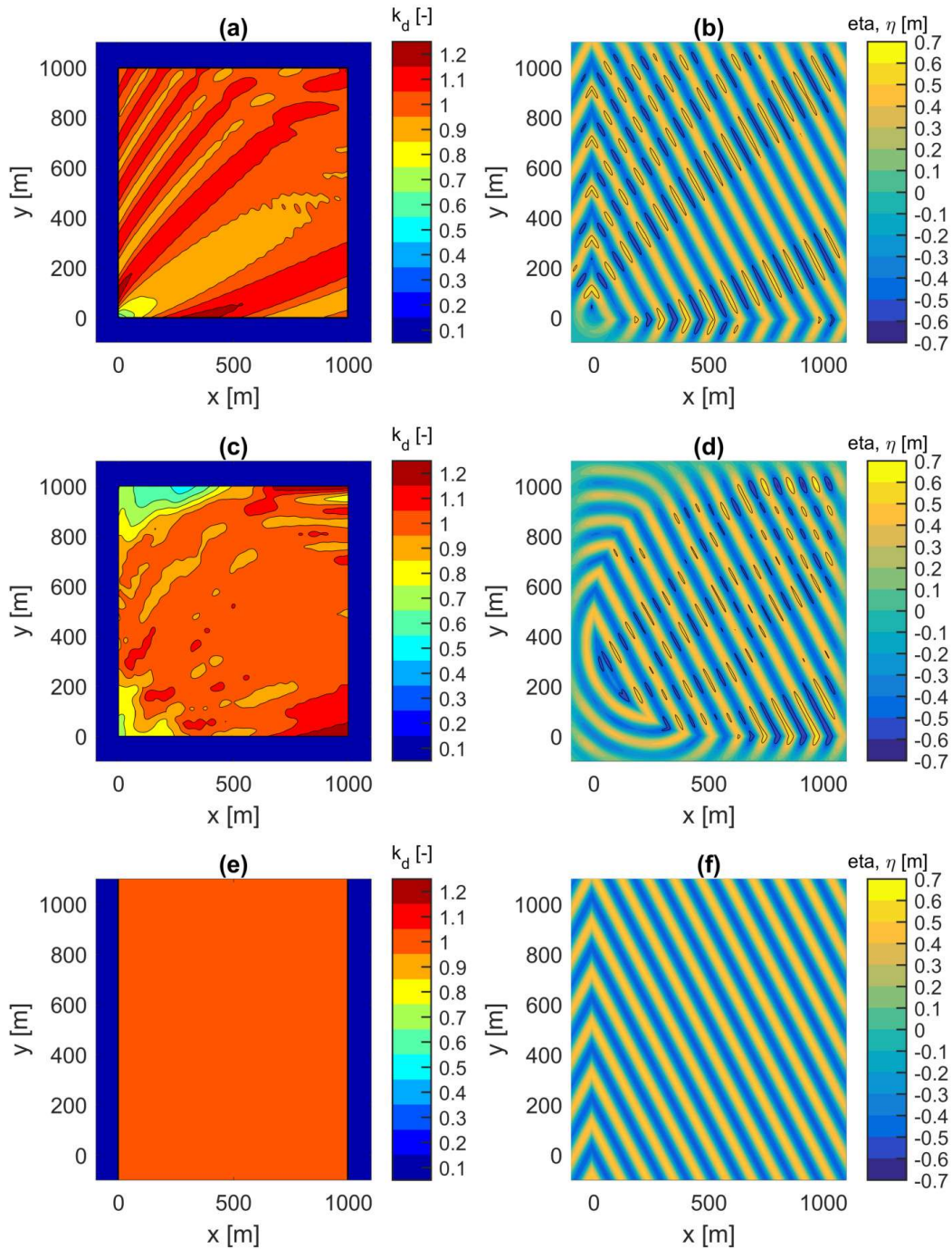


Figure 3.7: Disturbance coefficient, k_d , and water surface elevation, η , in the inner computational domain at $t = 80T$ for regular incident waves with $H = 1$ m, $T = 12$ s, and $\theta = 30^\circ$ generated by an L-shaped wave generation layout (a,b), an arc-shaped wave generation layout (c,d), and by the use of periodic boundaries (e,f).

To obtain a quantified difference between the three different wave generation layouts, the absolute error is calculated in a specific test area far from the sponge layers as in Lee and Yoon (2007). The error is determined as follows:

$$E = \frac{|H_c - H_t|}{H_t} \quad (3.11)$$

where H_c is the local resulting wave height at a point of the numerical domain and H_t is the target wave height. The test area in which the absolute error is calculated is $6L_w$ long and $6L_w$ wide and is indicated in Figure 3.6 (area of crosses).

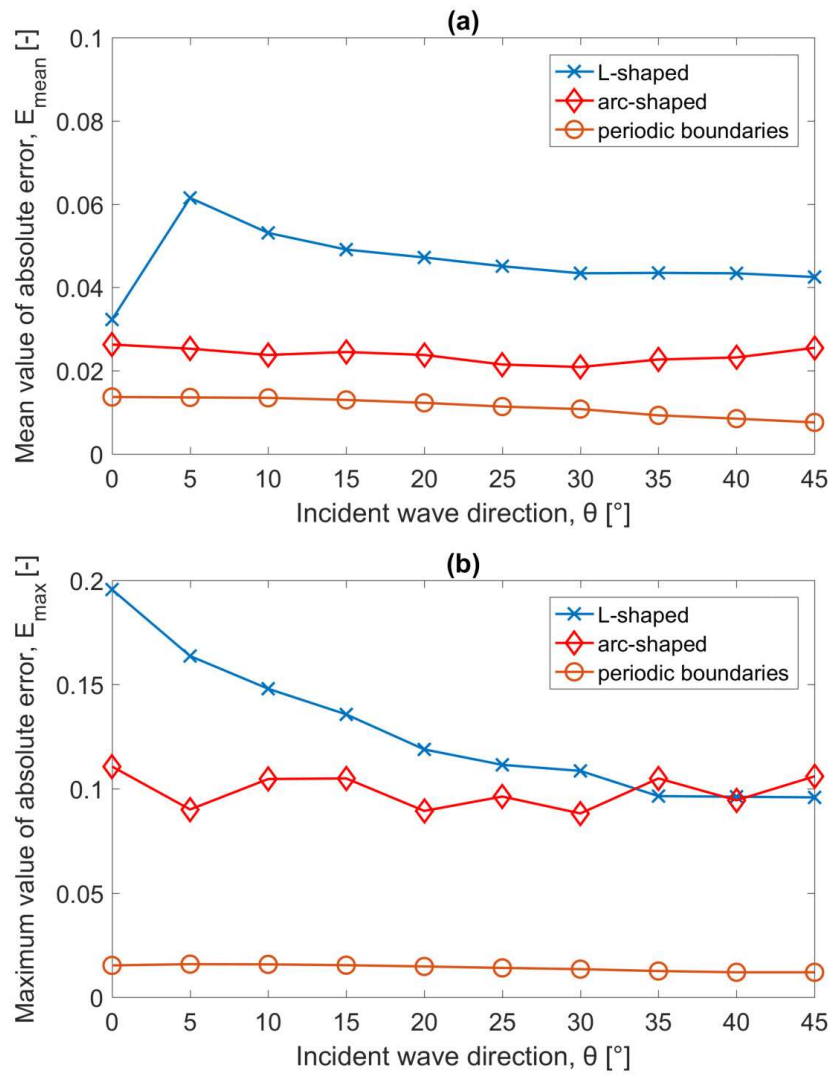


Figure 3.8: (a) Mean (E_{mean}) and (b) maximum (E_{max}) value of the absolute errors calculated using Equation 3.11 for each wave generation layout for a range of different incident wave angles, θ .

In Figure 3.8, the mean (E_{mean}) and the maximum (E_{max}) value of the calculated absolute errors for each wave generation layout for a range of different wave propagation angles are plotted. It is observed, as seen from Figure 3.7 for $\theta = 30^\circ$, that the periodic boundaries' wave generation layout provides the smallest value of E_{mean} and E_{max} for all θ values. For the L-shaped wave generation layout and the periodic boundaries' wave generation layout, E_{mean} is the lowest for $\theta = 45^\circ$ with values of 0.042 and 0.007, respectively, while for the arc-shaped wave generation layout, E_{mean} is the lowest for $\theta = 30^\circ$ with a value of 0.021. The trend of E_{max} (Figure 3.8b) is similar to that of the values of E_{mean} from Figure 3.8a. The E_{max} values of the oblique regular wave field generated using periodic boundaries are significantly smaller than the resulting E_{max} values for the L-shaped and the arc-shaped layouts for all wave directions. In addition, the comparison between the L-shaped wave generation layout and the arc-shaped wave generation layout reveals that in the case of the latter, the wave diffraction due to the intersection of the two generation lines is avoided (Lee and Yoon, 2007). However, for wave directions of θ larger than 30° , E_{max} is similar for both layouts with values around 0.105 while for the periodic boundaries' wave generation layout, it is only 0.012. Hence, this proves that a single wave generation line combined with periodic lateral boundaries provides results of a higher accuracy compared to the other two wave generation layouts and is capable of providing a homogeneous wave field of oblique waves with minimal error.

3.3.2 Generation of irregular long-crested waves

To generate irregular long-crested waves, a parameterized JONSWAP (Joint North Sea Wave Observation Project) spectrum, $S(f)$ (Equation 3.12), or a TMA (Texel, Marsen, Arsloe) spectrum (Equation 3.13), which is applicable in shallow water, can be used as an input spectrum in MILDwave.

$$S(f) = \frac{0.0624}{0.230 + 0.0336\gamma - \frac{0.185}{1.9+\gamma}} H_s^2 f_p^4 f^{-5} \gamma^{\exp\left(-\frac{(f-f_p)^2}{2\sigma^2 f_p^2}\right)} \exp\left(-\frac{5}{4} \left(\frac{f_p}{f}\right)^4\right) \quad (3.12)$$

$$S(f) = \frac{\alpha g^2}{(2\pi)^4 f^5} \exp\left(-\frac{5}{4} \left(\frac{f_p}{f}\right)^4 + (\ln \gamma) \exp\left(-\frac{(f-f_p)^2}{2\sigma^2 f_p^2}\right)\right) \phi(f, d) \quad (3.13)$$

where H_s is the significant wave height, f_p is the peak wave frequency, γ is the peak enhancement factor, α is the Phillips constant, and σ is the spectral width parameter, which depends on the value of the wave frequency:

$$\sigma = \begin{cases} 0.07 & f \leq f_p \\ 0.09 & f > f_p \end{cases} \quad (3.14)$$

The frequency dependent factor, $\phi(f, d)$, which takes into account the effect

of a finite water depth, d , is given by:

$$\phi(f, d) = \begin{cases} 0.5\omega_h^2 & \omega_h < 1 \\ 1 - 0.5(2 - \omega_h)^2 & 1 \leq \omega_h \leq 2 \\ 1 & \omega_h > 2 \end{cases} \quad \omega_h = 2\pi f \sqrt{\frac{d}{g}} \quad (3.15)$$

In this section, we consider a test case of uni-directional irregular waves fitting a JONSWAP spectrum, with a peak wave period, $T_p = 12$ s, a significant wave height, $H_s = 1$ m, and a peak enhancement factor, $\gamma = 3.3$. The frequency range is confined between $0.75f_p$ and $2f_p$, which covers 94% of the total energy, to ensure numerical stability. Periodic lateral boundaries are applied at the top and bottom of the domain similar to Section 3.3.1, while the width of the sponge layers at both ends of the numerical basin is determined by the longest wave length in the incident wave spectrum. The grid cell size, Δx , Δy , and the time step, Δt , are defined by considering the highest frequency ($2f_p$) and the lowest frequency ($0.75f_p$), respectively.

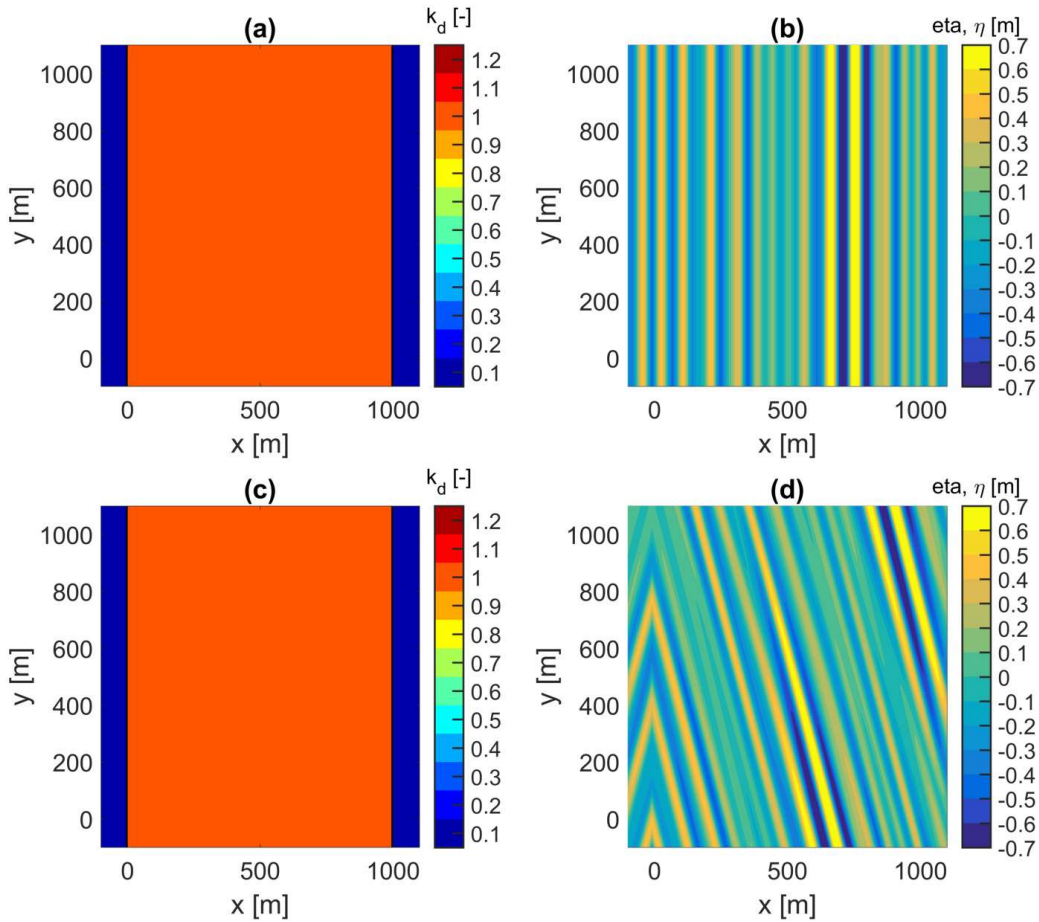


Figure 3.9: Disturbance coefficient, k_d , and water surface elevation, η , in the inner computational domain at $t = 7000$ s for irregular long-crested waves with $H_s = 1$ m, $T_p = 12$ s, and (a,b) $\theta = 0^\circ$ and (c,d) $\theta = 15^\circ$.

A single wave generation line is placed at the left boundary after the sponge layer. To achieve a steady state wave field, time series of the surface elevation of irregular waves are generated for a duration of 7200 s with a time step of $\Delta t = 0.2$ s. Figures 3.9 and 3.10 show the plan views of the k_d values and the water surface elevations in an inner domain (part of the domain without the left and right sponge layers) of 1 km in both directions, at a time instant of $t = 7000$ s, for wave propagation angles θ of 0° , 15° , 30° and 45° .

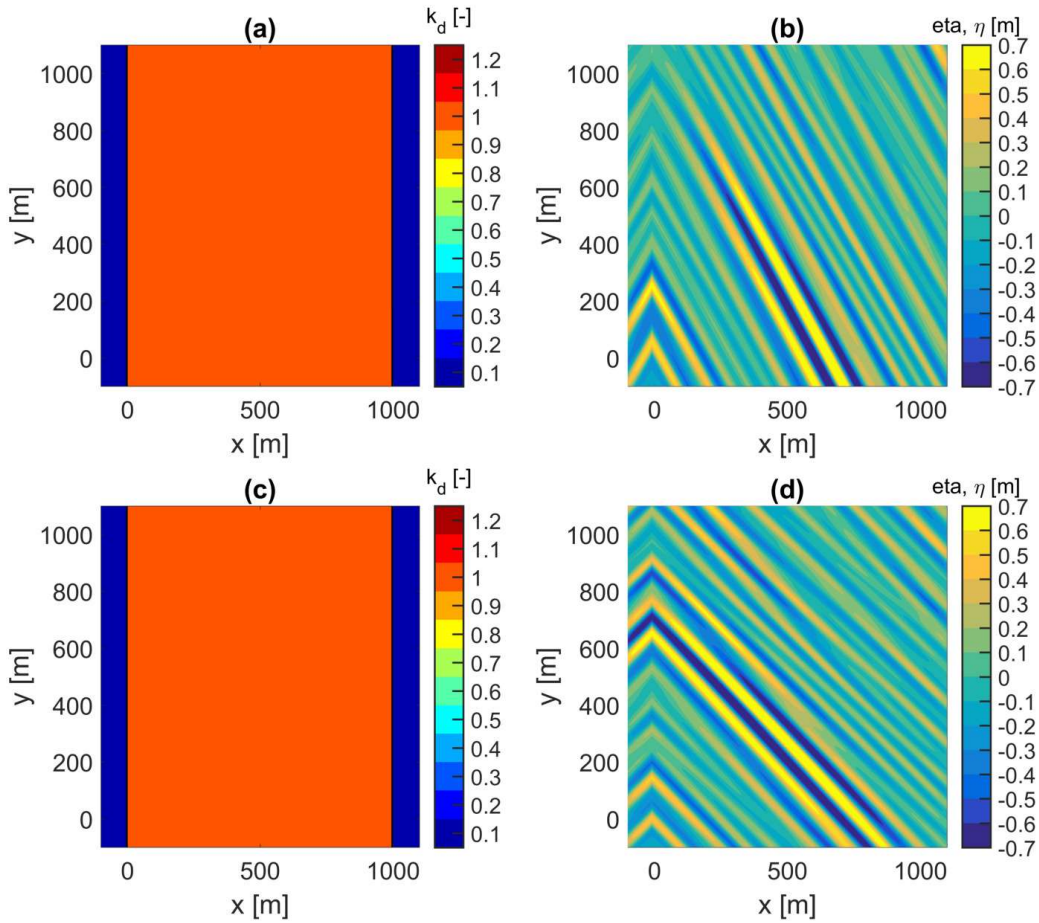


Figure 3.10: Disturbance coefficient, k_d , and water surface elevation, η , in the inner computational domain at $t = 7000$ s for irregular long-crested waves with $H_s = 1$ m, $T_p = 12$ s, and (a,b) $\theta = 30^\circ$ and (c,d) $\theta = 45^\circ$.

It is clear that for all wave propagation angles, the k_d is uniform all over the inner domain with values close to $k_{dt} = 1$. In addition, it is observed by comparing the surface elevation of the different wave directions that for the case of oblique waves, the surface is not as uniform along the crest as it is for the case of $\theta = 0^\circ$. This is happening due to the fact that in order to ensure that waves are periodic, the wave propagation angle, θ , of each wave component is slightly adjusted and a directional spread of the wave energy occurs as described in detail in Section 3.2.3. Hence, for the case of 45° , the wave propagation angle varies from 43.2° to 47.7° for the present wave conditions. However, the deviation from the mean wave

direction is small and the waves can be considered as uni-directional.

In Figure 3.11, a comparison is made between the target frequency spectrum (S_t) and the simulated frequency spectra (S_0 and S_{45}) for the cases of $\theta = 0^\circ$ and $\theta = 45^\circ$. The surface elevations, η , at the electronic wave gauges, which are positioned at the centre of the computational domain, are recorded from $t = 40T_p$ to $t = 600T_p$ with a sampling interval of 0.2 s. The recorded data are processed in segments of 2048 points per segment. The resulting frequency spectra agree well with S_t apart from those that correspond to wave frequencies higher than $2f_p$, since there is no energy for these frequencies in the MILDwave model. Furthermore, it is observed that the periodic lateral boundaries do not affect the waves since for both wave propagation angles, the frequency spectra are similar.

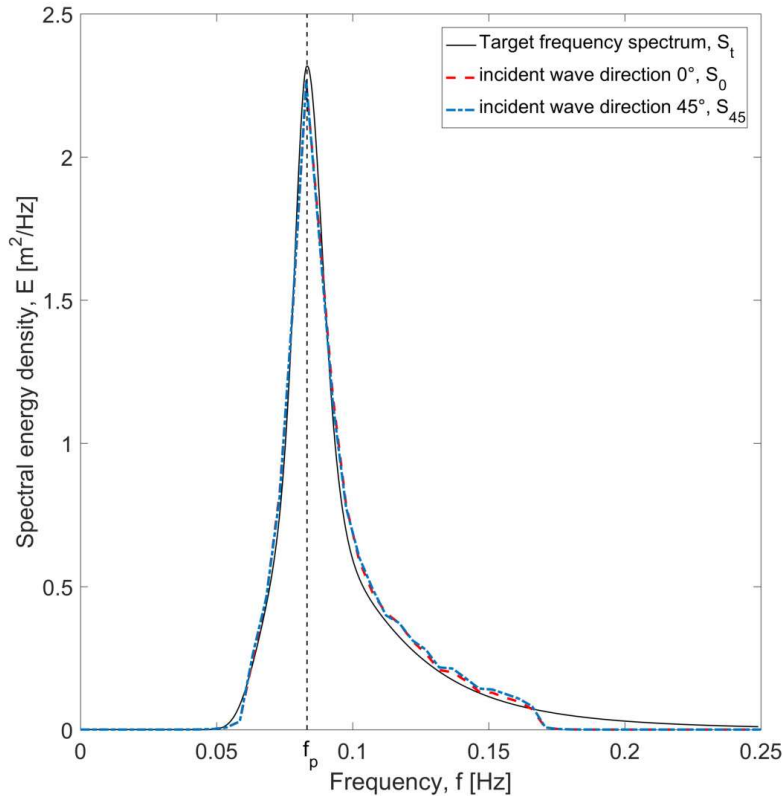


Figure 3.11: Comparison between the frequency spectra, S_0 and S_{45} , resulting from MILDwave simulations for different incident wave angles ($\theta = 0^\circ$ and $\theta = 45^\circ$, respectively), and the target frequency spectrum, S_t , for irregular waves with $H_s = 1$ m, $T_p = 12$ s, and $\gamma = 3.3$.

3.3.3 Generation of irregular short-crested waves

Finally, we consider a test case of irregular short-crested waves. To generate short-crested waves, two different wave synthesis methods are employed in the present

study, a single summation method proposed by Miles (1989) and a second single summation method proposed by Sand and Mynett (1987). In single summation models, each wave component must have a unique frequency and each frequency component can only travel in one direction, while several wave components are propagating in the same direction. According to the Miles method, the surface elevation is defined as follows:

$$\eta(x, y, t) = \sum_{n=1}^N \sum_{m=1}^M A_{nm} \cos(\omega_{nm}t - k_{nm}(x \cos \theta_m + y \sin \theta_m) + \epsilon_{nm}) \quad (3.16)$$

with the wave amplitude, $A_{nm} = \sqrt{2S(f_{nm})D(f_{nm}, \theta_m)M\Delta f\Delta\theta}$, the wave angular frequency, $\omega_{nm} = 2\pi f_{nm} = 2\pi(M(n-1)+m)\Delta f + 2\pi f_{min}$, the frequency interval, $\Delta f = (f_{max} - f_{min})/(NM - 1)$, the wave propagation angle, $\theta_m = (m-1)\Delta\theta + \theta_0 - \theta_{max}$, the wave propagation angle interval, $\Delta\theta = (2\theta_{max})/(M - 1)$, the random phase, ϵ_{nm} , and the maximum discrete wave direction, θ_{max} . In this way, the directional spreading function is discretized into M equally spaced wave directions ranging from θ_{min} to θ_{max} .

Sand and Mynett (1987) proposed a method in which the directional spectrum is decomposed as follows:

$$\eta(x, y, t) = \sum_{n=1}^N \sqrt{2S(f_n)\Delta f} \cos(\omega_n t - k_n(x \cos \theta_n + y \sin \theta_n) + \epsilon_n) \quad (3.17)$$

In this method, the wave propagation angles are selected at random according to the cumulative distribution function of the directional spreading function, $D(f, \theta)$, and are assigned to each frequency component. The Miles method (Miles, 1989) provides an accurate representation of the targeted spreading function shape, but introduces different localized distortions in the frequency spectrum to obtain a close fit to the spreading function. On the other hand, the Sand and Mynett method (Sand and Mynett, 1987) yields an exact match to the frequency spectrum.

Several semi-empirical proposed formulations of the directional spreading function, $D(f, \theta)$, have been reported, most of which consider the spreading function to be independent of the wave frequency. Here, an alternative of the well-known spreading function of Mitsuyasu et al. (1975) is employed (Frigaard et al., 1997):

$$D(f, \theta) = \frac{1}{\sqrt{\pi}} \frac{\Gamma(s_1 + 1)}{\Gamma(s_1 + \frac{1}{2})} \cos^{2s_1}(\theta - \theta_0), \quad -\frac{\pi}{2} < \theta - \theta_0 < \frac{\pi}{2} \quad (3.18)$$

where s_1 is the directional spreading parameter, Γ is the Gamma function, and θ_0 is the wave propagation angle.

To derive the relation between the directional spreading parameter, s_1 , and the

spreading standard deviation, σ_θ , the methodology of Kuik et al. (1988) is followed:

$$\sigma_\theta = \sqrt{2 \left(1 - \sqrt{\left(\int_0^{2\pi} D(f, \theta) \sin \theta d\theta \right)^2 + \left(\int_0^{2\pi} D(f, \theta) \cos \theta d\theta \right)^2} \right)} \quad (3.19)$$

Substitution of Equation 3.18 into Equation 3.19 yields:

$$\sigma_\theta = \sqrt{2 - \frac{2\Gamma^2(s_1 + 1)}{\Gamma(s_1 + \frac{1}{2})\Gamma(s_1 + \frac{3}{2})}} \quad (3.20)$$

The relation between s_1 and σ_θ is indicated in Figure 3.12. Hence, fixed values of s_1 and σ_θ are determined for wind and swell waves:

$$s_1 = \begin{cases} 1.17 & \rightarrow \sigma_\theta = 30^\circ & (\text{wind waves}) \\ 15.8 & \rightarrow \sigma_\theta = 10^\circ & (\text{swell waves}) \end{cases} \quad (3.21)$$

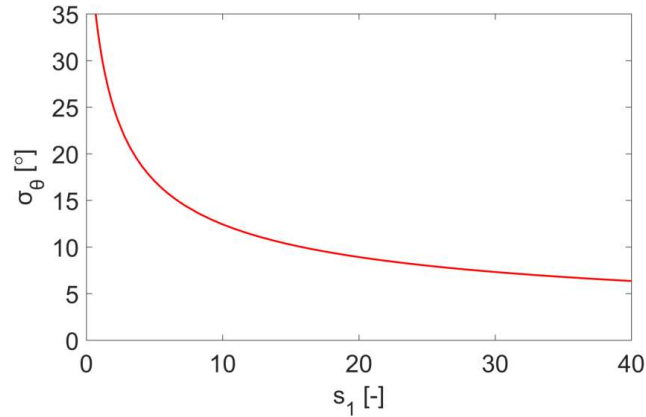


Figure 3.12: Relation between the directional spreading parameter, s_1 , and the spreading standard deviation, σ_θ .

The parameters of the input frequency spectrum are identical to the long-crested irregular waves ($H_s = 1$ m, $T_p = 12$ s, $\gamma = 3.3$) described in the previous section. Waves are generated for a duration of 7200 s with $\Delta t = 0.2$ s, while the two different wave synthesis methods described above have been employed to generate short-crested waves.

The directional wave spectrum was measured by a group of five wave gauges placed in the centre of the computational domain, using a ‘‘CERC 5’’ configuration as introduced by Borgman and Panicker (1970). The recorded normalised spreading function distributions, D_n , are compared with the target distribution, $D_{n,t}$, in Figure 3.13 for both wave synthesis methods and for the spreading standard deviation, $\sigma_\theta = 10^\circ$ (swell waves) and $\sigma_\theta = 30^\circ$ (wind waves). The normalised spreading

function is calculated by integrating the calculated 3D spectrum over all wave frequencies and normalising it. The difference between the two measured normalised spreading function distributions of the two methods is small and the agreement with the target distribution is very good. The Sand and Mynett method agrees slightly better with the target distribution, $D_{n,t}$, than the Miles method especially for the case of $\sigma_\theta = 30^\circ$.

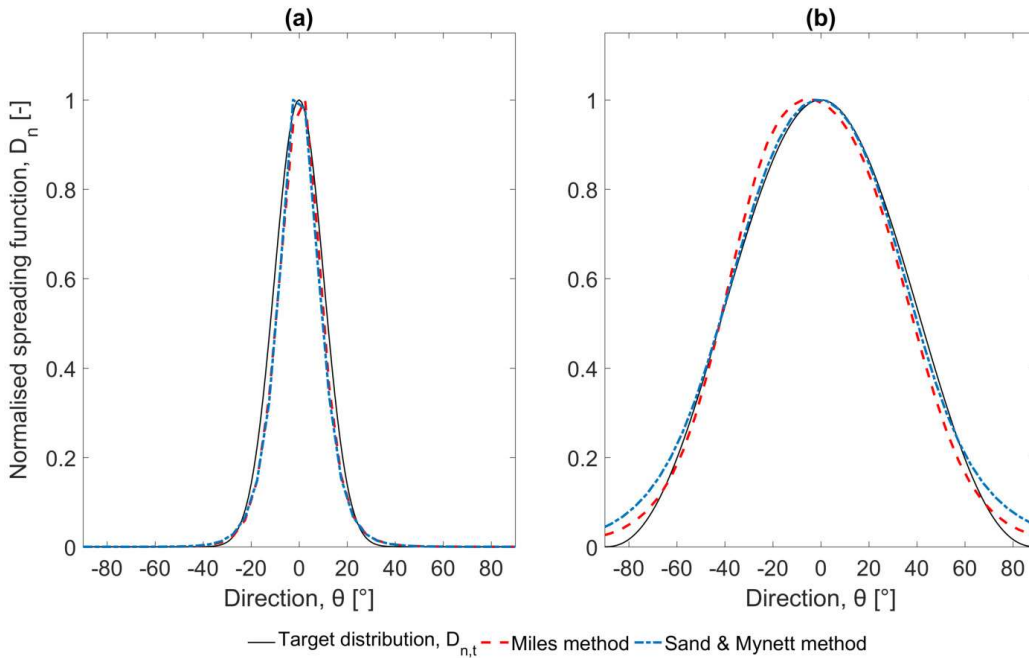


Figure 3.13: Comparison between the normalised spreading function distributions, D_n , calculated in MILDwave with the Miles and the Sand and Mynett wave synthesis methods and the target distribution, $D_{n,t}$, for irregular short-crested waves with a spreading standard deviation, σ_θ , of (a) 10° and (b) 30° .

Figures 3.14 and 3.15 show the plan views of the k_d values throughout the inner computational domain and the surface elevations at a time instant of $t = 7000$ s for each wave synthesis method for a mean wave propagation angle of $\theta = 0^\circ$ and spreading standard deviation of $\sigma_\theta = 10^\circ$ and $\sigma_\theta = 30^\circ$. The results are presented in an inner domain with dimensions of $10L_p \times 10L_p$, where L_p is the wave length that corresponds to the peak wave frequency, f_p . It is clear that the Sand and Mynett method yields a more homogenous wave field than the Miles method. Specifically, the maximum (E_{max}) value of the calculated absolute errors for the Miles method is 0.051 for $\sigma_\theta = 10^\circ$ and 0.085 for $\sigma_\theta = 30^\circ$, respectively, while for the Sand and Mynett method, E_{max} is 0.013 for $\sigma_\theta = 10^\circ$ and 0.029 for $\sigma_\theta = 30^\circ$, respectively. It is worth mentioning that in the Sand and Mynett method, the number of wave components, N_{tot} , is equal to the number of wave frequencies, N . This is happening due to the fact that the wave propagation angles are randomly selected according to the cumulative distribution function of the directional spreading function, $D(f, \theta)$, and are assigned to each wave frequency component. In contrast to that, in the Miles method, the number of the wave

components, N_{tot} , is equal to the product of the number of wave frequencies, N , multiplied with the number of wave angles, M . Thus, in the Sand and Mynett method, (i) the computational time, (ii) the number of corrections of the wave propagation angles in order to ensure the periodicity of the waves, and (iii) the non-homogeneity of the generated wave field are much smaller than those for the Miles method, making the Sand and Mynett method preferable when periodic lateral boundaries are applied in a mild-slope wave model. Specifically, the developed model simulation time for a test case of short-crested waves of a duration of 7200 s in a numerical basin, which is 2 km long and 2 km wide, is approximately 3 min on a PC with an Intel Core CPU (Central Processing Unit) 2.90 GHz.

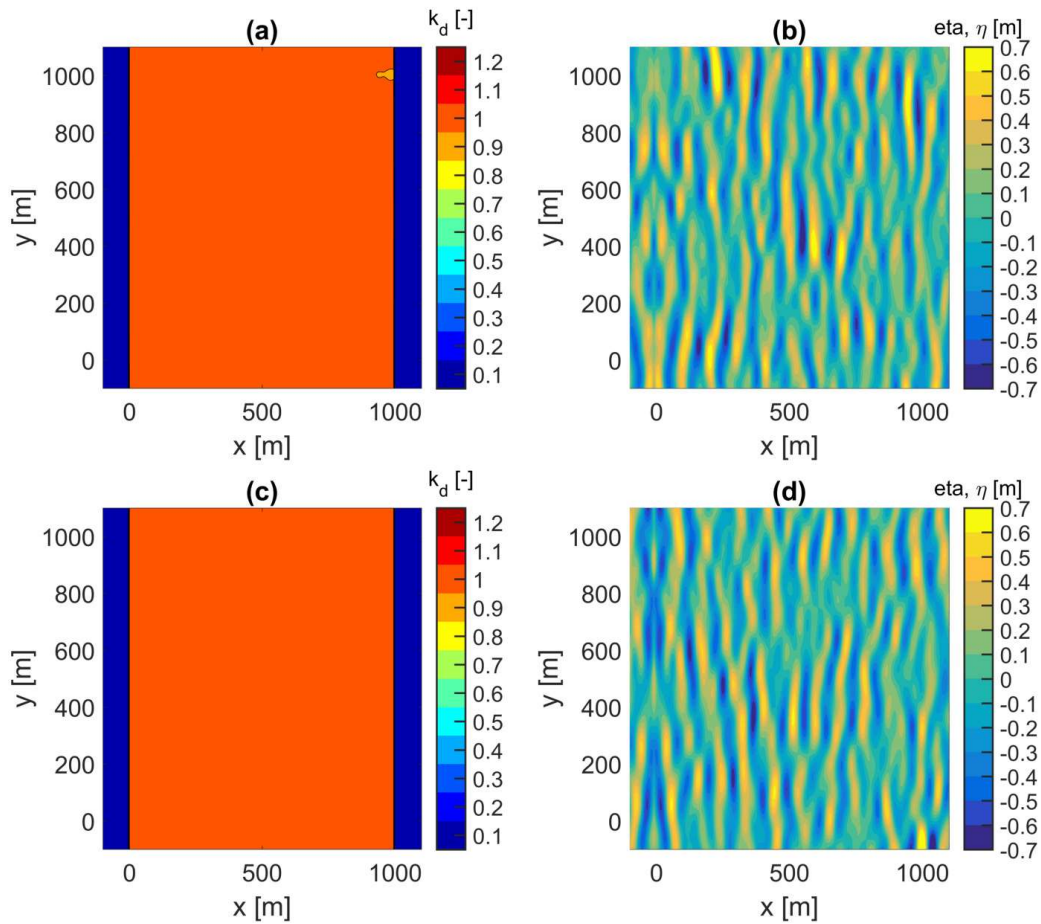


Figure 3.14: Disturbance coefficient, k_d , and water surface elevation, η , in the inner computational domain at $t = 7000$ s for irregular short-crested waves with $H_s = 1$ m, $T_p = 12$ s, $\theta = 0^\circ$, and $\sigma_\theta = 10^\circ$ synthesized by using the Miles method (a,b) and the Sand and Mynett method (c,d).

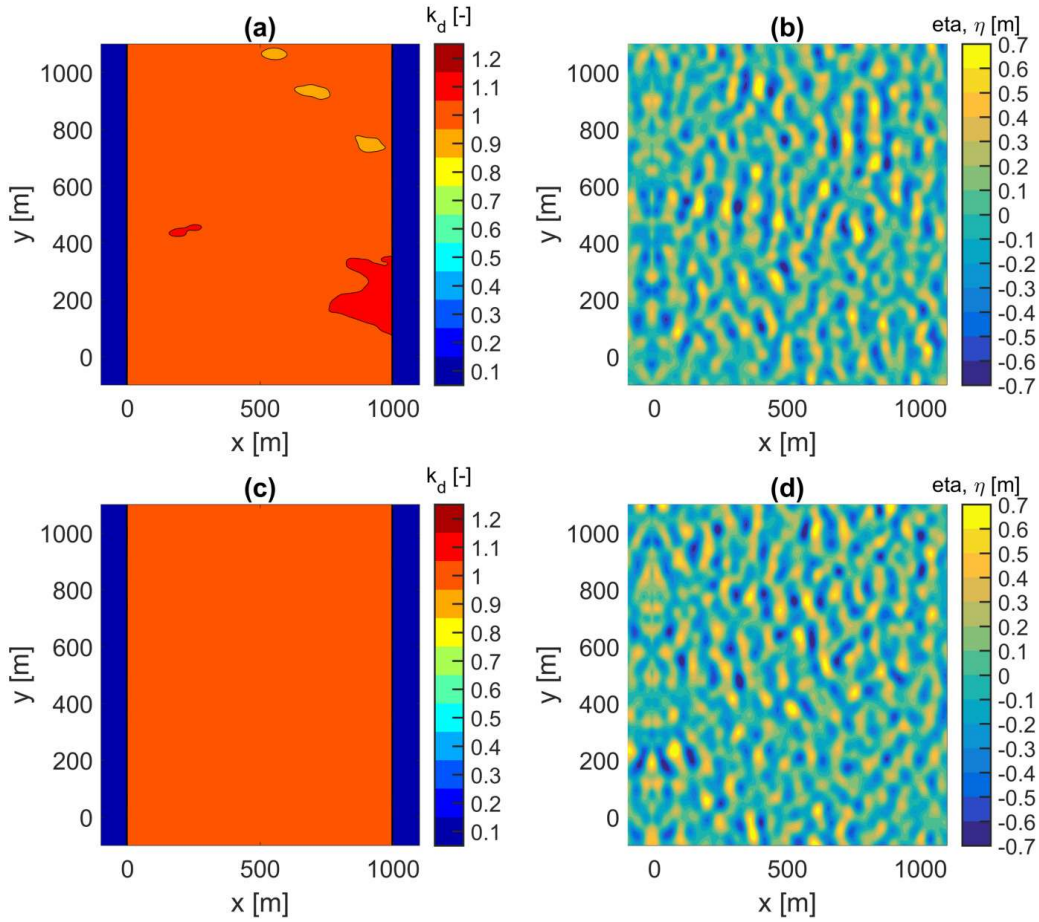


Figure 3.15: Disturbance coefficient, k_d , and water surface elevation, η , in the inner computational domain at $t = 7000$ s for irregular short-crested waves with $H_s = 1$ m, $T_p = 12$ s, $\theta = 0^\circ$, and $\sigma_\theta = 30^\circ$ synthesized by using the Miles method (a,b) and the Sand and Mynett method (c,d).

3.4 Numerical validation using the Vincent and Briggs shoal experiment

To demonstrate the strategic importance of periodic boundaries in the generation of a short-crested wave field over varying water depths, simulations are conducted for waves propagating over a shoal. A study of regular and irregular wave propagation over an elliptic shoal, which has been performed by Vincent and Briggs (1989), is used here for validation of the present numerical model.

The bathymetry of the experimental setup of Vincent and Briggs, implemented in MILDwave as it is illustrated in Figure 3.16, is defined as:

$$\left(\frac{x}{3.05}\right)^2 + \left(\frac{y}{3.96}\right)^2 = 1 \quad (3.22)$$

$$d_e = -0.4572 + 0.7620 \sqrt{1 - \left(\frac{x}{3.81}\right)^2 + \left(\frac{y}{4.95}\right)^2} \quad (3.23)$$

where x and y are the coordinates centered at the center of the shoal and d_e is the bottom level at any point inside the shoal area. The shoal is similar to that used in the experiments of Berkhoff et al. (1982), with a minimum water depth of $d_{min} = 15.24$ cm at the center of the shoal while the area around the shoal has a constant water depth of $d = 45.72$ cm. In addition, the simulated shoal is located at the center of the numerical domain to take advantage of the lateral periodic boundaries and create a fully developed wave field at the region of the shoal. The grid cell size is $\Delta x = \Delta y = 0.05$ m. To achieve a steady state wave field, the simulation duration is 400 s with a time step of $\Delta t = 0.01$ s.

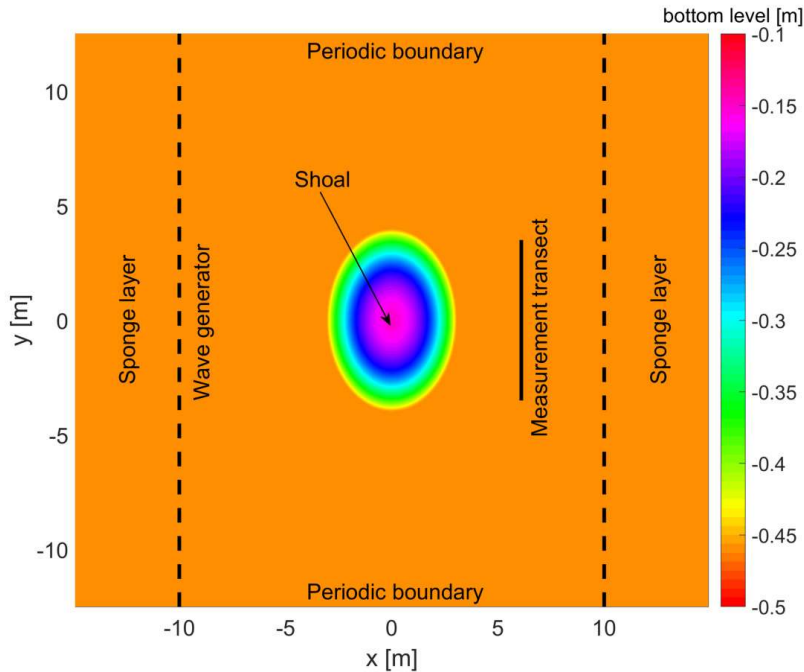


Figure 3.16: Bottom levels of the experimental setup used by Vincent and Briggs, as it is implemented in the numerical domain in MILDwave.

The experiments of Vincent and Briggs are conducted for three kinds of incident breaking and non-breaking waves, i.e., regular, irregular long-crested, and irregular short-crested waves. In the present study, only irregular long- and short-crested waves, where large scale breaking is not involved, are examined. The experimental and numerical input wave parameters for non-breaking series are listed in Table 1.

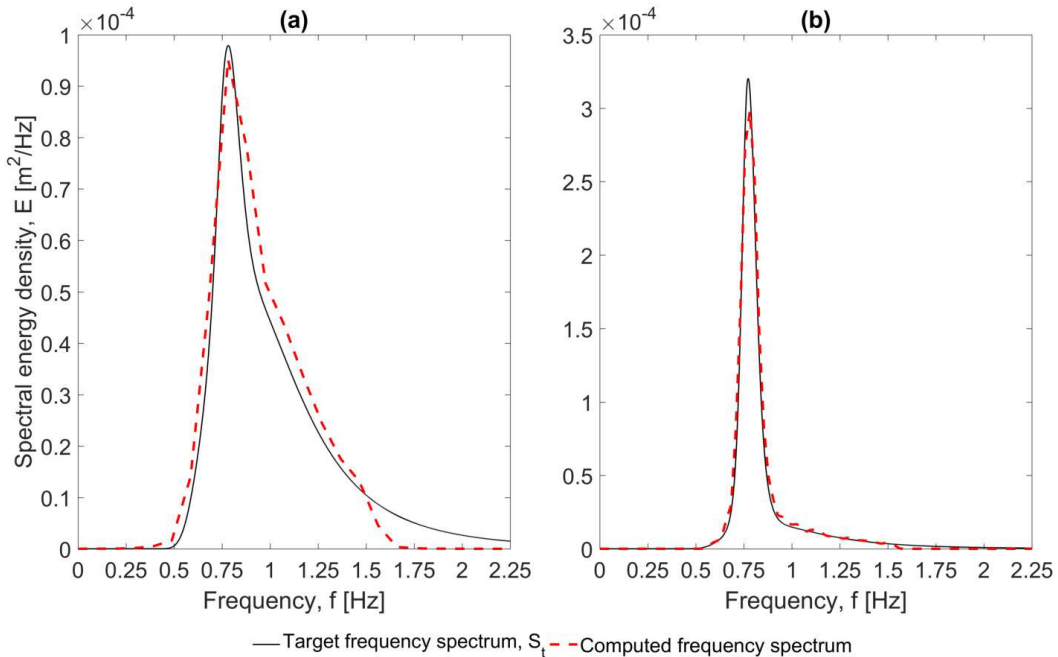
Following Vincent and Briggs (1989), we use the TMA spectrum (Bouws et al., 1985) as the target wave frequency spectrum in which the spectral energy density, $S(f)$, depends on the parameters, α (Phillip's constant), f_p (peak wave frequency), γ (peak enhancement factor), and σ (spectral width parameter), as described in Section 3.3.2. The parameter, γ , is assigned values of 2 for the broad frequency spectrum and 20 for the narrow frequency spectrum. Similarly, these frequency

Table 3.1: Numerical input wave conditions for non-breaking waves based on the Vincent and Briggs (1989) experimental wave conditions.

Test Case ID	Peak Period T_p [s]	Significant Wave Height H_s [cm]	Phillips Constant α [-]	Peak Enhancement Factor, γ [-]	Spreading Standard Deviation, σ_θ [°]
U3	1.3	2.54	0.00155	2	0
N3	1.3	2.54	0.00155	2	10
B3	1.3	2.54	0.00155	2	30
U4	1.3	2.54	0.00047	20	0
N4	1.3	2.54	0.00047	20	10
B4	1.3	2.54	0.00047	20	30

spectra are combined with narrow ($\sigma_\theta = 10^\circ$) and broad ($\sigma_\theta = 30^\circ$) directional spreading, while the α value is selected to correspond to the target wave height.

The directional spreading function, $D(f, \theta)$, given in Equation 3.18 is used instead of the wrapped normal spreading function used by Vincent and Briggs (1989). However, the directional spreading parameter, s_1 , is calculated according to Equation 3.20 in order to achieve the same distribution as the experimental one. Finally, the mean wave propagation angle is $\theta = 0^\circ$ and the number of wave components, N , varies from 50 to 400, with the highest value for the case of broad-banded directional spreading.


Figure 3.17: Comparison between the frequency spectra simulated in MILDwave and the target frequency spectrum for irregular waves with $H_s = 2.54$ cm, $T_p = 1.3$ s, $\sigma_\theta = 0^\circ$, and (a) $\gamma = 2$ and (b) $\gamma = 20$.

The computed frequency spectra are compared with the target spectrum (S_t) in Figure 3.17 for the two values of the peak enhancement factors used here (see Table 3.1). The agreement is very good for the narrow banded spectrum ($\gamma = 20$) where the measured spectrum replicates the desired target one. On the other hand, for the broad frequency spectrum ($\gamma = 2$) the agreement is not as good due to the nature of the governing equations of MILDwave that can account for transformation processes of linear irregular waves with a narrow frequency band (Section 2.3). This affects the accuracy of the model and consequently increases the numerical error for the test cases U3, N3 and B3.

Figure 3.18 shows the comparison of normalised wave heights, H/H_0 , (where H is the local significant wave height and H_0 is the significant wave height at the wave generation boundary) between numerical model results and experimental data along the measurement transect shown in Figure 3.16 for the test cases of non-breaking waves listed in Table 3.1. Additionally, to evaluate the model, the root mean square error (RMSE) and the skill factor for the normalised wave heights are calculated as:

$$RMSE = \sqrt{\frac{\sum_{i=1}^N (P_i - O_i)^2}{N}} \quad (3.24)$$

$$Skill = 1 - \sqrt{\frac{\sum_{i=1}^N (P_i - O_i)^2}{\sum_{i=1}^N O_i^2}} \quad (3.25)$$

where O and P indicate the observed and predicted values, respectively.

Very good agreement between the numerical model and the experimental model is observed (Figure 3.18 and Table 3.2). MILDwave with the addition of the periodic boundaries correctly predicts the wave focusing behind the shoal for the case of irregular long-crested waves where the wave height is strongly affected by the change of the water depth. The model gives a maximum normalised wave height of around 2.05 at $y = 0$ for both the broad frequency spectrum (Test Case U3) and the narrow frequency spectrum (Test Case U4). On the other hand, a broad directional spreading distribution (Test Case B3, Test Case B4) yields much less spatial wave height variation and the effect of wave refraction is significantly diminished.

Table 3.2: Root mean square error (RMSE) and skill factor of the normalised wave heights.

Test Case ID	U3	N3	B3	U4	N4	B4
RMSE	0.141	0.125	0.068	0.068	0.062	0.070
Skill	0.869	0.883	0.936	0.940	0.942	0.924

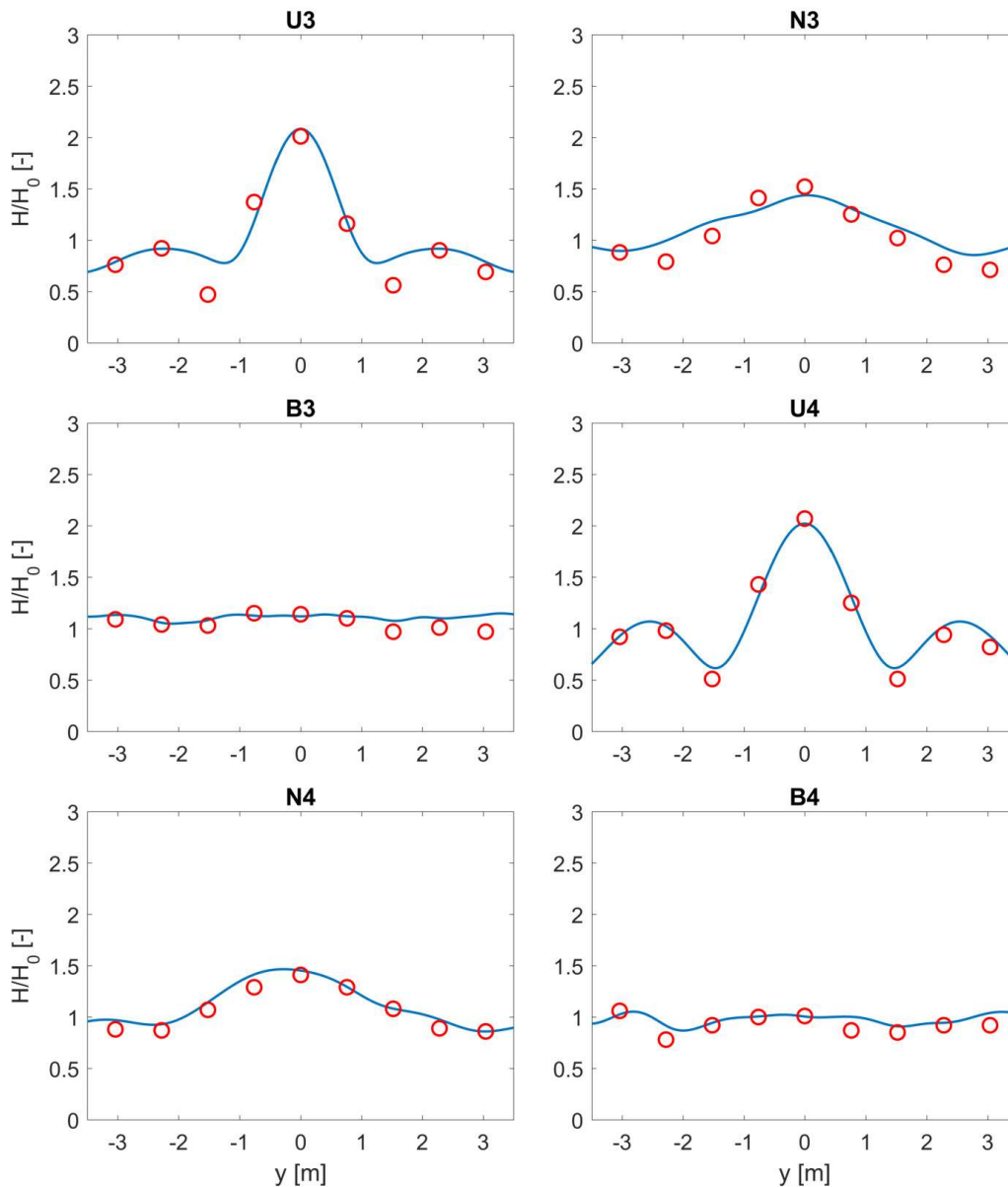


Figure 3.18: Comparison of normalised wave heights, H/H_0 , between numerical model results (blue solid lines) and experimental data (red circles) along the measurement transect of Figure 3.16 for the test cases of non-breaking waves of Table 3.1.

3.5 Application to wave energy converter farms

The results show that the MILDwave model with the addition of the periodic boundaries is capable of reproducing a homogeneous short-crested wave field in the whole computational domain as well as the target frequency spectrum and the target directional spectrum. Thus, a WEC farm and its effect on the near and far field can be examined under real sea waves by coupling the developed model with a

wave-structure interaction solver (NEMOH) as described in Balitsky et al. (2018) and Verao Fernandez et al. (2018).

More precisely, during this coupling methodology, firstly, the short-crested wave field is calculated by the developed model at the position of the WEC farm. Subsequently, this wave field (time series of surface elevation) is used as an input for a wave-structure interaction solver (NEMOH) to simulate the diffracted and radiated wave field generated by the presence of the WEC farm. Finally, the resulting wave field is coupled back to MILDwave and propagates throughout the whole numerical domain. As a result, with the coupling methodology in MILDwave, the impact of WEC farms, especially the far field, can be studied using accurate real sea waves.

Verao Fernandez (2019) used the developed model with the addition of the periodic boundaries to study a nine Heaving Cylindrical Wave Energy Converter (HCWEC) array under the effect of irregular short-crested waves with $H_s = 2.0$ m, $T_p = 6.0$ s and $\sigma_\theta = 10^\circ$. In Figure 3.19, where the plan view of the k_d value is presented, an increase and a decrease of the wave height at the front and lee side of the WEC array, respectively, are observed due to wave diffraction and reflection. Additionally, the results of the coupled model (MILDwave-NEMOH) are compared with the NEMOH results where a very good agreement is observed (Figure 3.20).

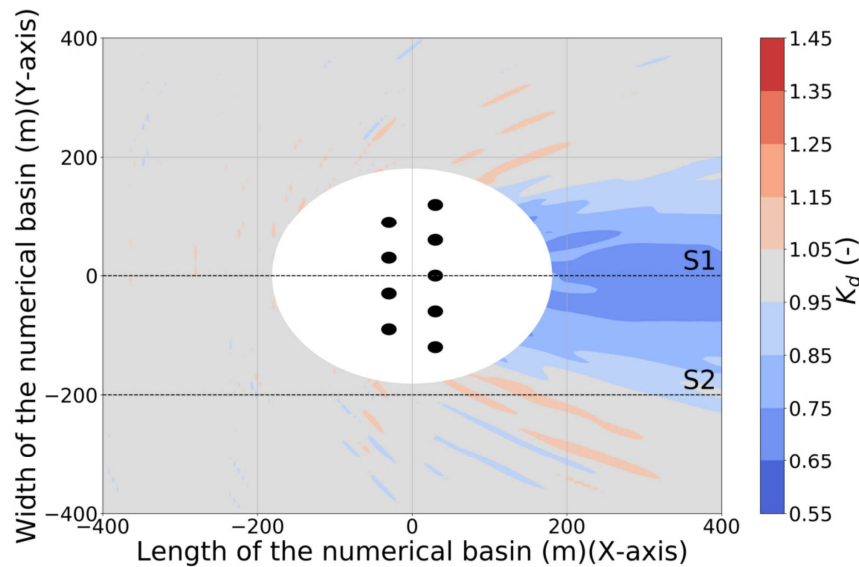


Figure 3.19: Disturbance coefficient, k_d , for a nine Heaving Cylindrical Wave Energy Converter (HCWEC) array under the effect of irregular short-crested waves with $H_s = 2.0$ m, $T_p = 6.0$ s and $\sigma_\theta = 10^\circ$. Figure adopted from Verao Fernandez (2019).

Moreover, Balitsky et al. (2019) studied two WEC farms composed of 2 5-WEC and 10 5-WEC arrays of Oscillating Surging Wave Energy Converters (OSWECs) under oblique waves. The wave conditions and the implemented bathymetry were based on a proposed OSWEC array project for the coast of Bretagne, France. In Figure 3.21, the absolute value of the complex wave amplitude $|\eta|$ for the regular wave of $H = 2$ m, $T = 10$ s and $\theta = -24^\circ$ is presented for a 10 WEC 2-array farm. A very strong interference pattern between the two WEC arrays in the WEC farm

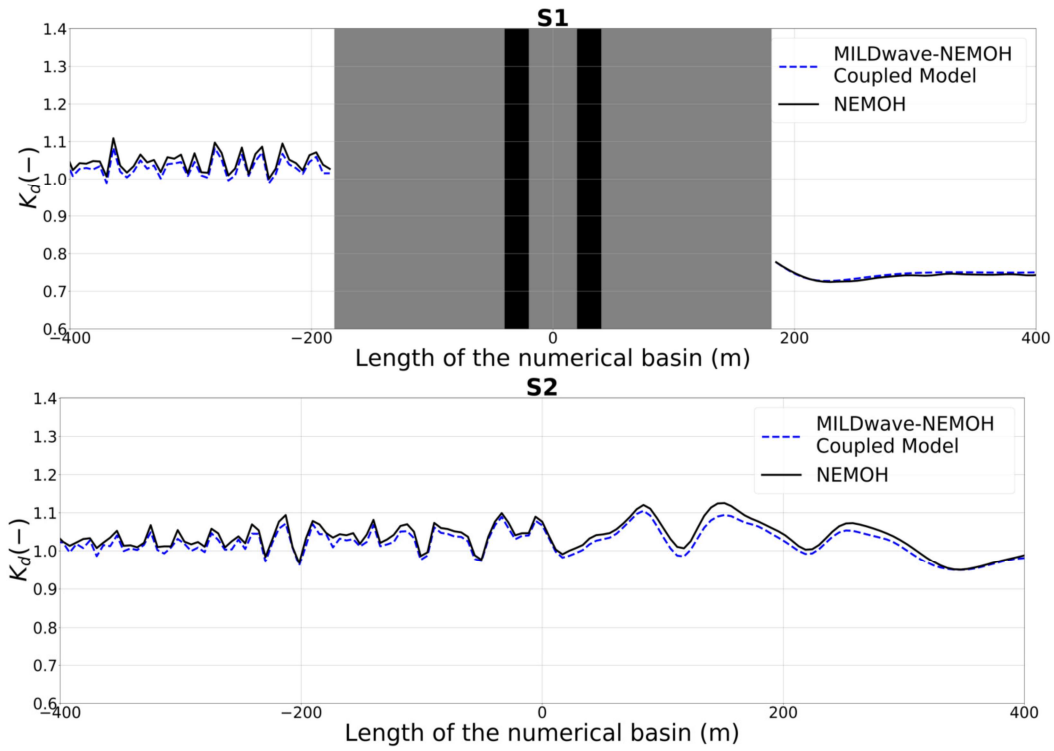


Figure 3.20: Disturbance coefficient, k_d , along two cross-sections S1 (up) and S2 (bottom) as indicated in Figure 3.19 for a nine Heaving Cylindrical Wave Energy Converter (HCWEC) array under the effect of irregular short-crested waves with $H_s = 2.0$ m, $T_p = 6.0$ s and $\sigma_\theta = 10^\circ$. Figure adopted from Verao Fernandez (2019).

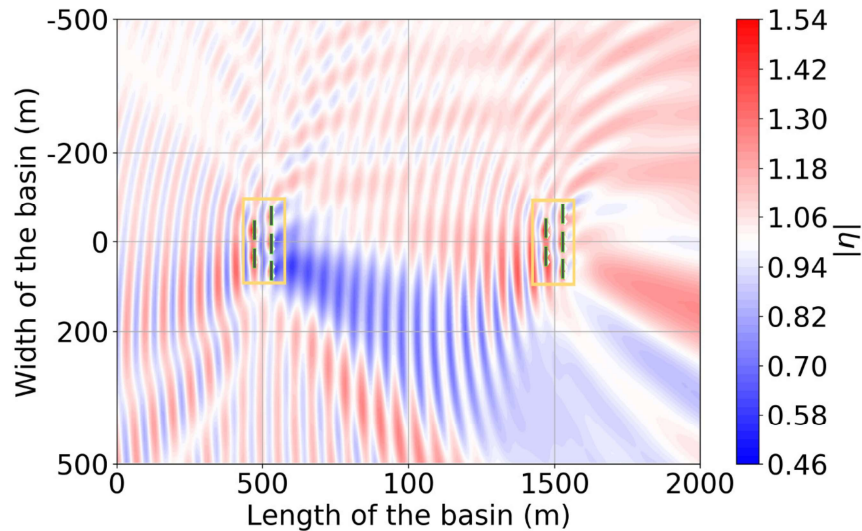


Figure 3.21: Absolute value of the complex wave amplitude $|\eta|$ for the regular wave of $H = 2$ m, $T = 10$ s and $\theta = -24^\circ$ for a 10 WEC 2-array farm. Figure adopted from Balitsky et al. (2019).

can be noticed, while analogous with the contour plots of the k_d in Figure 3.19, there are areas of enhancement (hot spots) and reduction (wake zones) of $|\eta|$.

3.6 Conclusions

In the present chapter, periodic lateral boundaries have been developed in a time dependent mild-slope equation model, MILDwave, for the accurate and fast generation of regular and irregular waves in any direction.

Initially, three different wave generation layouts are examined and compared. The first wave generation layout is an L-shaped wave generator, which is composed of two orthogonal lines. The second wave generation layout is an arc-shaped wave generator where two parallel lines are connected to a semicircle. The third wave generation layout consists of a single wave generation line parallel to the y-axis and periodic lateral boundaries. Numerical experiments are conducted for regular waves with wave propagation angles from $\theta = 0^\circ$ to $\theta = 45^\circ$ (Section 3.3.1). The results are presented by means of contour plots, in terms of a disturbance coefficient (k_d) for the calculation domain, allowing easy comparisons between the different layouts. The wave generation layout with the periodic boundaries shows the best results since this layout leads to a homogeneous wave field, which is not disturbed by unwanted wave diffraction patterns in contrast to the other two wave generation layouts.

Then, this wave generation layout is used to simulate irregular long- (Section 3.3.2) and short-crested (Section 3.3.3) waves by using two different wave synthesis methods: A method proposed by Miles (1989) and a method proposed by Sand and Mynett (1987). The results indicate that the MILDwave model with the addition of the periodic boundaries is capable of reproducing a homogeneous wave field (especially when the Sand and Mynett method is used) as well as the target frequency spectrum and the target directional spectrum.

The developed model is also used to study wave transformation over an elliptical shoal (Vincent and Briggs shoal experiment, Section 3.4), where very good agreement was observed between the numerical model and the experimental results. Finally, an illustration of a practical application of the developed model is given, as presented in more detail in Verao Fernandez (2019) and Balitsky et al. (2019).

The aforementioned observations indicate that periodic boundaries make the mild-slope wave model, MILDwave, an essential tool to generate multi-directional waves and study their transformation due to its significantly small computational cost and its high numerical stability and robustness.

Chapter 4

Linear and nonlinear properties of SWASH Model

In this fourth chapter of the thesis the governing equations of SWASH (introduced in Section 2.4) are analysed for the case of a flat bottom in order to define the linear and nonlinear properties of the model when up to four vertical layers are applied. In this way, knowledge gap 2, as defined in Section 1.2, is tackled (Figure 1.3). Expressions are derived for linear dispersion, second and third order surface components, amplitude dispersion and finally second order transfer functions for subharmonic and superharmonic interactions. The derived expressions are compared with the exact solutions from the literature presented in Chapter 2. It is proved that the SWASH model predicts very well the linear and nonlinear properties of the waves over a wide range of water depths.

4.1 Introduction

An alternative to the mild-slope wave models are the non-hydrostatic wave models which are able to accurately describe coastal phenomena characterised by strong wave nonlinearity. Non-hydrostatic wave models can directly resolve the vertical and horizontal flow structure by retaining the 3D momentum equations and can improve their wave dispersion and the degree of nonlinearity by making use of a few vertical layers.

In the present chapter, the governing equations of the non-hydrostatic wave model, SWASH, are analysed in order to examine the linear and nonlinear properties of the model. A Stokes-type Fourier analysis on a flat bottom is performed in order to define the higher order equations and subsequently expressions are derived for the corresponding solutions. This kind of analysis has served as a standard tool to define and compare the linear and nonlinear properties of different Boussinesq wave models (Madsen and Sørensen, 1993; Madsen and Schäffer, 1998; Kennedy et al., 2001; Memos et al., 2016; Lynett and Liu, 2004a; Gobbi et al., 2000). Bai and Cheung (2013) have performed a similar analysis for their non-hydrostatic wave

model where the governing equations were transformed to a Boussinesq form with the vertical velocity and non-hydrostatic pressure eliminated and second order solutions were derived up to three vertical layers. Here, the layer integrated equations are used directly for the derivation, while solutions up to the third order and up to four equidistant vertical layers are derived. This research approach has never been used before in literature for non-hydrostatic models and constitutes the novelty of the present study. The governing equations, the derivation procedure and the resulting expressions will be presented in detail for the case of two equidistant layers in this chapter, while the solutions for the other three cases (one, three and four layers) are shown in the Appendix B. It has to be mentioned that another layer arrangement (apart from the equidistant) can be utilised to optimise the linear or nonlinear properties of the model. However, optimising the layer arrangement to achieve a better representation of the linear wave dispersion will not necessarily lead to a better representation of the nonlinear properties as well and vice versa. Thus, the solutions for the case that equidistant vertical layers are employed will be presented here since this case is the most frequently applied by the users.

The goal of this chapter is to quantify how the model improves its linear and nonlinear properties by increasing the number of vertical layers and to provide tables with water depth ranges over which the model achieves the target accuracy depending on the number of layers employed. These tables form a tool for SWASH users to decide on the number of vertical layers to be applied taking into account the wave conditions and the acceptable error on the linear and nonlinear properties of each specific case. Additionally, the derived solutions are essential to formulate higher order boundary conditions for regular and irregular waves, and in this way to improve further the homogeneity of the generated wave field.

This chapter has the following structure. The layer integrated governing equations of SWASH are described in Section 4.2. The linearised equations and the frequency dispersion relation are derived in Section 4.3. Section 4.4 provides a detailed presentation of the nonlinear properties of SWASH model. More precisely, the second and third order equations are defined and the corresponding solutions are derived in Sections 4.4.1 and 4.4.2. In addition, the second order transfer functions for subharmonic and superharmonic interactions are derived in Section 4.4.3. In Section 4.5 a sensitivity analysis is executed regarding the effect of the advection terms of the vertical momentum equation. The final section includes the conclusions of the present study.

4.2 Governing equations

In this section the governing equations of SWASH are derived for the case of two equidistant vertical layers, following Zijlema and Stelling (2005) and Zijlema and Stelling (2008).

The SWASH model is based on the Euler equations for an incompressible fluid with a free surface η and a constant density ρ_0 . The numerical domain is bounded vertically by the free-surface $z = \eta$ and the bottom $z = -d$, while the equations for a 2DV domain are given by:

$$\frac{\partial u}{\partial x} + \frac{\partial w}{\partial z} = 0 \quad (4.1)$$

$$\frac{\partial u}{\partial t} + \frac{\partial uu}{\partial x} + \frac{\partial uw}{\partial z} + g \frac{\partial \eta}{\partial x} + \frac{\partial q}{\partial x} = 0 \quad (4.2)$$

$$\frac{\partial w}{\partial t} + \frac{\partial uw}{\partial x} + \frac{\partial ww}{\partial z} + \frac{\partial q}{\partial z} = 0 \quad (4.3)$$

where u and w are the horizontal and vertical velocities and q is the non-hydrostatic pressure.

The kinematic conditions at the free surface and the bottom are given in Equations 4.4 and 4.5, respectively:

$$w_s = \frac{\partial \eta}{\partial t} + u \frac{\partial \eta}{\partial x} \quad z = \eta \quad (4.4)$$

$$w_b = -u \frac{\partial d}{\partial x} \quad z = -d \quad (4.5)$$

The free surface equation is obtained by integrating the continuity equation for the entire water column $h = d + \eta$ and applying the kinematic condition at the free surface:

$$\frac{\partial \eta}{\partial t} + \frac{\partial}{\partial x} \int_{-d}^{\eta} u dz = 0 \quad (4.6)$$

The numerical implementation is based on an explicit, second order finite difference method, where the mass and momentum are strictly conserved at a discrete level. A staggered grid arrangement is applied, where the horizontal u and the vertical w velocity components are located at the cell faces, as presented in Figure 4.1. Regarding the non-hydrostatic pressure two arrangements are possible: a) central differences scheme (Figure 4.1a), where the pressure is defined at the centre of the cell or b) Keller Box scheme (Figure 4.1b), where the pressure is defined at the cell face (same location as w). As it has been proved by Zijlema and Stelling (2008), the Keller Box scheme leads to better dispersive properties than

the central differences scheme when coarse vertical resolution is applied, while in case of a fine vertical resolution the central differences scheme is more robust and thus preferable.

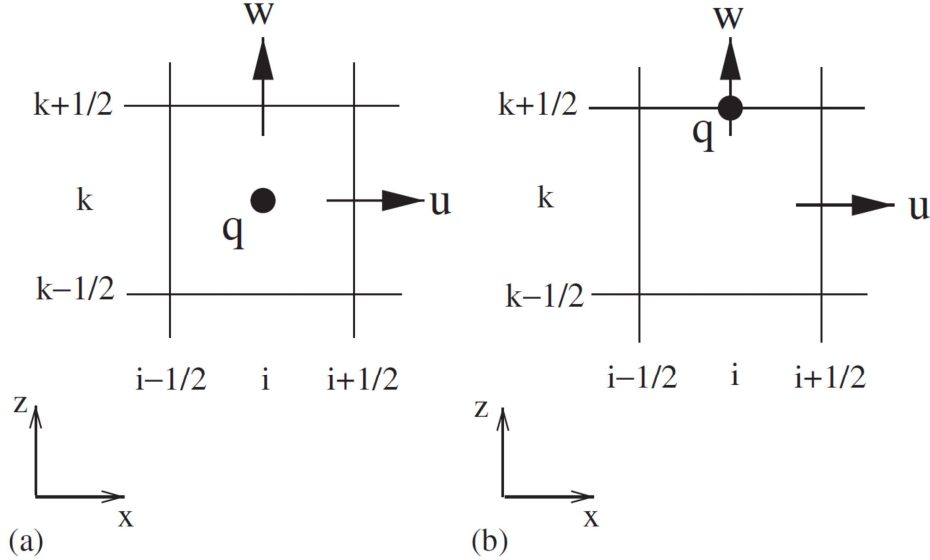


Figure 4.1: Arrangement of the unknowns in a staggered grid: (a) Central differences scheme and (b) Keller Box scheme. Figure adopted from Zijlema and Stelling (2008).

In order to derive the governing equations for the system of two layers, the layer-integrated Euler equations should be defined, by depth integrating over each layer the Equations 4.1-4.3. The layer integrated continuity equation (Equation 4.1) and momentum equations (Equations 4.2 and 4.3) for layer k ($z_{k-1/2} \leq z \leq z_{k+1/2}$) are given by:

$$\frac{\partial h_k u_k}{\partial x} - u_{k+1/2} \frac{\partial z_{k+1/2}}{\partial x} + u_{k-1/2} \frac{\partial z_{k-1/2}}{\partial x} + w_{k+1/2} - w_{k-1/2} = 0 \quad (4.7)$$

$$\begin{aligned} \frac{\partial h_k u_k}{\partial t} + \frac{\partial h_k u_k u_k}{\partial x} + u_{k+1/2} w_{rel,k+1/2} - u_{k-1/2} w_{rel,k-1/2} \\ + h_k g \frac{\partial \eta}{\partial x} + \frac{\partial h_k q_k}{\partial x} - q_{k+1/2} \frac{\partial z_{k+1/2}}{\partial x} + q_{k-1/2} \frac{\partial z_{k-1/2}}{\partial x} = 0 \end{aligned} \quad (4.8)$$

$$\begin{aligned} \frac{\partial h_k w_k}{\partial t} + \frac{\partial h_k u_k w_k}{\partial x} + w_{k+1/2} w_{rel,k+1/2} - w_{k-1/2} w_{rel,k-1/2} \\ + q_{k+1/2} - q_{k-1/2} = 0 \end{aligned} \quad (4.9)$$

where w_{rel} is the relative vertical velocity at the layer interface, defined as the difference between the vertical velocity along the streamline and the vertical velocity along the interface:

$$w_{rel,k+1/2} = w_{k+1/2} - \frac{\partial z_{k+1/2}}{\partial t} - u_{k+1/2} \frac{\partial z_{k+1/2}}{\partial x} \quad (4.10)$$

In Figure 4.2, the definition sketch for the case of two equidistant vertical layers ($h_1 = h_2 = h/2$) and the location of the flow parameters with respect to z-axis are presented. As observed, a Keller Box scheme is considered for the pressures which are defined at the vertical boundaries of each layer (surface, interface and bottom). Additionally, the non-hydrostatic pressure at the free surface is $q_s = 0$ since the surface tension is neglected and the vertical velocity at the bottom is $w_b = 0$ since a flat bottom is considered in this chapter ($\partial d/\partial x = 0$, Equation 4.5).

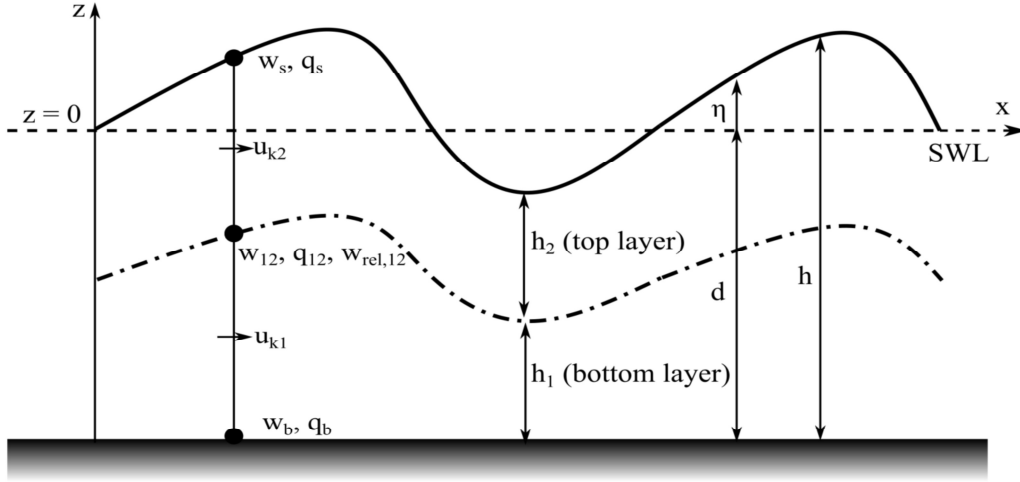


Figure 4.2: Definition sketch for the case of two vertical layers and positioning of flow parameters with respect to z-axis.

Applying the layer-integrated equations (Equations 4.7-4.9) for this two-layer system yields the following governing equations:

$$\frac{\partial \eta}{\partial t} + \frac{1}{2} \frac{\partial h(u_{k1} + u_{k2})}{\partial x} = 0 \quad (4.11)$$

$$\frac{1}{2} \frac{\partial h u_{k2}}{\partial x} - u_{k2} \frac{\partial \eta}{\partial x} + \frac{1}{4} (u_{k1} + u_{k2}) \frac{\partial (h - 2d)}{\partial x} + w_s - w_{12} = 0 \quad (4.12)$$

$$\frac{1}{2} \frac{\partial h u_{k1}}{\partial x} - \frac{1}{4} (u_{k1} + u_{k2}) \frac{\partial (h - 2d)}{\partial x} + w_{12} = 0 \quad (4.13)$$

$$\begin{aligned} \frac{1}{2} \frac{\partial h u_{k2}}{\partial t} + \frac{1}{2} \frac{\partial h u_{k2} u_{k2}}{\partial x} - \frac{1}{2} (u_{k1} + u_{k2}) w_{rel,12} + \frac{1}{2} h g \frac{\partial \eta}{\partial x} \\ + \frac{1}{4} \frac{\partial h q_{12}}{\partial x} + \frac{1}{2} q_{12} \frac{\partial (h - 2d)}{\partial x} = 0 \end{aligned} \quad (4.14)$$

$$\begin{aligned} \frac{1}{2} \frac{\partial h u_{k1}}{\partial t} + \frac{1}{2} \frac{\partial h u_{k1} u_{k1}}{\partial x} + \frac{1}{2} (u_{k1} + u_{k2}) w_{rel,12} + \frac{1}{2} h g \frac{\partial \eta}{\partial x} \\ + \frac{1}{4} \frac{\partial h (q_{12} + q_b)}{\partial x} - \frac{1}{2} q_{12} \frac{\partial (h - 2d)}{\partial x} - q_b \frac{\partial d}{\partial x} = 0 \end{aligned} \quad (4.15)$$

$$\frac{1}{4} \frac{\partial h (w_s + w_{12})}{\partial t} + \frac{1}{4} \frac{\partial h u_{k2} (w_s + w_{12})}{\partial x} - w_{rel,12} w_{12} - q_{12} = 0 \quad (4.16)$$

$$\frac{1}{4} \frac{\partial h w_{12}}{\partial t} + \frac{1}{4} \frac{\partial h u_{k1} w_{12}}{\partial x} + w_{rel,12} w_{12} + q_{12} - q_b = 0 \quad (4.17)$$

where u_{k2} and u_{k1} are the horizontal layer-integrated velocities of the top and bottom layer, q_{12} and q_b are the non-hydrostatic pressures at the two layers' interface and the bottom, w_s and w_{12} are the vertical velocities at the free surface and the two layers' interface, and finally $w_{rel,12}$ is the relative vertical velocity defined as:

$$w_{rel,12} = w_{12} - \frac{1}{2} \frac{\partial (h - 2d)}{\partial t} - \frac{1}{4} (u_{k1} + u_{k2}) \frac{\partial (h - 2d)}{\partial x} \quad (4.18)$$

As it is observed for a system of two vertical layers ($K = 2$), we have seven governing equations ($3K + 1$) with seven unknowns: one free surface equation (Equation 4.11), two continuity equations (Equations 4.12 and 4.13), two horizontal (Equations 4.14 and 4.15) and two vertical momentum equations (Equations 4.16 and 4.17).

In order to determine the linear and nonlinear properties of SWASH model, the first, second and third order equations are derived through perturbation expansions, which for the case of two layers are given by:

$$\eta = \epsilon \eta^{(1)} + \epsilon^2 \eta^{(2)} + \epsilon^3 \eta^{(3)} \quad (4.19)$$

$$u_{k1} = \epsilon u_{k1}^{(1)} + \epsilon^2 u_{k1}^{(2)} + \epsilon^3 u_{k1}^{(3)} \quad (4.20)$$

$$u_{k2} = \epsilon u_{k2}^{(1)} + \epsilon^2 u_{k2}^{(2)} + \epsilon^3 u_{k2}^{(3)} \quad (4.21)$$

$$w_s = \epsilon w_s^{(1)} + \epsilon^2 w_s^{(2)} + \epsilon^3 w_s^{(3)} \quad (4.22)$$

$$w_{12} = \epsilon w_{12}^{(1)} + \epsilon^2 w_{12}^{(2)} + \epsilon^3 w_{12}^{(3)} \quad (4.23)$$

$$q_{12} = \epsilon q_{12}^{(1)} + \epsilon^2 q_{12}^{(2)} + \epsilon^3 q_{12}^{(3)} \quad (4.24)$$

$$q_b = \epsilon q_b^{(1)} + \epsilon^2 q_b^{(2)} + \epsilon^3 q_b^{(3)} \quad (4.25)$$

where ϵ is an ordering parameter and the superscripts (1), (2) and (3) stand for the first, second and third order solutions respectively.

In the following sections, a Stokes-type Fourier analysis is executed for the case of a flat bottom, where by substituting Equations 4.19-4.25 into Equations 4.11-4.17 we derive the first, second and third order equations and the corresponding solutions. It has to be mentioned that in SWASH when coarse vertical resolution is applied combined with the Keller Box scheme for the discretization of the pressure, then the third term in the vertical momentum equations (Equations 4.16 and 4.17) including the relative vertical velocity ($w_{rel,12}$) is neglected for robustness reasons. Thus, in the following sections, the term $w_{rel,12}w_{12}$ will be neglected. However, a sensitivity analysis will be executed in Section 4.5, in order to study the influence of the horizontal and vertical advection terms of the vertical momentum equations on the second order nonlinear properties of the model.

4.3 Derivation of linear properties

After substituting the perturbation expansions (Equations 4.19-4.25) into the governing equations of the two layer system (Equations 4.11-4.17) and retaining only the $O(\epsilon)$ terms, the first order or linear equations are determined:

$$2\frac{\partial\eta^{(1)}}{\partial t} + d\frac{\partial u_{k1}^{(1)}}{\partial x} + d\frac{\partial u_{k2}^{(1)}}{\partial x} = 0 \quad (4.26)$$

$$d\frac{\partial u_{k2}^{(1)}}{\partial x} + 2w_s^{(1)} - 2w_{12}^{(1)} = 0 \quad (4.27)$$

$$d\frac{\partial u_{k1}^{(1)}}{\partial x} + 2w_{12}^{(1)} = 0 \quad (4.28)$$

$$2\frac{\partial u_{k2}^{(1)}}{\partial t} + 2g\frac{\partial\eta^{(1)}}{\partial x} + \frac{\partial q_{12}^{(1)}}{\partial x} = 0 \quad (4.29)$$

$$2\frac{\partial u_{k1}^{(1)}}{\partial t} + 2g\frac{\partial\eta^{(1)}}{\partial x} + \frac{\partial q_{12}^{(1)}}{\partial x} + \frac{\partial q_b^{(1)}}{\partial x} = 0 \quad (4.30)$$

$$d\frac{\partial w_s^{(1)}}{\partial t} + d\frac{\partial w_{12}^{(1)}}{\partial t} - 4q_{12}^{(1)} = 0 \quad (4.31)$$

$$d\frac{\partial w_{12}^{(1)}}{\partial t} + 4q_{12}^{(1)} - 4q_b^{(1)} = 0 \quad (4.32)$$

The correct representation of the linear dispersion relation, which relates the wavelength to the wave period, is an important characteristic of a wave model and indicates that the model is applicable in deep water conditions. To derive the linear dispersion relation of SWASH model, we consider a wave traveling along the

x-direction with angular frequency ω and wave number k . The first order solutions have the following form:

$$\eta^{(1)} = \eta_{01} \cos(kx - \omega t) \quad (4.33)$$

$$u_{k1}^{(1)} = u_{k1,01} \cos(kx - \omega t) \quad (4.34)$$

$$u_{k2}^{(1)} = u_{k2,01} \cos(kx - \omega t) \quad (4.35)$$

$$w_s^{(1)} = w_{s,01} \sin(kx - \omega t) \quad (4.36)$$

$$w_{12}^{(1)} = w_{12,01} \sin(kx - \omega t) \quad (4.37)$$

$$q_{12}^{(1)} = q_{12,01} \cos(kx - \omega t) \quad (4.38)$$

$$q_b^{(1)} = q_{b,01} \cos(kx - \omega t) \quad (4.39)$$

Substituting the above solutions into Equations 4.26-4.32, the linear dispersion relation of the model for the case of two equidistant layers ($K = 2$) is obtained:

$$\omega_{K2} = \frac{4\sqrt{gk^2d(16 + k^2d^2)}}{\sqrt{256 + 96k^2d^2 + k^4d^4}} \quad (4.40)$$

Following the same procedure, the dispersion relations for one, three and four layers ($K = 1$, $K = 3$ and $K = 4$ respectively) are derived:

$$\omega_{K1} = 2\sqrt{\frac{gk^2d}{4 + k^2d^2}} \quad (4.41)$$

$$\omega_{K3} = \frac{6\sqrt{gk^2d(1296 + 120k^2d^2 + k^4d^4)}}{\sqrt{46656 + 19440k^2d^2 + 540k^4d^4 + k^6d^6}} \quad (4.42)$$

$$\omega_{K4} = \frac{8\sqrt{gk^2d(262144 + 28672k^2d^2 + 448k^4d^4 + k^6d^6)}}{\sqrt{16777216 + 7340032k^2d^2 + 286720k^4d^4 + 1792k^6d^6 + k^8d^8}} \quad (4.43)$$

By increasing the number of layers, higher order polynomials in terms of kd are included in the numerator and denominator. In Figure 4.3, the ratio $\omega_{SWASH}/\omega_{Airy}$ and the corresponding relative error for one, two, three and four vertical layers as a function of the dimensionless depth kd are presented. It is observed that by increasing the number of layers, a better fit is achieved with the exact linear dispersion relation (Equation 2.11) up to larger kd values and thus deeper water.

This indicates that the model improves its wave dispersion by making use of a few vertical layers. More precisely, for three layers the relative error is smaller than 1% up to a kd value of 16.41, while for four vertical layers up to a kd value of 28.59 (Table 4.1).

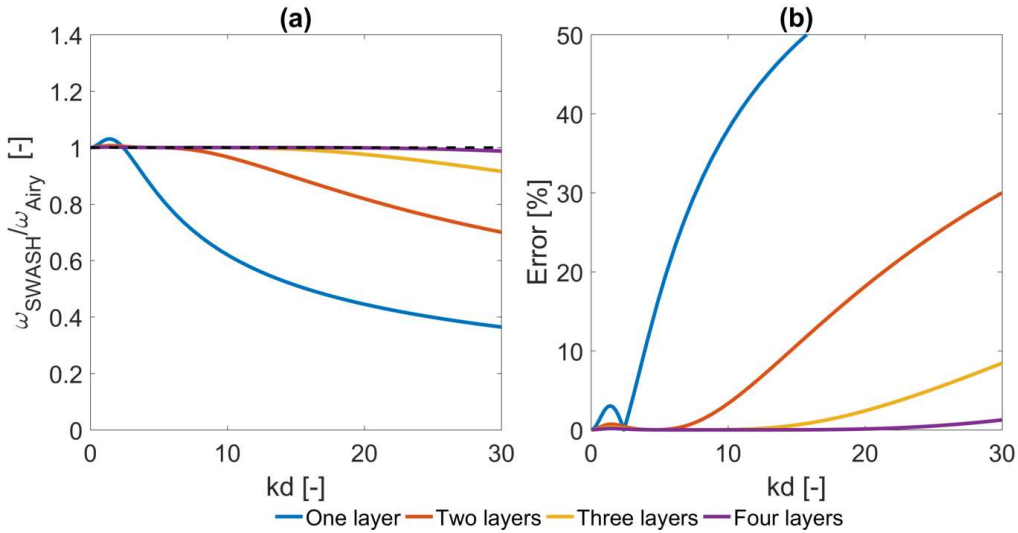


Figure 4.3: (a) Ratio $\omega_{SWASH}/\omega_{Airy}$ and (b) the corresponding relative error for one, two, three and four vertical layers as a function of the dimensionless depth kd .

Table 4.1: Range of dimensionless depth kd as a function of the number of vertical layers and the corresponding relative error in the dispersion relation.

Number of Layers	kd [-]	Error [%]
1	≤ 0.53	≤ 1
1	≤ 2.90	≤ 3
2	≤ 7.71	≤ 1
2	≤ 9.74	≤ 3
3	≤ 16.41	≤ 1
3	≤ 21.20	≤ 3
4	≤ 28.59	≤ 1

4.4 Derivation of nonlinear properties

Apart from the correct representation of the linear dispersion relation, the nonlinear properties of a wave model are also important. The nonlinearity in water wave theory arises from the treatment of the free surface boundary condition which is nonlinear. As the waves propagate to water of decreasing depth the profile of the waves is no longer symmetric as the sinusoidal one given by the linear wave theory. The waves have steeper crests and flatter troughs. In shallow water, the nonlinearity is governed by near-resonant interactions among triads of waves, where energy

is transferred to high and low frequency components. In this section, the second and third order governing equations of SWASH are defined and the corresponding solutions are presented. In addition, the second order transfer functions for subharmonics and superharmonics are derived.

4.4.1 Second order equations and solutions

Substituting the perturbation expansions (Equations 4.19-4.25) into the governing equations (Equations 4.11-4.17) and retaining only the $O(\epsilon^2)$ terms, we get the second order equations:

$$2\frac{\partial\eta^{(2)}}{\partial t} + d\frac{\partial u_{k1}^{(2)}}{\partial x} + d\frac{\partial u_{k2}^{(2)}}{\partial x} = -\eta^{(1)}\left(\frac{\partial u_{k1}^{(1)}}{\partial x} + \frac{\partial u_{k2}^{(1)}}{\partial x}\right) - (u_{k1}^{(1)} + u_{k2}^{(1)})\frac{\partial\eta^{(1)}}{\partial x} \quad (4.44)$$

$$2d\frac{\partial u_{k2}^{(2)}}{\partial x} + 4w_s^{(2)} - 4w_{12}^{(2)} = -2\eta^{(1)}\frac{\partial u_{k2}^{(1)}}{\partial x} + (u_{k2}^{(1)} - u_{k1}^{(1)})\frac{\partial\eta^{(1)}}{\partial x} \quad (4.45)$$

$$2d\frac{\partial u_{k1}^{(2)}}{\partial x} + 4w_{12}^{(2)} = -2\eta^{(1)}\frac{\partial u_{k1}^{(1)}}{\partial x} + (u_{k2}^{(1)} - u_{k1}^{(1)})\frac{\partial\eta^{(1)}}{\partial x} \quad (4.46)$$

$$2d\frac{\partial u_{k2}^{(2)}}{\partial t} + 2dg\frac{\partial\eta^{(2)}}{\partial x} + d\frac{\partial q_{12}^{(2)}}{\partial x} = -\eta^{(1)}\left(2g\frac{\partial\eta^{(1)}}{\partial x} + \frac{\partial q_{12}^{(1)}}{\partial x} + 2\frac{\partial u_{k2}^{(1)}}{\partial t}\right) - 3q_{12}^{(1)}\frac{\partial\eta^{(1)}}{\partial x} - u_{k1}^{(1)}\left(\frac{\partial\eta^{(1)}}{\partial t} - 2w_{12}^{(1)}\right) - u_{k2}^{(1)}\left(3\frac{\partial\eta^{(1)}}{\partial t} + 4d\frac{\partial u_{k2}^{(1)}}{\partial x} - 2w_{12}^{(1)}\right) \quad (4.47)$$

$$2d\frac{\partial u_{k1}^{(2)}}{\partial t} + 2dg\frac{\partial\eta^{(2)}}{\partial x} + d\frac{\partial q_{12}^{(2)}}{\partial x} + d\frac{\partial q_b^{(2)}}{\partial x} = -\eta^{(1)}\left(2g\frac{\partial\eta^{(1)}}{\partial x} + \frac{\partial q_{12}^{(1)}}{\partial x} + \frac{\partial q_b^{(1)}}{\partial x} + 2\frac{\partial u_{k1}^{(1)}}{\partial t}\right) - (q_b^{(1)} - q_{12}^{(1)})\frac{\partial\eta^{(1)}}{\partial x} + u_{k2}^{(1)}\left(\frac{\partial\eta^{(1)}}{\partial t} - 2w_{12}^{(1)}\right) - u_{k1}^{(1)}\left(\frac{\partial\eta^{(1)}}{\partial t} + 4d\frac{\partial u_{k1}^{(1)}}{\partial x} + 2w_{12}^{(1)}\right) \quad (4.48)$$

$$\begin{aligned}
d \frac{\partial w_s^{(2)}}{\partial t} + d \frac{\partial w_{12}^{(2)}}{\partial t} - 4q_{12}^{(2)} &= -du_{k2}^{(1)} \left(\frac{\partial w_{12}^{(1)}}{\partial x} + \frac{\partial w_s^{(1)}}{\partial x} \right) \\
&- \eta^{(1)} \left(\frac{\partial w_{12}^{(1)}}{\partial t} + \frac{\partial w_s^{(1)}}{\partial t} \right) - w_{12}^{(1)} \left(d \frac{\partial u_{k2}^{(1)}}{\partial x} + \frac{\partial \eta^{(1)}}{\partial t} \right) \\
&- w_s^{(1)} \left(d \frac{\partial u_{k2}^{(1)}}{\partial x} + \frac{\partial \eta^{(1)}}{\partial t} \right)
\end{aligned} \tag{4.49}$$

$$\begin{aligned}
d \frac{\partial w_{12}^{(2)}}{\partial t} + 4q_{12}^{(2)} - 4q_b^{(2)} &= -du_{k1}^{(1)} \frac{\partial w_{12}^{(1)}}{\partial x} - \eta^{(1)} \frac{\partial w_{12}^{(1)}}{\partial t} \\
&- w_{12}^{(1)} \left(d \frac{\partial u_{k1}^{(1)}}{\partial x} + \frac{\partial \eta^{(1)}}{\partial t} \right)
\end{aligned} \tag{4.50}$$

As it is observed, the linear solutions provide forcing to the second order solutions on the right hand side of Equations 4.44-4.50. More precisely, the linear solutions create self-interacting second order harmonics which have the following form:

$$\eta^{(2)} = \eta_{02} \cos(2kx - 2\omega t) \tag{4.51}$$

$$u_{k1}^{(2)} = u_{k1,02} \cos(2kx - 2\omega t) \tag{4.52}$$

$$u_{k2}^{(2)} = u_{k2,02} \cos(2kx - 2\omega t) \tag{4.53}$$

$$w_s^{(2)} = w_{s,02} \sin(2kx - 2\omega t) \tag{4.54}$$

$$w_{12}^{(2)} = w_{12,02} \sin(2kx - 2\omega t) \tag{4.55}$$

$$q_{12}^{(2)} = q_{12,02} \cos(2kx - 2\omega t) \tag{4.56}$$

$$q_b^{(2)} = q_{b,02} \cos(2kx - 2\omega t) \tag{4.57}$$

Substituting the first (4.34-4.39) and second (4.51-4.57) order harmonics into the second order Equations 4.44-4.50 and using the linear equations of Section 4.3, a system of fourteen equations ($2(3K+1)$) is obtained, from which the amplitudes of the second order harmonics (4.51-4.57) are derived in terms of kd and η_{01} . Here, we focus on the second order amplitude of the surface elevation, η_{02} , which for the case of two layers is given by (see Appendix B.2 for one, three and four vertical layers solutions):

$$\eta_{02,K2} = \frac{\eta_{01}^2 (49152 + 33792k^2d^2 + 9792k^4d^4 + 892k^6d^6 + 7k^8d^8)}{12k^2d^3 (5120 + 640k^2d^2 + 36k^4d^4 + k^6d^6)} \tag{4.58}$$

The approximate expressions form $[6(K-1)+2, 6(K-1)]$ rational polynomials in terms of kd , which means that for the case of two layers we have an eighth order and a sixth order polynomial in the numerator and denominator respectively. The derived second order surface amplitude expressions are compared with the exact solution given by Stokes wave theory (Equation 4.59) in order to study how the SWASH model improves its second order nonlinear properties as the number of layers increases.

$$\eta_{02,St} = \frac{1}{4}k\eta_{01}^2 \coth(kd)(3 \coth^2(kd) - 1) \quad (4.59)$$

In Figure 4.4, the normalised second order amplitude of the surface elevation, $\eta_{02,SWASH}/\eta_{02,St}$, and the corresponding relative error for one, two, three and four vertical layers are presented as a function of the dimensionless depth kd . It is noticed that by increasing the number of layers, the kd range over which SWASH can accurately represent the Stokes second order surface component is getting larger. For the case of one layer and $kd \rightarrow 0$, the relative error is around 33%, while it stays below 5% only for a short range of kd values, $0.78 \leq kd \leq 0.94$. On the other hand, for three and four vertical layers the nonlinear properties of the model improve significantly, since the error stays below 5% up to kd values of 2.09 and 3.41 respectively (Table 4.2).

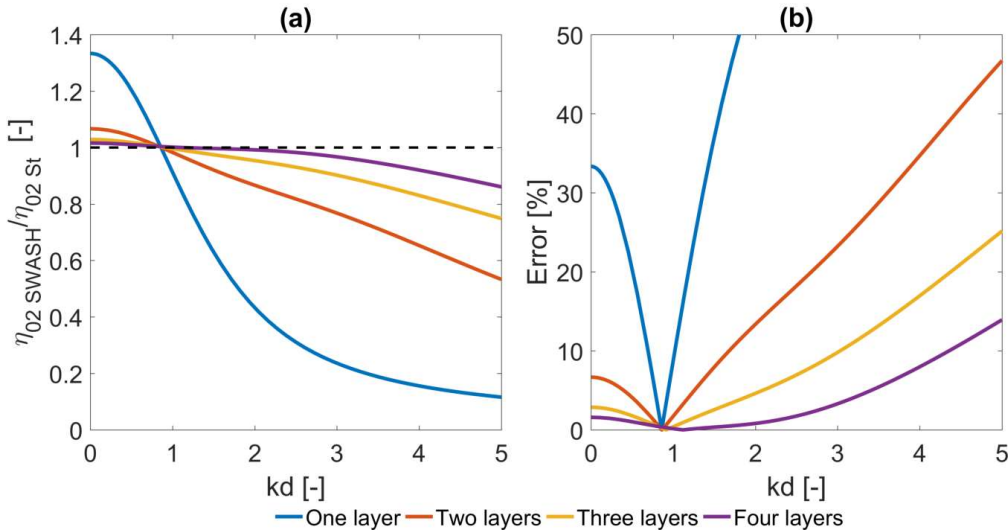


Figure 4.4: Comparison of (a) normalised second order amplitude of the surface elevation, $\eta_{02,SWASH}/\eta_{02,St}$, and (b) the corresponding relative error for one, two, three and four vertical layers as a function of the dimensionless depth kd .

Table 4.2: Range of dimensionless depth kd as a function of the number of vertical layers and the corresponding relative error in the second order amplitude of the surface elevation.

Number of Layers	Range of Dimensionless Depth [-]	Error [%]
1	$0.78 \leq kd \leq 0.94$	≤ 5
1	$0.69 \leq kd \leq 1.02$	≤ 10
2	$0.40 \leq kd \leq 1.26$	≤ 5
2	$kd \leq 1.68$	≤ 10
3	$kd \leq 2.09$	≤ 5
3	$kd \leq 3.03$	≤ 10
4	$kd \leq 3.41$	≤ 5
4	$kd \leq 4.36$	≤ 10

4.4.2 Third order solutions

Continuing the Stokes-type Fourier analysis to the third order, we seek for third order harmonics of the form:

$$\eta^{(3)} = \eta_{03} \cos(3kx - 3\omega t) \quad (4.60)$$

$$u_{k1}^{(3)} = u_{k1,03} \cos(3kx - 3\omega t) \quad (4.61)$$

$$u_{k2}^{(3)} = u_{k2,03} \cos(3kx - 3\omega t) \quad (4.62)$$

$$w_s^{(3)} = w_{s,03} \sin(3kx - 3\omega t) \quad (4.63)$$

$$w_{12}^{(3)} = w_{12,03} \sin(3kx - 3\omega t) \quad (4.64)$$

$$q_{12}^{(3)} = q_{12,03} \cos(3kx - 3\omega t) \quad (4.65)$$

$$q_b^{(3)} = q_{b,03} \cos(3kx - 3\omega t) \quad (4.66)$$

However, in this case secular terms are going to arise (Whitham, 1999). The secular terms create a nonuniformity in the expansion and become unbounded in time. The problem is avoided by expanding the first order dispersion and harmonics as (Madsen et al., 2003):

$$\omega = \omega_1(1 + \epsilon^2 \omega_{13}) \quad (4.67)$$

$$u_{k1}^{(1)} = u_{k1,01}(1 + \epsilon^2 u_{k1,13}) \cos(kx - \omega t) \quad (4.68)$$

$$u_{k2}^{(1)} = u_{k2,01}(1 + \epsilon^2 u_{k2,13}) \cos(kx - \omega t) \quad (4.69)$$

$$w_s^{(1)} = w_{s,01}(1 + \epsilon^2 w_{s,13}) \sin(kx - \omega t) \quad (4.70)$$

$$w_{12}^{(1)} = w_{12,01}(1 + \epsilon^2 w_{12,13}) \sin(kx - \omega t) \quad (4.71)$$

$$q_{12}^{(1)} = q_{12,01}(1 + \epsilon^2 q_{12,13}) \cos(kx - \omega t) \quad (4.72)$$

$$q_b^{(1)} = q_{b,01}(1 + \epsilon^2 q_{b,13}) \cos(kx - \omega t) \quad (4.73)$$

where ω_{13} is the amplitude dispersion and terms with subscript "13" (x_{13}) represent the third order correction to the first order amplitudes. Substituting the perturbation expansions (Equations 4.19-4.25) into the governing equations (Equations 4.11-4.17) and replacing the first (4.68-4.73), second (4.51-4.57) and third (4.60-4.66) order harmonics, the third order solutions of SWASH governing equations are derived by retaining only the $O(\epsilon^3)$ terms.

Here, we focus on the amplitude dispersion, ω_{13} , and the third order component of the surface elevation, η_{03} , which using the Stokes wave theory are given by (Skjelbreia, 1959):

$$\omega_{13,St} = \frac{1}{16} \eta_{01}^2 k^2 \frac{9 \tanh^4(kd) - 10 \tanh^2(kd) + 9}{\tanh^4(kd)} \quad (4.74)$$

$$\eta_{03,St} = \frac{3}{64} \eta_{01}^3 k^2 \frac{1 + 8 \cosh^6(kd)}{\sinh^6(kd)} \quad (4.75)$$

The amplitude dispersion and subsequently the third order component of the surface elevation are derived by requiring the coefficients of $\sin(kx - \omega t)$ and $\cos(kx - \omega t)$ to be zero (avoid secular unbounded solutions) in the third order equations. Thus, trigonometrical identities are applied to make all the terms be proportional to $\sin(kx - \omega t)$, $\cos(kx - \omega t)$ and $\sin(3kx - 3\omega t)$, $\cos(3kx - 3\omega t)$. For the case of two layers the derived expressions are given by:

$$\begin{aligned} \omega_{13,K2} = & \eta_{01}^2 (1207959552 + 855638016k^2 d^2 + 687341568k^4 d^4 \\ & + 147062784k^6 d^6 + 17270784k^8 d^8 + 1173504k^{10} d^{10} \\ & + 16568k^{12} d^{12} + 89k^{14} d^{14}) / (96k^2 d^4 (16 + k^2 d^2)^2 \\ & (81920 + 35840k^2 d^2 + 2496k^4 d^4 + 116k^6 d^6 + k^8 d^8)) \end{aligned} \quad (4.76)$$

$$\begin{aligned} \eta_{03,K2} = & \eta_{01}^3 (1207959552 + 1962934272k^2 d^2 + 1738014720k^4 d^4 \\ & + 682622976k^6 d^6 + 145885184k^8 d^8 + 14327296k^{10} d^{10} \\ & + 267928k^{12} d^{12} + 2853k^{14} d^{14}) / (384k^4 d^6 (16 + k^2 d^2) \\ & (320 + 20k^2 d^2 + k^4 d^4) (1280 + 160k^2 d^2 + 9k^4 d^4)) \end{aligned} \quad (4.77)$$

In Figures 4.5 and 4.6, the normalised amplitude dispersion ($\omega_{13,SWASH}/\omega_{13,St}$) and third order amplitude of the surface elevation ($\eta_{03,SWASH}/\eta_{03,St}$) and the corresponding relative errors for one, two, three and four vertical layers are presented as a function of the dimensionless depth kd .

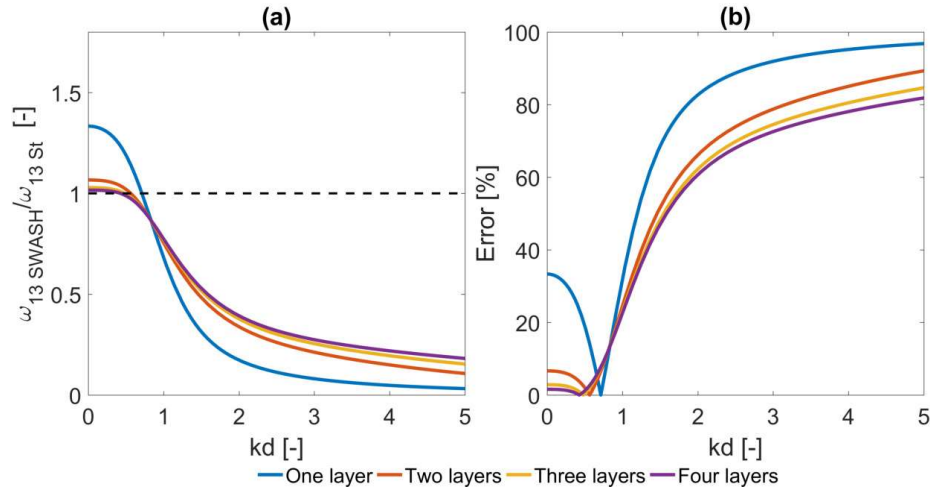


Figure 4.5: Comparison of (a) normalised amplitude dispersion, $\omega_{13,SWASH} / \omega_{13,St}$, and (b) the corresponding relative error for one, two, three and four vertical layers as a function of the dimensionless depth kd .

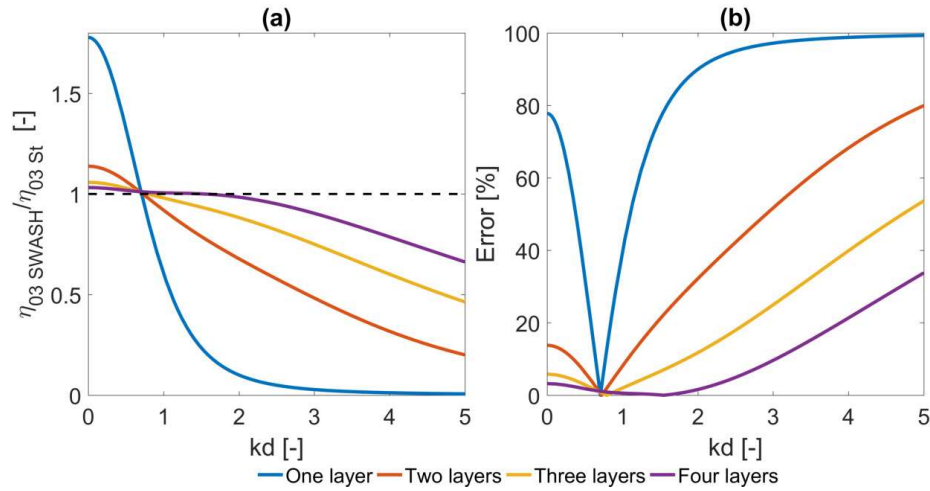


Figure 4.6: Comparison of (a) normalised third order amplitude of the surface elevation, $\eta_{03,SWASH} / \eta_{03,St}$, and (b) the corresponding relative error for one, two, three and four vertical layers as a function of the dimensionless depth kd .

As observed from Figure 4.5, the model underestimates significantly the amplitude dispersion for kd values larger than 1, while increasing the number of layers improves the accuracy only in shallow water (Table 4.3). On the other hand, the capability of the model to represent the third order amplitude of the surface elevation increases considerably when more than two layers are applied. More precisely,

the relative error stays below 10% up to kd values of 1.85 and 3.04 (Table 4.4), for three and four layers, respectively.

Table 4.3: Range of dimensionless depth kd as a function of the number of vertical layers and the corresponding relative error in the amplitude dispersion.

Number of Layers	Range of Dimensionless Depth [-]	Error [%]
1	$0.66 \leq kd \leq 0.76$	≤ 5
1	$0.61 \leq kd \leq 0.80$	≤ 10
2	$0.35 \leq kd \leq 0.68$	≤ 5
2	$kd \leq 0.77$	≤ 10
3	$kd \leq 0.66$	≤ 5
3	$kd \leq 0.77$	≤ 10
4	$kd \leq 0.65$	≤ 5
4	$kd \leq 0.77$	≤ 10

Table 4.4: Range of dimensionless depth kd as a function of the number of vertical layers and the corresponding relative error in the third order amplitude of the surface elevation.

Number of Layers	Range of Dimensionless Depth [-]	Error [%]
1	$0.68 \leq kd \leq 0.74$	≤ 5
1	$0.65 \leq kd \leq 0.78$	≤ 10
2	$0.55 \leq kd \leq 0.90$	≤ 5
2	$0.34 \leq kd \leq 1.07$	≤ 10
3	$0.24 \leq kd \leq 1.33$	≤ 5
3	$kd \leq 1.85$	≤ 10
4	$kd \leq 2.51$	≤ 5
4	$kd \leq 3.04$	≤ 10

4.4.3 Transfer functions for subharmonics and superharmonics

In coastal regions, waves with different frequencies interact with each other, leading to the generation of bound subharmonics and superharmonics at the difference and sum of the frequencies of the primary waves. During this process substantial spectral energy is being transferred from the peak- to the low- and high-frequency part of the spectrum.

One of the important properties for a nonlinear wave model is to be able to represent accurately these wave-wave interactions, and thus in this section we examine the capability of SWASH model to describe the second order interactions between two first order wave components. A first order wave group composed of two harmonics with frequencies ω_m and ω_n and wave numbers k_m and k_n is described as follows for the case of two layers:

$$\eta^{(1)} = \eta_{01m} \cos(k_m x - \omega_m t) + \eta_{01n} \cos(k_n x - \omega_n t) \quad (4.78)$$

$$u_{k1}^{(1)} = u_{k1,01m} \cos(k_m x - \omega_m t) + u_{k1,01n} \cos(k_n x - \omega_n t) \quad (4.79)$$

$$u_{k2}^{(1)} = u_{k2,01m} \cos(k_m x - \omega_m t) + u_{k2,01n} \cos(k_n x - \omega_n t) \quad (4.80)$$

$$w_s^{(1)} = w_{s,01m} \sin(k_m x - \omega_m t) + w_{s,01n} \sin(k_n x - \omega_n t) \quad (4.81)$$

$$w_{12}^{(1)} = w_{12,01m} \sin(k_m x - \omega_m t) + w_{12,01n} \sin(k_n x - \omega_n t) \quad (4.82)$$

$$q_{12}^{(1)} = q_{12,01m} \cos(k_m x - \omega_m t) + q_{12,01n} \cos(k_n x - \omega_n t) \quad (4.83)$$

$$q_b^{(1)} = q_{b,01m} \cos(k_m x - \omega_m t) + q_{b,01n} \cos(k_n x - \omega_n t) \quad (4.84)$$

In the above first order wave group, both harmonics are considered solutions of the linearised governing Equations 4.26-4.32 and subsequently frequencies ω_m and ω_n satisfy the linear dispersion relation derived in Section 4.3 (Equation 4.40). Through the nonlinear terms a first order bichromatic wave group will force a second order wave group composed of four components, one subharmonic, $\omega_m - \omega_n$, and three superharmonics, $2\omega_m$, $2\omega_n$ and $\omega_m + \omega_n$. These components are bound (phase locked) to the first order wave group, while frequencies $\omega_m - \omega_n$, $2\omega_m$, $2\omega_n$ and $\omega_m + \omega_n$ do not satisfy the linear dispersion relation. The second order wave group is described as follows for the case of two layers:

$$\begin{aligned} \eta^{(2)} &= G_\eta^{m-n} \cos(\vartheta_m - \vartheta_n) + G_\eta^{2m} \cos(2\vartheta_m) \\ &+ G_\eta^{m+n} \cos(\vartheta_m + \vartheta_n) + G_\eta^{2n} \cos(2\vartheta_n) \end{aligned} \quad (4.85)$$

$$\begin{aligned} u_{k1}^{(2)} &= G_{u_{k1}}^{m-n} \cos(\vartheta_m - \vartheta_n) + G_{u_{k1}}^{2m} \cos(2\vartheta_m) \\ &+ G_{u_{k1}}^{m+n} \cos(\vartheta_m + \vartheta_n) + G_{u_{k1}}^{2n} \cos(2\vartheta_n) \end{aligned} \quad (4.86)$$

$$\begin{aligned} u_{k2}^{(2)} &= G_{u_{k2}}^{m-n} \cos(\vartheta_m - \vartheta_n) + G_{u_{k2}}^{2m} \cos(2\vartheta_m) \\ &+ G_{u_{k2}}^{m+n} \cos(\vartheta_m + \vartheta_n) + G_{u_{k2}}^{2n} \cos(2\vartheta_n) \end{aligned} \quad (4.87)$$

$$\begin{aligned} w_s^{(2)} &= G_{w_s}^{m-n} \sin(\vartheta_m - \vartheta_n) + G_{w_s}^{2m} \sin(2\vartheta_m) \\ &+ G_{w_s}^{m+n} \sin(\vartheta_m + \vartheta_n) + G_{w_s}^{2n} \sin(2\vartheta_n) \end{aligned} \quad (4.88)$$

$$\begin{aligned} w_{12}^{(2)} &= G_{w_{12}}^{m-n} \sin(\vartheta_m - \vartheta_n) + G_{w_{12}}^{2m} \sin(2\vartheta_m) \\ &+ G_{w_{12}}^{m+n} \sin(\vartheta_m + \vartheta_n) + G_{w_{12}}^{2n} \sin(2\vartheta_n) \end{aligned} \quad (4.89)$$

$$\begin{aligned}
q_{12}^{(2)} &= G_{q_{12}}^{m-n} \cos(\vartheta_m - \vartheta_n) + G_{q_{12}}^{2m} \cos(2\vartheta_m) \\
&+ G_{q_{12}}^{m+n} \cos(\vartheta_m + \vartheta_n) + G_{q_{12}}^{2n} \cos(2\vartheta_n)
\end{aligned} \tag{4.90}$$

$$\begin{aligned}
q_b^{(2)} &= G_{q_b}^{m-n} \cos(\vartheta_m - \vartheta_n) + G_{q_b}^{2m} \cos(2\vartheta_m) \\
&+ G_{q_b}^{m+n} \cos(\vartheta_m + \vartheta_n) + G_{q_b}^{2n} \cos(2\vartheta_n)
\end{aligned} \tag{4.91}$$

where G^{m-n} is the subharmonic transfer function, G^{2m} , G^{2n} and G^{m+n} are the superharmonic transfer functions and ϑ_m and ϑ_n are given by:

$$\vartheta_m = k_m x - \omega_m t \quad \text{and} \quad \vartheta_n = k_n x - \omega_n t \tag{4.92}$$

Substituting the first (4.78-4.84) and second (4.85-4.91) order wave groups into the second order Equations 4.44-4.50, the second order transfer functions are derived in terms of $k_m d$, $k_n d$, ω_m , ω_n , η_{01m} and η_{01n} . Here, we focus on the second order transfer functions of the surface elevation, G_η^{m-n} and G_η^{m+n} , which for the case of two layers are given by Equations 4.93 and 4.94 (see Appendices B.4 and B.5 for one, three and four vertical layers solutions).

$$\begin{aligned}
G_\eta^{m-n} &= \eta_{01m} \eta_{01n} (k_m - k_n)^2 (65536 \omega_m \omega_n (k_n^2 \omega_m^2 + 4k_m k_n \omega_m \omega_n + k_m^2 \omega_n^2) \\
&- 65536 g k_m k_n d (2k_n^2 \omega_m^2 + k_m k_n \omega_m \omega_n + 2k_m^2 \omega_n^2) + k_m^3 (k_m - k_n)^2 \\
&k_n^3 d^8 \omega_m \omega_n (-k_n (k_m + 4k_n) \omega_m^2 + 2(k_m^2 + 3k_m k_n + k_n^2) \omega_m \omega_n - k_m \\
&(4k_m + k_n) \omega_n^2) + 4096 g k_m k_n d^3 (-k_n^2 (-4k_m^2 + 8k_m k_n + k_n^2) \omega_m^2 \\
&+ 6k_m (k_m - k_n)^2 k_n \omega_m \omega_n - k_m^2 (k_m^2 + 8k_m k_n - 4k_n^2) \omega_n^2) + 256 g \\
&k_m k_n d^5 (k_n^2 (-10k_m^4 + 4k_m^3 k_n + 10k_m^2 k_n^2 - 6k_m k_n^3 + k_n^4) \omega_m^2 - k_m k_n \\
&(k_m^4 + k_m^3 k_n - 5k_m^2 k_n^2 + k_m k_n^3 + k_n^4) \omega_m \omega_n + k_m^2 (k_m^4 - 6k_m^3 k_n \\
&+ 10k_m^2 k_n^2 + 4k_m k_n^3 - 10k_n^4) \omega_n^2) + 16 g k_m^3 (k_m - k_n)^2 k_n^3 d^7 (k_n^2 \omega_m \\
&(3\omega_m + \omega_n) + k_m^2 \omega_n (\omega_m + 3\omega_n) - k_m k_n (4\omega_m^2 + 5\omega_m \omega_n + 4\omega_n^2)) \\
&+ 4096 d^2 (32 g^2 k_m^3 k_n^3 + \omega_m \omega_n (-2k_n^4 \omega_m^2 + 6k_m^3 k_n \omega_m \omega_n - 2k_m^4 \omega_n^2 \\
&+ 6k_m k_n^3 \omega_m \omega_n + k_m^2 k_n^2 (-9\omega_m^2 + 14\omega_m \omega_n - 9\omega_n^2))) + 16 k_m k_n d^6 \\
&(-16 g^2 k_m^2 (k_m - k_n)^4 k_n^2 + \omega_m \omega_n (-2k_m^6 \omega_m \omega_n - 2k_n^6 \omega_m \omega_n + k_m k_n^5 \\
&(2\omega_m + \omega_n) (12\omega_m + \omega_n) + k_m^5 k_n (\omega_m + 2\omega_n) (\omega_m + 12\omega_n) \\
&+ 2k_m^4 k_n^2 (\omega_m^2 + 2\omega_m \omega_n - 21\omega_n^2) + 2k_m^3 k_n^3 (\omega_m^2 - 3\omega_m \omega_n + \omega_n^2) \\
&+ 2k_m^2 k_n^4 (-21\omega_m^2 + 2\omega_m \omega_n + \omega_n^2))) + 256 d^4 (16 g^2 k_m^3 (k_m - k_n)^2 \\
&k_n^3 + \omega_m \omega_n (k_n^6 \omega_m^2 + k_m^6 \omega_n^2 + k_m^4 k_n^2 (-9\omega_m^2 + 28\omega_m \omega_n - 15\omega_n^2) \\
&+ k_m^2 k_n^4 (-15\omega_m^2 + 28\omega_m \omega_n - 9\omega_n^2) + 2k_m^3 k_n^3 (23\omega_m^2 - 40\omega_m \omega_n \\
&+ 23\omega_n^2))) / (2k_m^2 k_n^2 d (-16 + k_m^2 d^2) (-16 + k_n^2 d^2) \omega_m (-256 g \\
&(k_m - k_n)^2 d - 16 g (k_m - k_n)^4 d^3 + 256 (\omega_m - \omega_n)^2 + 96 (k_m - k_n)^2 \\
&d^2 (\omega_m - \omega_n)^2 + (k_m - k_n)^4 d^4 (\omega_m - \omega_n)^2) \omega_n)
\end{aligned} \tag{4.93}$$

$$\begin{aligned}
G_\eta^{m+n} = & \eta_{01m}\eta_{01n}(k_m + k_n)^2(65536\omega_m\omega_n(k_n^2\omega_m^2 + 4k_mk_n\omega_m\omega_n + k_m^2\omega_n^2) \\
& - 65536gk_mk_nd(2k_n^2\omega_m^2 + k_mk_n\omega_m\omega_n + 2k_m^2\omega_n^2) + 4096gk_mk_nd^3 \\
& (k_n^2(4k_m^2 + 8k_mk_n - k_n^2)\omega_m^2 + 6k_mk_n(k_m + k_n)^2\omega_m\omega_n + k_m^2(-k_m^2 \\
& + 8k_mk_n + 4k_n^2)\omega_n^2) - 16gk_m^3k_n^3(k_m + k_n)^2d^7(k_m^2(\omega_m - 3\omega_n)\omega_n \\
& + k_n^2\omega_m(-3\omega_m + \omega_n) + k_mk_n(-4\omega_m^2 + 5\omega_m\omega_n - 4\omega_n^2)) + k_m^3k_n^3 \\
& (k_m + k_n)^2d^8\omega_m\omega_n(2k_n^2\omega_m(2\omega_m + \omega_n) + 2k_m^2\omega_n(\omega_m + 2\omega_n) \\
& - k_mk_n(\omega_m^2 + 6\omega_m\omega_n + \omega_n^2)) + 256gk_mk_nd^5(k_n^6\omega_m^2 + k_mk_n^5\omega_m \\
& (6\omega_m - \omega_n) + k_m^6\omega_n^2 + k_m^5k_n\omega_n(-\omega_m + 6\omega_n) + k_m^2k_n^4(10\omega_m^2 \\
& + \omega_m\omega_n - 10\omega_n^2) + k_m^3k_n^3(-4\omega_m^2 + 5\omega_m\omega_n - 4\omega_n^2) + k_m^4k_n^2 \\
& (-10\omega_m^2 + \omega_m\omega_n + 10\omega_n^2)) + 16k_mk_nd^6(-16g^2k_m^2k_n^2(k_m + k_n)^4 \\
& + \omega_m\omega_n(k_m^5k_n(\omega_m - 12\omega_n)(\omega_m - 2\omega_n) - 2k_m^6\omega_m\omega_n - 2k_n^6\omega_m\omega_n \\
& - 2k_m^4k_n^2(\omega_m^2 - 2\omega_m\omega_n - 21\omega_n^2) + 2k_n^2k_n^4(21\omega_m^2 + 2\omega_m\omega_n - \omega_n^2) \\
& + k_mk_n^5(24\omega_m^2 - 14\omega_m\omega_n + \omega_n^2) + 2k_m^3k_n^3(\omega_m^2 + 3\omega_m\omega_n + \omega_n^2))) \\
& + 4096d^2(32g^2k_m^3k_n^3 + \omega_m\omega_n(-2k_n^4\omega_m^2 + 6k_m^3k_n\omega_m\omega_n \\
& + 6k_mk_n^3\omega_m\omega_n - 2k_m^4\omega_n^2 - k_m^2k_n^2(9\omega_m^2 + 14\omega_m\omega_n + 9\omega_n^2))) \\
& + 256d^4(16g^2k_m^3k_n^3(k_m + k_n)^2 + \omega_m\omega_n(k_n^6\omega_m^2 + k_m^6\omega_n^2 - k_m^2k_n^4 \\
& (15\omega_m^2 + 28\omega_m\omega_n + 9\omega_n^2) - k_m^4k_n^2(9\omega_m^2 + 28\omega_m\omega_n + 15\omega_n^2) \\
& - 2k_m^3k_n^3(23\omega_m^2 + 40\omega_m\omega_n + 23\omega_n^2)))/(2k_m^2k_n^2d(-16 + k_m^2d^2) \\
& (-16 + k_n^2d^2)\omega_m\omega_n(-256g(k_m + k_n)^2d - 16g(k_m + k_n)^4d^3 \\
& + 256(\omega_m + \omega_n)^2 + 96(k_m + k_n)^2d^2(\omega_m + \omega_n)^2 + (k_m + k_n)^4 \\
& d^4(\omega_m + \omega_n)^2))
\end{aligned} \tag{4.94}$$

Similar expressions can be derived for the transfer functions of velocity and non-hydrostatic components but they will not be presented here, since this chapter focuses on the ability of SWASH to describe the theoretical surface elevation. Additionally, the self interacting superharmonic transfer functions, G_η^{2m} and G_η^{2n} , are the same as the second order solution derived and analysed in Section 4.4.1. Substituting the linear dispersion relation (Equation 4.40) for ω_m and ω_n in Equations 4.93 and 4.94, we can compare the derived approximate transfer functions with the exact ones given by Schäffer (1996) for the subharmonics and by Sand and Mansard (1986) for the superharmonics. Their second order solutions are derived from the nonlinear boundary value problem for the Laplace equation using a perturbation method as presented in Section 2.1.3.

In Figures 4.7 and 4.8 the normalised subharmonic transfer function $G_{SWASH}^{m-n} / G_{theor}^{m-n}$ and the corresponding relative error are presented as a function of the dimensionless depths k_md and k_nd . As observed, the model's agreement with the exact solution improves significantly when two layers are used instead of one. On the other hand, when more than two layers are applied the green area where the relative error is less than 10% is quite similar for all the cases.

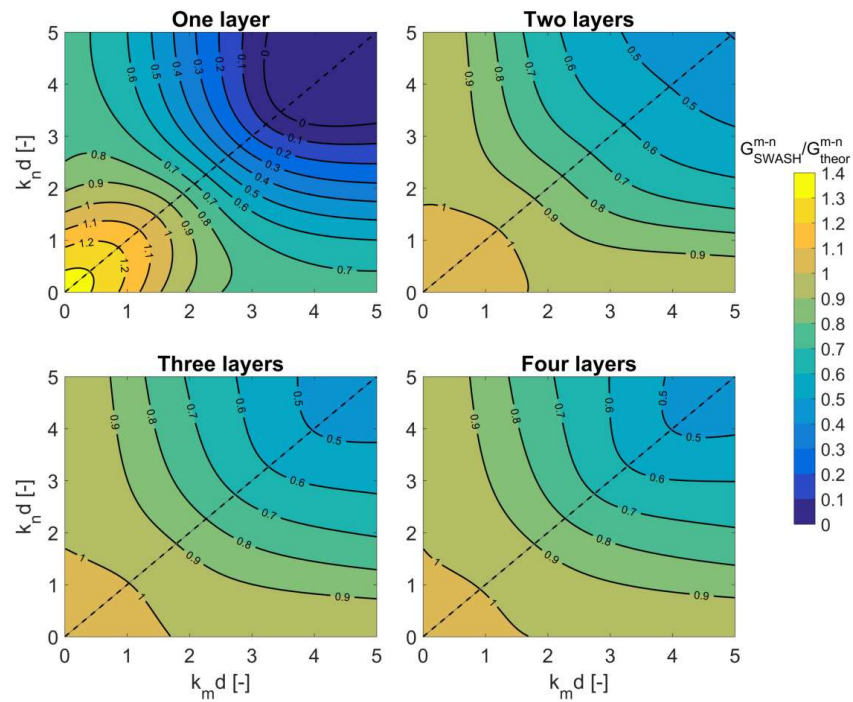


Figure 4.7: Normalised subharmonic transfer function $G_{SWASH}^{m-n} / G_{theor}^{m-n}$ for one, two, three and four vertical layers as a function of the dimensionless depths $k_m d$ and $k_n d$.

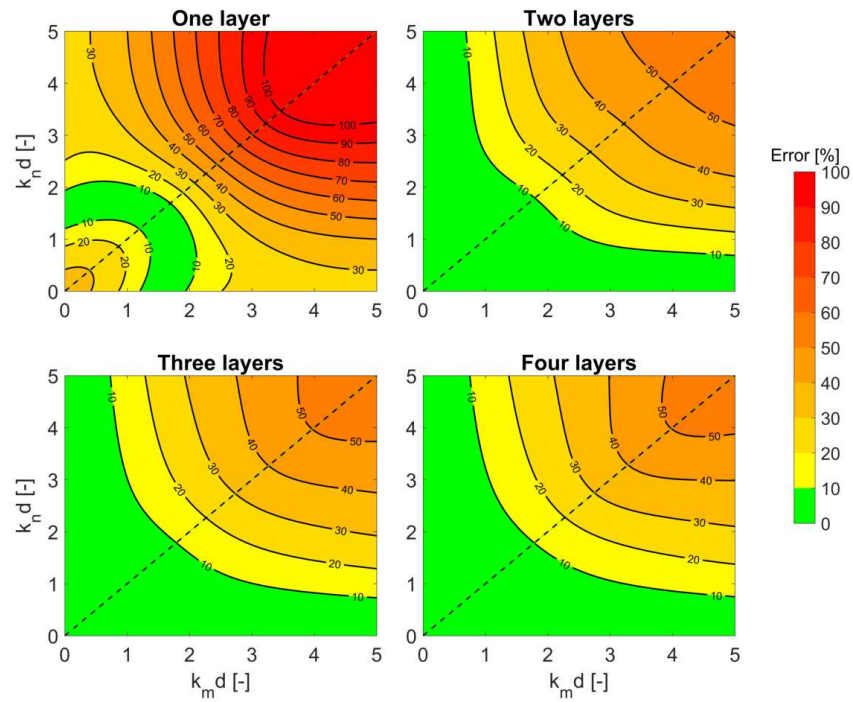


Figure 4.8: Relative error in the normalized subharmonic transfer function $G_{SWASH}^{m-n} / G_{theor}^{m-n}$ for one, two, three and four vertical layers as a function of the dimensionless depths $k_m d$ and $k_n d$.

In general, for multi-layer layout the SWASH model is capable of accounting for second order interactions between shallow water waves (e.g. $k_m d \leq 0.7$) and intermediate-deep water waves (e.g. $k_n d \geq 1.0$). However, for second order interactions between intermediate and deep water waves ($k_n d, k_m d \geq 1.8$) the error is larger than 10%. Fortunately, the second order subharmonic transfer function is most important in the shallow water region, where the model has good accuracy, since the transfer of energy in this region is high. A comparison of the normalised subharmonic transfer function $G_{SWASH}^{m-n}/G_{theor}^{m-n}$ for the cases that $k_n d \rightarrow k_m d$, $k_n d = 0.5k_m d$ and $k_n d = 1.5k_m d$ is shown in Figure 4.9. The case of $k_n d \rightarrow k_m d$ (blue line) corresponds to the setdown under a wave group and as it is noticed for kd values up to 1.79 the error stays below 10% for two or more layers.

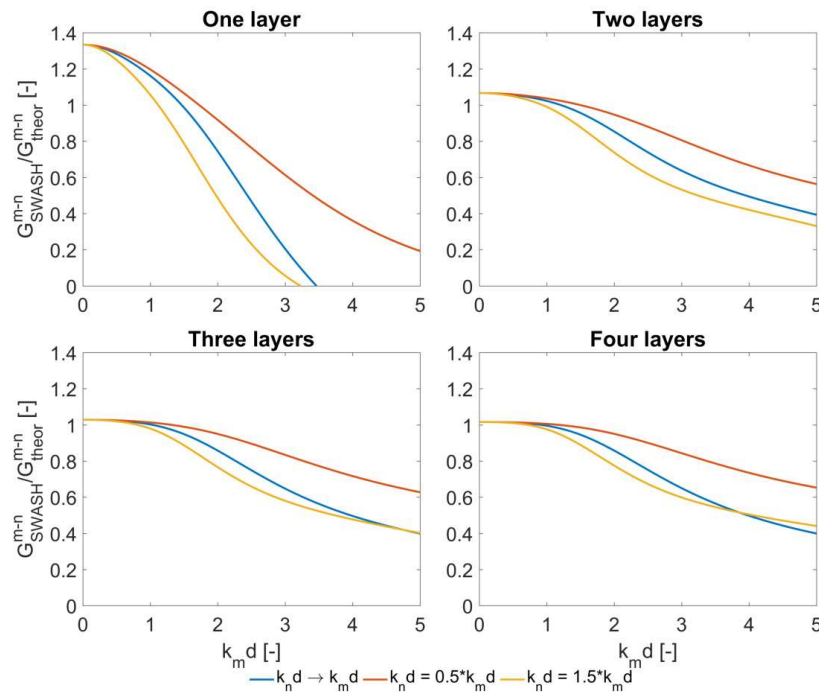


Figure 4.9: Comparison of normalised subharmonic transfer function $G_{SWASH}^{m-n} / G_{theor}^{m-n}$ for the case that $k_n d \rightarrow k_m d$, $k_n d = 0.5k_m d$ and $k_n d = 1.5k_m d$.

In Figures 4.10 and 4.11 the normalised superharmonic transfer function $G_{SWASH}^{m+n} / G_{theor}^{m+n}$ and the corresponding relative error for one, two, three and four vertical layers are presented as a function of the dimensionless depths $k_m d$ and $k_n d$. The agreement with the exact expression of the superharmonic transfer function for the case of one layer is better than what was observed with the subharmonic transfer function. Moreover, the combinations of $k_m d$ and $k_n d$ for which the error is less than 10% (green area in Figure 4.11) increase remarkably with the number of layers and consequently for three and four layers the SWASH model is capable of accounting for second order interactions between intermediate and deep water waves.

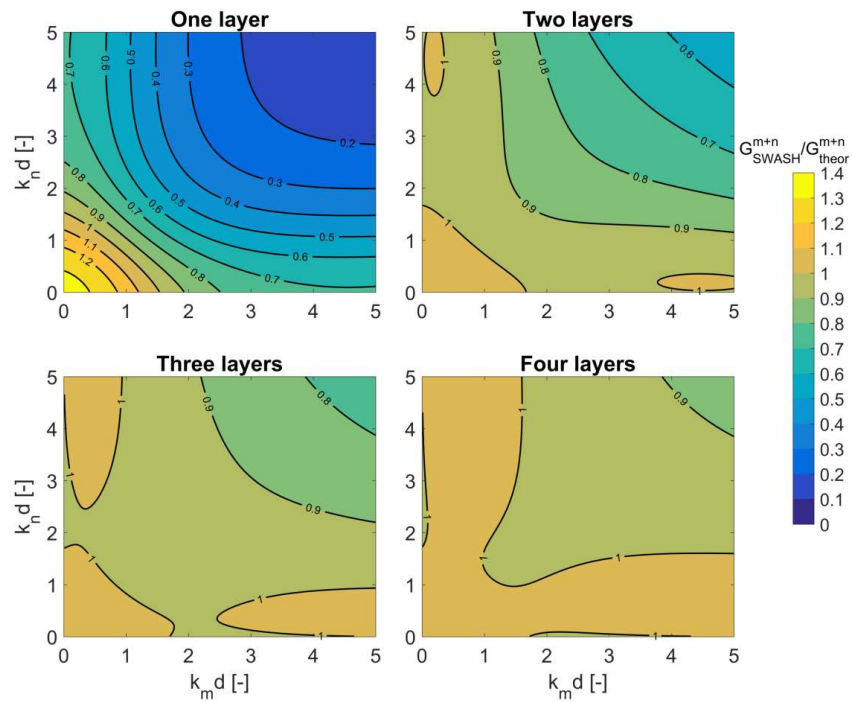


Figure 4.10: Normalised superharmonic transfer function $G_{SWASH}^{m+n} / G_{theor}^{m+n}$ for one, two, three and four vertical layers as a function of the dimensionless depths $k_m d$ and $k_n d$.

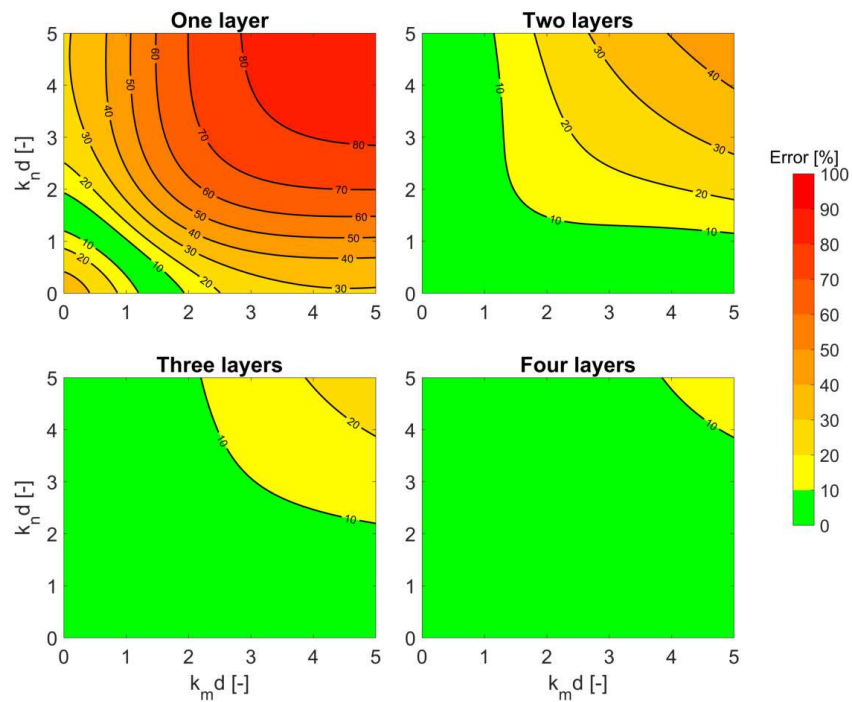


Figure 4.11: Relative error in the normalised superharmonic transfer function $G_{SWASH}^{m+n} / G_{theor}^{m+n}$ for one, two, three and four vertical layers as a function of the dimensionless depths $k_m d$ and $k_n d$.

Also here, a comparison of the normalised superharmonic transfer function $G_{SWASH}^{m+n}/G_{theor}^{m+n}$ for the cases that $k_n = k_m d$, $k_n d = 0.5k_m d$ and $k_n d = 1.5k_m d$ is shown in Figure 4.12, where the same conclusions as above are obtained. The case of $k_n d = k_m d$ corresponds to the self interacting superharmonic transfer functions, G_{η}^{2m} and G_{η}^{2n} , and thus the blue lines are the same as the ones corresponding to the normalised second order amplitude of the surface elevation, $\eta_{02,SWASH}/\eta_{02,St}$, presented in Figure 4.4.

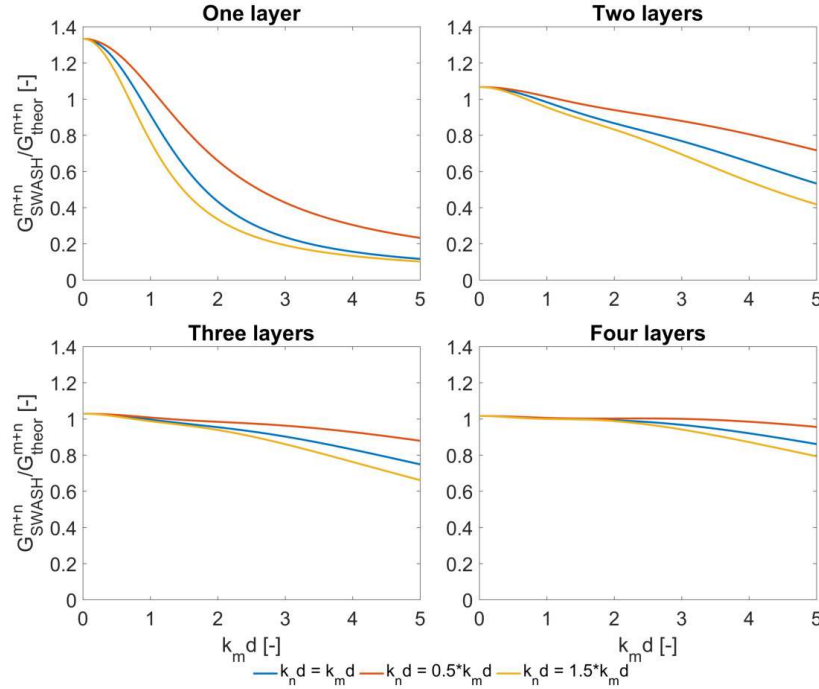


Figure 4.12: Comparison of normalised superharmonic transfer function $G_{SWASH}^{m+n} / G_{theor}^{m+n}$ for the case that $k_n d = k_m d$, $k_n d = 0.5k_m d$ and $k_n d = 1.5k_m d$.

Moreover, the derived second order subharmonic and superharmonic transfer functions of SWASH model are evaluated using the following index of agreement (Kennedy et al., 2001):

$$IA = 1 - \sqrt{\frac{1}{2\kappa'_m \kappa'_n} \int_0^{\kappa'_m} \int_0^{\kappa'_n} \left(\frac{G_{SWASH}^{m+n}}{G_{theor}^{m+n}} - 1 \right)^2 + \left(\frac{G_{SWASH}^{m-n}}{G_{theor}^{m-n}} - 1 \right)^2 d(\kappa_m) d(\kappa_n)} \quad (4.95)$$

where $\kappa_m = k_m d$ and $\kappa_n = k_n d$, while the model is evaluated for two cases: a) $\kappa'_m = \kappa'_n = 3$ and b) $\kappa'_m = \kappa'_n = 5$. The results are summarised in Table 4.5, where it is noticed that the index of agreement increases from 0.663 for one layer to 0.924 for four layers for the first case and from 0.403 for one layer to 0.818 for four layers for the second case.

Table 4.5: Index of agreement of the second order subharmonic and superharmonic transfer functions of SWASH model.

Number of Layers	Index of Agreement	
	$\kappa'_m = \kappa'_n = 3$	$\kappa'_m = \kappa'_n = 5$
1	0.663	0.403
2	0.895	0.760
3	0.919	0.805
4	0.924	0.818

4.5 Sensitivity analysis on advection terms of vertical momentum equation

Finally, in this section a sensitivity analysis is executed regarding the effect of the horizontal and vertical advection terms of the vertical momentum equation on the second order nonlinear properties of the model. To get a more complete understanding of these terms, we re-write the vertical momentum equations for the case of two equidistant layers:

$$\frac{1}{4} \frac{\partial h(w_s + w_{12})}{\partial t} + \overbrace{\frac{1}{4} \frac{\partial h u_{k2}(w_s + w_{12})}{\partial x}}^{\text{hor. advect.}} - \overbrace{w_{rel,12} w_{12}}^{\text{vert. advect.}} - q_{12} = 0 \quad (4.96)$$

$$\frac{1}{4} \frac{\partial h w_{12}}{\partial t} + \overbrace{\frac{1}{4} \frac{\partial h u_{k1} w_{12}}{\partial x}}^{\text{hor. advect.}} + \overbrace{w_{rel,12} w_{12}}^{\text{vert. advect.}} + q_{12} - q_b = 0 \quad (4.97)$$

In the previous sections, for the derivation and analysis of the nonlinear properties of SWASH model the third term in the vertical momentum equations including the relative vertical velocity ($w_{rel,12}$) was neglected and here we examine the effect of this assumption. In case that we include both horizontal and vertical advection terms of Equations 4.96 and 4.97 in our analysis, the second order amplitude of the surface elevation, η_{02} , is given by Equation 4.98, while in case that we exclude them, it is given by Equation 4.99.

$$\eta_{02,K2} = \frac{\eta_{01}^2 (49152 + 33792k^2d^2 + 9280k^4d^4 + 796k^6d^6 + 15k^8d^8)}{12k^2d^3 (5120 + 640k^2d^2 + 36k^4d^4 + k^6d^6)} \quad (4.98)$$

$$\eta_{02,K2} = \frac{\eta_{01}^2 (49152 + 13312k^2d^2 + 5184k^4d^4 + 428k^6d^6 + 3k^8d^8)}{12k^2d^3 (5120 + 640k^2d^2 + 36k^4d^4 + k^6d^6)} \quad (4.99)$$

It has to be mentioned that the solution 4.98 is identical to the one derived by Bai and Cheung (2013) where the governing equations of their non-hydrostatic

model were transformed to an equivalent Boussinesq form for the derivation. In Figure 4.13, a comparison of the normalised second order amplitude of the surface elevation, $\eta_{02,SWASH}/\eta_{02,St}$, for two and four vertical layers is presented for the cases that: a) both advection terms are included (blue line), b) vertical advection term is excluded (orange line) and c) both advection terms are excluded (yellow line).

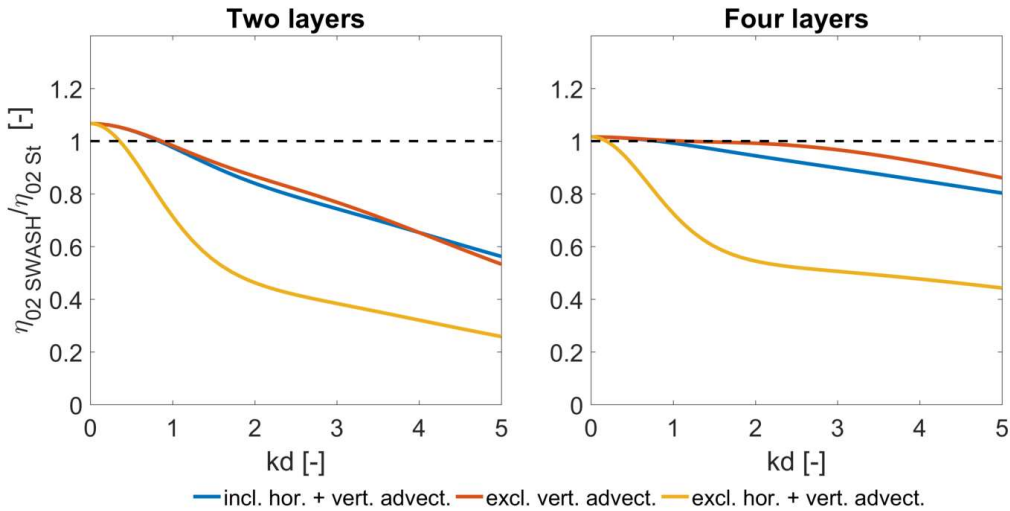


Figure 4.13: Comparison of normalised second order amplitude of the surface elevation, $\eta_{02,SWASH}/\eta_{02,St}$, for two and four vertical layers for the cases that: a) both advection terms are included (blue line), b) only horizontal advection term is included (orange line) and c) both advection terms are excluded (yellow line).

Additionally, the kd range over which the relative error in the second order amplitude of the surface elevation stays below 10% is defined in Table 4.6. From Figure 4.13 and Table 4.6 it is noticed that excluding both the horizontal and vertical advection term in the vertical momentum equation reduces significantly the capability of the model to accurately represent the Stokes second order surface component. The error is less than 10% up to a kd value of 0.60 and 0.53 for two and four layers, respectively, in contrast to the case that only the vertical advection term is neglected where the corresponding kd values are 1.68 and 4.36. On the other hand, comparing the case where both advection terms are included with the one in which only the horizontal advection term is included, the solutions are similar with a slight improvement for the later case.

Consequently, from this sensitivity analysis, it can be concluded that when a few vertical layers are used together with the Keller Box scheme (Figure 4.1b) for the discretization of the pressure, the terms in the vertical momentum equation including the relative vertical velocity ($w_{rel,12}$) can be neglected for robustness reasons since this assumption does not deteriorate the second order nonlinear properties of the model. However, when more layers are applied combined with the central differences scheme (Figure 4.1a), then this term should be included since it is expected that neglecting it will lead to an overestimation of the second order

amplitude compared to the Stokes solution.

Table 4.6: Range of dimensionless depth kd over which the relative error in the second order amplitude of the surface elevation, stays below 10%.

Cases	Range of Dimensionless Depth [-]		Error [%]
	2 Layers	4 Layers	
incl. hor. & vert. advect.	$kd \leq 1.52$	$kd \leq 2.95$	≤ 10
excl. vert. advect.	$kd \leq 1.68$	$kd \leq 4.36$	≤ 10
excl. hor. & vert. advect.	$kd \leq 0.60$	$kd \leq 0.53$	≤ 10

4.6 Conclusions

In this chapter, the governing equations of the non-hydrostatic wave model, SWASH, have been analysed in order to examine the linear and nonlinear properties of the model when up to four vertical layers are applied.

First, a Stokes-type Fourier analysis on a flat bottom has been performed in order to define the first, second and third order equations. Subsequently, expressions have been derived for linear frequency dispersion, amplitude dispersion and second and third order solutions for weakly nonlinear monochromatic waves. From the linear analysis presented in Section 4.3, it can be argued that the model can achieve excellent dispersion accuracy using a few vertical layers, since for the case of 3 layers the error stays below 1% up to a kd value of 16.41. Sections 4.4.1 and 4.4.2 contain the second and third order solutions, while the Stokes third order theory has been used as the reference solution for analytical comparison. A major improvement of the capability of the model to represent the Stokes second order surface component is noticed when a multi-layer layout is applied. Additionally, the Stokes third order surface component and the amplitude dispersion are also satisfactorily described by the governing equations of the model although for a smaller range of kd values than the second order.

Next, second order transfer functions for subharmonic and superharmonic interactions have been derived in Section 4.4.3 and the results have been compared with the exact solutions from the nonlinear boundary value problem for the Laplace equation. As expected, results are much improved by increasing the number of layers and it has been shown that the SWASH model predicts very well the transfer functions over a wide range of water depths.

Finally, in Section 4.5 a sensitivity analysis was executed regarding the effect of the horizontal and vertical advection terms of the vertical momentum equation on the second order nonlinear properties of the model.

In conclusion, the derivations and analyses made in this chapter have resulted in the identification of kd ranges over which the model achieves the target accuracy depending on the number of layers employed. These ranges have been summarised in tables from which SWASH users can decide on the number of vertical layers to

be applied, taking into account the kd value and the acceptable error on the linear and nonlinear properties of each specific case. Apart from the above, the derived solutions are essential to formulate higher order boundary conditions for regular and irregular waves. More precisely, using the derived solutions of the governing equations as input at the wave generation boundary ensures that the wave shapes are maintained throughout the whole test area and thus the generated wave field remains homogeneous.

Chapter 5

Development of internal wave generation in SWASH model

In this fifth chapter of the thesis, internal wave generation methods are developed in the non-hydrostatic wave model, SWASH, whose governing equations have been analysed in Chapter 4. The goal is to tackle knowledge gap 3, as defined in Section 1.2 and in this way to improve the capability of the model to accurately generate regular and irregular long- and short-crested waves. Two different internal wave generation methods are examined: a source term addition method where additional surface elevation is added to the calculated surface elevation in a specific location in the domain and a spatially distributed source function where a spatially distributed mass is added in the free surface equation. Additionally, a comparison is made between the performance of the new internal wave generation method and the weakly reflective wave generation method. It is shown that using the internal wave generation leads to a significantly more accurate prediction of the resulting wave field in case of waves reflected back to the numerical boundary. The numerical results show a very good agreement with the analytical solutions and the experimental data indicating that SWASH with the addition of the proposed internal wave generation method can be used to study wave propagation of highly dispersive short-crested waves in coastal environments with minimal reflection from the boundaries. The research presented is based on the following articles:

originally published as (Vasarmidis et al., 2019a, 2020, 2021):

Vasarmidis, P., Stratigaki, V., Suzuki, T., Zijlema, M., Troch, P., (2019a). Internal Wave Generation in a Non-Hydrostatic Wave Model. *Water* 11, 986.
<https://doi.org/10.3390/w11050986>

Vasarmidis, P., Stratigaki, V., Suzuki, T., Zijlema, M., Troch, P. (2020). An internal wave generation method for the non-hydrostatic model SWASH. *Coastal Engineering Proceedings*, (36v), waves.16.

<https://doi.org/10.9753/icce.v36v.waves.16>

Vasarmidis, P., Stratigaki, V., Suzuki, T., Zijlema, M., Troch, P., (2021). On the accuracy of internal wave generation method in a non-hydrostatic wave model to generate and absorb dispersive and directional waves. *Ocean Eng.* 219, 108303. <https://doi.org/10.1016/j.oceaneng.2020.108303>

5.1 Introduction

The correct simulation of the waves in the nearshore zone requires the accurate modelling of all the processes involved, such as the generation of the waves, their propagation, transformation and reflection or absorption at the domain boundaries. There are three main methods to generate waves in numerical models. Method 1: weakly reflective wave generation (Higuera et al., 2013a; Wei and Kirby, 1995; Zijlema et al., 2011), method 2: moving boundary wave generation (Altomare et al., 2017; Grilli et al., 2002; Grilli and Horrillo, 1997; Higuera et al., 2015; Orszaghova et al., 2012), and method 3: internal wave generation (Altomare et al., 2018; Jacobsen et al., 2012; Larsen and Dancy, 1983; Lee et al., 2001; Schäffer and Sørensen, 2006; Wei et al., 1999).

Method 1 (Figure 5.1a) is the most popular since the computational cost is the least. According to this method, the horizontal velocity components of the target incident waves are imposed at the boundary of the computational domain over the vertical direction. In addition, in order to avoid reflections in front of the wave generator, a weakly reflective boundary condition is applied at the same location, according to which the total velocity is a linear superposition of the velocity of the target waves and the velocity of the waves propagating towards the boundary. This method is making use of the assumption that the waves propagating towards the boundary of the computational domain are shallow water waves with small amplitude and direction perpendicular to the domain boundary and thus, this method is considered weakly reflective when dispersive and directional waves are examined. Furthermore, Wei and Kirby (1995) found that this type of radiation condition at the wave generator boundary can lead to numerical errors when long time simulations are performed. Recently, a generating absorbing boundary condition (GABC) has been developed which is an enhanced type of a weakly reflective wave generation boundary condition and can partially absorb dispersive and directional waves (Wellens, 2012; Wellens and Borsboom, 2020). However, in this method the level of reflection strongly depends on the initial approximations since the characteristics of the reflected waves (i.e., wave angle, wave celerity) inside the numerical domain cannot be estimated a priori. In general, it is not possible to find practical boundary conditions that do the above task perfectly.

Method 2 (Figure 5.1b) mimics the exact behavior of wave generation paddles of the experimental facilities. Therefore, a moving boundary is applied to generate and absorb waves, while the validity of the absorption is similar to method 1. The moving boundary requires mesh deformation and thus method 2 is slower and more

complicated than method 1.

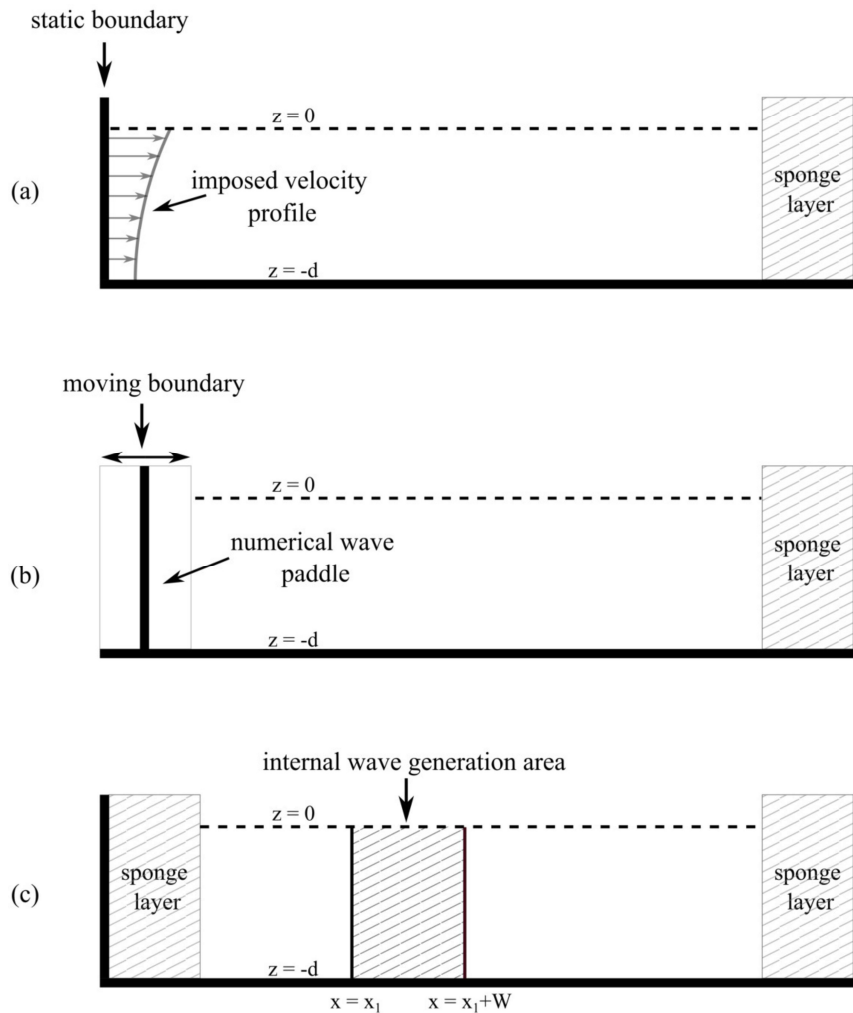


Figure 5.1: Definition sketches of the three main methods to generate waves in numerical models; a) Method 1: weakly reflective wave generation, b) Method 2: moving boundary wave generation and c) Method 3: Internal wave generation.

Models that are using sponge layers, on the other hand, can absorb waves of different frequencies effectively with minimal reflection. To make this absorption optimal, each specific case requires tuning of the sponge layer thickness based on the lowest frequency component that has to be absorbed. The presence of the sponge layers requires that the generation of the waves takes place inside the computational domain (Figure 5.1c) and not on the boundary. This internal wave generation method in combination with numerical wave absorbing sponge layers was firstly proposed by Larsen and Dancy (1983) for Peregrine's classical Boussinesq equations (Peregrine, 1967). Later, Lee and Suh (1998) and Lee et al. (2001) achieved wave generation for the mild slope equations of Radder and Dingemans (1985) and the extended Boussinesq equations of Nwogu (1993), respectively, by applying the source term addition method. Lee et al. (2001) have shown empirically

that the velocity of disturbances caused by the incident wave can be properly obtained from the viewpoint of energy transport. Further, Schäffer and Sørensen (2006) theoretically derived the energy velocity by adding the delta source function to the mass conservation type equation and integrated asymptotically the resulting equation at the generation point. However, Wei et al. (1999) found that the source term addition method in a single source line may cause high frequency noise in case of a non-staggered computational grid. To deal with this problem, Wei et al. (1999) derived a spatially distributed (Gaussian shape) source function for internal wave generation, where a mass source is added in the continuity equation. Later, Choi and Yoon (2009) and Ha et al. (2013) used this method in a Reynolds-averaged Navier-Stokes (RANS) equations model and a Navier-Stokes equations (NSE) model, respectively. However, in both cases they used directly the formula of Wei et al. (1999), which was derived using the extended Boussinesq equations of Nwogu (1993). Thus, their model was not capable of accurately generating deep water waves and consequently high-frequency components in case of irregular waves. The derivation of method 3 requires the knowledge of the underlying model equations, and thus its formulation differs depending on the governing equations.

Although method 3 makes use of a larger numerical domain and thus the computational cost is higher, it is advantageous compared to the other two methods when it comes to the study of the interaction of the waves with structures (e.g., breakwaters, reefs, artificial islands) and wave energy converter (WEC) farms, where dispersive and directional waves are reflected or radiated back to the numerical domain boundary. Note, however, that the size of the sponge layers is usually significantly smaller than the area of interest in view of the coastal wave models (e.g. Boussinesq-type, non-hydrostatic models). Moreover, SWASH has already been used in the field of marine energy by simulating the wave-induced response of a submerged wave-energy converter (Rijnsdorp et al., 2018). This kind of application requires a homogeneous wave field in the whole numerical domain. Thus, the implementation of internal wave generation is important as it introduces noteworthy improvements in the model, which can then make full use of its benefits for the study of WEC farms.

In the present research, a source term addition method and a spatially distributed source function for internal wave generation are implemented in the non-hydrostatic model SWASH. In addition, the energy velocity is derived for the governing equations of SWASH in case a multi-layer layout is implemented. To the present authors' knowledge, these internal wave generation methods which are commonly used in Boussinesq models and mild-slope wave models, have not been derived and used in a non-hydrostatic wave model before, due to the complexity of the governing equations. Further, in order to evaluate the method's performance with respect to its ability to accurately generate highly dispersive regular and irregular long-crested and short-crested waves and to avoid reflections at the location of the wave generator, the model was validated against analytical solutions and experimental data. Three benchmark experimental tests have been used, which include wave propagation over a shoal and wave diffraction around a vertical wall. Finally, a comparison is carried out between the performance of the newly developed internal wave generation (method 3) in non-hydrostatic models and the

traditional weakly reflective wave generation (method 1) for the case of waves that are reflected back to the numerical boundary due to the presence of a structure. So, the main objective of the present study concerns the implementation of the internal wave generation in SWASH to accurately generate even highly dispersive and directional waves, while at the same time reflections at the position of the wave generator are vanishing.

The structure of the chapter is presented as follows. The weakly reflective wave generation boundary is described in Section 5.2. The implemented internal wave generation methods are derived in Section 5.3. Section 5.4 provides a detailed presentation of the results of the SWASH model for the case of regular and irregular long- and short-crested waves, where these results are compared with analytical solutions. In addition, validation results are presented in comparison with experimental data in Section 5.5, in order to evaluate the accuracy of the newly developed model. A comparison between the performance of methods 1 and 3 is presented in Sections 5.4 and 5.5. The final section includes the conclusions of the present study.

5.2 Weakly reflective wave generation boundary

In the SWASH model, incident waves are generated by prescribing their horizontal velocity component normal to the boundary of the computational domain over the vertical direction. To prevent reflections in front of the numerical wave generator, a weakly reflective wave generation boundary condition is adopted. The inflow depth-averaged horizontal velocity at the boundary for the case of one layer is given by:

$$u(t) = \frac{\omega}{kd} \eta_t + \frac{c_0}{d \cos \alpha} (\eta_t - \eta_i) \quad (5.1)$$

where k is the wave number, ω is the angular frequency, c_0 is the local linear wave speed, α is the wave propagation angle, η_t and η_i are the target and the instantaneous surface elevations, respectively. In case of a multi-layer formulation of the model, the inflow horizontal velocity is described by a hyperbolic cosine profile. The values of c_0 and α should be chosen a priori from the user and in case that the wave propagates towards the boundary of the computational domain with a wave speed of $c = \omega/k = c_0$ and with a wave angle of $\theta = \alpha$, then the wave will be perfectly absorbed at the boundary (Higdon, 1987).

Equation 5.1 is obtained by combining the Sommerfeld condition with a 1D approximation of the continuity equation (Blayo and Debreu, 2005):

$$\frac{\partial \eta}{\partial t} + \frac{c_0}{\cos \alpha} \frac{\partial \eta}{\partial x} = 0 \quad (5.2)$$

$$\frac{\partial \eta}{\partial t} + d \frac{\partial u}{\partial x} = 0 \quad (5.3)$$

Substituting Equation 5.2 into Equation 5.3:

$$\frac{\partial u}{\partial x} - \frac{c_0}{d \cos \alpha} \frac{\partial \eta}{\partial x} = 0 \quad (5.4)$$

The plane wave solution of Equations 5.2 - 5.4 can be written as:

$$\eta = \eta_1 \exp[i(\omega t - kx \cos \theta)] + \eta_2 \exp[i(\omega t + kx \cos \theta)] \quad (5.5)$$

$$u = u_1 \exp[i(\omega t - kx \cos \theta)] + u_2 \exp[i(\omega t + kx \cos \theta)] \quad (5.6)$$

where the subscripts 1 and 2 stand for incoming and reflected modes, respectively. Substituting Equations 5.5 and 5.6 in Equation 5.3 gives:

$$u_1 - u_2 = \frac{\omega}{kd \cos \theta} (\eta_1 + \eta_2) \quad (5.7)$$

Substituting Equations 5.5 and 5.6 in Equation 5.4 we obtain:

$$u_1 - u_2 = \frac{c_0}{d \cos \alpha} (\eta_1 - \eta_2) \quad (5.8)$$

Finally, eliminating u_1 and u_2 using Equation 5.7, the reflection coefficient is obtained:

$$R = \frac{\eta_1}{\eta_2} = -\frac{c \cos \alpha - c_0 \cos \theta}{c \cos \alpha + c_0 \cos \theta} \quad (5.9)$$

It can be noticed that the amount of reflection is indeed zero for the case that the incoming wave speed is equal to c_0 and the incident wave angle is equal to α . In Figure 5.2, the absolute reflection coefficient as a function of the incident wave angle θ and the dimensionless depth kd is plotted for the case that $c_0 = \sqrt{gd}$ and $\alpha = 0^\circ$ which are the conditions that have been applied in the present study. It is clearly observed that the absolute reflection coefficient increases for larger values of dimensionless depth kd and wave angle θ . The reason that the shallow water wave speed ($c_0 = \sqrt{gd}$) is used as an input, is based on the fact that in most nearshore applications the high frequency energy is dissipated near the shoreline while the long waves are reflected back. However, in case that man-made structures are considered, both short and long waves are reflected back towards the wave generation boundary with a range of wave speeds that cannot be estimated a priori. This problem can be partly alleviated through the extension of the Sommerfeld condition (Equation 5.2) by means of rational polynomials in kd of the dispersive wave celerity, $c_0 = c_0(kd)$, along with the second order vertical derivative of the surface elevation (Wellens and Borsboom, 2020). Yet, this approach is less suitable for non-hydrostatic models using a few layers. In addition, for the above described wave generation method, a linear superposition of the incident and reflected wave is assumed and thus can only be applied to small amplitude waves.

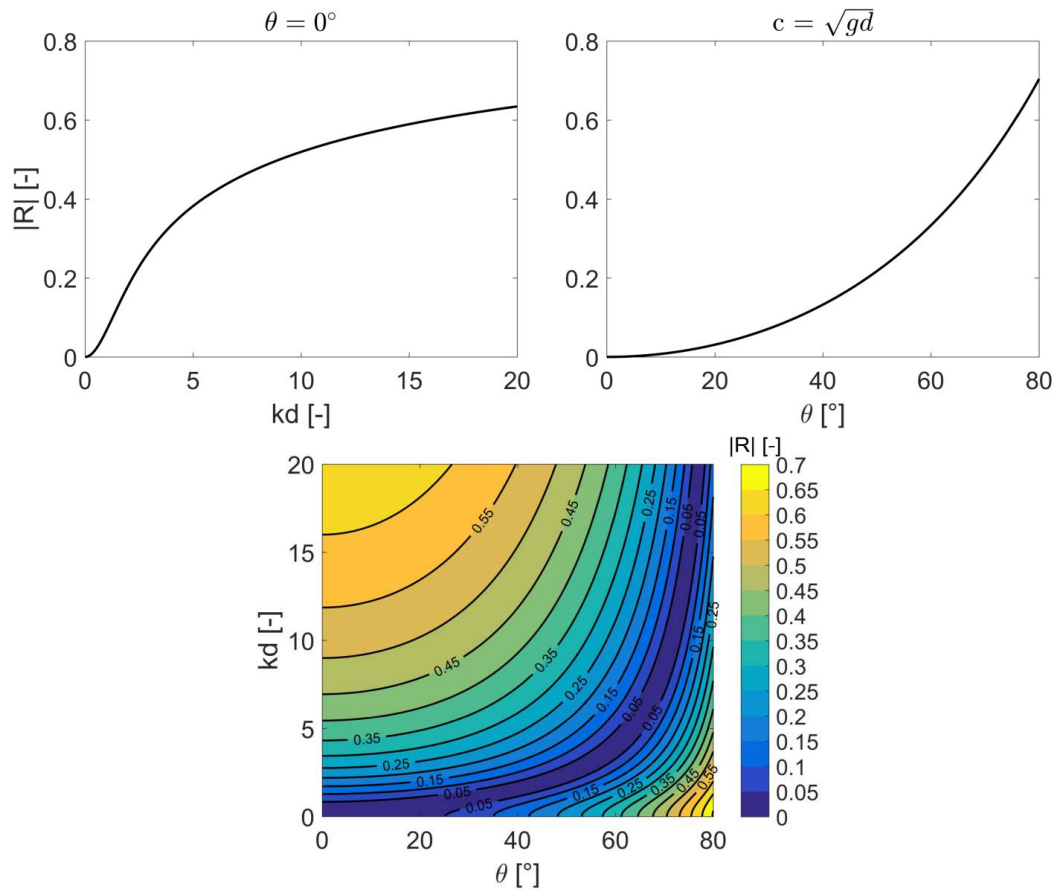


Figure 5.2: Absolute reflection coefficient as a function of the incident wave angle θ and the dimensionless depth kd for the case that $c_0 = \sqrt{gd}$ and $\alpha = 0^\circ$.

5.3 Internal wave generation

In cases of directional and dispersive waves an internal wave generation method (method 3) can be applied to avoid reflections due to the weakly reflective wave generation boundary (method 1), as described in Section 5.2. Two different internal wave generation methods are proposed here and are implemented in the SWASH model. The first one is a source term addition method proposed by Lee et al. (2001), while the second one is a spatially distributed source function proposed by Wei et al. (1999).

5.3.1 Energy Velocity

At first, a new energy velocity for the system of SWASH equations is mathematically derived following the methodology of Schäffer and Sørensen (2006) who derived the energy velocity for Nwogu's Boussinesq equations. In this section, the derivation for the case of two equidistant vertical layers is presented, while the extension to more layers is straightforward.

Bai and Cheung (2013) showed that the governing Equations 2.37-2.40 can be converted into a Boussinesq form by expressing the non-hydrostatic pressure and vertical velocity component in terms of surface elevation and horizontal velocity component. Adding a point source to the continuity equation, the linear governing equations on a constant depth for the case of two equidistant vertical layers read:

$$\frac{\partial \eta}{\partial t} + d \frac{\partial u}{\partial x} = \Lambda(t) \delta(x) \quad (5.10)$$

$$\frac{\partial u}{\partial t} + g \frac{\partial \eta}{\partial x} - \frac{5}{16} d^2 \frac{\partial^3 u}{\partial x^2 \partial t} - \frac{1}{8} d^2 \frac{\partial^3 \hat{u}}{\partial x^2 \partial t} = 0 \quad (5.11)$$

$$\frac{\partial \hat{u}}{\partial t} - \frac{1}{8} d^2 \frac{\partial^3 u}{\partial x^2 \partial t} - \frac{1}{16} d^2 \frac{\partial^3 \hat{u}}{\partial x^2 \partial t} = 0 \quad (5.12)$$

where u is the depth integrated horizontal velocity component, \hat{u} is the inter-layer velocity variations, δ is the Dirac delta function and Λ is the source function applied to a single point. From Equation 5.10 it can be noticed that the $\partial u / \partial x$ term must be the one balancing the Dirac delta function and thus u and \hat{u} have a discontinuity.

Taking the time derivative of Equation 5.11 and eliminating η using Equation 5.10 gives:

$$\frac{\partial^2 u}{\partial t^2} - g d \frac{\partial^2 u}{\partial x^2} - \frac{5}{16} d^2 \frac{\partial^4 u}{\partial x^2 \partial t^2} - \frac{1}{8} d^2 \frac{\partial^4 \hat{u}}{\partial x^2 \partial t^2} = -g \Lambda \frac{\partial \delta}{\partial x} \quad (5.13)$$

Eliminating the second and third term of Equation 5.13 using Equation 5.12 to get:

$$\frac{\partial^2 u}{\partial t^2} - 8 \frac{g}{d} \hat{u} + \frac{1}{2} g d \frac{\partial^2 \hat{u}}{\partial x^2} - \frac{5}{2} \frac{\partial^2 \hat{u}}{\partial t^2} + \frac{1}{32} d^2 \frac{\partial^4 \hat{u}}{\partial x^2 \partial t^2} = -g \Lambda \frac{\partial \delta}{\partial x} \quad (5.14)$$

Taking the x derivative two times and eliminating the first term using Equation 5.12 gives:

$$8 \frac{1}{d^2} \frac{\partial^2 \hat{u}}{\partial t^2} - 8 \frac{g}{d} \frac{\partial^2 \hat{u}}{\partial x^2} + \frac{1}{2} g d \frac{\partial^4 \hat{u}}{\partial x^4} - 3 \frac{\partial^4 \hat{u}}{\partial x^2 \partial t^2} + \frac{1}{32} d^2 \frac{\partial^6 \hat{u}}{\partial x^4 \partial t^2} = -g \Lambda \frac{\partial^3 \delta}{\partial x^3} \quad (5.15)$$

Integrating four times Equation 5.15 from $x = -\epsilon$ to $x = +\epsilon$, with the limit $\epsilon \rightarrow 0$ and requiring the integrals of \hat{u} to be continuous at $x = 0$, we get:

$$\frac{1}{2} g d (\hat{u}^+ - \hat{u}^-) + \frac{1}{32} d^2 \left(\frac{\partial^2 \hat{u}^+}{\partial t^2} - \frac{\partial^2 \hat{u}^-}{\partial t^2} \right) = -g \Lambda \quad (5.16)$$

In Equation 5.16, \hat{u} is an odd function and thus the left and right contributions are identical.

In SWASH an approximation of the exact linear dispersion relation, which depends on the number of vertical layers, is used (see Chapter 4). For the case of two equidistant layers it is given by:

$$\omega^2 = gk^2d \frac{1 + \frac{1}{16}(kd)^2}{1 + \frac{3}{8}(kd)^2 + \frac{1}{256}(kd)^4} \quad (5.17)$$

In addition, at the wave generation boundary, apart from the progressive waves, evanescent modes are included as well. These evanescent modes are a general characteristic of the Equations 5.10–5.12. Hence, Equation 5.17 can be rewritten as:

$$\frac{\omega^2 d}{g} = \frac{\omega_e^2 d}{g} \quad (5.18)$$

$$(kd)^2 \frac{1 + \frac{1}{16}(kd)^2}{1 + \frac{3}{8}(kd)^2 + \frac{1}{256}(kd)^4} = (k_e d)^2 \frac{1 + \frac{1}{16}(k_e d)^2}{1 + \frac{3}{8}(k_e d)^2 + \frac{1}{256}(k_e d)^4} \quad (5.19)$$

where k and k_e are the wave numbers for progressive waves and evanescent modes, respectively. Equation 5.19 yields two solutions:

$$(k_e d)^2 \rightarrow (kd)^2, \quad (k_e d)^2 \rightarrow -\frac{1 + \frac{1}{16}(kd)^2}{\frac{1}{16} + \frac{5}{256}(kd)^2} \quad (5.20)$$

Furthermore, away from the source point, $x = 0$, the solutions of Equations 5.10–5.12 are written as:

$$\eta = \eta_{p0} \exp[i(\omega t - kx)] + \eta_{e0} \exp[i(\omega t - k_e x)] \quad (5.21)$$

$$u = u_{p0} \exp[i(\omega t - kx)] + u_{e0} \exp[i(\omega t - k_e x)] \quad (5.22)$$

$$\hat{u} = \hat{u}_{p0} \exp[i(\omega t - kx)] + \hat{u}_{e0} \exp[i(\omega t - k_e x)] \quad (5.23)$$

where the subscripts p and e stand for progressive and evanescent modes, respectively. By using Equations 5.11 and 5.12, the inter-layer velocity amplitude \hat{u}_{p0} can be expressed in terms of surface elevation amplitude η_{p0} :

$$\hat{u}_{p0} = -\frac{1}{8} \frac{gk}{\omega} \frac{(kd)^2}{1 + \frac{3}{8}(kd)^2 + \frac{1}{256}(kd)^4} \eta_{p0} \quad (5.24)$$

In addition, the double integral of \hat{u} with respect to x gives an odd function and it must vanish at the source point, $x = 0$ and thus from Equation 5.23 we can write:

$$\hat{u}_{e0} = -\frac{k_e^2}{k^2} \hat{u}_{p0} \quad (5.25)$$

Finally, Equation 5.23 at $x \rightarrow 0^+$ is imported in Equation 5.16 and eventually \hat{u}_{e0} and \hat{u}_{p0} are going to be replaced using Equations 5.24 and 5.25 respectively. As a result, Equation 5.16 becomes:

$$\Lambda = 2C_e\eta_p \quad (5.26)$$

where

$$\eta_p = \eta_{p0} \exp[i\omega t] \quad (5.27)$$

$$C_e = \frac{1}{8} \frac{gk}{\omega} d \left(\frac{(kd)^2}{1 + \frac{3}{8}(kd)^2 + \frac{1}{256}(kd)^4} \right) \left(1 - \frac{k_e^2}{k^2} \right) \left(\frac{1}{2} - \frac{1}{32} \frac{\omega^2 d}{g} \right) \quad (5.28)$$

By eliminating ω and k_e using Equations 5.17 and 5.20, respectively, it is noticed that the energy velocity C_e is equal to the group velocity C_g as it can be calculated from the approximated dispersion relation by taking the derivative of ω with respect to k ($C_g = \partial\omega/\partial k$). Similarly, the energy velocity (group velocity) C_e can be derived for any number of vertical layers.

The energy velocity C_e for one, two and three equidistant vertical layers is given by Equations 5.29, 5.30 and 5.31.

$$C_{e,1} = \frac{8\sqrt{gd}}{\sqrt{(4 + (kd)^2)^3}} \quad (5.29)$$

$$C_{e,2} = \frac{64\sqrt{gd}(256 + 32(kd)^2 + 5(kd)^4)}{\sqrt{(16 + (kd)^2)(256 + 96(kd)^2 + (kd)^4)^3}} \quad (5.30)$$

$$C_{e,3} = \frac{72\sqrt{gd}(5038848 + 933120(kd)^2 + 147744(kd)^4 + 3024(kd)^6 + 35(kd)^8)}{\sqrt{(1296 + 120(kd)^2 + (kd)^4)(46656 + 19440(kd)^2 + 540(kd)^4 + (kd)^6)^3}} \quad (5.31)$$

In Figure 5.3, the normalised energy velocities C_e/C_{gAiry} and the corresponding relative error for one, two and three vertical layers are plotted as a function of the dimensionless depth kd . In addition, the range of dimensionless depth kd as a function of the number of vertical layers where the relative error in the normalised energy velocities C_e/C_{gAiry} stays below 3% is given in Table 5.1. It is noticed that the relative error is getting smaller as the number of layers increases, which extends the applicability of the model to higher values of kd (dispersive waves) and thus the achieved accuracy to deeper water. For three vertical layers the corresponding relative error in the normalised energy velocity C_e/C_{gAiry} is smaller than 3% for $kd \leq 12.5$.

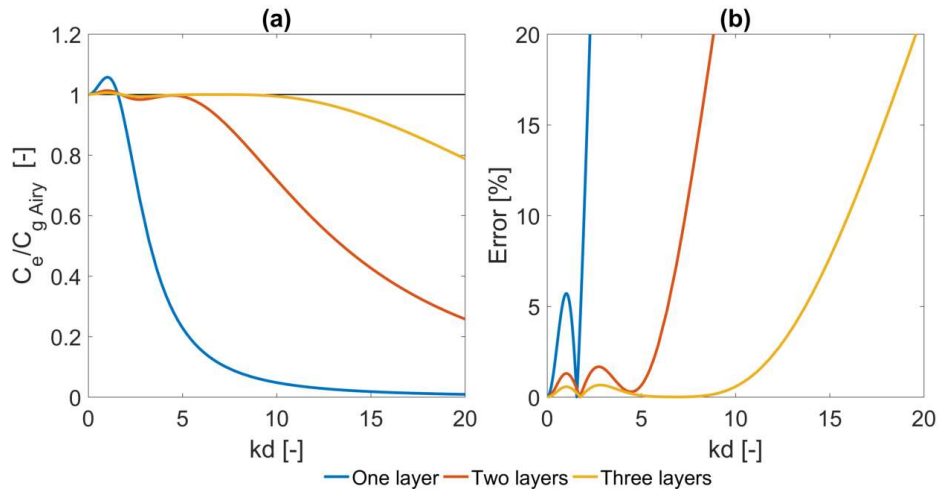


Figure 5.3: (a) The normalised energy velocities C_e/C_{gAiry} and (b) the corresponding relative error for one, two and three vertical layers as a function of the dimensionless depth kd .

Table 5.1: Range of dimensionless depth kd as a function of the number of vertical layers and the corresponding relative error in the normalised energy velocities C_e/C_{gAiry} .

Number of layers	kd [-]	Error [%]
1	≤ 0.55	≤ 3
2	≤ 6.00	≤ 3
3	≤ 12.50	≤ 3

5.3.2 Source term addition method

In the source term addition method proposed by Lee et al. (2001), additional surface elevation η^* is added with the desired energy to the calculated surface elevation η at the wave generation line (Figure 5.4) for each time step and is given by:

$$\eta^* = 2\eta^I \frac{C_e \Delta t}{\Delta x} \cos \theta \quad (5.32)$$

where Δx is the grid size in the x -axis, Δt is the time step, θ is the angle of the incident wave ray from x -axis, η^I is the water surface elevation of incident waves and C_e is the energy velocity.

5.3.3 Spatially distributed source function

The spatially distributed source function was proposed by Wei et al. (1999) for the depth averaged Boussinesq-type equations. According to this method, a spatially distributed mass is added in the free surface equation over an area called the “wave generation source area”, while sponge layers (relaxation zones) are used at the domain boundaries to absorb the incoming waves. Hence, the spatially

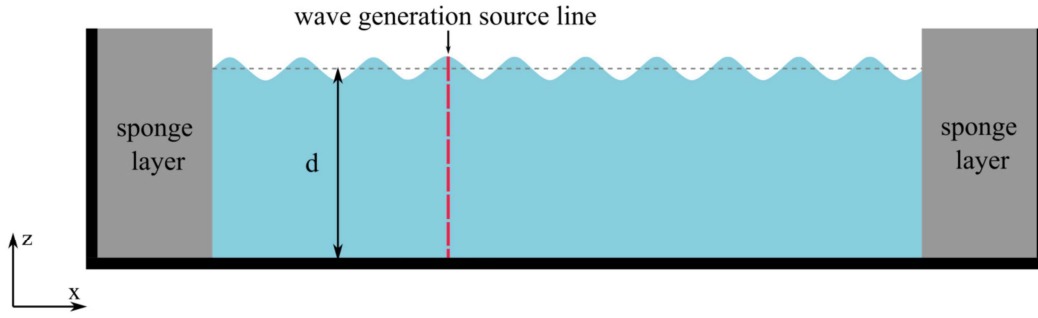


Figure 5.4: Source term addition method definition in a 2D vertical domain.

distributed source function is applied on an area in contrast to the source term addition method which is applied on a line as it is demonstrated in Figures 5.4 and 5.5.

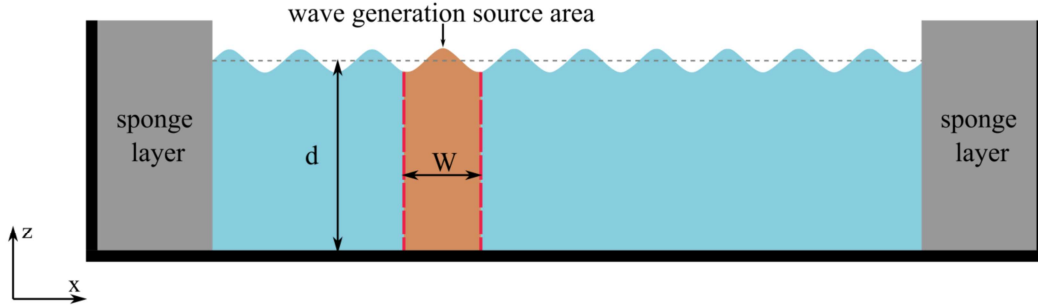


Figure 5.5: Spatially distributed source function definition in a 2D vertical domain.

For a single wave component, the source function is defined as follows:

$$f(x, y, t) = g(x)D \cos(\omega t - ky \sin \theta) \quad (5.33)$$

where D is the amplitude of the source function and $g(x)$ is the shape of the source function which can be arbitrarily chosen. Here, a smooth Gaussian shape has been applied. Wei et al. (1999) derived the source function amplitude D for the extended Boussinesq equations of Nwogu (1993) and is given by:

$$D = \frac{2\eta_0(\omega^2 - \alpha_1 g k^4 d^3) \cos \theta}{\omega k I (1 - \alpha(kd)^2)} \quad (5.34)$$

where $\alpha = -0.390$ and $\alpha_1 = \alpha + 1/3$.

Equation 5.34 is derived for the extended Boussinesq equations of Nwogu and thus cannot be applied directly to the SWASH equations for the case of a multi-layer layout. However, Equation 5.34 can be written in terms of the energy velocity:

$$D = 2C_e \eta_0 \frac{\cos \theta}{I} \quad (5.35)$$

where I is an integral defined by (Wei et al., 1999):

$$I = \sqrt{\frac{\pi}{\beta}} \exp\left(-\frac{(k \cos \theta)^2}{4\beta}\right) \quad (5.36)$$

where β has a value of $\beta = 20/W^2$ and W represents the width of the wave generation source area. The width of the source area is related to the target wave length L by using the auxiliary coefficient δ as $W = \delta L/2$. For all the simulations of the present study, δ is in the range of 0.5 - 0.8 (defined after iterations), where the larger values stand for larger wave heights.

Equation 5.35 can be implemented in SWASH by using the energy velocity that corresponds to the number of vertical layers used in the model. The energy velocity for the case of two vertical layers has already been derived in Section 5.3.1. In this way, the developed method avoids the limitation that Choi and Yoon (2009) and Ha et al. (2013) have observed, where the applied internal wave generation in their models, using Equation 5.34, was not accurate for deeper water conditions.

As a result, the free surface equation inside the wave generation source area for the case that the number of layers in the vertical direction is K , is given by:

$$\frac{\partial \eta}{\partial t} + \frac{\partial Q_{u,K}}{\partial x} + \frac{\partial Q_{v,K}}{\partial y} = 2g(x)C_{e,K}\eta_0 \cos(\omega t - ky \sin \theta) \frac{\cos \theta}{I} \quad (5.37)$$

where $C_{e,K}$ is the energy velocity for K number of layers. Using Equation 5.37 the temporal evolution of the free surface is calculated inside the source area and subsequently the new layer thicknesses are determined for each time step. In this way the source mass is distributed over the water column.

The above described method of internal wave generation has been included and made freely available through SWASH version 6.01, while the implemented code is presented in Appendix C.

5.4 Validation with analytical solutions

The internal wave generation methods, implemented in SWASH as described in Section 5.3, have been used to generate regular and irregular long- and short-crested waves. The obtained results are validated against analytical solutions including water surface elevations, orbital velocities, frequency spectra, spreading function distributions and wave heights.

5.4.1 Generation of regular waves

Firstly, the applicability and accuracy of the internal wave generation methods to generate linear regular waves in transitional and deep water conditions are examined. The numerical flume is presented in Figure 5.6 with sponge layers at the left and right boundaries with a width of $3L$ (where L is the wave length) and a flat

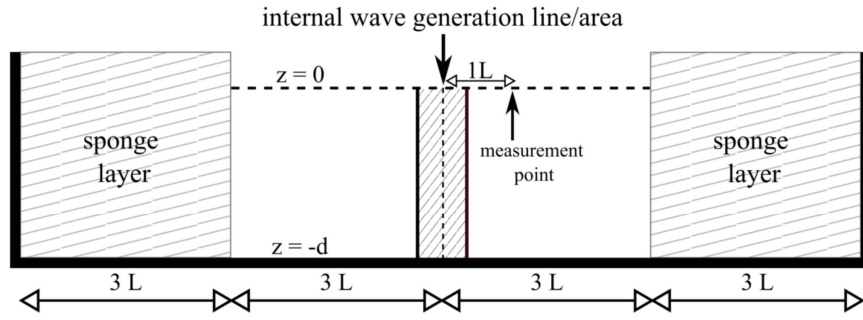


Figure 5.6: Definition sketch of the implemented numerical set-up for the study of regular waves.

bottom. The internal wave generator is positioned at a distance of $3L$ from the sponge layer.

Two different wave conditions are examined (Table 5.2): one in transitional water ($kd = \pi/6$) and one in deep water ($kd = \pi$, highly dispersive wave). For dimensionless depth $kd = \pi/6$ one vertical layer is applied while for dimensionless depth $kd = \pi$ two equidistant vertical layers are applied in order to keep the relative error below 3% (Figure 5.3, Table 5.1). For both cases, the grid cell size is chosen so that $\Delta x = L/50$, while the time step is equal to $\Delta t \approx T/350$, where T is the wave period.

Table 5.2: Wave conditions of the examined linear regular waves.

Wave Height H [m]	Wave Period T [s]	Water Depth d [m]	Dimensionless Depth kd [-]	Number of Layers
0.01	4.000	1.0	$\pi/6$	1
0.01	3.584	10.0	π	2

In Figure 5.7, the normalised water surface elevation η/η_0 (where η_0 is the generated wave amplitude) calculated using the source term addition method (blue dashed lines) and the spatially distributed source function (red dashed lines) is presented. The computed results at a distance of $1L$ from the internal wave generator and at a time period of $t = 10T$ to $t = 18T$ are compared to the results of the analytical solution (solid black lines) for the same conditions. The agreement is very good while the behavior of the two internal wave generation methods is similar, with a small deviation for the case of the highly dispersive wave (Figure 5.7c,d). For the latter case, the spatially distributed source function provides a slightly better fit with the analytical solution.

In the proposed internal wave generation methods, the horizontal velocity component is not prescribed over the vertical direction in contrast to the weakly reflective wave generation (Section 5.2). However, as it is observed from Figure 5.8 the horizontal and vertical velocity profiles are correctly calculated for both internal wave generation methods at a distance of $1L$ from the generation point. The generated wave height is $H = 0.02$ m, the wave period is $T = 3$ s and the water

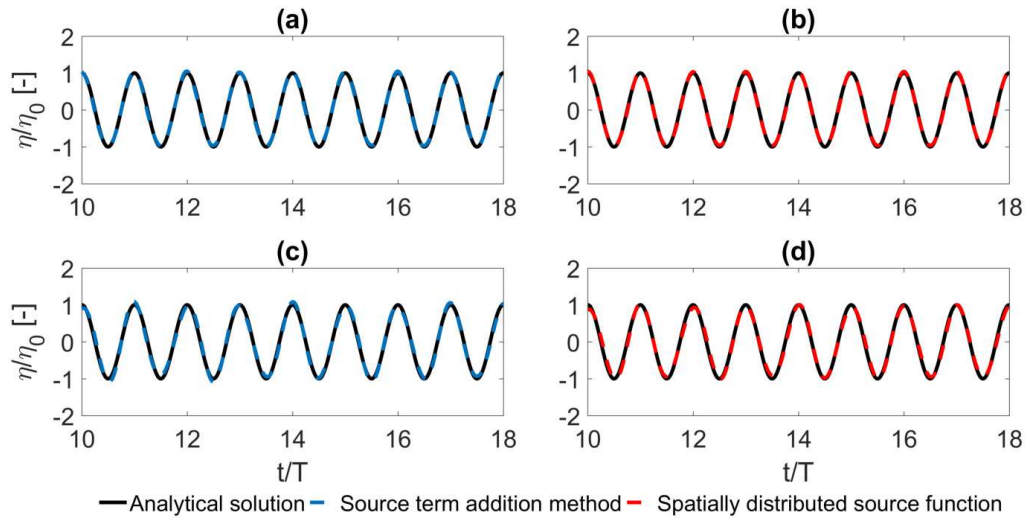


Figure 5.7: Comparison between computed (dashed lines) and target (solid lines) normalised water surface elevation η/η_0 for the case of linear waves with dimensionless depth (a,b) $kd = \pi/6$ (one layer) and (c,d) $kd = \pi$ (two equidistant layers).

depth is $d = 10$ m, while ten equidistant vertical layers have been applied in order to achieve a good agreement with the analytical hyperbolic profile.

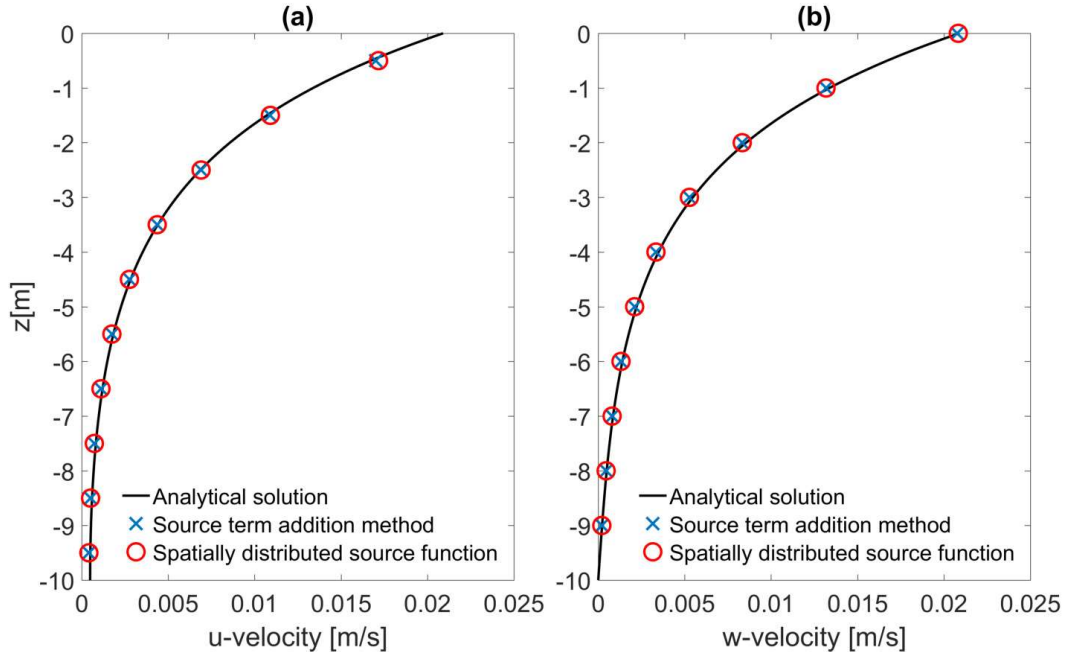


Figure 5.8: Comparison between computed (markers) and target (solid lines) maximum (a) horizontal and (b) vertical velocity profiles using two internal wave generation methods for the case of deep water linear waves ($H = 0.02$ m, $T = 3.0$ s, $d = 10$ m, ten equidistant layers).

In all the previous tests in this section, linear waves have been examined. In order to study the behaviour of the internal wave generation methods under nonlinear waves, waves with different wave heights are tested. The internal wave generator is positioned at the middle of the computational domain which has a total length of $32L$ with sponge layers at the left and right boundaries and a flat bottom. The wave heights are $H = 0.1\text{ m}$, 1 m , 2 m , 3 m , while the wave period is $T = 6\text{ s}$ and the water depth is $d = 10\text{ m}$ (Table 5.3). These wave conditions give a kd value of 1.3 and thus two equidistant vertical layers are applied. The model is applied with a grid cell size of $\Delta x = 2.0\text{ m}$ and a time step of $\Delta t = 0.025\text{ s}$.

Table 5.3: Wave conditions of the examined nonlinear regular waves.

Wave Height H [m]	Wave Period T [s]	Water Depth d [m]	Dimensionless Depth kd [-]	H/d [-]
0.10	6.00	10.0	1.3	0.01
1.00	6.00	10.0	1.3	0.10
2.00	6.00	10.0	1.3	0.20
3.00	6.00	10.0	1.3	0.30

Figure 5.9 shows snapshots of normalised water surface elevation η/η_0 at $t = 50T$ for the different wave heights. Profiles generated using the spatially distributed source function are only presented here since the source term addition method becomes unstable for high wave heights.

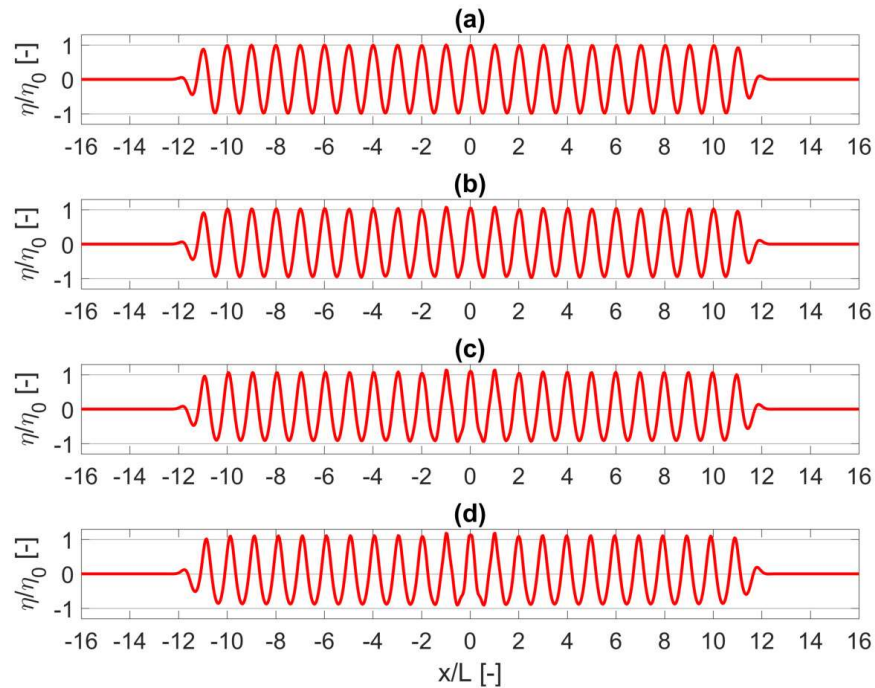


Figure 5.9: Snapshots of normalised water surface elevation η/η_0 at $t = 50T$ using the spatially distributed source function wave generation method for (a) $H/d = 0.01$ (linear), (b) $H/d = 0.1$, (c) $H/d = 0.2$ and (d) $H/d = 0.3$.

From Figure 5.9, it is observed that by increasing the ratio H/d , the waves are transforming from linear (Figure 5.9a) to nonlinear where the wave crests are becoming sharper and the wave troughs flatter.

5.4.2 Reflected dispersive waves

In order to check the capability of the proposed internal wave generation methods for handling reflected dispersive waves, a computational domain ($12L$ long, where L is the wave length) with a sponge layer at the left boundary ($-6L \leq x \leq -3L$) and a closed right boundary (fully reflective wall, $x = 6L$) is used (Figure 5.10b). In addition the performance of the internal wave generation method (method 3) is compared with the one of the weakly reflective wave generation method (method 1).

The wave generation source area/line is placed at the middle of the computational domain ($x = 0$). The domain for method 1 is halved ($0 \leq x \leq 6L$) with the weakly reflective wave generator positioned at the left boundary ($x = 0$) and a fully reflective wall positioned at the right boundary ($x = 6L$) as illustrated in Figure 5.10a. The generated waves have a height of $H = 0.02$ m and a period of $T = 3.0$ s, while the still water depth is $d = 10$ m and the dimensionless depth is $kd = 4.5$. The model is applied with two equidistant vertical layers (error $\leq 3\%$ for $kd \leq 6.0$, Figure 5.3, Table 5.1), a uniform grid resolution of $\Delta x = 0.3$ m and an initial time step of $\Delta t = 0.0125$ s.

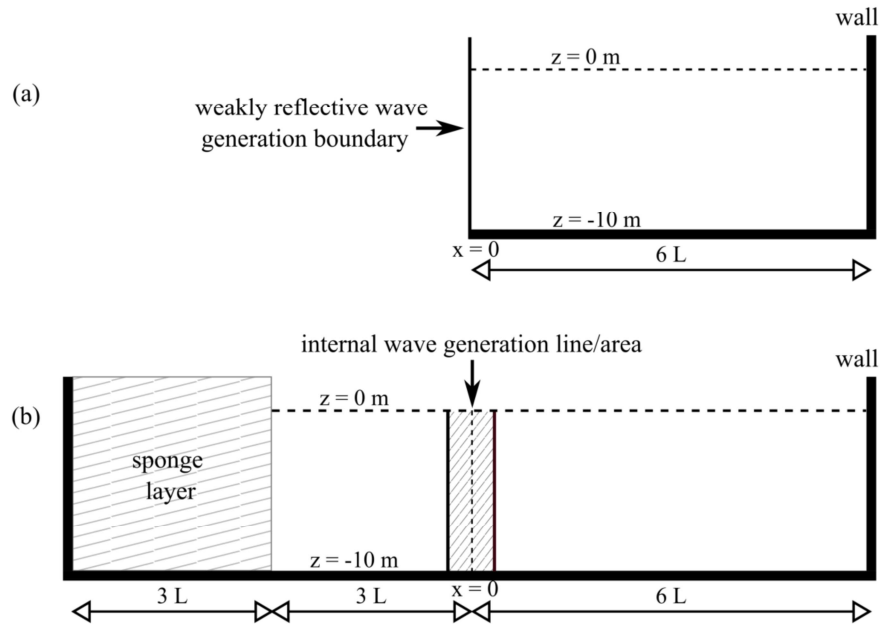


Figure 5.10: Definition sketch of the implemented numerical set-up for the study of reflected dispersive waves using a) weakly reflective wave generation and b) internal wave generation.

Figure 5.11 shows a snapshot of normalised water surface elevation η/η_0 at $t = 50T$ generated using the source term addition method (blue solid line) and the

spatially distributed source function (red dashed line). The two computed profiles are identical, while their agreement with the analytical solution (black markers) is excellent.

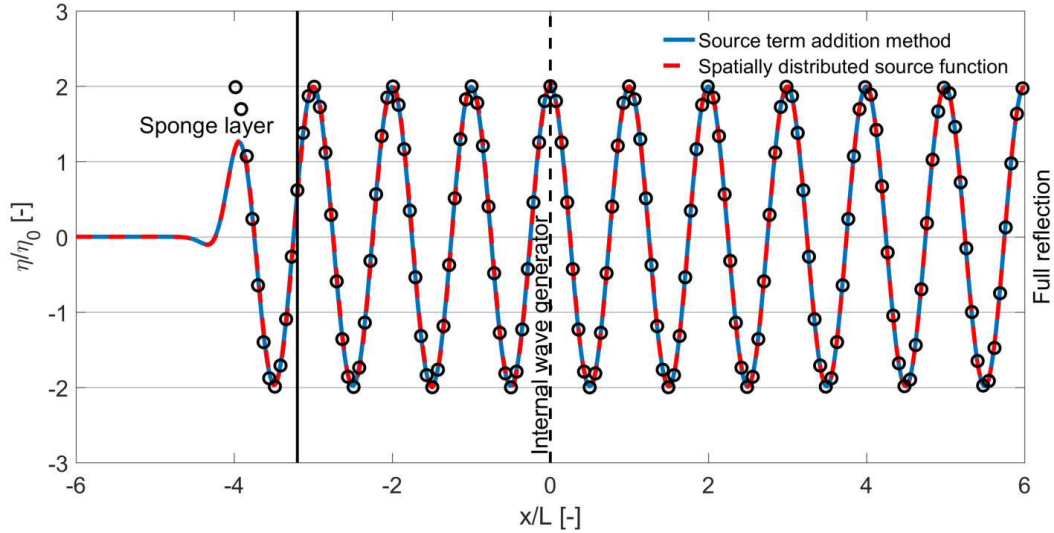


Figure 5.11: Snapshot of normalised water surface elevation η/η_0 at $t = 50T$ using two internal wave generation methods and the analytical solution (black markers) for the case of deep water linear waves ($H = 0.02$ m, $T = 3.0$ s, $d = 10$ m, two equidistant layers) with a sponge layer at the left boundary and a fully reflective wall at the right boundary.

Additionally, Figure 5.12 shows two snapshots of normalised water surface elevations η/η_0 at $t = 28T$ and $t = 100T$, generated using the spatially distributed source function (method 3, red solid line) and weakly reflective (method 1, blue dashed line) wave generation. The waves that are generated at the source area propagate towards both sides of the computational domain. The right boundary is fully reflecting the incoming waves, while the sponge layer on the other end is absorbing them. On the other hand, for method 1 the waves are generated at the left boundary and propagate towards the right boundary. At the right boundary, full reflection of the incoming waves occurs, while at the weakly reflective boundary the waves are being absorbed. Additionally, the target wave has the form of a linear wave and the horizontal dimension of the computational domain is an integer number of the considered wave length. The above gives as a result a theoretical profile (black circles) that has a known analytical expression from literature and is a standing wave with perfect nodal points.

In Figure 5.12a, where the reflected waves have not yet arrived at the generation point, the water surface elevations, computed using wave generation methods 1 and 3, are identical and in excellent agreement with the analytical solution. However, in Figure 5.12b the profile generated with method 1 differs significantly from the analytical solution. On the other hand, the profile generated with method 3 agrees very well with the analytical solution. The reflected dispersive waves pass through the internal wave generation area without affecting the generated waves and are fully absorbed by the sponge layer. Method 1 is not applicable in this case since the

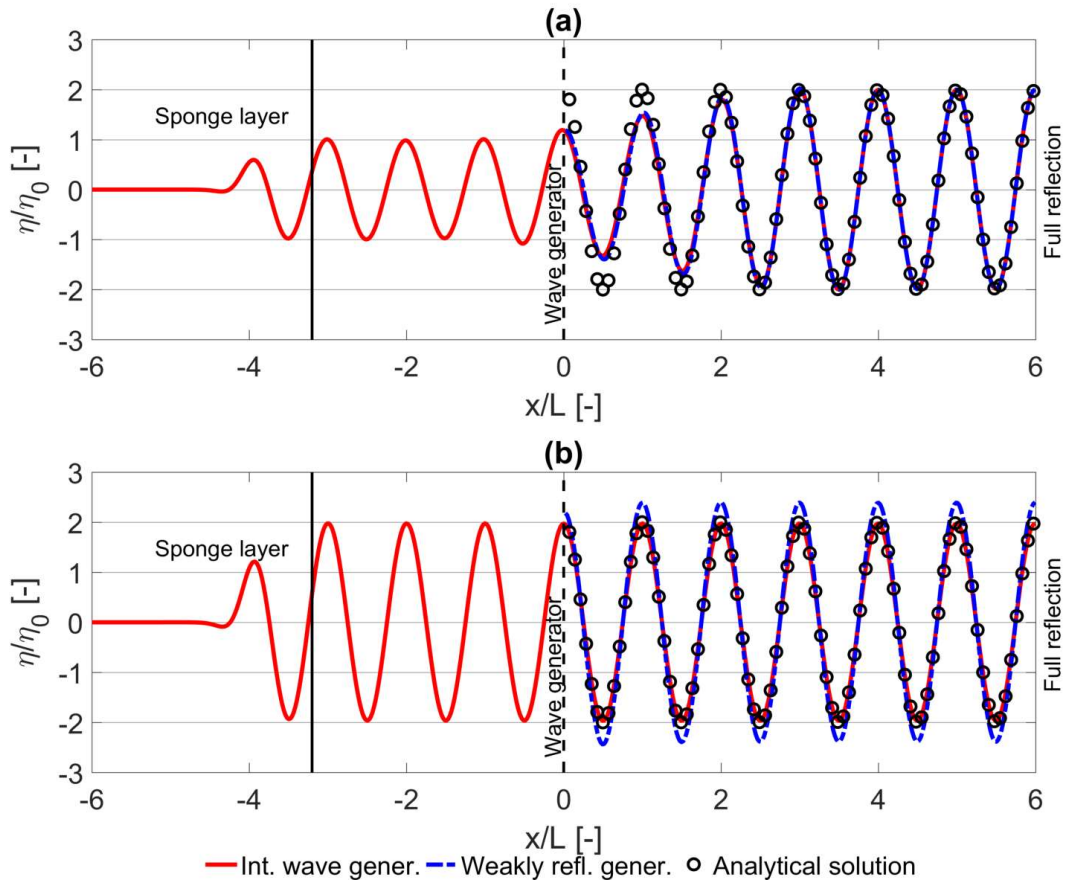


Figure 5.12: Snapshots of normalised water surface elevations η/η_0 at (a) $t = 28T$ and (b) $t = 100T$ using internal wave generation (method 3, red solid line) and weakly reflective wave generation (method 1, blue dashed line) compared with the analytical solution (black circles) for the case of dispersive waves.

assumption that the waves propagating towards the boundary of the computational domain are shallow water waves with a phase velocity of $c = \sqrt{gd}$ is not valid and thus reflections are created. The theoretical reflection coefficient for the weakly reflective boundary as a function of the incident wave angle θ and the dimensionless depth kd is derived in Section 5.2. For $kd = 4.5$ the theoretical reflection coefficient is 37% (Figure 5.2) and the calculated one is 39% (Figure 5.12).

Additionally, it has to be mentioned that when using method 1, a sharp decrease of the wave height was noticed at the first computational cells next to the weakly reflective wave generation boundary. This is happening due to the fact that the hyperbolic profile of the target velocity component cannot be accurately described when coarse vertical resolution is used and thus method 1 needs calibration in case of deep water waves, to generate accurately the target wave height. For the case of irregular waves this calibration is becoming even more difficult, since the behavior of the generation boundary is different for each frequency component. On the other hand, method 3 that is presented in this study does not need any calibration, since the method is directly connected with the surface elevation (Equation 5.37)

rather than the horizontal velocity component.

Finally, the influence of the distance between the sponge layer and the center of the wave generation source area has been examined. Two additional simulations have been executed with the sponge layer at the left boundary located at $-6L \leq x \leq -2L$ and $-6L \leq x \leq -1L$. The resulted normalised water surface elevations η/η_0 at $t = 100T$ are shown in Figure 5.13, where it is noticed that the resulted profiles are identical for all the cases outside the sponge layer zone. The above comparison leads to the conclusion that the sponge layer can be positioned at a distance of only one wave length from the wave generation area without influencing the results and thus the computational area and subsequently the computational cost can be reduced.

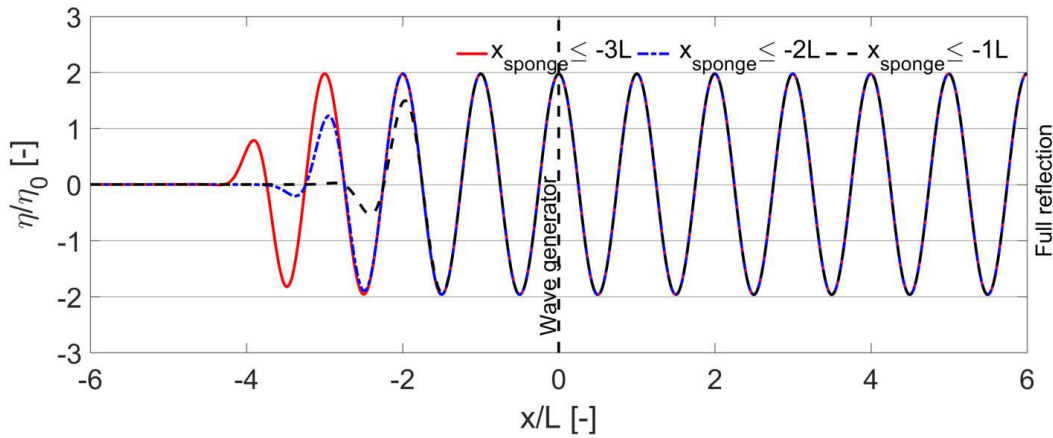


Figure 5.13: Snapshots of normalised water surface elevations η/η_0 at $t = 100T$ using internal wave generation for three different sponge layer positions, $x_{sponge} \leq -3L$ (red solid line), $x_{sponge} \leq -2L$ (blue dash-dot line) and $x_{sponge} \leq -1L$ (black dashed line).

5.4.3 Irregular long-crested waves in a numerical basin with constant depth

We consider two test cases of irregular long-crested waves fitting a JONSWAP (Joint North Sea Wave Observation Project) spectrum, with a significant wave height, $H_s = 0.5$ m, a water depth, $d = 10$ m, a peak enhancement factor, $\gamma = 3.3$ and two different peak wave periods, $T_p = 12$ s and $T_p = 8$ s (Table 5.4).

Table 5.4: Wave conditions of the examined irregular long-crested waves.

Significant Wave Height H_s [m]	Peak Period T_p [s]	Water depth d [m]	Peak Enhancement Factor γ [-]	Number of Layers
0.50	12.0	10.0	3.3	1
0.50	8.0	10.0	3.3	2

The frequency range is confined between $0.5f_p$ and $3f_p$. The internal wave generator is positioned at the middle of the computational domain and sponge

layers are placed at the left and right boundaries. For both test cases, the model is applied with a grid cell size of $\Delta x = 1.0$ m and a time step of $\Delta t = 0.025$ s. However, for the case of $T_p = 8$ s two equidistant vertical layers have been applied to correctly describe the high-frequency part of the spectrum in contrast to the case of $T_p = 12$ s where one layer is enough.

In Figure 5.14, a comparison is made between the target frequency spectrum (S_t) and the simulated frequency spectra generated using the two internal wave generation methods for the cases of $T_p = 12$ s (Figure 5.14a) and $T_p = 8$ s (Figure 5.14b). The surface elevations η at the electronic wave gauges, which are positioned at a distance of $3L_p$ (where L_p is the wave length corresponding to the peak period) from the internal wave generator, are recorded from $t = 25T_p$ to $t = 300T_p$ with a sampling interval of 0.2 s. The recorded data are processed in segments of 2048 points per segment. The resulting frequency spectra agree very well with S_t apart from the one that corresponds to the source term addition method for the case of $T_p = 12$ s, where high-frequency noise is observed. In addition, it is found that the magnitude of this noise strongly depends on the grid resolution since a coarser resolution leads to less noise. Moreover, the small difference around the peak of the frequency spectrum in Figure 5.14b could be caused by numerical dissipation since the electronic wave gauges are positioned at a distance of $3L_p$ from the internal wave generator.

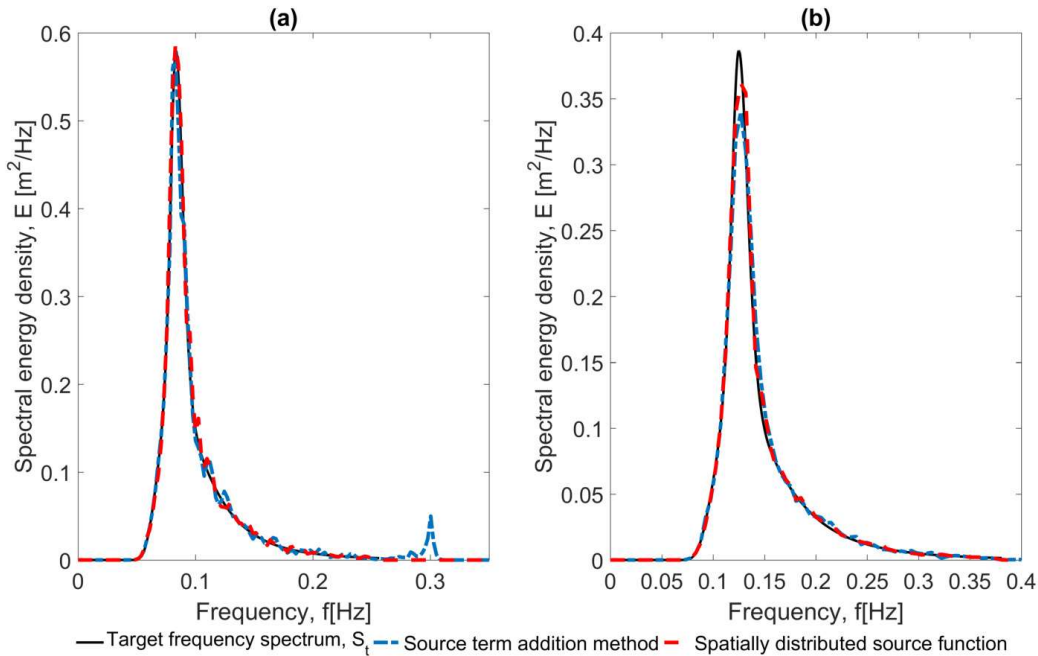


Figure 5.14: Comparison between the frequency spectra resulting from using two internal wave generation methods and the target frequency spectrum S_t for irregular waves with $H_s = 0.5$ m, $d = 10$ m (a) $T_p = 12$ s (one layer) and (b) $T_p = 8$ s (two equidistant layers).

It has to be mentioned that the overall performance of the spatially distributed source function is better than the source term addition method, since the latter

becomes unstable for large wave heights and may cause high frequency noise. Thus, in the following sections only the spatially distributed source function is applied.

5.4.4 Oblique waves in a numerical basin with constant depth

In this section, oblique waves are generated in a basin with constant depth by using the internal wave generation method. The numerical basin is 190 m long, 90 m wide and 1 m deep (Figure 5.15). Sponge layers are placed at the left and right boundaries with a width of 50 m while periodic boundaries are applied at the top and bottom of the domain. The internal wave generator is parallel to the y -axis and is positioned at a distance of 100 m ($x = 0$) from the left boundary. The wave height is $H = 0.01$ m, the wave period is $T = 4$ s and the wave propagation angle is $\theta = 15^\circ$. θ is the angle between the positive x -axis and the propagation direction, measured counterclockwise. The grid cell size is chosen so that $\Delta x = \Delta y = 0.15$ m. In order to achieve a steady state wave field, the simulation duration is 180 s with a time step $\Delta t = 0.0125$ s.

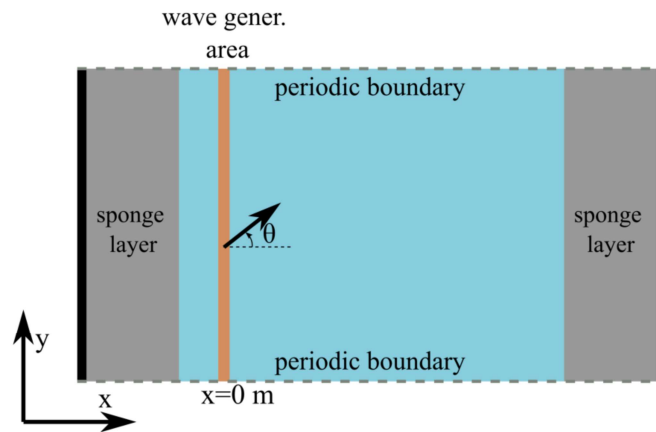


Figure 5.15: Definition sketch for the case of one internal wave generators at $x = 0$ m.

Figures 5.16 and 5.17 present comparisons between the computed normalised water surface elevation η/η_0 at $t = 40T$ and the corresponding analytical solution. It is observed that the computed solution coincides with the analytical solution except for the region of the sponge layers.

Additionally, the performance of the proposed internal wave generation method for handling incoming oblique waves, that are propagating in a numerical basin with constant depth by using two internal wave generation areas (Figure 5.18), is also examined. In this case, the numerical basin is 210 m long in x -direction, 60 m wide in y -direction and 1 m deep. The internal wave generation areas are parallel to the y -axis and are positioned at a distance of 75 m from the left and right boundaries ($x = 0$ m and $x = 60$ m). Sponge layers are placed behind the wave generation areas with a width of 60 m, while periodic conditions are applied at the top and bottom boundaries of the computational domain.

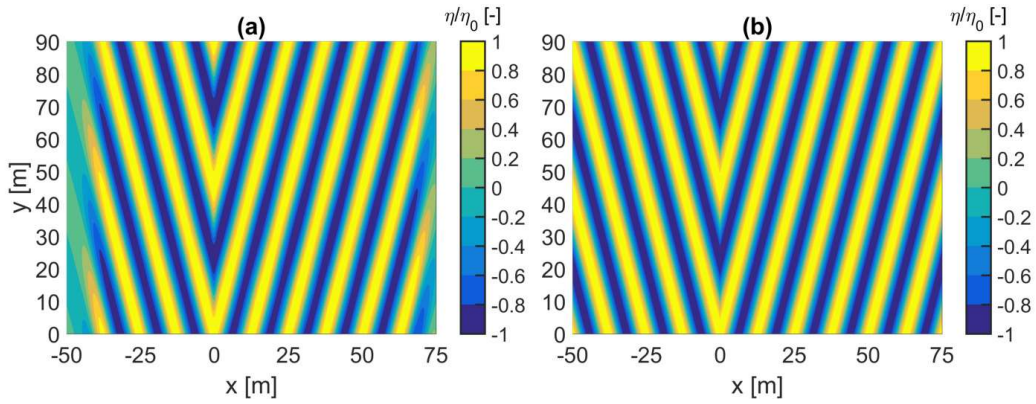


Figure 5.16: Comparison between (a) computed and (b) target normalised water surface elevation η/η_0 at $t = 40T$ for the case of oblique linear waves ($H = 0.01$ m, $T = 4.0$ s, $d = 1.0$ m and $\theta = 15^\circ$) with a sponge layer at the left and right boundaries and periodic boundaries at y -direction.

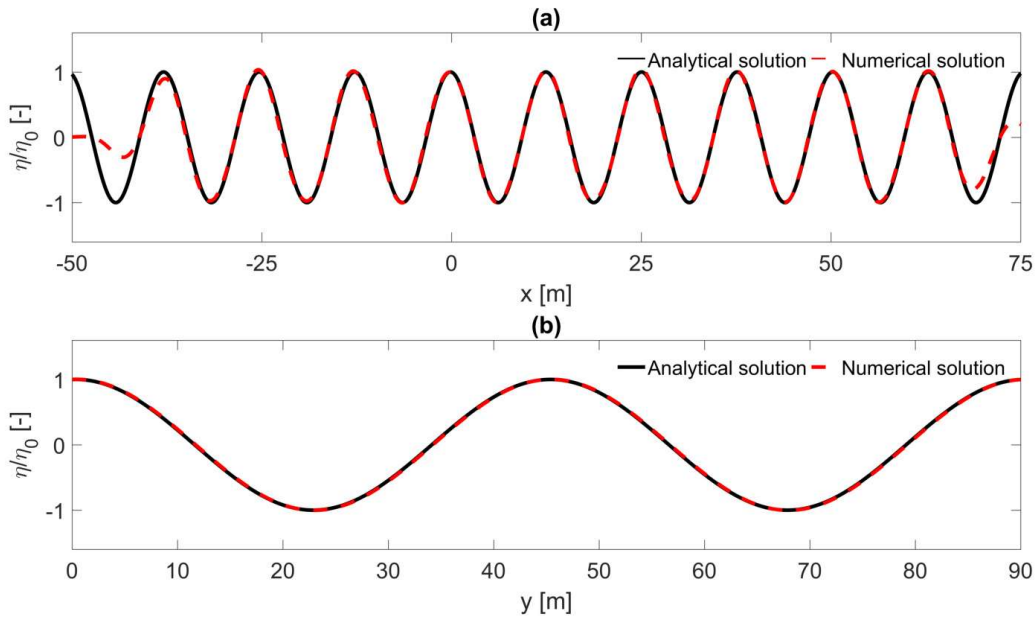


Figure 5.17: Comparison between computed (dashed line) and target (solid line) normalised water surface elevation η/η_0 at $t = 40T$ for the case of oblique linear waves ($H = 0.01$ m, $T = 4.0$ s, $d = 1.0$ m and $\theta = 15^\circ$): (a) cross section at $y = 45$ m, (b) cross section at $x = 0$ m.

The target waves at both internal wave generation areas have a height of $H = 0.01$ m, a period of $T = 4.0$ s and a dimensionless depth of $kd = 0.52$. One vertical layer is applied since the error is smaller than 3% for $kd \leq 0.55$ in case of one layer (Figure 5.3, Table 5.1). Two different wave propagation angle combinations are examined, one with $\theta_1 = 15^\circ$, $\theta_2 = 195^\circ$ and one with $\theta_1 = 15^\circ$, $\theta_2 = 165^\circ$ where the subscripts 1 and 2 stand for the left ($x = 0$ m) and the right ($x = 60$ m) internal wave generators, respectively. The grid resolution and time

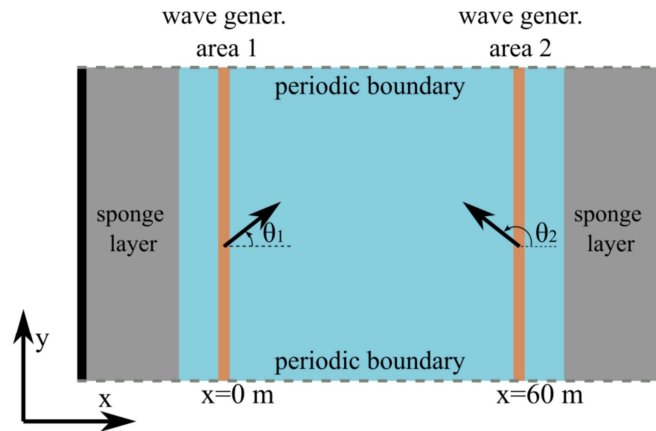


Figure 5.18: Definition sketch for the case of two internal wave generators at $x = 0$ m and $x = 60$ m.

step are the same as in the previous case ($\Delta x = \Delta y = 0.15$ m, $\Delta t = 0.0125$ s), while a duration of 120 s is considered, targeting a steady state wave field.

The computed wave field (normalised water surface elevation η/η_0) is compared with the corresponding analytical solution at $t = 30T$, in Figure 5.19 and Figure 5.20.

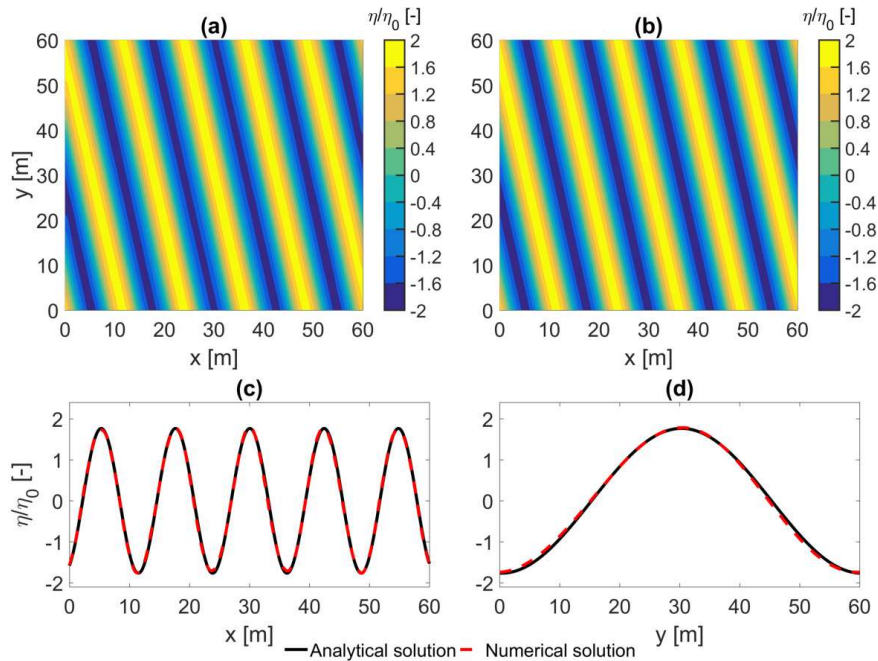


Figure 5.19: Comparison between (a) computed and (b) analytical normalised water surface elevation η/η_0 at $t = 30T$ for $\theta_1 = 15^\circ$, $\theta_2 = 195^\circ$:(c) cross section at $y = 35$ m (d) cross section at $x = 18$ m.

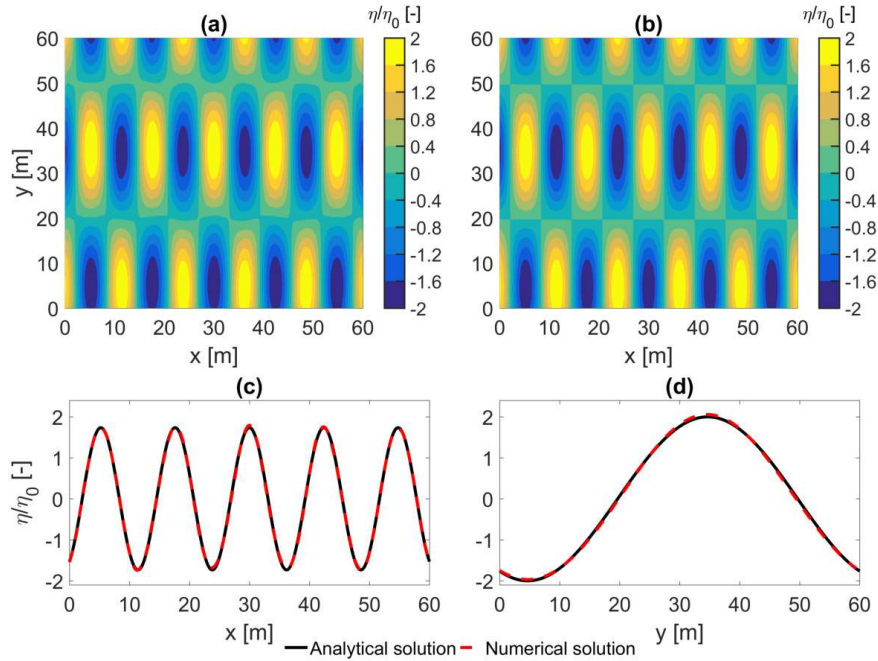


Figure 5.20: Comparison between (a) computed and (b) analytical normalised water surface elevation η/η_0 at $t = 30T$ for $\theta_1 = 15^\circ$, $\theta_2 = 165^\circ$:(c) cross section at $y = 35$ m (d) cross section at $x = 18$ m.

The computed solution agrees very well with the analytical one in the whole domain for both wave propagation angle combinations. The excellent agreement indicates that the internal wave generation is able to generate oblique waves and that oblique waves can pass through the wave generation area without any distortion.

It has to be mentioned that an internal wave generation area parallel to y -axis is not able to generate a wave which propagates along y -axis. For that reason, in case that the target incident wave forms an angle between -10° and 10° with the y -axis, an internal wave generation area parallel to x -axis should be applied. In addition, an L-shape wave generation layout can be used to generate oblique waves. According to this layout, two internal wave generations areas with sponge layers behind them are applied, one parallel to the y -axis and one parallel to the x -axis of the numerical domain. However, it has been shown in Chapter 3 that this layout leads to wave diffraction patterns inside the numerical domain, caused by the two wave generation areas intersecting with each other and interacting with the lateral sponge layers, and thus periodic lateral boundaries are preferred in order to avoid such diffractions.

5.4.5 Irregular short-crested waves in a numerical basin with constant depth

In this section, a test case of short-crested waves is considered, in which the target wave frequency spectrum is a JONSWAP spectrum, with a significant wave height $H_s = 0.5$ m, a peak wave period $T_p = 12.0$ s and a dimensionless depth $kd = 0.48$

for the peak frequency. The frequency range is defined between $0.5f_p$ and $3f_p$ and the peak enhancement factor is $\gamma = 3.3$. Two cases with spreading standard deviation $\sigma_\theta = 10^\circ$ (swell waves) and $\sigma_\theta = 30^\circ$ (wind waves) are examined (Table 5.5).

Table 5.5: Wave conditions of the examined irregular short-crested waves.

Significant Wave Height H_s [m]	Peak Period T_p [s]	Peak Enhancement Factor γ [-]	Spreading Standard Deviation, σ_θ [°]
0.50	12.0	3.3	10
0.50	12.0	3.3	30

The numerical basin is 1500 m long, 500 m wide and 7.6 m deep (Figure 5.21). Sponge layers are placed at the right and left boundaries with a width determined by the peak wave length, while periodic conditions are applied at the top and bottom boundaries of the computational domain. The highest frequency ($3f_p$) and the lowest frequency ($0.5f_p$) are used to define the grid cell size and the initial time step Δt , respectively.

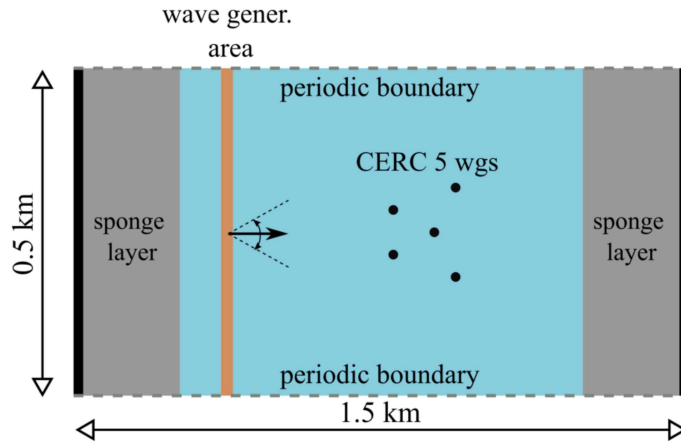


Figure 5.21: Definition sketch of the implemented numerical set-up for the study of short-crested waves.

Additionally, the following directional spreading function is employed (Frigaard et al., 1997):

$$D(f, \theta) = \frac{1}{\sqrt{\pi}} \frac{\Gamma(s_1 + 1)}{\Gamma(s_1 + \frac{1}{2})} \cos^{2s_1}(\theta - \theta_0), \quad -\frac{\pi}{2} < \theta - \theta_0 < \frac{\pi}{2} \quad (5.38)$$

where s_1 is the directional spreading parameter, Γ is the Gamma function, and θ_0 is the wave propagation angle.

The relation between the directional spreading parameter, s_1 , and the spreading

standard deviation, σ_θ , is given by (see Section 3.3.3 for derivation):

$$\sigma_\theta = \sqrt{2 - \frac{2\Gamma^2(s_1 + 1)}{\Gamma(s_1 + \frac{1}{2})\Gamma(s_1 + \frac{3}{2})}} \quad (5.39)$$

The duration of the simulations is 3 hrs with a time step $\Delta t = 0.05$ s, while the wave synthesis method proposed by Sand and Mynett (1987) has been employed.

A group of 5 wave gauges (WGs) measuring the surface elevations has been positioned in the center of the computational domain, following the configuration ‘‘CERC 5’’ (Figure 5.21) proposed by Borgman and Panicker (1970). The measured time series of surface elevations are used to calculate the frequency spectra and the normalised spreading function distributions, which are compared with the analytical solution in Figure 5.22 for spreading standard deviation $\sigma_\theta = 10^\circ$ and $\sigma_\theta = 30^\circ$.

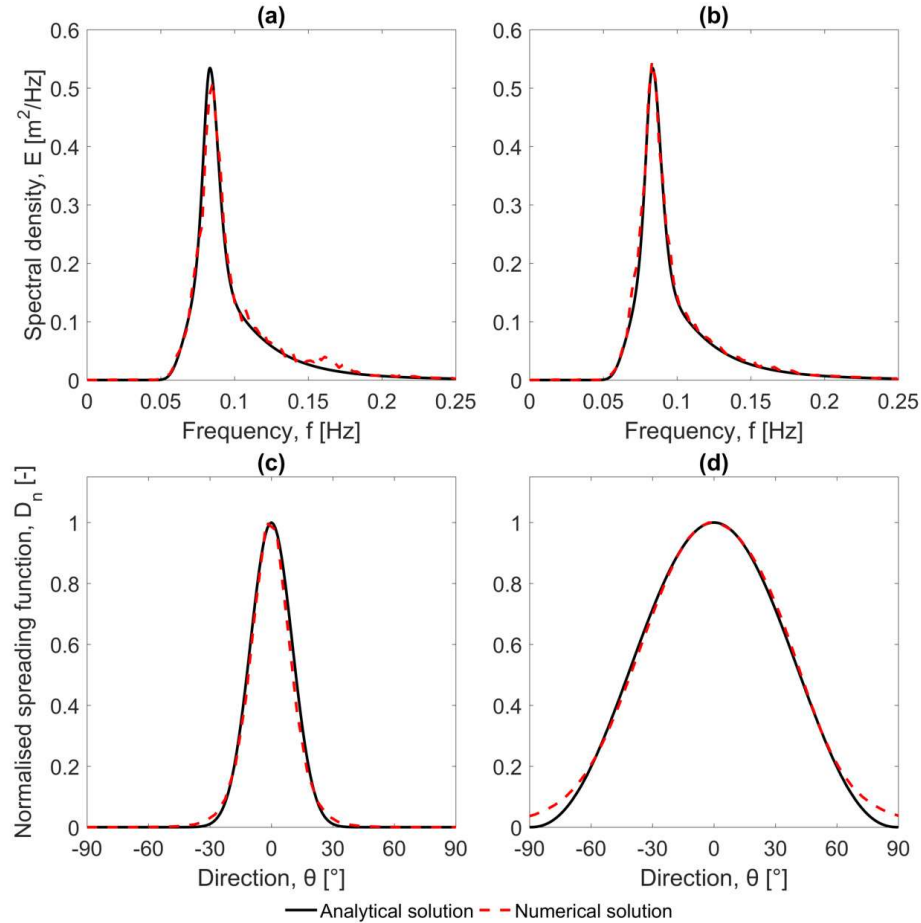


Figure 5.22: The frequency spectra (top panels) and the normalised spreading function distributions (bottom panels) resulting from the use of method 3 (red dashed line), compared with the analytical solution (black solid line) for irregular short-crested waves with spreading standard deviation σ_θ of (a,c) 10° and (b,d) 30° .

The agreement with the analytical solution for both cases is very good indicating that the proposed internal wave generation method (method 3) is capable

of generating accurately the target short-crested wave field. A mismatch between the calculated and the analytical frequency spectra for $\sigma_\theta = 10^\circ$ (Figure 5.22a) is observed in the frequency range of 0.15 Hz to 0.18 Hz, where the model slightly overestimates the spectral density. This mismatch could be due to the position of the wave gauges with respect to the wave generation area or due to a small reflection from the sponge layers. However, this overestimation is not observed in the case of $\sigma_\theta = 30^\circ$ (Figure 5.22b).

5.5 Validation with experimental data

The developed model with the addition of the internal wave generation method is also validated against experimental data. Three benchmark experimental tests have been used: 1) propagation of regular waves over a shoal resting on a plane sloping seabed (Berkhoff et al., 1982), 2) propagation of irregular long- and short-crested waves over a shoal (Vincent and Briggs, 1989) and 3) wave diffraction around a vertical wall (Briggs et al., 1995). Finally, a comparison is carried out between the performance of the newly developed internal wave generation (method 3) in non-hydrostatic models and the traditional weakly reflective wave generation (method 1) for the third benchmark test where oblique and dispersive waves are reflected back to the numerical boundary due to the presence of the vertical wall.

5.5.1 Numerical validation using the Berkhoff shoal experiment

The experiment conducted by Berkhoff et al. (1982) has served as a standard test case for validating phase-resolving wave models, since it combines wave refraction, shoaling and diffraction. The bathymetry of the experimental setup consists of an elliptic shoal resting on a plane sloping seabed and the entire slope is turned at an angle of 20° with respect to the x-axis (Figure 5.23a). Detailed information on the geometry can be found in Berkhoff et al. (1982). The numerical basin is 45 m long ($-20 < y < 25$) and 20 m wide ($-10 < x < 10$). The internal wave generator is parallel to the x-axis and is positioned at a distance of 10 m ($y = -10$ m) from the bottom boundary. The remaining numerical domain includes two sidewalls at $x = -10$ m and $x = 10$ m and two sponge layers at $y = -15$ m and $y = 20$ m with a width of 5 m.

The wave height is $H = 0.0464$ m, the wave period is $T = 1$ s and the water depth at the position of the internal wave generator is $d = 0.45$ m. These wave conditions give a dimensionless depth of $kd = 1.9$ and thus two equidistant vertical layers are applied. The model runs for 50 s without any stability issues since the reflected waves that are reaching the offshore boundary are absorbed by the sponge layer, which is positioned behind the internal wave generator. The model is applied with a grid cell size of $\Delta x = \Delta y = 0.05$ m, while the time step is automatically adjusted during the simulation depending on the CFL (Courant–Friedrichs–Lewy) condition where a maximum CFL value of 0.5 is used.

Figure 5.23b shows the plan view of the normalised wave height H/H_0 (where

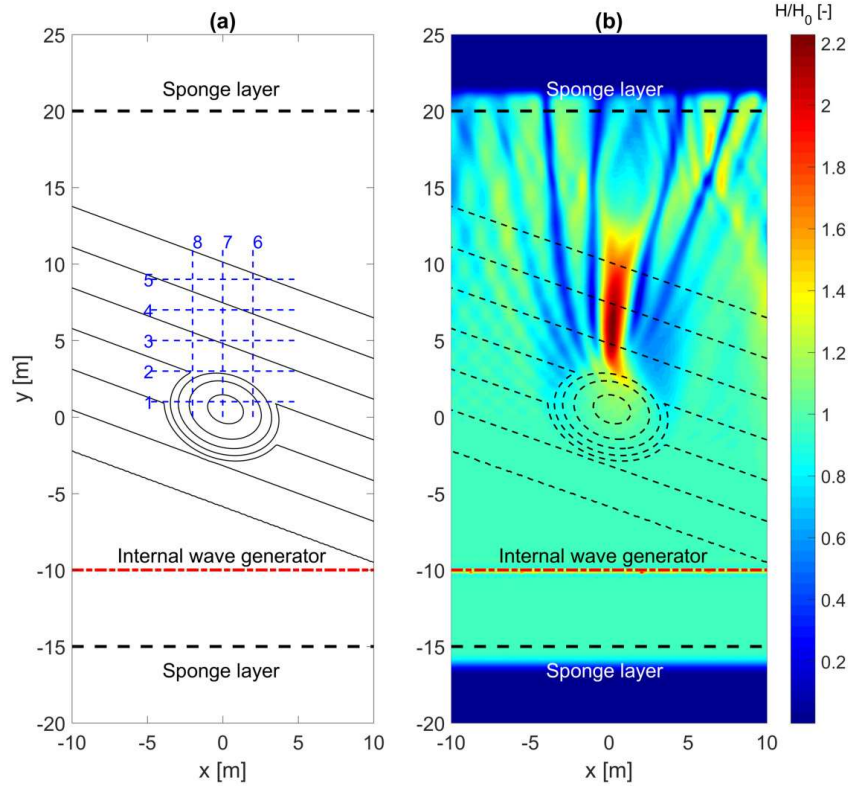


Figure 5.23: (a) The experimental setup as introduced in the numerical domain in SWASH, (b) Normalised wave height H/H_0 in the whole computational domain for the experiment of Berkhoff et al. (1982).

H is the local wave height and H_0 is the wave height at the wave generation boundary) in the whole computational domain where the diffraction and refraction patterns of the waves are visible. The wave heights of the model are obtained by averaging those of the last ten wave periods of the simulation (from $t = 40$ s to $t = 50$ s).

Figure 5.24 shows the comparison of normalised wave heights H/H_0 between numerical model results (red lines) and experimental data (black circles) along eight measurement transects (see Figure 5.23a) near the shoal. Additionally, in order to evaluate the model, the root mean square error (RMSE) and the Skill factor for the normalised wave heights of each section are calculated as:

$$RMSE = \sqrt{\frac{\sum_{i=1}^N (P_i - O_i)^2}{N}} \quad (5.40)$$

$$Skill = 1 - \sqrt{\frac{\sum_{i=1}^N (P_i - O_i)^2}{\sum_{i=1}^N O_i^2}} \quad (5.41)$$

where O and P indicate the observed and predicted values, respectively. Very

good agreement between the numerical model and the experimental model is observed (Figure 5.24 and Table 5.6). The wave focusing behind the shoal and the combined effects of refraction and diffraction (Figure 5.25) are accurately described by the model, which indicates that the internal wave generation method is capable of generating the target dispersive waves ($kd = 1.9$ at the internal wave generator).

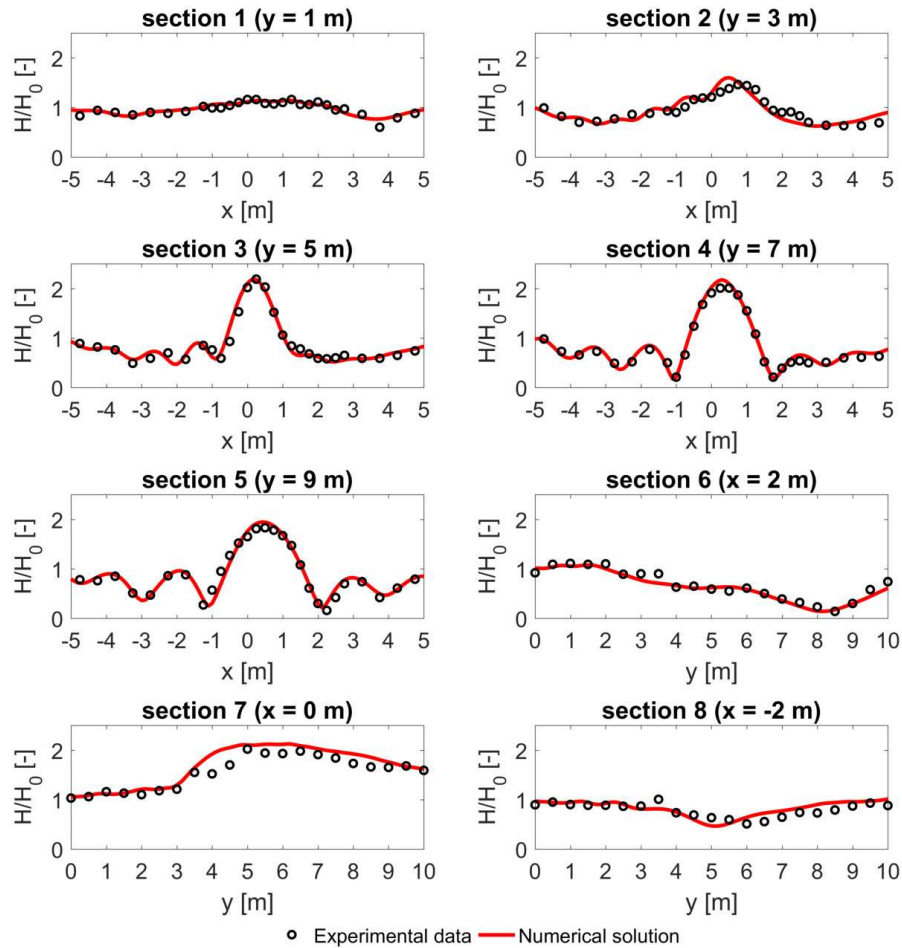


Figure 5.24: Comparison of normalised wave heights H/H_0 between numerical model results (red solid lines) and experimental data (black circles) along different measurement transects.

Table 5.6: Root mean square error (RMSE) and Skill factor of the normalised wave heights for each section.

Section	1	2	3	4	5	6	7	8
RMSE	0.056	0.116	0.102	0.074	0.103	0.082	0.157	0.108
Skill	0.944	0.884	0.901	0.929	0.902	0.889	0.901	0.865

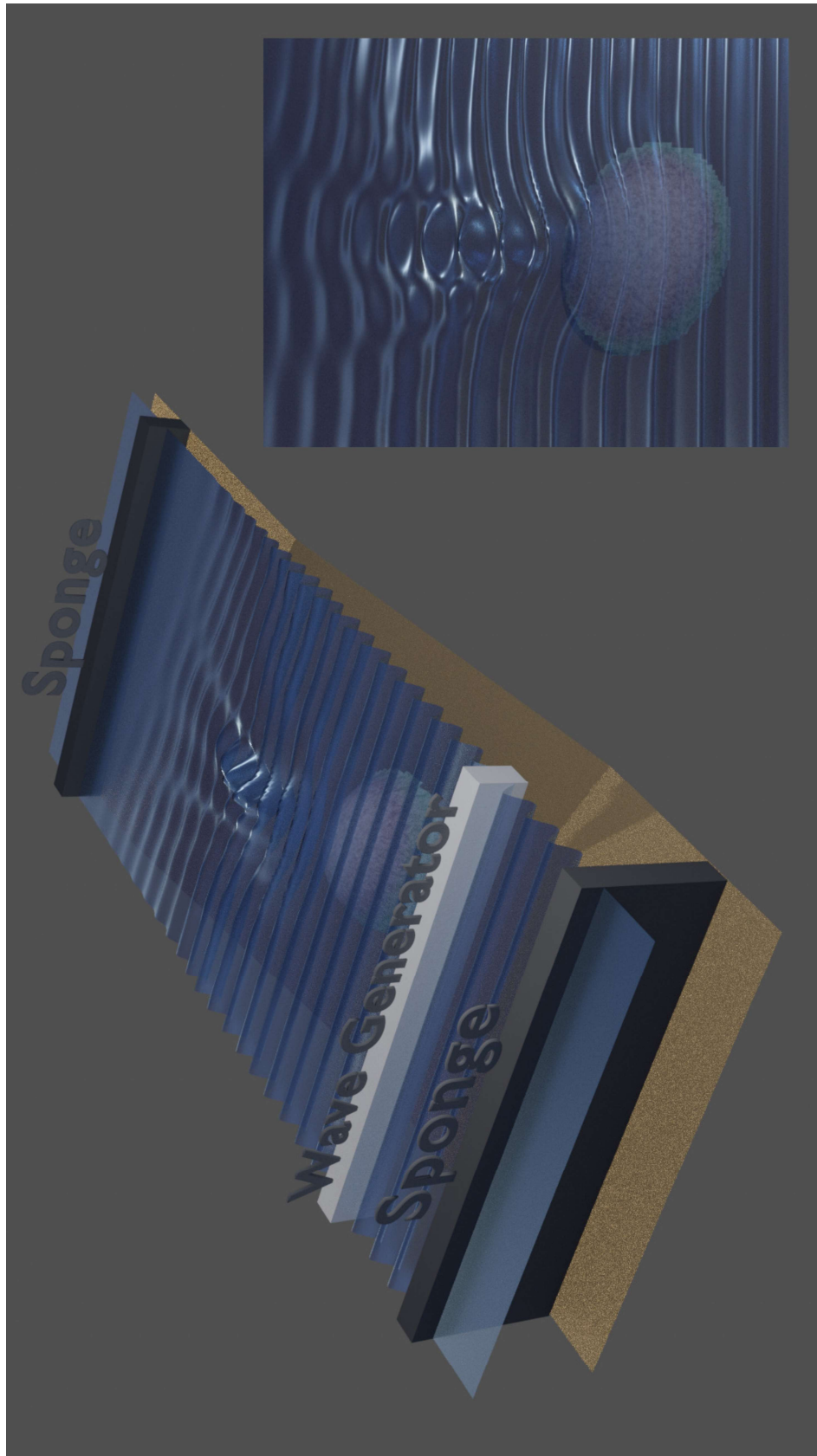


Figure 5.25: 3D visualisation of regular waves propagating over the Berkhoff shoal.

5.5.2 Numerical validation using the Vincent and Briggs shoal experiment

In this section, a three-dimensional (3D) version of the developed model with the internal wave generation, method 3, is applied to study regular and irregular long- and short-crested waves propagating over an elliptic shoal. The experiment that was carried out by Vincent and Briggs (1989) has been repeatedly used as a standard test case for validating wave propagation models (Section 3.4) and hence it is used here for validation purposes of the present numerical model. It has to be mentioned that only the internal wave generation method is examined for this experimental layout, since there are no waves that are reflected back to the numerical wave generation boundary, and thus a similar behavior is to be expected when using the weakly reflective wave generation method (method 1).

The bathymetry of the experimental setup of Vincent and Briggs (1989) as implemented in SWASH is illustrated in Figure 5.26 and is defined as:

$$\left(\frac{x}{3.05}\right)^2 + \left(\frac{y}{3.96}\right)^2 = 1 \quad (5.42)$$

$$d_e = -0.4572 + 0.7620\sqrt{1 - \left(\frac{x}{3.81}\right)^2 - \left(\frac{y}{4.95}\right)^2} \quad (5.43)$$

where x and y are the coordinates with $x = y = 0$ at the center of the shoal and d_e is the bed level inside the shoal area.

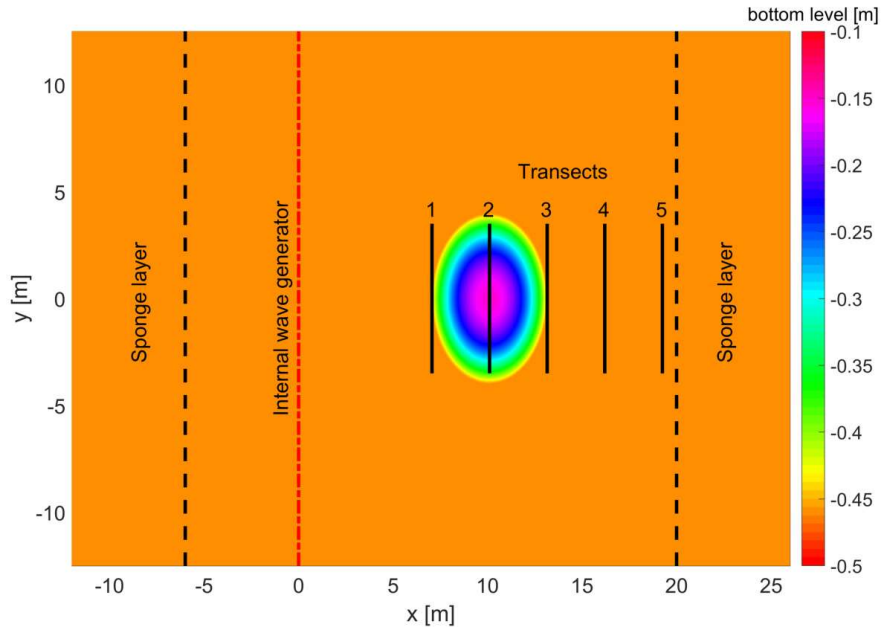


Figure 5.26: Bottom levels of the experimental setup of Vincent and Briggs (1989) experiment as introduced in the numerical domain in SWASH.

The shoal geometry follows the one used in the experiments of Berkhoff et al.

(1982), but with a flat bottom ($d = 45.72$ cm) outside the shoal area.

In total 9 numerical test cases are executed including breaking and non-breaking waves of the following types: regular waves, irregular long- and short-crested waves. The numerical and experimental input parameters for all the test series are listed in Table 5.7. The dimensionless depth is $kd = 1.27$ for the peak frequency and thus two equidistant vertical layers are applied. A uniform grid resolution of $\Delta x = \Delta y = 0.05$ m is used, while an automatic time step control is applied based on the CFL condition.

The target frequency spectrum is a TMA spectrum (Bouws et al., 1985) in all the irregular test cases where broad ($\gamma = 2$) and narrow ($\gamma = 20$) frequency spectra are examined. Additionally, the above spectra are combined with standard deviation $\sigma_\theta = 10^\circ$ (narrow directional spreading) and $\sigma_\theta = 30^\circ$ (broad directional spreading). The wave heights of the numerical model are obtained by sampling the surface elevation for 36.4 s and 260 s for the regular and irregular cases, respectively, similar to the experiment.

Table 5.7: Numerical input wave conditions based on the Vincent and Briggs (1989) experimental wave conditions.

Test Case ID	(Peak) Period T, T_p [s]	(Significant) Wave Height H, H_s [cm]	Phillips Constant α [-]	Peak Enhancement Factor, γ [-]	Spreading Standard Deviation, σ_θ [°]
M1	1.3	2.54	-	-	-
U3	1.3	2.54	0.00155	2	0
N3	1.3	2.54	0.00155	2	10
B3	1.3	2.54	0.00155	2	30
U4	1.3	2.54	0.00047	20	0
N4	1.3	2.54	0.00047	20	10
B4	1.3	2.54	0.00047	20	30
N5	1.3	19.0	0.02620	20	10
B5	1.3	19.0	0.08650	2	30

In Figure 5.27 the resulted normalised wave heights H/H_0 of the numerical model (red lines) are compared with the experimental data (black circles) along five measurement transects (shown in Figure 5.26) for the case of regular waves (test case M1). As it is observed, the numerical and the experimental data show a very good agreement.

The normalised wave heights along transect 4 for the cases of irregular non-breaking and breaking waves are presented in Figures 5.28 and 5.29, respectively.

SWASH correctly predicts the wave focusing due to the presence of the shoal for the case of non-breaking waves (Figure 5.30). The broad and narrow frequency spectra, test case U3 and U4 respectively, give a maximum normalised wave height at $y = 0$ with a value around 2.0. On the other hand, in test cases with directional spreading (test cases N3, B3, N4 and B4) it is noticed that the influence of the shoal on the resulted wave field is reduced.

For the case of breaking waves a reduction of the normalised wave height behind the shoal is observed. This is happening due to the wave induced current (Figure

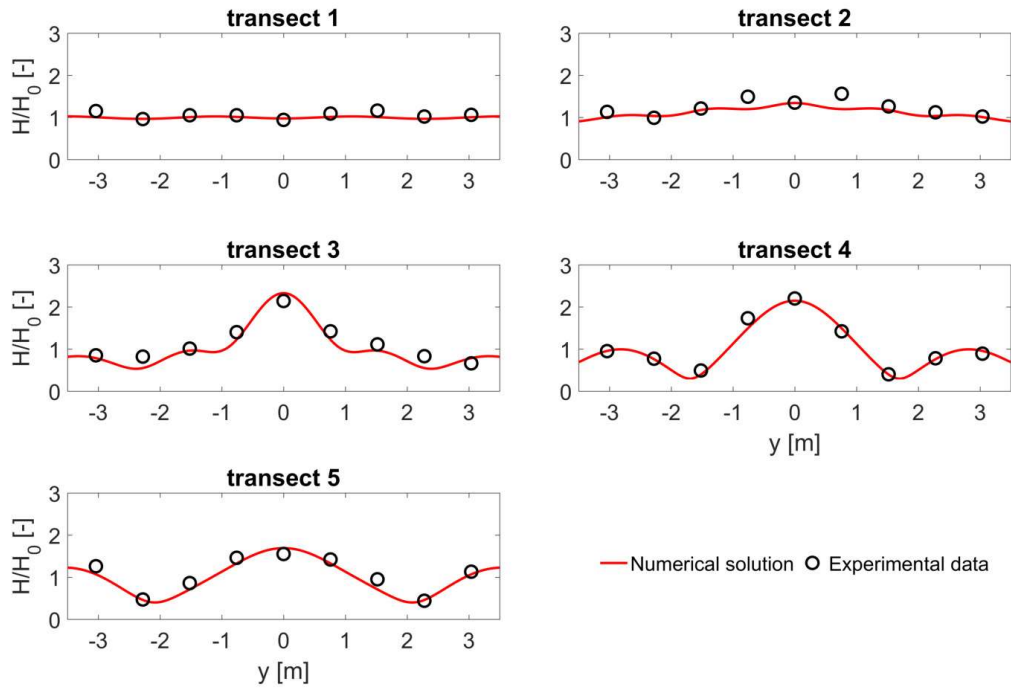


Figure 5.27: Comparison of normalised wave heights H/H_0 between numerical model results (red solid lines) and experimental data (black circles) along different measurement transects for test case M1.

5.29) which defocuses wave rays behind the shoal. Choi et al. (2009) proved that numerical models that neglect the effect of wave induced current are not able to predict the aforementioned physical process.

As in the previous section (Section 5.5.1), the root mean square error (Equation 5.40) and the Skill factor (Equation 5.41) are utilised for each test case in order to evaluate the model capability to predict the normalised wave heights. The small error and the high skill factor (Table 5.8) indicate that the model is able to correctly predict the transformation of waves propagating over a shoal.

Table 5.8: Root mean square error (RMSE) and Skill factor of the normalised wave heights for each test case.

Test Case ID	U3	N3	B3	U4	N4	B4	N5	B5
RMSE	0.073	0.070	0.060	0.060	0.044	0.069	0.024	0.033
Skill	0.933	0.935	0.943	0.948	0.960	0.925	0.970	0.956

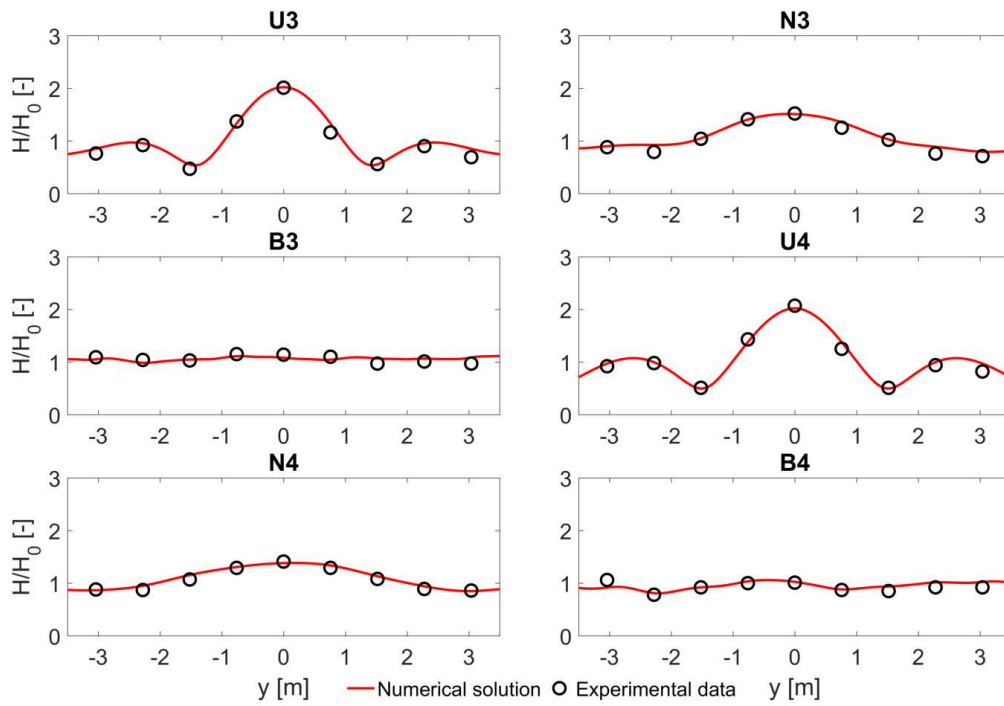


Figure 5.28: Comparison of normalised wave heights H/H_0 between numerical model results (red solid lines) and experimental data (black circles) along transect 4 for non-breaking irregular waves.

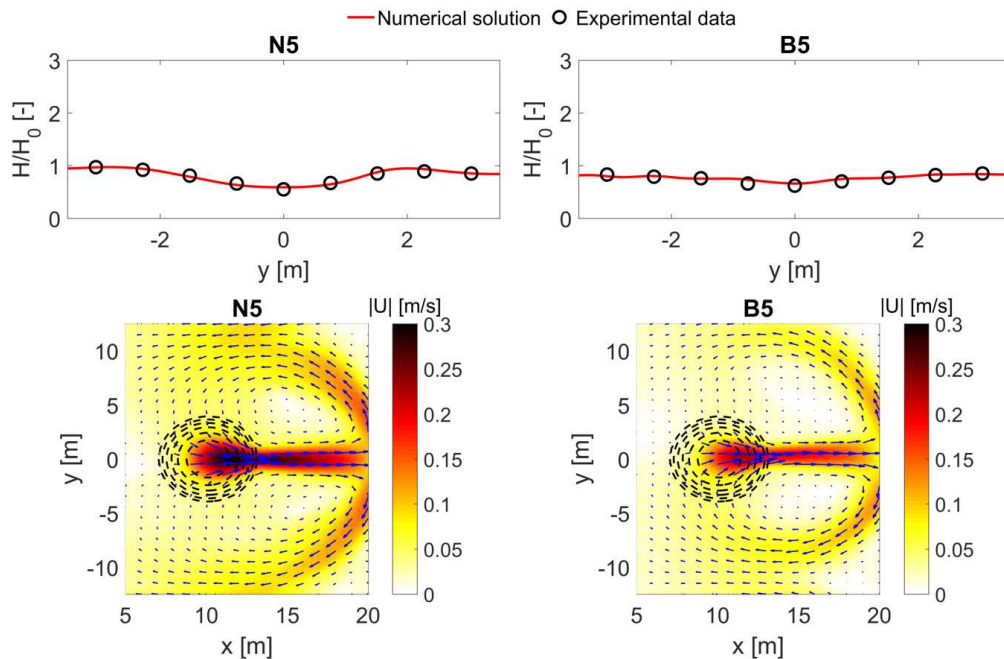


Figure 5.29: Normalised wave heights H/H_0 along transect 4 and wave-induced currents for breaking irregular waves.

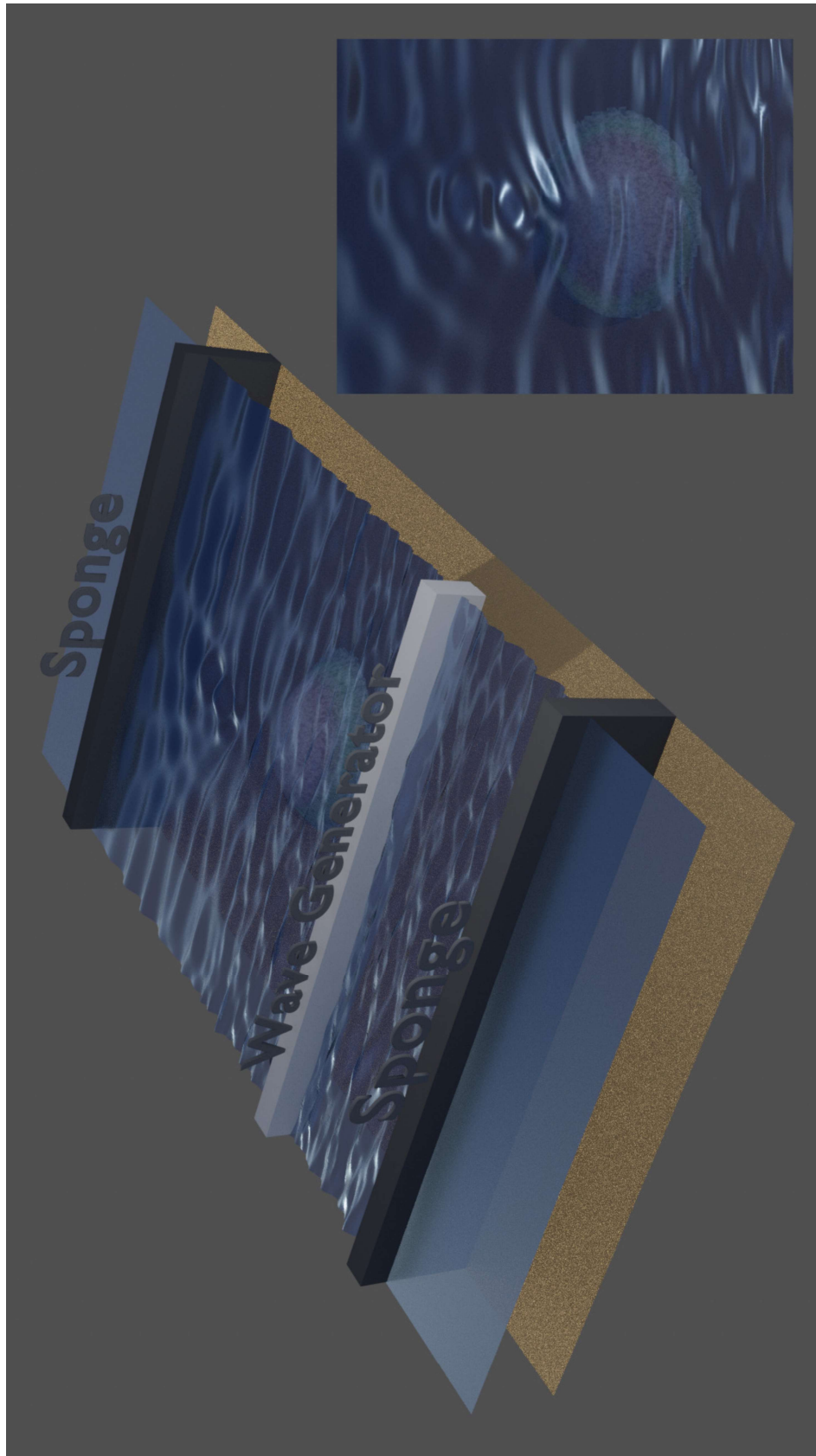


Figure 5.30: 3D visualisation of short-crested waves propagating over the shoal of Vincent and Briggs (1989) experiment (test case N3).

5.5.3 Wave diffraction around a vertical wall

Finally, to verify the added value of the internal wave generation (method 3) in comparison with the weakly reflective wave generation boundary (method 1), simulations are conducted for regular and irregular waves diffracting around a breakwater. In this way, the two different wave generation methods will be evaluated for the case that oblique waves propagate back towards the generation area. The experiment of Briggs et al. (1995), where waves diffract around an impermeable vertical wall, is used here to validate the developed model.

The experimental setup consists of a vertical, rigid and thin wall which is positioned parallel to the wave paddles, extending from the centerline to the side wall of the basin. The bottom of the basin is flat with a still water depth of $d = 45.72$ cm, while wave absorber material is piled on the seaward side of the wall to minimize reflections. Detailed information on the experimental setup and results can be found in Briggs et al. (1995), where additionally, it is shown that the experimental results compared well with the theoretical methods for estimating diffraction.

The numerical basin is 46 m long ($-24 \leq x \leq 22$) and 25 m wide ($-12.5 \leq y \leq 12.5$). The internal wave generation area is parallel to the y -axis and is placed at a distance of 8 m ($x = -8$ m) from the vertical wall ($x = 0$ m). Closed lateral boundaries are used at $y = -12.5$ m and $y = 12.5$ m and sponge layers with a width of 10 m are placed at $x = -14$ m and $x = 12$ m. In Figure 5.31 the experimental setup as introduced in the numerical domain in SWASH is presented.

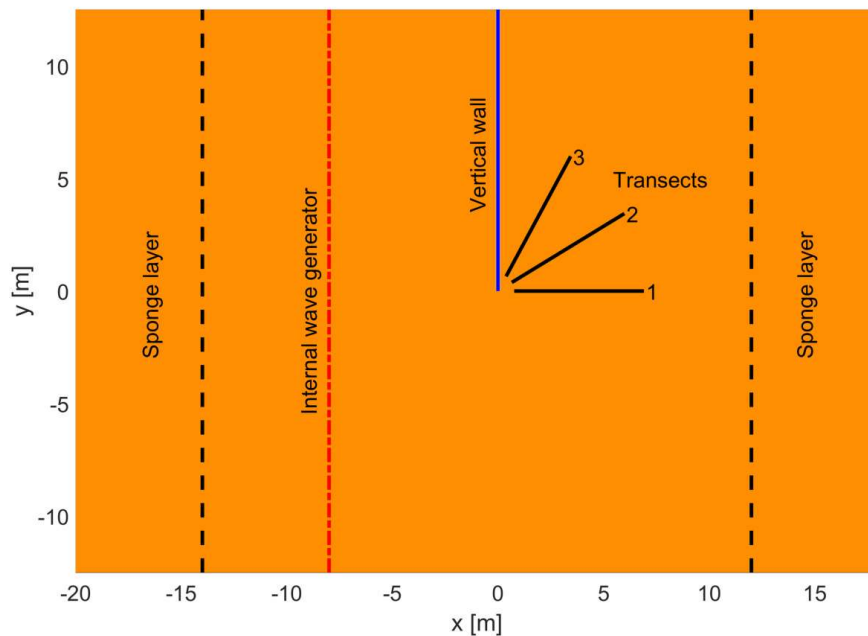


Figure 5.31: Experimental setup of Briggs et al. (1995) as introduced in the numerical domain in SWASH.

In total 6 numerical test cases are conducted: two with regular waves and four with irregular short-crested waves. The target wave characteristics are similar to those in Section 5.5.2 and are listed in Table 5.9. The dimensionless depth

is $kd = 1.27$ for the peak frequency and thus two equidistant vertical layers are applied. The wave heights of the numerical model are obtained by sampling the surface elevation for 36.4 s and 260 s for the regular and irregular cases, respectively, along three measurement transects (Figure 5.31) that are forming an angle of 90° (transect 1), 60° (transect 2) and 30° (transect 3) with the wall tip. A uniform grid resolution of $\Delta x = \Delta y = 0.05$ m is used, while an automatic time step control is applied based on the CFL condition.

Table 5.9: Numerical input wave conditions based on the Briggs et al. (1995) experimental wave conditions.

Test Case ID	(Peak) Period T, T_p [s]	(Significant) Wave Height H, H_s [cm]	Phillips Constant α [-]	Peak Enhancement Factor, γ [-]	Spreading Standard Deviation, σ_θ [°]
M1	1.3	5.50	-	-	-
M4	1.3	7.75	-	-	-
N1	1.3	7.75	0.0144	2	10
N2	1.3	7.75	0.0044	20	10
B1	1.3	7.75	0.0144	2	30
B2	1.3	7.75	0.0044	20	30

In Figures 5.32-5.37, comparisons of diffraction coefficients between numerical model results (red plus signs) and experimental data (black circles) for all test cases are presented. The diffraction coefficient K_d (K_{ds} for irregular) is computed as the ratio of the diffracted wave height H_d (H_{ds} for irregular) to the incident wave height H_i (H_s for irregular). The x-axis corresponds to the distance from the wall tip, normalised by the wave length ($L = L_p = 2.25$ m). In general, the agreement is very good between the numerical model and experimental results. The largest deviation is observed for the case of the regular waves (M1, M4), where the numerical model underpredicts the diffraction coefficients along measurement transect 3. On the other hand, the numerical model matches the observed values for the case of irregular short-crested waves very well along all the measurement transects. In addition, it is observed that the wave penetration is greater for the case of the broad directional spreading distribution ($\sigma_\theta = 30^\circ$), while the directional spreading affects the diffraction coefficients more rather than the frequency spreading.

Furthermore, the weakly reflective wave generation (method 1) has been used to simulate the above wave conditions. The numerical set up is the same as in the case with method 3, apart from the fact that the length of the domain is smaller ($-8 \leq x \leq 22$) since no sponge layer is used behind the generation line. Figure 5.38 presents a comparison between the performance of the internal wave generation (method 3, red plus signs) and the weakly reflective generation (method 1, blue circles) for predicting the diffraction coefficients observed by Briggs et al. (1995) experiment. To calculate the diffraction coefficient the generated wave height at the location of the tip of the wall in case of an empty basin (without the wall) has been used as incident wave height. In this way, the deficiency of the weakly reflective generation boundary to generate precisely the target wave height,

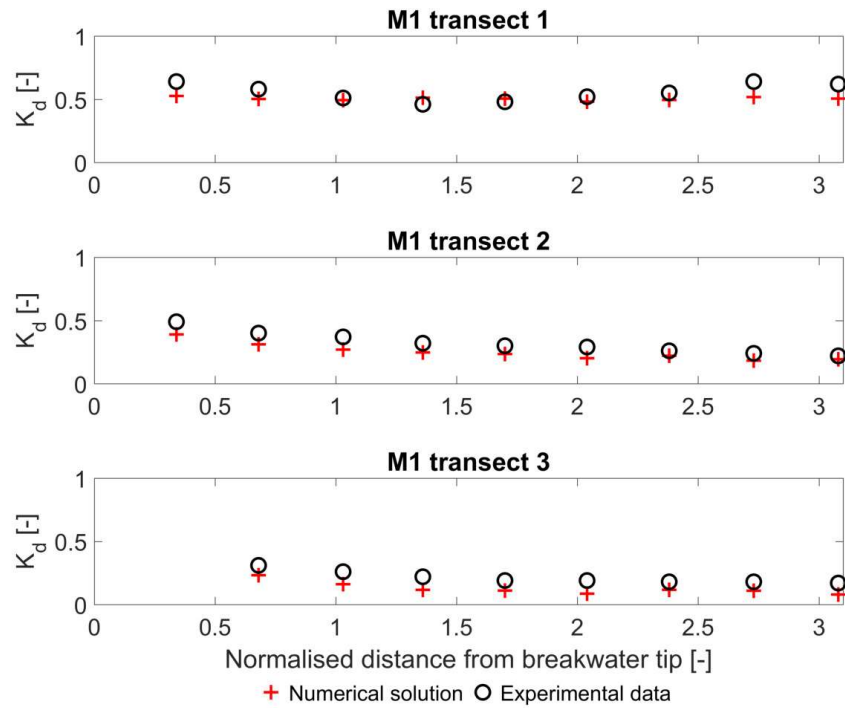


Figure 5.32: Comparison of diffraction coefficients between numerical model results (red plus signs) and experimental data (black circles) for test case M1.

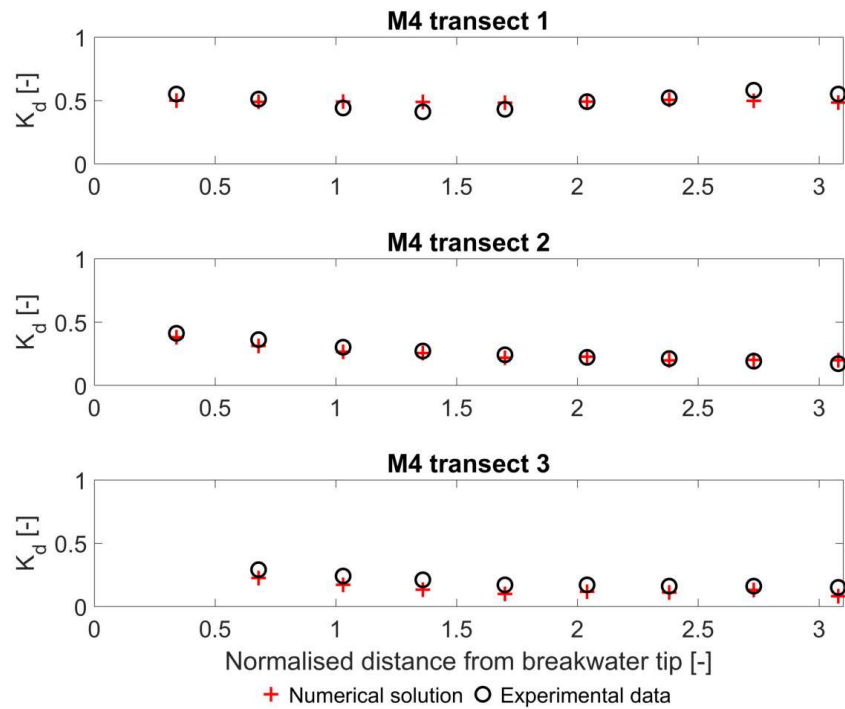


Figure 5.33: Comparison of diffraction coefficients between numerical model results (red plus signs) and experimental data (black circles) for test case M4.

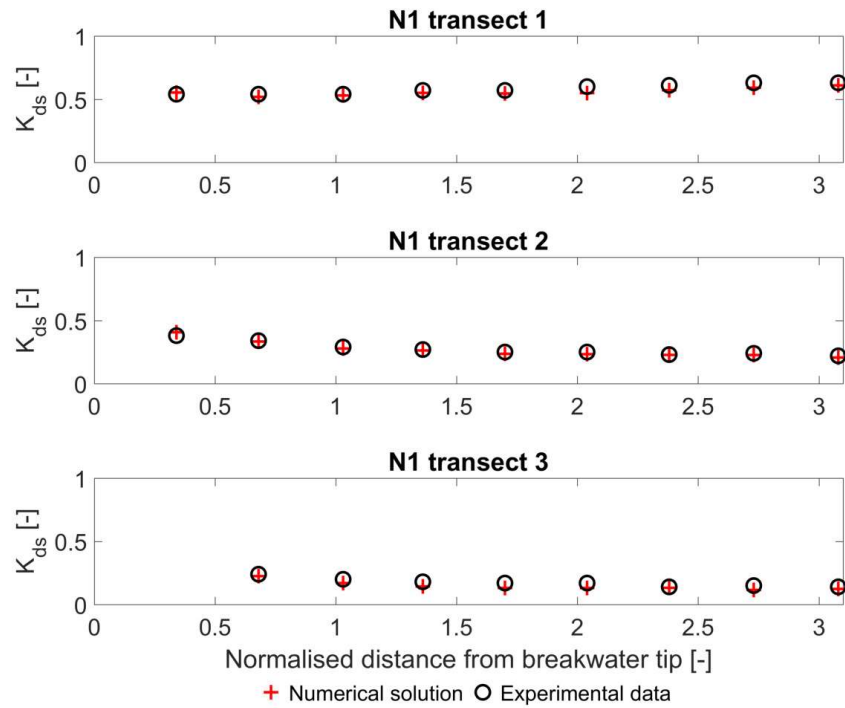


Figure 5.34: Comparison of diffraction coefficients between numerical model results (red plus signs) and experimental data (black circles) for test case N1.

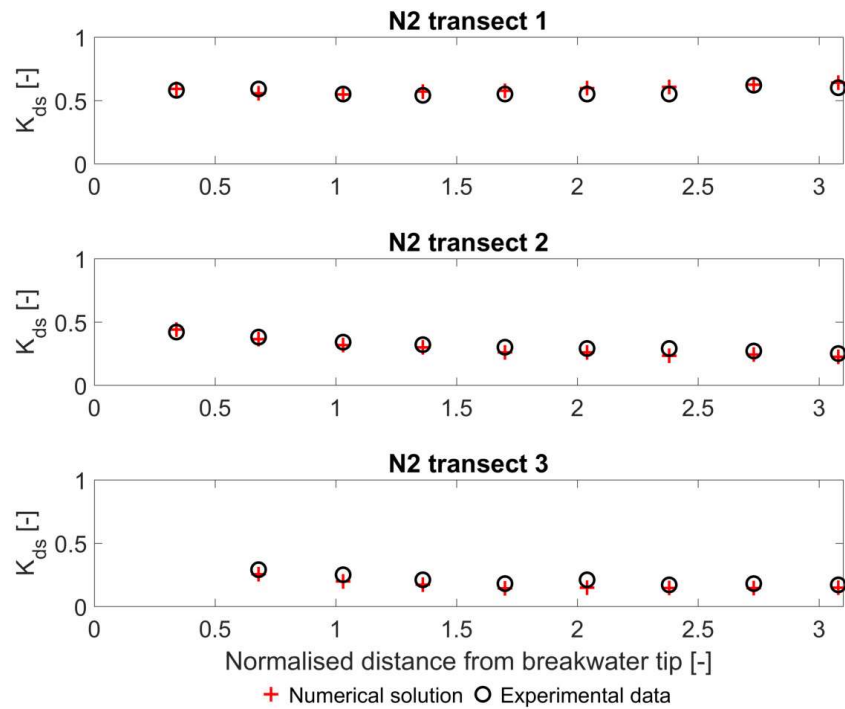


Figure 5.35: Comparison of diffraction coefficients between numerical model results (red plus signs) and experimental data (black circles) for test case N2.

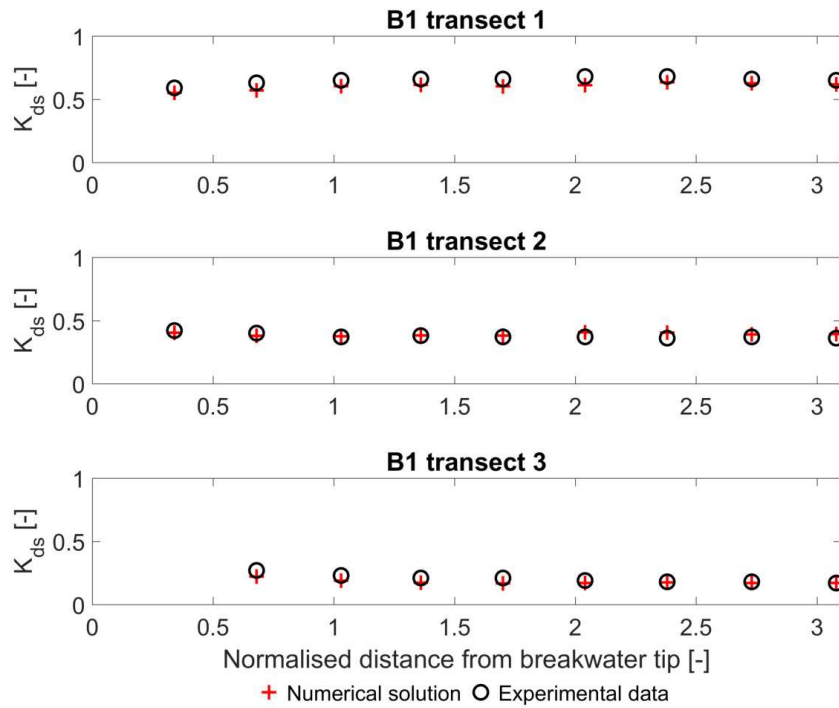


Figure 5.36: Comparison of diffraction coefficients between numerical model results (red plus signs) and experimental data (black circles) for test case B1.

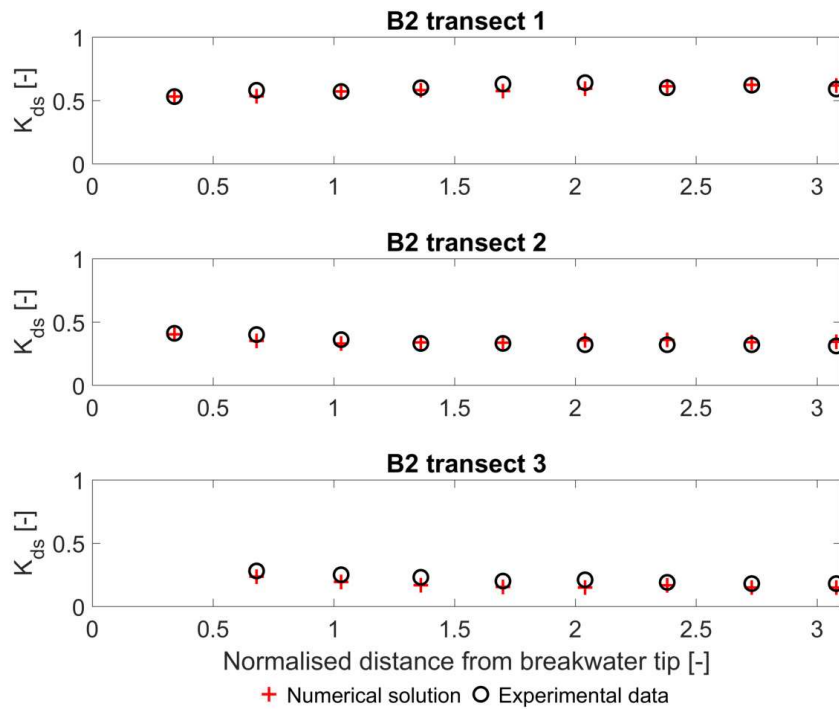


Figure 5.37: Comparison of diffraction coefficients between numerical model results (red plus signs) and experimental data (black circles) for test case B2.

as mentioned in Section 5.4.2, is not taken into account for the calculation of the RMSE.

As it is observed, the performance of the two wave generation methods is almost identical for the case of regular waves (M1, M4) despite the waves being slightly dispersive. This is happening due to the fact that the simulation time is only 54.6 s (sampling duration 36.4 s) similar to the experiment and thus the reflected waves due to the weakly reflective generation boundary have not yet reached the lee side of the wall. For longer simulations the wave fields inside the two numerical domains differ significantly, but they cannot be compared with the experimental data due to the reflections from the side walls. However, for the case of irregular waves where the simulation times are longer, the performance of method 3 is better, since the calculated RMSE for method 1 is at least double than the one corresponding to method 3. In addition, the RMSE of method 1 is larger in case of the broad directional spreading distribution especially along the transect 1. This is explained by the fact that the waves are propagating back towards the generation boundary with a larger wave angle than in case of the narrow directional spreading distribution. In Section 5.2, where the theoretical reflection coefficient is derived for the weakly reflective boundary as a function of the incident wave angle θ , it can be observed that the reflection increases for larger incident wave angles (Figure 5.2).

Finally, in Figure 5.39 a three-dimensional visualisation of the short-crested waves diffracting around the vertical wall for test case N1 is presented. The diffraction patterns at the lee side of the wall as well as the increase of the wave amplitude due to the reflection in front of the wall are clearly visible.

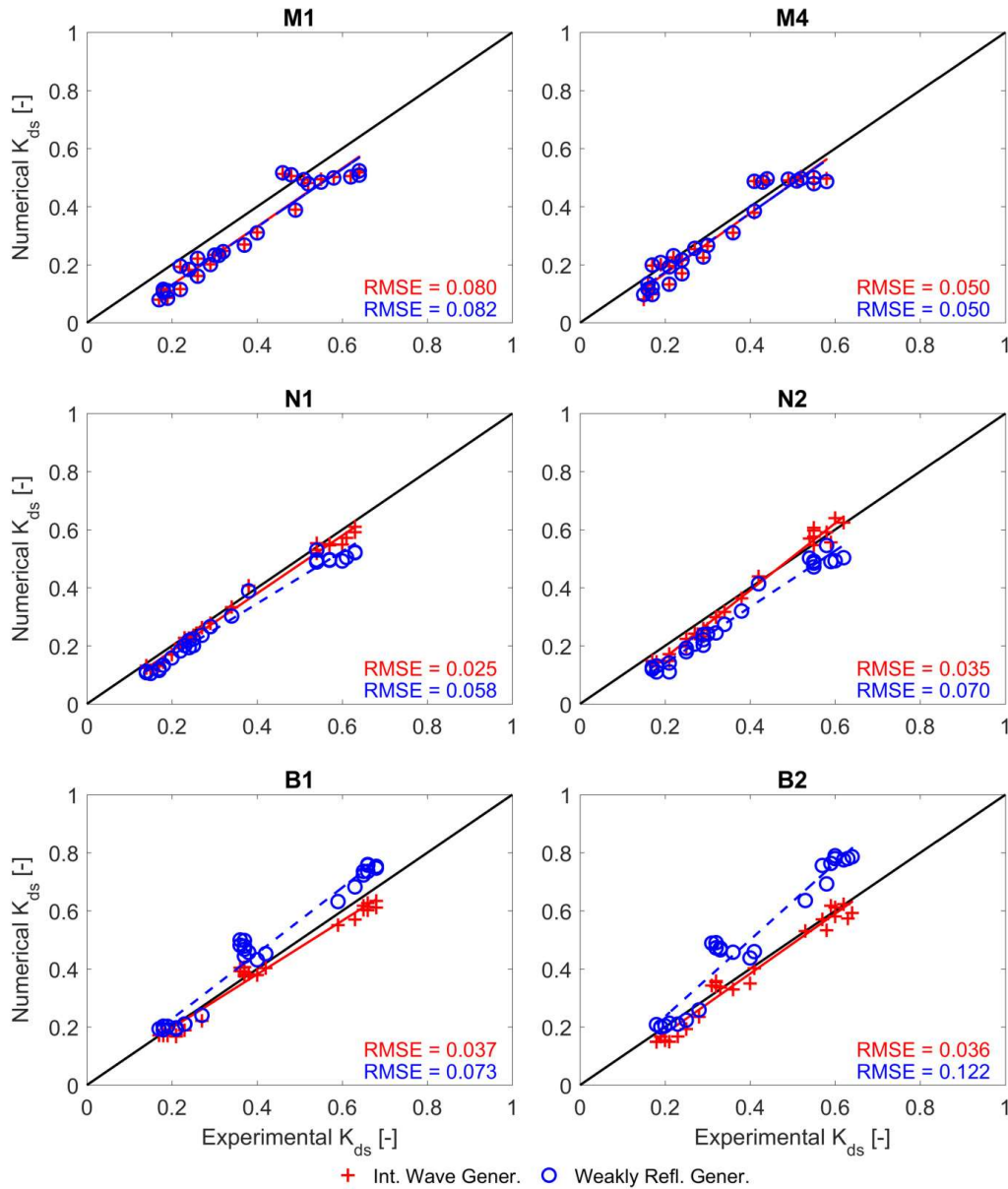


Figure 5.38: Comparison between the performance of the internal wave generation (method 3, red plus signs) and the weakly reflective generation (method 1, blue circles) for predicting the diffraction coefficients observed by Briggs et al. (1995) experiment. Black solid lines represent perfect agreement, while red solid line and the blue dashed line are the fitting lines for method 3 and method 1, respectively.

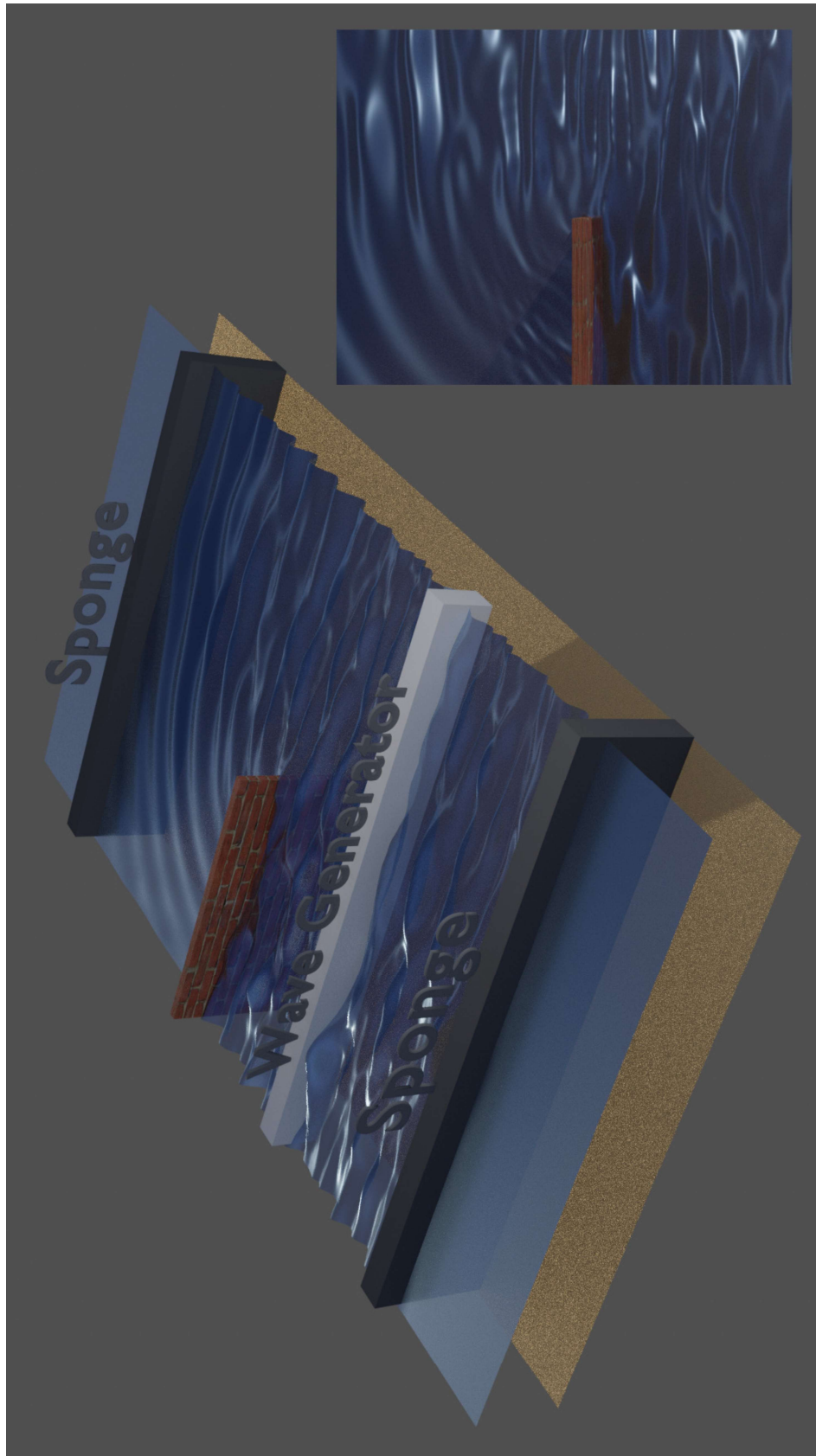


Figure 5.39: 3D visualisation of short-crested waves diffracting around the vertical wall of Briggs et al. (1995) experiment (test case N1).

5.6 Conclusions

In the present study new internal wave generation methods have been developed in an open source non-hydrostatic wave model, SWASH, for accurate generation of regular and irregular long- and short-crested waves, enabling the study of long-existing engineering problems in a more accurate way.

Initially, two different internal wave generation methods have been developed and implemented in the SWASH model. The first one is a source term addition method based on the method proposed by Lee et al. (2001), while the second one is a spatially distributed source function based on the method proposed by Wei et al. (1999). In the source term addition method additional surface elevation is added to the calculated surface elevation while in the spatially distributed source function a spatially distributed mass is added in the free surface equation. At the same time, sponge layers are used at the domain boundaries to absorb the incoming waves. In both cases, the source term propagates with a velocity which is called the energy velocity and for the system of SWASH equations is mathematically derived in Section 5.3.1.

Subsequently, these wave generation methods have been used to generate regular and irregular long-crested waves. The results indicate that the developed model is capable of reproducing the target surface elevations as well as the target frequency spectrum. The overall performance of the spatially distributed source function is better than the source term addition method since the latter becomes unstable for large wave heights and may cause high frequency noise.

The developed model with the addition of the internal wave generation method has also been validated against experimental data. Three benchmark experimental tests have been used: 1) propagation of regular waves over a shoal resting on a plane sloping seabed (Berkhoff et al., 1982), 2) propagation of irregular long- and short-crested waves over a shoal (Vincent and Briggs, 1989) and 3) wave diffraction around a vertical wall (Briggs et al., 1995). Through this comparison, a very good agreement is observed between the numerical model and the experimental results.

In addition, the performance of the internal wave generation (method 3) is compared with this of the weakly reflective wave generation boundary (method 1) for the case of waves that are reflected back to the numerical boundary due to the presence of a structure. Method 3 needs an extension of the numerical domain to accommodate the sponge layer and the source area contrary to the weakly reflective wave generation boundary. Thus, the computational cost increases 15–30%, where the lower values stand for larger computational domains. However, the main advantage of the internal wave generation is that in cases of directional and dispersive waves the reflected waves are absorbed by the sponge layer that is positioned behind the internal wave generator in contrast with the weakly reflective wave generation boundary, which is not valid for these wave conditions due to the limitations described in Section 5.2. In the present study, it has been proven that the internal wave generation is advantageous compared to the weakly reflective wave generation boundary since it is able to generate more accurately the target wave characteristics even in case of highly dispersive and directional waves and at the same time any reflection due to the presence of the weakly reflective wave

generator is avoided.

The aforementioned observations reveal that the internal wave generation method developed here in SWASH can be successfully used to study in a more accurate way man-made structures (e.g. breakwaters, artificial reefs, artificial islands) and wave energy converter (WEC) farms, where the reflected and radiated waves cannot be estimated a priori.

Chapter 6

Conclusions and Further Work

6.1 Summary of the key findings

The core aim of the present dissertation was to improve the homogeneity of the generated wave fields in phase-resolving numerical models by enhancing their capability to accurately generate the target wave conditions and at the same time by minimising the disturbance of the generated wave field by unwanted wave diffraction and reflection patterns due to the imposed numerical boundaries. In this context, we pursued further developments and validation of the mild-slope wave propagation model MILDwave and the non-hydrostatic wave model SWASH.

Mild-slope wave models are able to consider a range of transformation processes of linear waves, such as wave refraction, diffraction, shoaling, and reflection. Applications of this type of models include wave diffraction around an obstacle, wave penetration inside harbours and wave energy converters. In chapter 3, a new wave generation layout using periodic lateral boundaries was developed where a single internal wave generation line parallel to the y-axis was combined with periodic lateral boundaries at the top and bottom of the domain. With regard to this development the following conclusions are drawn:

- The proposed wave generation layout is advantageous compared to the L-shaped and arc-shaped wave generation layouts since it leads to a homogeneous wave field, which is not disturbed by unwanted wave diffraction patterns in contrast to the other two widely used wave generation layouts.
- Two different wave synthesis methods were employed to generate short-crested waves, a method proposed by Miles (1989) and a method proposed by Sand and Mynett (1987). After thorough analysis, in the Sand and Mynett method, (i) the computational time, (ii) the number of corrections of the wave propagation angles in order to ensure the periodicity of the waves, and (iii) the non-homogeneity of the generated wave field are much smaller than

those for the Miles method, making the Sand and Mynett method preferable when periodic lateral boundaries are applied in a mild-slope wave model.

- The results showed that the MILDwave model with the addition of the periodic boundaries is capable of reproducing the target frequency and directional spectrum.
- The developed model is able to account for wave propagation of short-crested waves over an elliptic shoal (validated against Vincent and Briggs (1989) shoal experiment).
- The periodic boundaries make the mild-slope wave model, MILDwave, an essential tool to generate multi-directional waves and study their transformation due to its significantly small computational cost and its high numerical stability and robustness.

Although mild-slope wave models produce reasonably good results in deep and intermediate water, their accuracy in shallow water deteriorates as nonlinearity is becoming strong and thus not negligible. In cases that nonlinear processes such as wave breaking, wave-wave interaction or harmonic generation are important, models based on the non-hydrostatic approach are an attractive alternative. A representative model of this category is the non-hydrostatic model SWASH. In Chapter 4 the linear and nonlinear properties of SWASH model were examined and the following conclusions are stated:

- The model can achieve excellent linear dispersion accuracy using only a few vertical layers, since for three layers the relative error is smaller than 1% up to a kd value of 16.41, while for four layers up to a kd value of 28.59.
- A significant improvement of the capability of the model to represent the Stokes second order surface component is noticed when a multi-layer layout is applied. The relative error stays below 5% up to kd values of 2.09 and 3.41 for three and four layers, respectively.
- The Stokes third order surface component and the amplitude dispersion are also satisfactorily described by the governing equations of the model, although for a smaller range of kd values than the second order.
- SWASH is capable of accounting for second order subharmonic and superharmonic interactions between shallow water waves and intermediate-deep water waves and for second order superharmonic interactions between intermediate and deep water waves.
- From the sensitivity analysis regarding the effect of the horizontal and vertical advection terms of the vertical momentum equation it was found that: (i) neglecting the horizontal advection term reduces significantly the capability of the model to accurately represent the Stokes second order surface component, (ii) neglecting the vertical advection term does not deteriorate the second order nonlinear properties of the model when coarse vertical resolution is applied (up to four vertical layers).

In the context of developing further the wave generation capabilities of SWASH model, two different internal wave generation methods were developed and examined in Chapter 5. The first one is a source term addition method based on the method proposed by Lee et al. (2001), while the second one is a spatially distributed source function based on the method proposed by Wei et al. (1999). Additionally, a comparison was made between the performance of the proposed internal wave generation methods and the weakly reflective wave generation method. The key findings are summarised below:

- In both internal wave generation methods the source term propagates with a velocity which is called the energy velocity C_e and for the governing equations of the SWASH model it was mathematically derived and proved to be equal to the group velocity ($C_g = \partial\omega/\partial k$).
- Both internal wave generation methods were used to generate regular and irregular long-crested waves. The results indicate that the developed model is capable of reproducing the target surface elevations as well as the target frequency spectrum.
- The overall performance of the spatially distributed source function is better than the source term addition method since the latter becomes unstable for large wave heights and may cause high frequency noise.
- The spatially distributed source function was employed to generate oblique regular waves and short-crested waves in a numerical basin with constant depth. A very good agreement with analytical solutions was observed, showing that the internal wave generation method is able to generate directional waves and that oblique waves can pass through the wave generation area without any distortion.
- The developed model was validated against three benchmark experimental tests: (i) propagation of regular waves over a shoal resting on a plane sloping seabed (Berkhoff et al., 1982), (ii) propagation of irregular long- and short-crested waves over a shoal (Vincent and Briggs, 1989) and (iii) wave diffraction around a vertical wall (Briggs et al., 1995). An excellent agreement was observed between the numerical model and the experimental data.
- It was proved that the internal wave generation is advantageous compared to the weakly reflective wave generation boundary since it is able to generate more accurately the target wave characteristics even in case of highly dispersive and directional waves and at the same time any reflection due to the presence of the weakly reflective wave generator is avoided.
- SWASH model with the addition of the internal wave generation method can be successfully used to study in a more accurate way man-made structures (e.g., breakwaters, artificial reefs, artificial islands) and wave energy converter (WEC) farms, where the reflected and radiated waves cannot be estimated a priori.

6.2 Recommendations for future research

This final section provides a number of recommendations for future research to extend the capabilities of the developments in MILDwave and SWASH and to exploit their advantages to study real scale applications:

1. Validate the proposed generation layout in MILDwave with field measurements;
The periodic boundaries make the mild-slope wave model, MILDwave, an essential tool that can be utilised to study short-crested waves penetrating in harbours or diffracting around an artificial island. In this way, the model can be further validated and possible limitations of the proposed generation layout can be examined in detail. Additionally, Verao Fernandez (2019) and Balitsky et al. (2019) have used the developed model to study WEC arrays under irregular short-crested and regular oblique waves, respectively. Their results are promising and indicate the need for further validation under real ocean waves.
2. Extend the nonlinear analysis of SWASH equations;
The Stokes-type Fourier analysis can be extended to higher order to identify the capability of the governing equations to describe short waves with large amplitudes. Additionally, the third order subharmonic and superharmonic transfer functions can be derived, while the solutions for the case that more than four vertical layers are applied can be obtained as well. Using the derived expressions, higher order nonlinear boundary conditions can be formulated. Furthermore, the derived solutions can be compared with the corresponding values of other models, e.g. low- and high-order Boussinesq-type wave models, to further highlight the high accuracy of SWASH.
3. Extend the capabilities of the implemented internal wave generation method in SWASH;
The rational expressions of the energy velocity C_e for the system of SWASH equations have been derived by using the linearised governing equations. This means that these expressions are less accurate in case that the target generated wave is highly nonlinear. However, the derived solutions of Chapter 4 can be used to include higher order corrections in the proposed internal wave generation method. In this way, free spurious high order waves, that are inevitably introduced due to first order wave generation, are eliminated. In addition, the effectiveness of the developed method to generate cnoidal and solitary waves or time series of surface elevations provided by wave gauges or other numerical models has to be explored.
4. Validate the proposed internal wave generation method in SWASH with field measurements;
In Chapter 5, the proposed method was validated against three benchmark experimental tests and analytical solutions. There is still a need to investigate the degree of improvement of the accuracy of the model with the use of the

internal wave generation method when studying wave processes under real coastal environments characterised by different bathymetric features. Thanks to the capability of the proposed method to handle dispersive and directional waves, it is expected that it will lead to more accurate results when waves are reflected or radiated back to the generation boundary due to the presence of an artificial or natural obstacle. In addition, due to the improvement of the accuracy of the model in predicting wave transformation in complex coastal environments, extending SWASH to account for coastal morphodynamics should be definitely considered as a future work.

5. Compare further internal wave generation with other wave generation methods.

In Chapter 5, the developed internal wave generation method was compared with the traditional weakly reflective wave generation method in SWASH. It is strongly recommended that a comparison between the proposed and the moving boundary method be executed as well. Moreover, the performance of the different wave generation methods in case that an unsteady wave induced current flows towards the generation area deserves a detailed investigation. These kind of comparisons can reveal possible advantages and disadvantages of the different methods and can prove to be very helpful for modelers worldwide in order to decide which method is most appropriate for the case that they wish to investigate.

Appendices

Appendix A

Comparison of different wave generation layouts in MILDwave

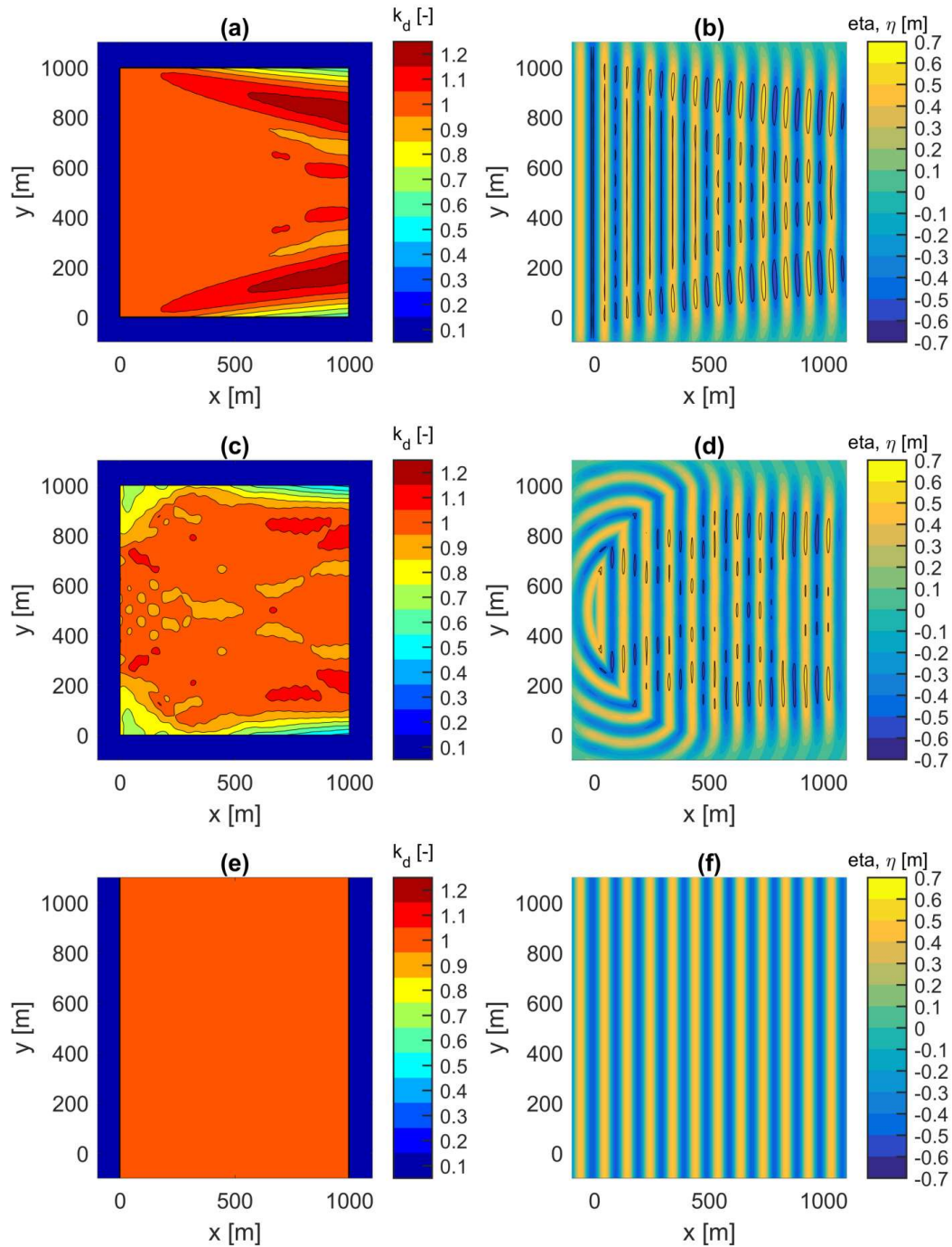


Figure A.1: Disturbance coefficient, k_d , and water surface elevation, η , in the inner computational domain at $t = 80T$ for regular incident waves with $H = 1$ m, $T = 12$ s, and $\theta = 0^\circ$ generated by an L-shaped wave generation layout (a,b), an arc-shaped wave generation layout (c,d), and by the use of periodic boundaries (e,f).

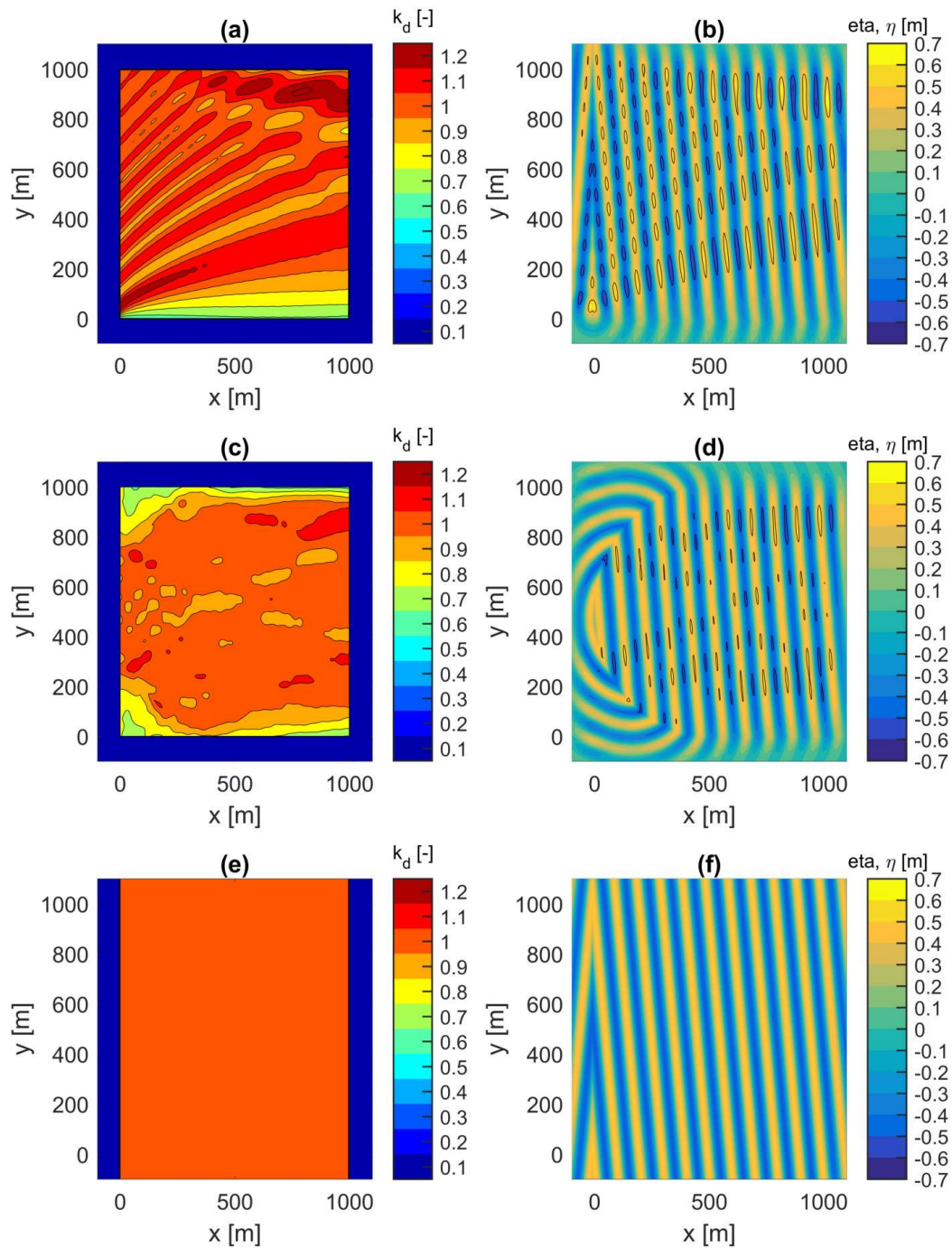


Figure A.2: Disturbance coefficient, k_d , and water surface elevation, η , in the inner computational domain at $t = 80T$ for regular incident waves with $H = 1$ m, $T = 12$ s, and $\theta = 5^\circ$ generated by an L-shaped wave generation layout (a,b), an arc-shaped wave generation layout (c,d), and by the use of periodic boundaries (e,f).

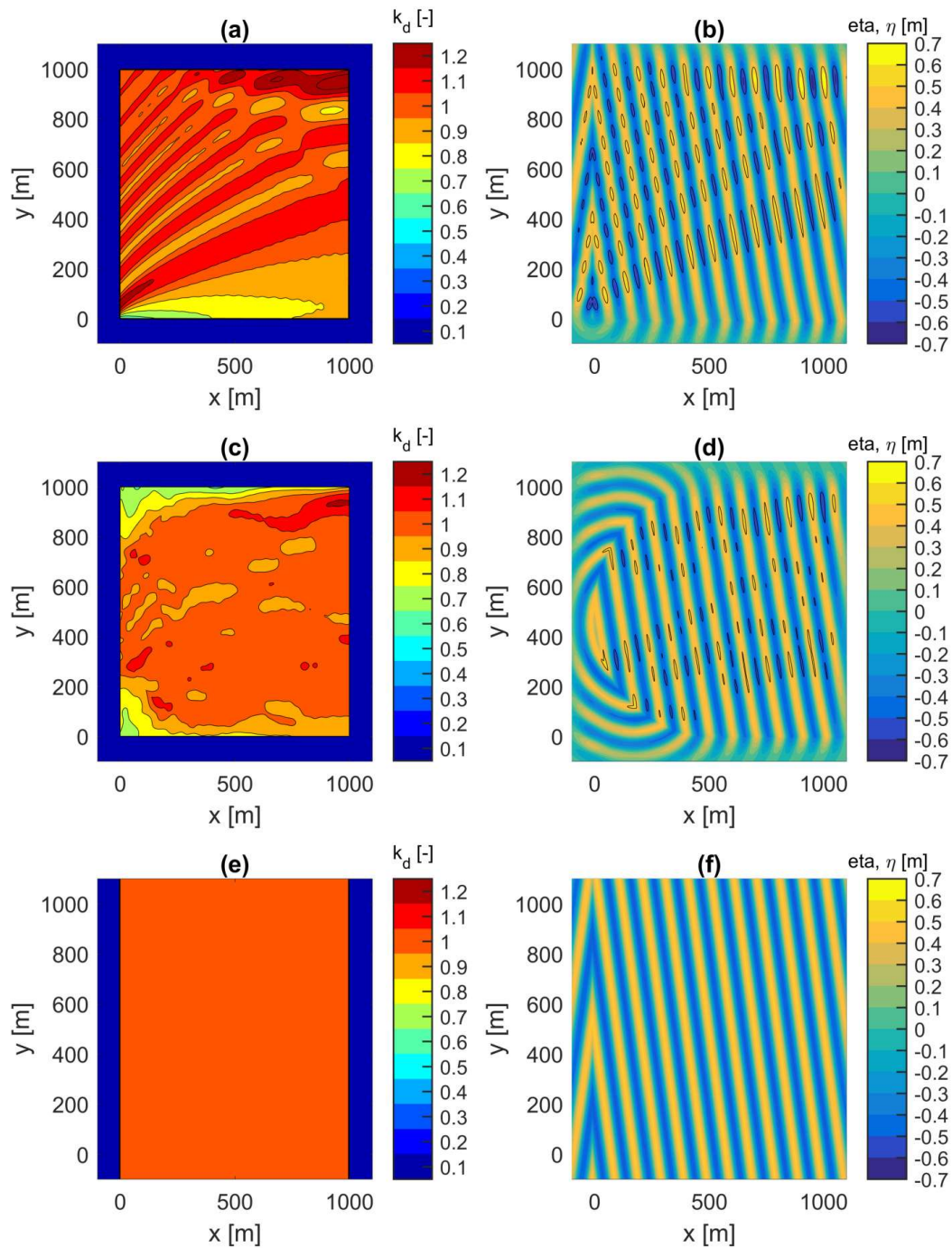


Figure A.3: Disturbance coefficient, k_d , and water surface elevation, η , in the inner computational domain at $t = 80T$ for regular incident waves with $H = 1$ m, $T = 12$ s, and $\theta = 10^\circ$ generated by an L-shaped wave generation layout (a,b), an arc-shaped wave generation layout (c,d), and by the use of periodic boundaries (e,f).

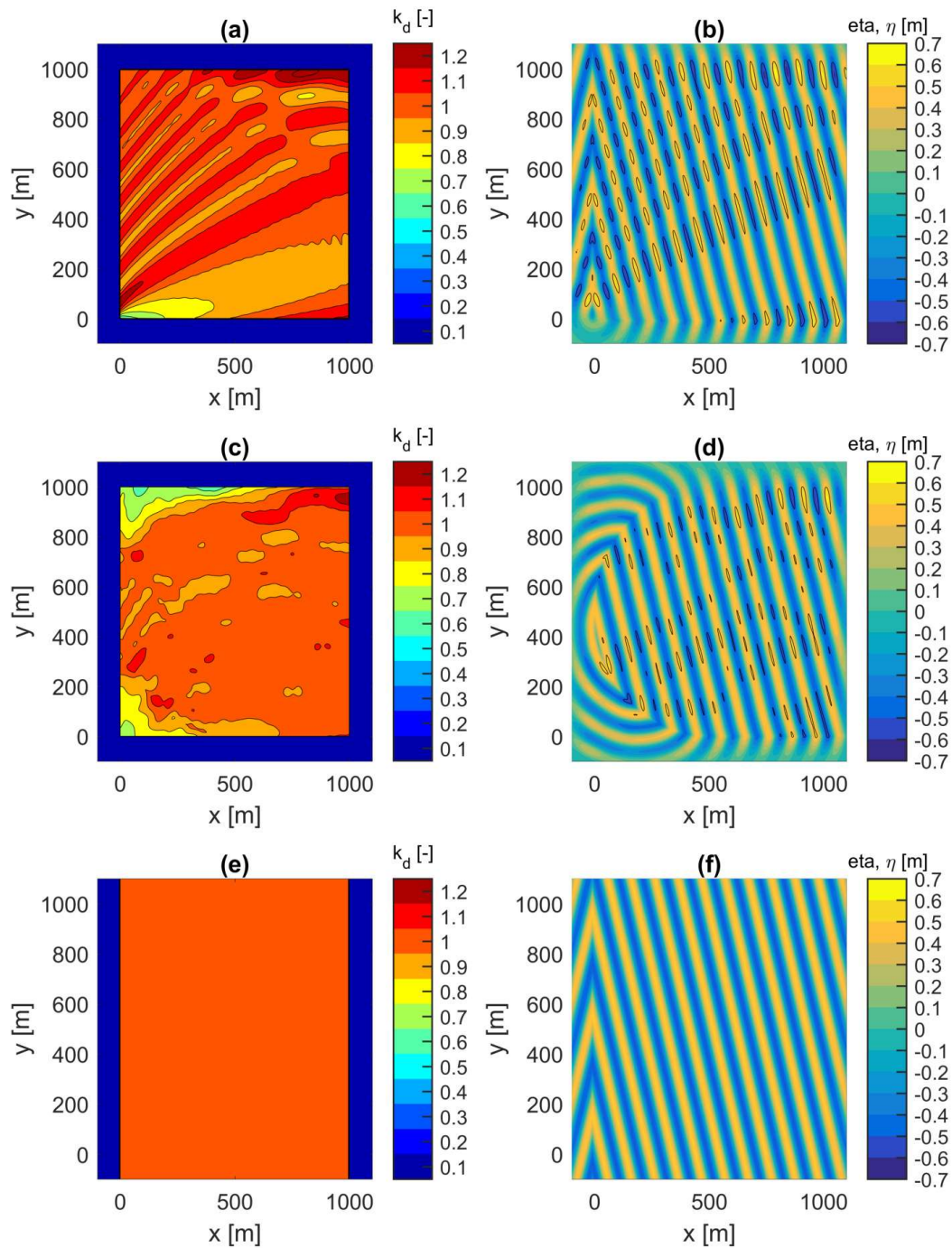


Figure A.4: Disturbance coefficient, k_d , and water surface elevation, η , in the inner computational domain at $t = 80T$ for regular incident waves with $H = 1$ m, $T = 12$ s, and $\theta = 15^\circ$ generated by an L-shaped wave generation layout (a,b), an arc-shaped wave generation layout (c,d), and by the use of periodic boundaries (e,f).

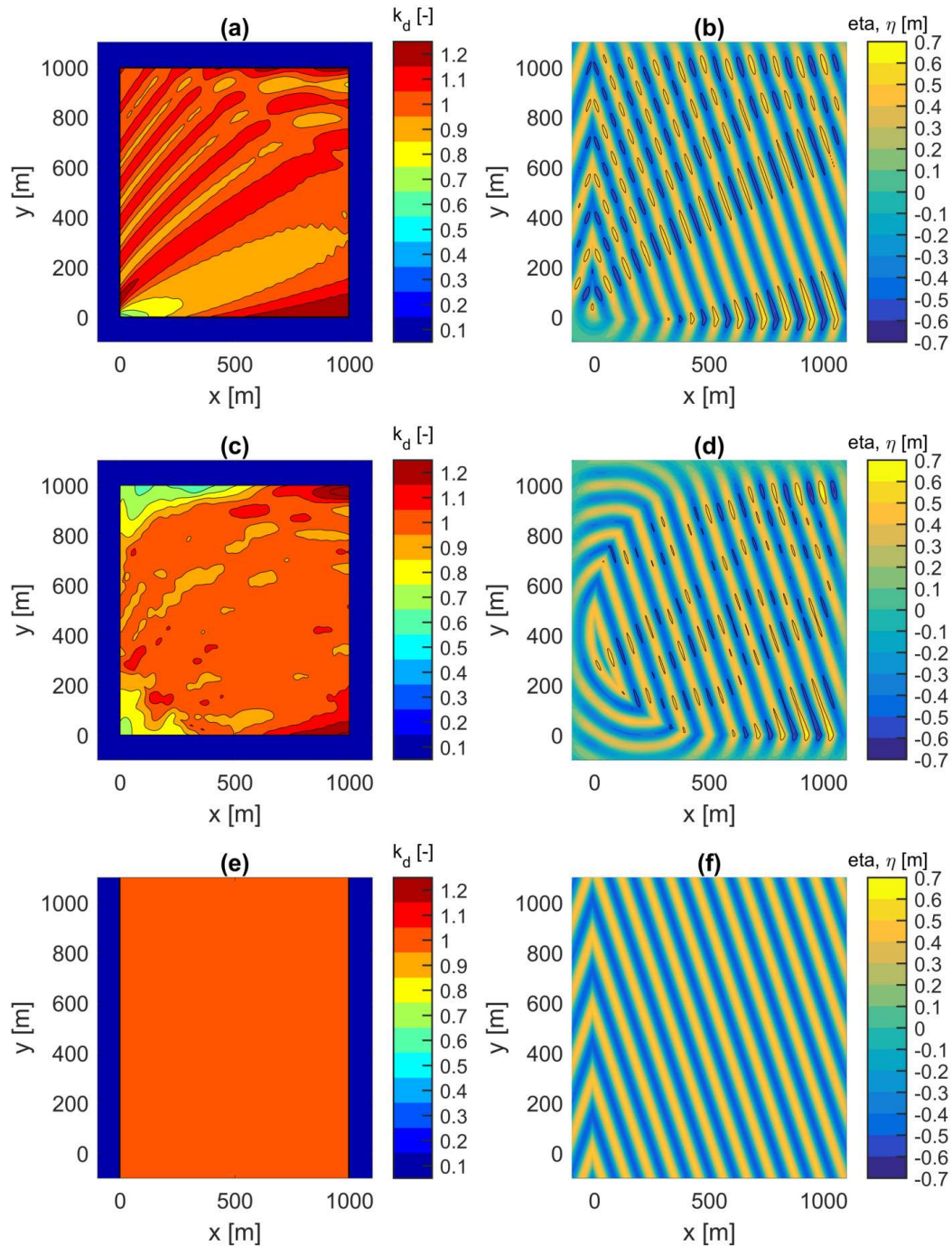


Figure A.5: Disturbance coefficient, k_d , and water surface elevation, η , in the inner computational domain at $t = 80T$ for regular incident waves with $H = 1$ m, $T = 12$ s, and $\theta = 20^\circ$ generated by an L-shaped wave generation layout (a,b), an arc-shaped wave generation layout (c,d), and by the use of periodic boundaries (e,f).

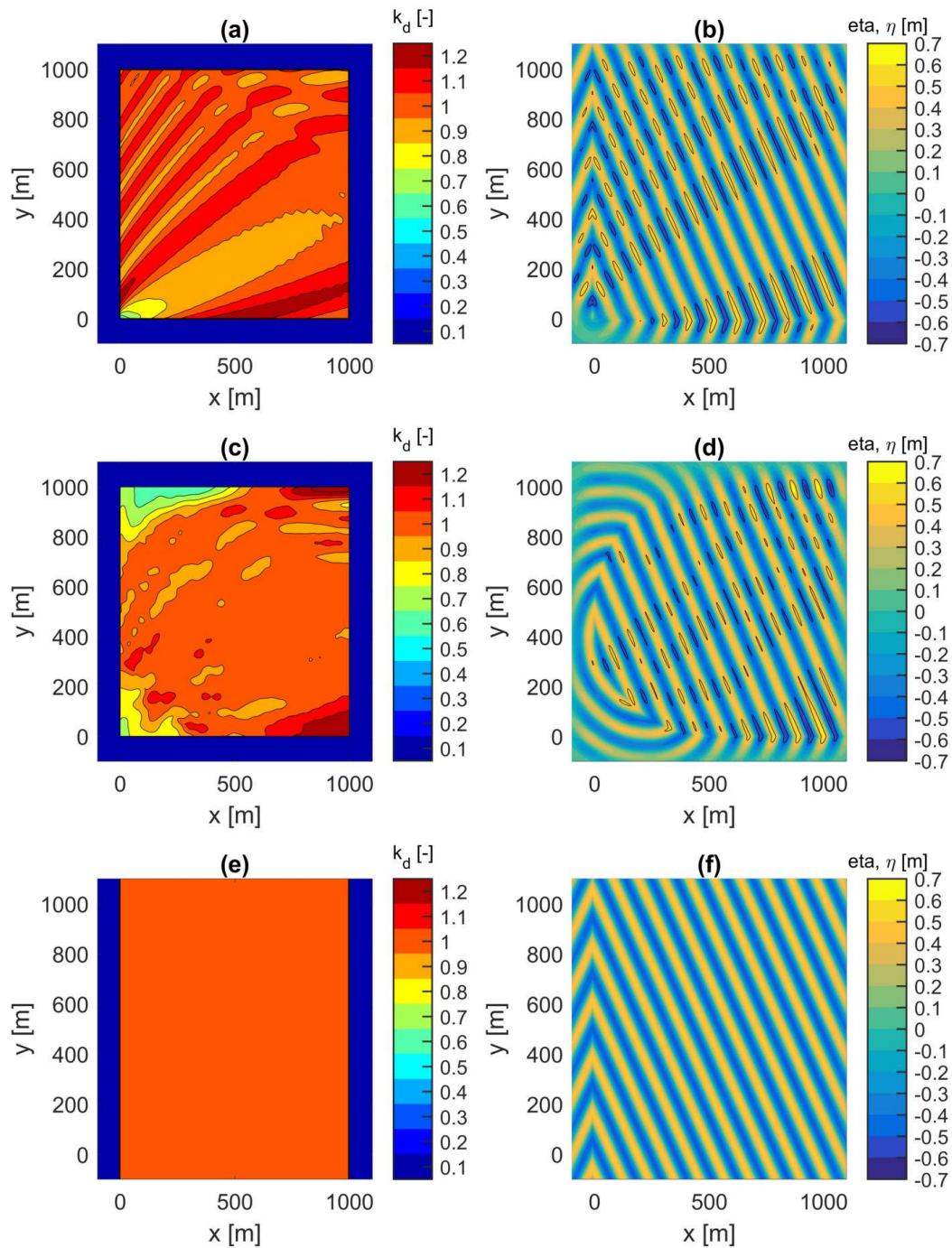


Figure A.6: Disturbance coefficient, k_d , and water surface elevation, η , in the inner computational domain at $t = 80T$ for regular incident waves with $H = 1$ m, $T = 12$ s, and $\theta = 25^\circ$ generated by an L-shaped wave generation layout (a,b), an arc-shaped wave generation layout (c,d), and by the use of periodic boundaries (e,f).

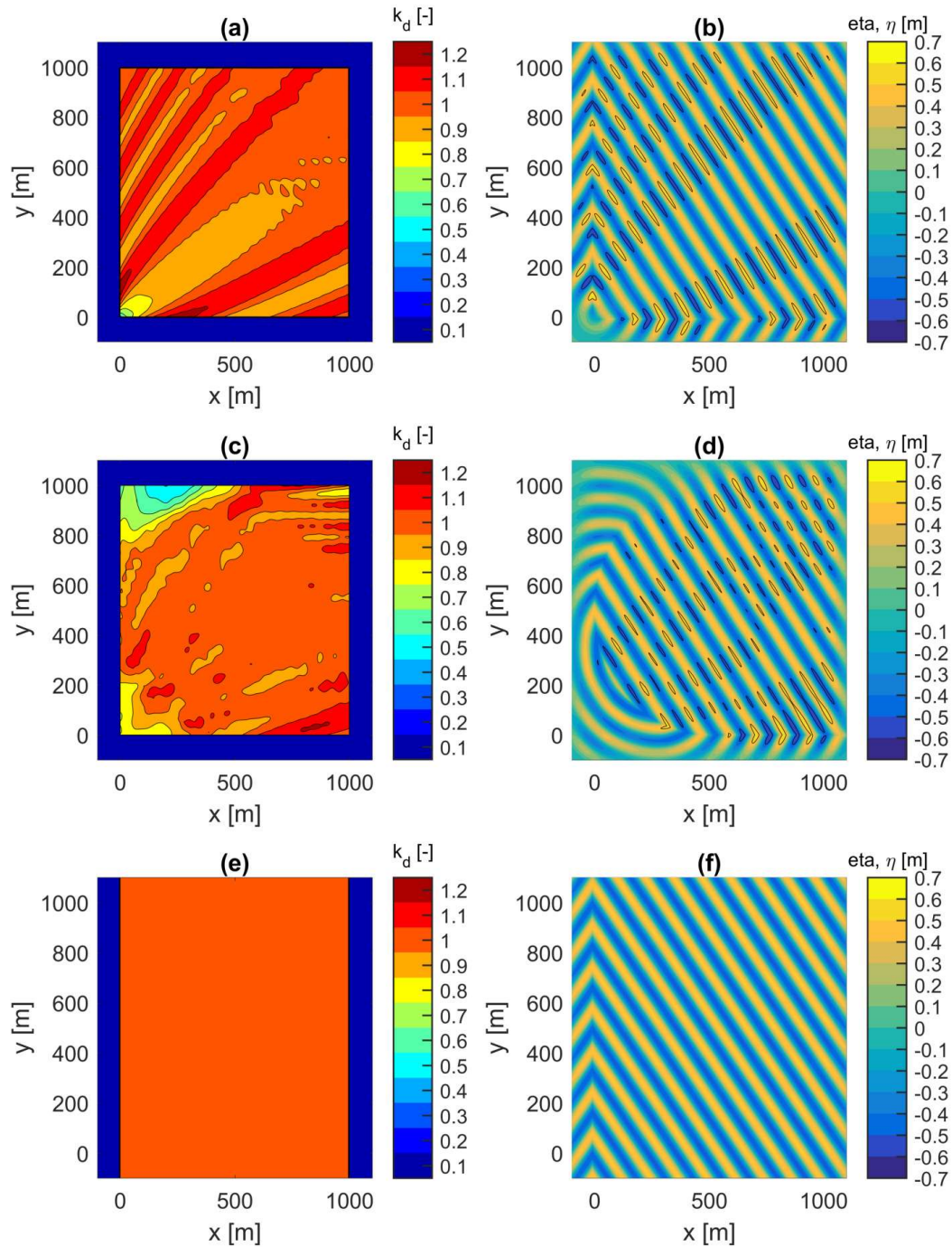


Figure A.7: Disturbance coefficient, k_d , and water surface elevation, η , in the inner computational domain at $t = 80T$ for regular incident waves with $H = 1$ m, $T = 12$ s, and $\theta = 35^\circ$ generated by an L-shaped wave generation layout (a,b), an arc-shaped wave generation layout (c,d), and by the use of periodic boundaries (e,f).

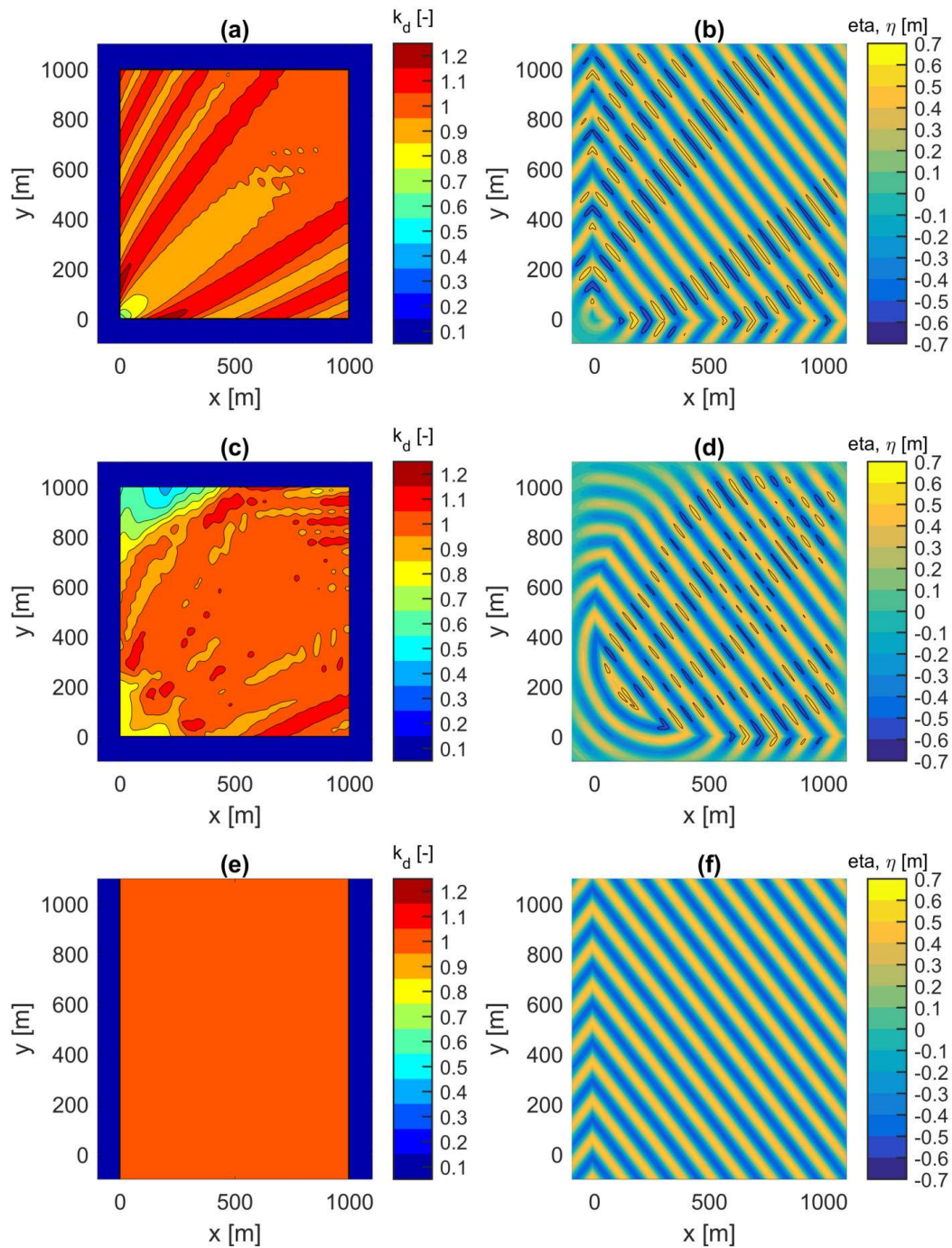


Figure A.8: Disturbance coefficient, k_d , and water surface elevation, η , in the inner computational domain at $t = 80T$ for regular incident waves with $H = 1$ m, $T = 12$ s, and $\theta = 40^\circ$ generated by an L-shaped wave generation layout (a,b), an arc-shaped wave generation layout (c,d), and by the use of periodic boundaries (e,f).

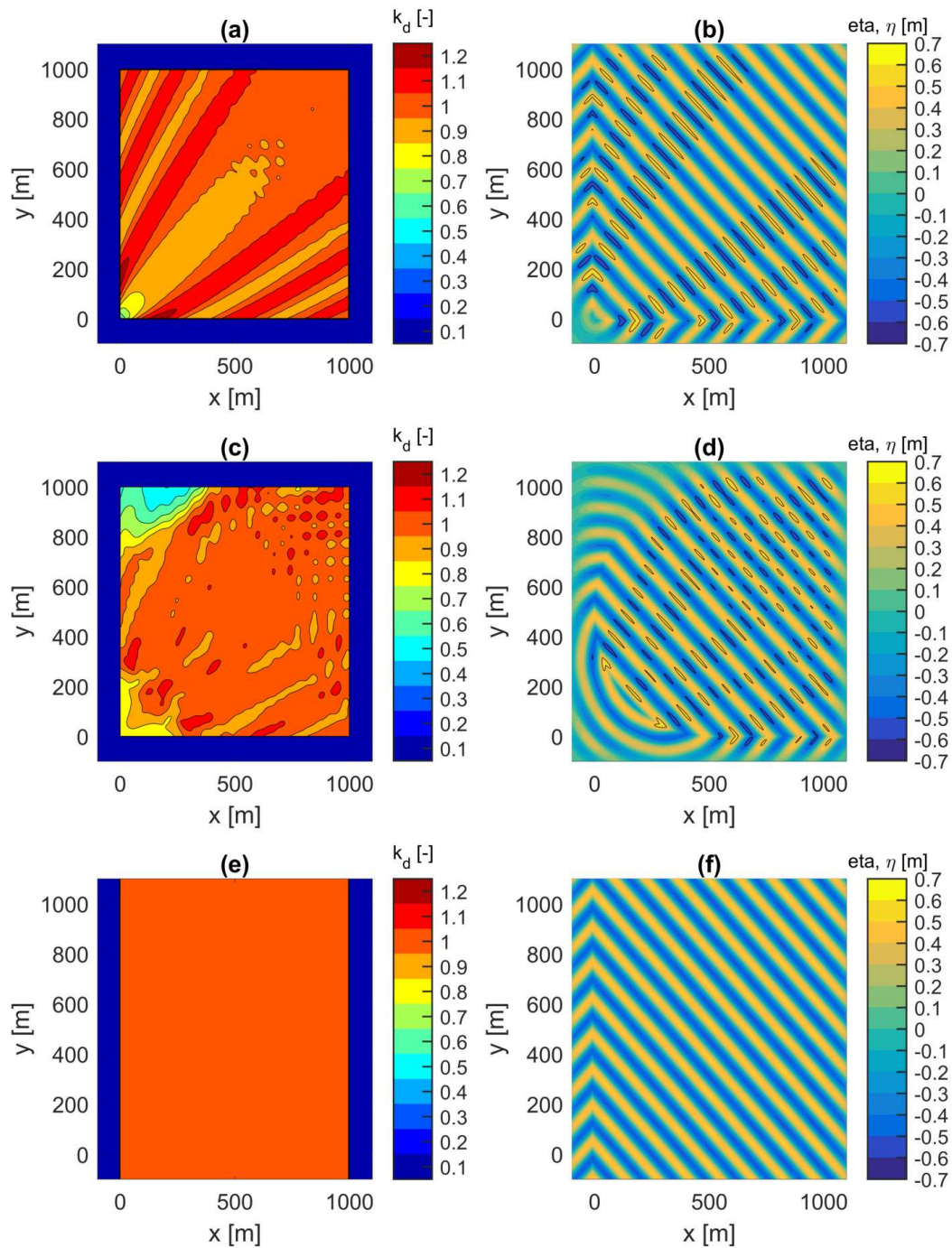


Figure A.9: Disturbance coefficient, k_d , and water surface elevation, η , in the inner computational domain at $t = 80T$ for regular incident waves with $H = 1$ m, $T = 12$ s, and $\theta = 45^\circ$ generated by an L-shaped wave generation layout (a,b), an arc-shaped wave generation layout (c,d), and by the use of periodic boundaries (e,f).

Appendix B

Analysis of SWASH equations using Wolfram Mathematica

This Appendix chapter is composed of a series of Wolfram Mathematica scripts used for Chapter 4. The procedure followed to derive the linear and nonlinear properties of SWASH for the case of two layers are presented in Appendix B.1. The solutions for the second and third order amplitudes of the surface elevation (η_{02} and η_{03}) up to four vertical layers are provided in Appendix B.2 and Appendix B.3. Finally, the derived expressions for the transfer functions for subharmonics (G_{η}^{m-n}) and superharmonics (G_{η}^{m+n}) are given in Appendix B.4 and Appendix B.5.

B.1 Stokes-type Fourier analysis for two layers

Derivation of First, second and third order solutions

```

$Assumptions = g > 0 && d > 0;
eta[t_, x_] = ε * eta1[t, x] + ε2 * eta2[t, x] + ε3 * eta3[t, x];
uk1[t_, x_] = ε * uk11[t, x] + ε2 * uk12[t, x] + ε3 * uk13[t, x] (*bottom layer*);
uk2[t_, x_] = ε * uk21[t, x] + ε2 * uk22[t, x] + ε3 * uk23[t, x] (*surface layer*);
qb[t_, x_] = ε * qb1[t, x] + ε2 * qb2[t, x] + ε3 * qb3[t, x];
q12[t_, x_] = ε * q121[t, x] + ε2 * q122[t, x] + ε3 * q123[t, x];
ws[t_, x_] = ε * ws1[t, x] + ε2 * ws2[t, x] + ε3 * ws3[t, x];
w12[t_, x_] = ε * w121[t, x] + ε2 * w122[t, x] + ε3 * w123[t, x];
h = d + eta[t, x];
ωnew = ω * (1 + ε2 * ω13);
eta1[t_, x_] = eta01 * Cos[(k * x - ωnew * t)];
uk11[t_, x_] = uk101 * (1 + ε2 * uk1013) * Cos[(k * x - ωnew * t)];
uk21[t_, x_] = uk201 * (1 + ε2 * uk2013) * Cos[(k * x - ωnew * t)];
qb1[t_, x_] = qb01 * (1 + ε2 * qb013) * Cos[(k * x - ωnew * t)];
q121[t_, x_] = q1201 * (1 + ε2 * q12013) * Cos[(k * x - ωnew * t)];
ws1[t_, x_] = ws01 * (1 + ε2 * ws013) * Sin[(k * x - ωnew * t)];
w121[t_, x_] = w1201 * (1 + ε2 * w12013) * Sin[(k * x - ωnew * t)];
eta2[t_, x_] = eta02 * Cos[2 * (k * x - ωnew * t)];
uk12[t_, x_] = uk102 * Cos[2 * (k * x - ωnew * t)];
uk22[t_, x_] = uk202 * Cos[2 * (k * x - ωnew * t)];
qb2[t_, x_] = qb02 * Cos[2 * (k * x - ωnew * t)];
q122[t_, x_] = q1202 * Cos[2 * (k * x - ωnew * t)];
ws2[t_, x_] = ws02 * Sin[2 * (k * x - ωnew * t)];
w122[t_, x_] = w1202 * Sin[2 * (k * x - ωnew * t)];
eta3[t_, x_] = eta03 * Cos[3 * (k * x - ωnew * t)];
uk13[t_, x_] = uk103 * Cos[3 * (k * x - ωnew * t)];
uk23[t_, x_] = uk203 * Cos[3 * (k * x - ωnew * t)];
qb3[t_, x_] = qb03 * Cos[3 * (k * x - ωnew * t)];
q123[t_, x_] = q1203 * Cos[3 * (k * x - ωnew * t)];
ws3[t_, x_] = ws03 * Sin[3 * (k * x - ωnew * t)];
w123[t_, x_] = w1203 * Sin[3 * (k * x - ωnew * t)];
qs[t, x] = 0;
wb[t, x] = 0 (*flat bottom*);
wrel12[t, x] = w12[t, x] -  $\frac{1}{2}$  * D[h - 2 * d, t] -  $\frac{1}{4}$  * (uk1[t, x] + uk2[t, x]) D[h - 2 * d, x];

```

$$\begin{aligned}
\text{trig} = & \left\{ \begin{aligned}
& \text{Cos}[\theta] \text{Cos}[2\theta] \rightarrow \left(\frac{1}{2} * \text{Cos}[\theta] + \frac{1}{2} * \text{Cos}[3 * \theta] \right), \\
& \text{Sin}[\theta] \text{Sin}[2\theta] \rightarrow \left(\frac{1}{2} * \text{Cos}[\theta] - \frac{1}{2} * \text{Cos}[3 * \theta] \right), \\
& \text{Cos}[\theta] \text{Sin}[2\theta] \rightarrow \left(\frac{1}{2} * \text{Sin}[3 * \theta] + \frac{1}{2} * \text{Sin}[\theta] \right), \text{Cos}[2 * \theta] \text{Sin}[\theta] \rightarrow \\
& \left(\frac{1}{2} * \text{Sin}[3 * \theta] - \frac{1}{2} * \text{Sin}[\theta] \right), \text{Cos}[\theta]^3 \rightarrow \frac{1}{4} * (\text{Cos}[3 * \theta] + 3 * \text{Cos}[\theta]), \\
& \text{Sin}[\theta]^3 \rightarrow \frac{1}{4} * (3 * \text{Sin}[\theta] - \text{Sin}[3 * \theta]), \text{Cos}[\theta]^2 \text{Sin}[\theta] \rightarrow \frac{1}{4} * (\text{Sin}[\theta] + \text{Sin}[3 * \theta]), \\
& \text{Sin}[\theta]^2 \text{Cos}[\theta] \rightarrow \frac{1}{4} * (\text{Cos}[\theta] - \text{Cos}[3 * \theta]);
\end{aligned} \right\};
\end{aligned}$$

Governing Equations

Free surface equation

$$\begin{aligned}
\text{eq1} = & \text{D}[\text{eta}[t, x], t] + \frac{1}{2} \text{D}[h * (\text{uk1}[t, x] + \text{uk2}[t, x]), x] == 0 /. \\
& k * x \rightarrow t * \omega (1 + \epsilon^2 * \omega13) + \theta // \text{Expand};
\end{aligned}$$

$$\begin{aligned}
\text{eq1new1} = & \text{Replace}[\text{Expand@eq1}, \text{p_Plus} \Rightarrow \text{DeleteCases}[p, _?(\text{FreeQ}[\epsilon])], \text{All}] /. \epsilon^{\wedge} b_ /; b \geq 2 \rightarrow 0 \\
& - \frac{1}{2} d k \text{uk101} \epsilon \text{Sin}[\theta] - \frac{1}{2} d k \text{uk201} \epsilon \text{Sin}[\theta] + \text{eta01} \epsilon \omega \text{Sin}[\theta] == 0
\end{aligned}$$

$$\begin{aligned}
\text{eq1new2} = & \text{Replace}[\text{Expand@eq1}, \text{p_Plus} \Rightarrow \text{DeleteCases}[p, _?(\text{FreeQ}[\epsilon])], \text{All}] /. \\
& \epsilon^{\wedge} b_ /; b \geq 3 \rightarrow 0 /. \epsilon^2 \rightarrow a /. \epsilon \rightarrow \theta /. a \rightarrow \epsilon^2 \\
& - \text{eta01} k \text{uk101} \epsilon^2 \text{Cos}[\theta] \text{Sin}[\theta] - \text{eta01} k \text{uk201} \epsilon^2 \text{Cos}[\theta] \text{Sin}[\theta] - \\
& d k \text{uk102} \epsilon^2 \text{Sin}[2\theta] - d k \text{uk202} \epsilon^2 \text{Sin}[2\theta] + 2 \text{eta02} \epsilon^2 \omega \text{Sin}[2\theta] == 0
\end{aligned}$$

$$\begin{aligned}
\text{eq1new3} = & \text{Replace}[\text{Expand@eq1}, \text{p_Plus} \Rightarrow \text{DeleteCases}[p, _?(\text{FreeQ}[\epsilon])], \text{All}] /. \epsilon^{\wedge} b_ /; b \geq 4 \rightarrow 0 /. \\
& \epsilon^3 \rightarrow a /. \epsilon \rightarrow \theta /. a \rightarrow \epsilon^3 /. \text{trig} \\
& - \frac{1}{2} d k \text{uk101} \text{uk1013} \epsilon^3 \text{Sin}[\theta] - \frac{1}{2} d k \text{uk201} \text{uk2013} \epsilon^3 \text{Sin}[\theta] + \text{eta01} \epsilon^3 \omega \omega13 \text{Sin}[\theta] - \\
& \frac{1}{2} \text{eta02} k \text{uk101} \epsilon^3 \left(-\frac{\text{Sin}[\theta]}{2} + \frac{1}{2} \text{Sin}[3\theta] \right) - \frac{1}{2} \text{eta01} k \text{uk102} \epsilon^3 \left(-\frac{\text{Sin}[\theta]}{2} + \frac{1}{2} \text{Sin}[3\theta] \right) - \\
& \frac{1}{2} \text{eta02} k \text{uk201} \epsilon^3 \left(-\frac{\text{Sin}[\theta]}{2} + \frac{1}{2} \text{Sin}[3\theta] \right) - \frac{1}{2} \text{eta01} k \text{uk202} \epsilon^3 \left(-\frac{\text{Sin}[\theta]}{2} + \frac{1}{2} \text{Sin}[3\theta] \right) - \\
& \text{eta02} k \text{uk101} \epsilon^3 \left(\frac{\text{Sin}[\theta]}{2} + \frac{1}{2} \text{Sin}[3\theta] \right) - \text{eta01} k \text{uk102} \epsilon^3 \left(\frac{\text{Sin}[\theta]}{2} + \frac{1}{2} \text{Sin}[3\theta] \right) - \\
& \text{eta02} k \text{uk201} \epsilon^3 \left(\frac{\text{Sin}[\theta]}{2} + \frac{1}{2} \text{Sin}[3\theta] \right) - \text{eta01} k \text{uk202} \epsilon^3 \left(\frac{\text{Sin}[\theta]}{2} + \frac{1}{2} \text{Sin}[3\theta] \right) - \\
& \frac{3}{2} d k \text{uk103} \epsilon^3 \text{Sin}[3\theta] - \frac{3}{2} d k \text{uk203} \epsilon^3 \text{Sin}[3\theta] + 3 \text{eta03} \epsilon^3 \omega \text{Sin}[3\theta] == 0
\end{aligned}$$

Continuity equations

$$\begin{aligned}
\text{eq2} = & \frac{1}{2} * \text{D}[h * \text{uk2}[t, x], x] - \text{uk2}[t, x] * \text{D}[\text{eta}[t, x], x] + \frac{1}{4} * (\text{uk1}[t, x] + \text{uk2}[t, x]) * \\
& \text{D}[h - 2 d, x] + \text{ws}[t, x] - \text{w12}[t, x] == 0 /. k * x \rightarrow t * \omega (1 + \epsilon^2 * \omega13) + \theta // \text{Expand};
\end{aligned}$$

$$\begin{aligned}
\text{eq2new1} = & \text{Replace}[\text{Expand@eq2}, \text{p_Plus} \Rightarrow \text{DeleteCases}[p, _?(\text{FreeQ}[\epsilon])], \text{All}] /. \epsilon^{\wedge} b_ /; b \geq 2 \rightarrow 0 \\
& - \frac{1}{2} d k \text{uk201} \epsilon \text{Sin}[\theta] - \text{w1201} \epsilon \text{Sin}[\theta] + \text{ws01} \epsilon \text{Sin}[\theta] == 0
\end{aligned}$$

```

eq2new2 = Replace[Expand@eq2, p_Plus -> DeleteCases[p, _?(FreeQ[ε])], All] /.
  ε^b_ /; b >= 3 -> 0 /. ε^2 -> a /. ε -> 0 /. a -> ε^2
- 1/4 eta01 k uk101 ε^2 Cos[θ] Sin[θ] - 1/4 eta01 k uk201 ε^2 Cos[θ] Sin[θ] -
  d k uk202 ε^2 Sin[2 θ] - w1202 ε^2 Sin[2 θ] + ws02 ε^2 Sin[2 θ] == 0

eq2new3 =
  Replace[Expand@eq2, p_Plus -> DeleteCases[p, _?(FreeQ[ε])], All] /. ε^b_ /; b ≥ 4 -> 0 /.
  ε^3 -> a /. ε -> 0 /. a -> ε^3 /. trig
- 1/2 d k uk201 uk2013 ε^3 Sin[θ] - w1201 w12013 ε^3 Sin[θ] + ws01 ws013 ε^3 Sin[θ] -
  1/4 eta01 k uk102 ε^3 (-Sin[θ]/2 + 1/2 Sin[3 θ]) - 1/2 eta02 k uk201 ε^3 (-Sin[θ]/2 + 1/2 Sin[3 θ]) +
  1/4 eta01 k uk202 ε^3 (-Sin[θ]/2 + 1/2 Sin[3 θ]) - 1/2 eta02 k uk101 ε^3 (Sin[θ]/2 + 1/2 Sin[3 θ]) +
  1/2 eta02 k uk201 ε^3 (Sin[θ]/2 + 1/2 Sin[3 θ]) - eta01 k uk202 ε^3 (Sin[θ]/2 + 1/2 Sin[3 θ]) -
  3/2 d k uk203 ε^3 Sin[3 θ] - w1203 ε^3 Sin[3 θ] + ws03 ε^3 Sin[3 θ] == 0

eq3 = 1/2 * D[h * uk1[t, x], x] - 1/4 * (uk1[t, x] + uk2[t, x]) * D[h - 2 d, x] + w12[t, x] == 0 /.
  k * x -> t * ω (1 + ε^2 * ω13) + θ // Expand;

eq3new1 =
  Replace[Expand@eq3, p_Plus -> DeleteCases[p, _?(FreeQ[ε])], All] /. ε^b_ /; b ≥ 2 -> 0
- 1/2 d k uk101 ε Sin[θ] + w1201 ε Sin[θ] == 0

eq3new2 = Replace[Expand@eq3, p_Plus -> DeleteCases[p, _?(FreeQ[ε])], All] /.
  ε^b_ /; b >= 3 -> 0 /. ε^2 -> a /. ε -> 0 /. a -> ε^2
- 3/4 eta01 k uk101 ε^2 Cos[θ] Sin[θ] +
  1/4 eta01 k uk201 ε^2 Cos[θ] Sin[θ] - d k uk102 ε^2 Sin[2 θ] + w1202 ε^2 Sin[2 θ] == 0

eq3new3 =
  Replace[Expand@eq3, p_Plus -> DeleteCases[p, _?(FreeQ[ε])], All] /. ε^b_ /; b ≥ 4 -> 0 /.
  ε^3 -> a /. ε -> 0 /. a -> ε^3 /. trig
- 1/2 d k uk101 uk1013 ε^3 Sin[θ] +
  w1201 w12013 ε^3 Sin[θ] - 1/2 eta02 k uk101 ε^3 (-Sin[θ]/2 + 1/2 Sin[3 θ]) -
  1/4 eta01 k uk102 ε^3 (-Sin[θ]/2 + 1/2 Sin[3 θ]) + 1/4 eta01 k uk202 ε^3 (-Sin[θ]/2 + 1/2 Sin[3 θ]) -
  1/2 eta02 k uk101 ε^3 (Sin[θ]/2 + 1/2 Sin[3 θ]) - eta01 k uk102 ε^3 (Sin[θ]/2 + 1/2 Sin[3 θ]) +
  1/2 eta02 k uk201 ε^3 (Sin[θ]/2 + 1/2 Sin[3 θ]) - 3/2 d k uk103 ε^3 Sin[3 θ] + w1203 ε^3 Sin[3 θ] == 0

```

Horizontal momentum equations

```

eq4 =
  1/2 * D[h * uk2[t, x], t] + 1/2 * D[h * uk2[t, x] * uk2[t, x], x] - 1/2 * (uk1[t, x] + uk2[t, x]) *
  wre112[t, x] + 1/2 * h * g * D[eta[t, x], x] + 1/4 * D[h * q12[t, x], x] +
  1/2 * q12[t, x] * D[h - 2 * d, x] == 0 /. k * x -> t * ω (1 + ε^2 * ω13) + θ // Expand;

eq4new1 =
  Replace[Expand@eq4, p_Plus -> DeleteCases[p, _?(FreeQ[ε])], All] /. ε^b_ /; b ≥ 2 -> 0
- 1/2 d eta01 g k ε Sin[θ] - 1/4 d k q1201 ε Sin[θ] + 1/2 d uk201 ε ω Sin[θ] == 0

```

$$\text{eq4new2} = \text{Replace}[\text{Expand@eq4}, \text{p_Plus} \Rightarrow \text{DeleteCases}[\text{p}, _?(\text{FreeQ}[\epsilon])], \text{All}] /. \epsilon^b _ / ; b >= 3 \rightarrow 0 /. \epsilon^2 \rightarrow a /. \epsilon \rightarrow 0 /. a \rightarrow \epsilon^2$$

$$\begin{aligned} & -\frac{1}{2} \text{eta01}^2 g k \epsilon^2 \text{Cos}[\theta] \text{Sin}[\theta] - \text{eta01} k q1201 \epsilon^2 \text{Cos}[\theta] \text{Sin}[\theta] - d k u k201^2 \epsilon^2 \text{Cos}[\theta] \text{Sin}[\theta] - \\ & \frac{1}{2} u k101 w1201 \epsilon^2 \text{Cos}[\theta] \text{Sin}[\theta] - \frac{1}{2} u k201 w1201 \epsilon^2 \text{Cos}[\theta] \text{Sin}[\theta] + \\ & \frac{1}{4} \text{eta01} u k101 \epsilon^2 \omega \text{Cos}[\theta] \text{Sin}[\theta] + \frac{5}{4} \text{eta01} u k201 \epsilon^2 \omega \text{Cos}[\theta] \text{Sin}[\theta] - \\ & d \text{eta02} g k \epsilon^2 \text{Sin}[2\theta] - \frac{1}{2} d k q1202 \epsilon^2 \text{Sin}[2\theta] + d u k202 \epsilon^2 \omega \text{Sin}[2\theta] = 0 \end{aligned}$$

$$\text{eq4new3} =$$

$$\text{Replace}[\text{Expand@eq4}, \text{p_Plus} \Rightarrow \text{DeleteCases}[\text{p}, _?(\text{FreeQ}[\epsilon])], \text{All}] /. \epsilon^b _ / ; b \geq 4 \rightarrow 0 /. \epsilon^3 \rightarrow a /. \epsilon \rightarrow 0 /. a \rightarrow \epsilon^3 /. \text{trig}$$

$$\begin{aligned} & -\frac{1}{4} d k q1201 q12013 \epsilon^3 \text{Sin}[\theta] + \frac{1}{2} d u k201 u k2013 \epsilon^3 \omega \text{Sin}[\theta] + \\ & \frac{1}{2} d u k201 \epsilon^3 \omega w13 \text{Sin}[\theta] - \frac{1}{2} \text{eta01} \text{eta02} g k \epsilon^3 \left(-\frac{\text{Sin}[\theta]}{2} + \frac{1}{2} \text{Sin}[3\theta] \right) - \\ & \frac{1}{4} \text{eta02} k q1201 \epsilon^3 \left(-\frac{\text{Sin}[\theta]}{2} + \frac{1}{2} \text{Sin}[3\theta] \right) - \frac{3}{4} \text{eta01} k q1202 \epsilon^3 \left(-\frac{\text{Sin}[\theta]}{2} + \frac{1}{2} \text{Sin}[3\theta] \right) - \\ & d k u k201 u k202 \epsilon^3 \left(-\frac{\text{Sin}[\theta]}{2} + \frac{1}{2} \text{Sin}[3\theta] \right) - \frac{1}{2} u k102 w1201 \epsilon^3 \left(-\frac{\text{Sin}[\theta]}{2} + \frac{1}{2} \text{Sin}[3\theta] \right) - \\ & \frac{1}{2} u k202 w1201 \epsilon^3 \left(-\frac{\text{Sin}[\theta]}{2} + \frac{1}{2} \text{Sin}[3\theta] \right) + \frac{1}{4} \text{eta01} u k102 \epsilon^3 \omega \left(-\frac{\text{Sin}[\theta]}{2} + \frac{1}{2} \text{Sin}[3\theta] \right) + \\ & \frac{1}{2} \text{eta02} u k201 \epsilon^3 \omega \left(-\frac{\text{Sin}[\theta]}{2} + \frac{1}{2} \text{Sin}[3\theta] \right) + \frac{3}{4} \text{eta01} u k202 \epsilon^3 \omega \left(-\frac{\text{Sin}[\theta]}{2} + \frac{1}{2} \text{Sin}[3\theta] \right) - \\ & \text{eta01} \text{eta02} g k \epsilon^3 \left(\frac{\text{Sin}[\theta]}{2} + \frac{1}{2} \text{Sin}[3\theta] \right) - \frac{3}{2} \text{eta02} k q1201 \epsilon^3 \left(\frac{\text{Sin}[\theta]}{2} + \frac{1}{2} \text{Sin}[3\theta] \right) - \\ & \frac{1}{2} \text{eta01} k q1202 \epsilon^3 \left(\frac{\text{Sin}[\theta]}{2} + \frac{1}{2} \text{Sin}[3\theta] \right) - 2 d k u k201 u k202 \epsilon^3 \left(\frac{\text{Sin}[\theta]}{2} + \frac{1}{2} \text{Sin}[3\theta] \right) - \\ & \frac{1}{2} u k101 w1202 \epsilon^3 \left(\frac{\text{Sin}[\theta]}{2} + \frac{1}{2} \text{Sin}[3\theta] \right) - \frac{1}{2} u k201 w1202 \epsilon^3 \left(\frac{\text{Sin}[\theta]}{2} + \frac{1}{2} \text{Sin}[3\theta] \right) + \\ & \frac{1}{2} \text{eta02} u k101 \epsilon^3 \omega \left(\frac{\text{Sin}[\theta]}{2} + \frac{1}{2} \text{Sin}[3\theta] \right) + \frac{3}{2} \text{eta02} u k201 \epsilon^3 \omega \left(\frac{\text{Sin}[\theta]}{2} + \frac{1}{2} \text{Sin}[3\theta] \right) + \\ & \text{eta01} u k202 \epsilon^3 \omega \left(\frac{\text{Sin}[\theta]}{2} + \frac{1}{2} \text{Sin}[3\theta] \right) - \frac{3}{2} d \text{eta03} g k \epsilon^3 \text{Sin}[3\theta] - \\ & \frac{3}{4} d k q1203 \epsilon^3 \text{Sin}[3\theta] + \frac{3}{2} d u k203 \epsilon^3 \omega \text{Sin}[3\theta] - \frac{1}{32} \text{eta01} k u k101^2 \epsilon^3 (\text{Sin}[\theta] + \text{Sin}[3\theta]) - \\ & \frac{1}{16} \text{eta01} k u k101 u k201 \epsilon^3 (\text{Sin}[\theta] + \text{Sin}[3\theta]) - \frac{13}{32} \text{eta01} k u k201^2 \epsilon^3 (\text{Sin}[\theta] + \text{Sin}[3\theta]) = 0 \end{aligned}$$

$$\text{eq5} = \frac{1}{2} * D[h * u k1[t, x], t] + \frac{1}{2} * D[h * u k1[t, x] * u k1[t, x], x] +$$

$$\frac{1}{2} * (u k1[t, x] + u k2[t, x]) * w r e l12[t, x] + \frac{1}{2} * h * g * D[\text{eta}[t, x], x] +$$

$$\frac{1}{4} * D[h * (q12[t, x] + q b[t, x]), x] - \frac{1}{2} * q12[t, x] * D[h - 2 * d, x] - q b * D[d, x] ==$$

$$0 /. k * x \rightarrow t * \omega (1 + \epsilon^2 * w13) + \theta // \text{Expand};$$

$$\text{eq5new1} =$$

$$\text{Replace}[\text{Expand@eq5}, \text{p_Plus} \Rightarrow \text{DeleteCases}[\text{p}, _?(\text{FreeQ}[\epsilon])], \text{All}] /. \epsilon^b _ / ; b \geq 2 \rightarrow 0$$

$$-\frac{1}{2} d \text{eta01} g k \epsilon \text{Sin}[\theta] - \frac{1}{4} d k q1201 \epsilon \text{Sin}[\theta] - \frac{1}{4} d k q b01 \epsilon \text{Sin}[\theta] + \frac{1}{2} d u k101 \epsilon \omega \text{Sin}[\theta] = 0$$

$$\text{eq5new2} = \text{Replace}[\text{Expand@eq5}, \text{p_Plus} \Rightarrow \text{DeleteCases}[\text{p}, _?(\text{FreeQ}[\epsilon])], \text{All}] /. \epsilon^b _ / ; b >= 3 \rightarrow 0 /. \epsilon^2 \rightarrow a /. \epsilon \rightarrow 0 /. a \rightarrow \epsilon^2$$

$$\begin{aligned} & -\frac{1}{2} \text{eta01}^2 g k \epsilon^2 \text{Cos}[\theta] \text{Sin}[\theta] - \frac{1}{2} \text{eta01} k q b01 \epsilon^2 \text{Cos}[\theta] \text{Sin}[\theta] - \\ & d k u k101^2 \epsilon^2 \text{Cos}[\theta] \text{Sin}[\theta] + \frac{1}{2} u k101 w1201 \epsilon^2 \text{Cos}[\theta] \text{Sin}[\theta] + \\ & \frac{1}{2} u k201 w1201 \epsilon^2 \text{Cos}[\theta] \text{Sin}[\theta] + \frac{3}{4} \text{eta01} u k101 \epsilon^2 \omega \text{Cos}[\theta] \text{Sin}[\theta] - \\ & \frac{1}{4} \text{eta01} u k201 \epsilon^2 \omega \text{Cos}[\theta] \text{Sin}[\theta] - d \text{eta02} g k \epsilon^2 \text{Sin}[2\theta] - \\ & \frac{1}{2} d k q1202 \epsilon^2 \text{Sin}[2\theta] - \frac{1}{2} d k q b02 \epsilon^2 \text{Sin}[2\theta] + d u k102 \epsilon^2 \omega \text{Sin}[2\theta] = 0 \end{aligned}$$

$$\begin{aligned}
& \text{eq5new3} = \\
& \text{Replace}[\text{Expand@eq5}, \text{p_Plus} \Rightarrow \text{DeleteCases}[\text{p}, _?(\text{FreeQ}[\epsilon])], \text{All}] /. \epsilon^{\wedge} \text{b_} /. ; \text{b} \geq 4 \rightarrow \theta /. \\
& \quad \epsilon^3 \rightarrow \text{a} /. \epsilon \rightarrow \theta /. \text{a} \rightarrow \epsilon^3 /. \text{trig} \\
& -\frac{1}{4} \text{d k q1201 q12013} \epsilon^3 \text{Sin}[\theta] - \frac{1}{4} \text{d k qb01 qb013} \epsilon^3 \text{Sin}[\theta] + \\
& \quad \frac{1}{2} \text{d uk101 uk1013} \epsilon^3 \omega \text{Sin}[\theta] + \frac{1}{2} \text{d uk101} \epsilon^3 \omega \omega_{13} \text{Sin}[\theta] - \\
& \quad \frac{1}{2} \text{eta01 eta02 g k} \epsilon^3 \left(-\frac{\text{Sin}[\theta]}{2} + \frac{1}{2} \text{Sin}[3\theta] \right) - \frac{1}{4} \text{eta02 k q1201} \epsilon^3 \left(-\frac{\text{Sin}[\theta]}{2} + \frac{1}{2} \text{Sin}[3\theta] \right) + \\
& \quad \frac{1}{4} \text{eta01 k q1202} \epsilon^3 \left(-\frac{\text{Sin}[\theta]}{2} + \frac{1}{2} \text{Sin}[3\theta] \right) - \frac{1}{4} \text{eta02 k qb01} \epsilon^3 \left(-\frac{\text{Sin}[\theta]}{2} + \frac{1}{2} \text{Sin}[3\theta] \right) - \\
& \quad \frac{1}{4} \text{eta01 k qb02} \epsilon^3 \left(-\frac{\text{Sin}[\theta]}{2} + \frac{1}{2} \text{Sin}[3\theta] \right) - \text{d k uk101 uk102} \epsilon^3 \left(-\frac{\text{Sin}[\theta]}{2} + \frac{1}{2} \text{Sin}[3\theta] \right) + \\
& \quad \frac{1}{2} \text{uk102 w1201} \epsilon^3 \left(-\frac{\text{Sin}[\theta]}{2} + \frac{1}{2} \text{Sin}[3\theta] \right) + \frac{1}{2} \text{uk202 w1201} \epsilon^3 \left(-\frac{\text{Sin}[\theta]}{2} + \frac{1}{2} \text{Sin}[3\theta] \right) + \\
& \quad \frac{1}{2} \text{eta02 uk101} \epsilon^3 \omega \left(-\frac{\text{Sin}[\theta]}{2} + \frac{1}{2} \text{Sin}[3\theta] \right) + \frac{1}{4} \text{eta01 uk102} \epsilon^3 \omega \left(-\frac{\text{Sin}[\theta]}{2} + \frac{1}{2} \text{Sin}[3\theta] \right) - \\
& \quad \frac{1}{4} \text{eta01 uk202} \epsilon^3 \omega \left(-\frac{\text{Sin}[\theta]}{2} + \frac{1}{2} \text{Sin}[3\theta] \right) - \text{eta01 eta02 g k} \epsilon^3 \left(\frac{\text{Sin}[\theta]}{2} + \frac{1}{2} \text{Sin}[3\theta] \right) + \\
& \quad \frac{1}{2} \text{eta02 k q1201} \epsilon^3 \left(\frac{\text{Sin}[\theta]}{2} + \frac{1}{2} \text{Sin}[3\theta] \right) - \frac{1}{2} \text{eta01 k q1202} \epsilon^3 \left(\frac{\text{Sin}[\theta]}{2} + \frac{1}{2} \text{Sin}[3\theta] \right) - \\
& \quad \frac{1}{2} \text{eta02 k qb01} \epsilon^3 \left(\frac{\text{Sin}[\theta]}{2} + \frac{1}{2} \text{Sin}[3\theta] \right) - \frac{1}{2} \text{eta01 k qb02} \epsilon^3 \left(\frac{\text{Sin}[\theta]}{2} + \frac{1}{2} \text{Sin}[3\theta] \right) - \\
& \quad 2 \text{d k uk101 uk102} \epsilon^3 \left(\frac{\text{Sin}[\theta]}{2} + \frac{1}{2} \text{Sin}[3\theta] \right) + \frac{1}{2} \text{uk101 w1202} \epsilon^3 \left(\frac{\text{Sin}[\theta]}{2} + \frac{1}{2} \text{Sin}[3\theta] \right) + \\
& \quad \frac{1}{2} \text{uk201 w1202} \epsilon^3 \left(\frac{\text{Sin}[\theta]}{2} + \frac{1}{2} \text{Sin}[3\theta] \right) + \frac{1}{2} \text{eta02 uk101} \epsilon^3 \omega \left(\frac{\text{Sin}[\theta]}{2} + \frac{1}{2} \text{Sin}[3\theta] \right) + \\
& \quad \text{eta01 uk102} \epsilon^3 \omega \left(\frac{\text{Sin}[\theta]}{2} + \frac{1}{2} \text{Sin}[3\theta] \right) - \frac{1}{2} \text{eta02 uk201} \epsilon^3 \omega \left(\frac{\text{Sin}[\theta]}{2} + \frac{1}{2} \text{Sin}[3\theta] \right) - \\
& \quad \frac{3}{2} \text{d eta03 g k} \epsilon^3 \text{Sin}[3\theta] - \frac{3}{4} \text{d k q1203} \epsilon^3 \text{Sin}[3\theta] - \frac{3}{4} \text{d k qb03} \epsilon^3 \text{Sin}[3\theta] + \\
& \quad \frac{3}{2} \text{d uk103} \epsilon^3 \omega \text{Sin}[3\theta] - \frac{11}{32} \text{eta01 k uk101}^2 \epsilon^3 (\text{Sin}[\theta] + \text{Sin}[3\theta]) + \\
& \quad \frac{1}{16} \text{eta01 k uk101 uk201} \epsilon^3 (\text{Sin}[\theta] + \text{Sin}[3\theta]) + \frac{1}{32} \text{eta01 k uk201}^2 \epsilon^3 (\text{Sin}[\theta] + \text{Sin}[3\theta]) = \theta
\end{aligned}$$

Vertical momentum equations

$$\begin{aligned}
& \text{eq6} = \frac{1}{4} * \text{D}[\text{h} * (\text{ws}[\text{t}, \text{x}] + \text{w12}[\text{t}, \text{x}]), \text{t}] + \frac{1}{4} * \text{D}[\text{h} * \text{uk2}[\text{t}, \text{x}] * (\text{ws}[\text{t}, \text{x}] + \text{w12}[\text{t}, \text{x}]), \text{x}] - \\
& \quad \theta * \text{wrel12}[\text{t}, \text{x}] * \text{w12}[\text{t}, \text{x}] - \text{q12}[\text{t}, \text{x}] = \theta /. \text{k} * \text{x} \rightarrow \text{t} * \omega (1 + \epsilon^2 * \text{w13}) + \theta // \text{Expand};
\end{aligned}$$

$$\begin{aligned}
& \text{eq6new1} = \\
& \text{Replace}[\text{Expand@eq6}, \text{p_Plus} \Rightarrow \text{DeleteCases}[\text{p}, _?(\text{FreeQ}[\epsilon])], \text{All}] /. \epsilon^{\wedge} \text{b_} /. ; \text{b} \geq 2 \rightarrow \theta
\end{aligned}$$

$$-\text{q1201} \epsilon \text{Cos}[\theta] - \frac{1}{4} \text{d w1201} \epsilon \omega \text{Cos}[\theta] - \frac{1}{4} \text{d ws01} \epsilon \omega \text{Cos}[\theta] = \theta$$

$$\begin{aligned}
& \text{eq6new2} = \text{Replace}[\text{Expand@eq6}, \text{p_Plus} \Rightarrow \text{DeleteCases}[\text{p}, _?(\text{FreeQ}[\epsilon])], \text{All}] /. \\
& \quad \epsilon^{\wedge} \text{b_} /. ; \text{b} \geq 3 \rightarrow \theta /. \epsilon^2 \rightarrow \text{a} /. \epsilon \rightarrow \theta /. \text{a} \rightarrow \epsilon^2
\end{aligned}$$

$$\begin{aligned}
& \frac{1}{4} \text{d k uk201 w1201} \epsilon^2 \text{Cos}[\theta]^2 + \frac{1}{4} \text{d k uk201 ws01} \epsilon^2 \text{Cos}[\theta]^2 - \\
& \quad \frac{1}{4} \text{eta01 w1201} \epsilon^2 \omega \text{Cos}[\theta]^2 - \frac{1}{4} \text{eta01 ws01} \epsilon^2 \omega \text{Cos}[\theta]^2 - \text{q1202} \epsilon^2 \text{Cos}[2\theta] - \\
& \quad \frac{1}{2} \text{d w1202} \epsilon^2 \omega \text{Cos}[2\theta] - \frac{1}{2} \text{d ws02} \epsilon^2 \omega \text{Cos}[2\theta] - \frac{1}{4} \text{d k uk201 w1201} \epsilon^2 \text{Sin}[\theta]^2 - \\
& \quad \frac{1}{4} \text{d k uk201 ws01} \epsilon^2 \text{Sin}[\theta]^2 + \frac{1}{4} \text{eta01 w1201} \epsilon^2 \omega \text{Sin}[\theta]^2 + \frac{1}{4} \text{eta01 ws01} \epsilon^2 \omega \text{Sin}[\theta]^2 = \theta
\end{aligned}$$

eq6new3 =

Replace[Expand@eq6, p_Plus \Rightarrow DeleteCases[p, _? (FreeQ[ϵ])], All] /. $\epsilon^b \rightarrow \theta$ /. $b \geq 4 \rightarrow \theta$ /. $\epsilon^3 \rightarrow a$ /. $\epsilon \rightarrow \theta$ /. $a \rightarrow \epsilon^3$ /. trig

$$\begin{aligned}
& -q1201 q12013 \epsilon^3 \cos[\theta] - \frac{1}{4} d w1201 w12013 \epsilon^3 \omega \cos[\theta] - \\
& \frac{1}{4} d w s01 w s013 \epsilon^3 \omega \cos[\theta] - \frac{1}{4} d w1201 \epsilon^3 \omega \omega13 \cos[\theta] - \\
& \frac{1}{4} d w s01 \epsilon^3 \omega \omega13 \cos[\theta] - \frac{1}{8} \text{eta01} k uk201 w1201 \epsilon^3 (\cos[\theta] - \cos[3\theta]) - \\
& \frac{1}{8} \text{eta01} k uk201 w s01 \epsilon^3 (\cos[\theta] - \cos[3\theta]) - \frac{1}{2} d k uk202 w1201 \epsilon^3 \left(\frac{\cos[\theta]}{2} - \frac{1}{2} \cos[3\theta] \right) - \\
& \frac{1}{4} d k uk201 w1202 \epsilon^3 \left(\frac{\cos[\theta]}{2} - \frac{1}{2} \cos[3\theta] \right) - \frac{1}{2} d k uk202 w s01 \epsilon^3 \left(\frac{\cos[\theta]}{2} - \frac{1}{2} \cos[3\theta] \right) - \\
& \frac{1}{4} d k uk201 w s02 \epsilon^3 \left(\frac{\cos[\theta]}{2} - \frac{1}{2} \cos[3\theta] \right) + \frac{1}{2} \text{eta02} w1201 \epsilon^3 \omega \left(\frac{\cos[\theta]}{2} - \frac{1}{2} \cos[3\theta] \right) + \\
& \frac{1}{4} \text{eta01} w1202 \epsilon^3 \omega \left(\frac{\cos[\theta]}{2} - \frac{1}{2} \cos[3\theta] \right) + \frac{1}{2} \text{eta02} w s01 \epsilon^3 \omega \left(\frac{\cos[\theta]}{2} - \frac{1}{2} \cos[3\theta] \right) + \\
& \frac{1}{4} \text{eta01} w s02 \epsilon^3 \omega \left(\frac{\cos[\theta]}{2} - \frac{1}{2} \cos[3\theta] \right) + \frac{1}{4} d k uk202 w1201 \epsilon^3 \left(\frac{\cos[\theta]}{2} + \frac{1}{2} \cos[3\theta] \right) + \\
& \frac{1}{2} d k uk201 w1202 \epsilon^3 \left(\frac{\cos[\theta]}{2} + \frac{1}{2} \cos[3\theta] \right) + \frac{1}{4} d k uk202 w s01 \epsilon^3 \left(\frac{\cos[\theta]}{2} + \frac{1}{2} \cos[3\theta] \right) + \\
& \frac{1}{2} d k uk201 w s02 \epsilon^3 \left(\frac{\cos[\theta]}{2} + \frac{1}{2} \cos[3\theta] \right) - \frac{1}{4} \text{eta02} w1201 \epsilon^3 \omega \left(\frac{\cos[\theta]}{2} + \frac{1}{2} \cos[3\theta] \right) - \\
& \frac{1}{2} \text{eta01} w1202 \epsilon^3 \omega \left(\frac{\cos[\theta]}{2} + \frac{1}{2} \cos[3\theta] \right) - \frac{1}{4} \text{eta02} w s01 \epsilon^3 \omega \left(\frac{\cos[\theta]}{2} + \frac{1}{2} \cos[3\theta] \right) - \\
& \frac{1}{2} \text{eta01} w s02 \epsilon^3 \omega \left(\frac{\cos[\theta]}{2} + \frac{1}{2} \cos[3\theta] \right) - q1203 \epsilon^3 \cos[3\theta] - \frac{3}{4} d w1203 \epsilon^3 \omega \cos[3\theta] - \\
& \frac{3}{4} d w s03 \epsilon^3 \omega \cos[3\theta] + \frac{1}{16} \text{eta01} k uk201 w1201 \epsilon^3 (3 \cos[\theta] + \cos[3\theta]) + \\
& \frac{1}{16} \text{eta01} k uk201 w s01 \epsilon^3 (3 \cos[\theta] + \cos[3\theta]) = 0
\end{aligned}$$

$$\begin{aligned}
\text{eq7} &= \frac{1}{4} * D[h * (wb[t, x] + w12[t, x]), t] + \frac{1}{4} * D[h * uk1[t, x] * (wb[t, x] + w12[t, x]), x] + \\
& q12[t, x] - qb[t, x] + \theta * wre112[t, x] * w12[t, x] = 0 /. \\
& k * x \rightarrow t * \omega (1 + \epsilon^2 * \omega13) + \theta // \text{Expand};
\end{aligned}$$

eq7new1 =

Replace[Expand@eq7, p_Plus \Rightarrow DeleteCases[p, _? (FreeQ[ϵ])], All] /. $\epsilon^b \rightarrow \theta$ /. $b \geq 2 \rightarrow \theta$

$$q1201 \in \cos[\theta] - qb01 \in \cos[\theta] - \frac{1}{4} d w1201 \in \omega \cos[\theta] = 0$$

eq7new2 = Replace[Expand@eq7, p_Plus \Rightarrow DeleteCases[p, _? (FreeQ[ϵ])], All] /. $\epsilon^b \rightarrow \theta$ /. $b \geq 3 \rightarrow \theta$ /. $\epsilon^2 \rightarrow a$ /. $\epsilon \rightarrow \theta$ /. $a \rightarrow \epsilon^2$

$$\begin{aligned}
& \frac{1}{4} d k uk101 w1201 \epsilon^2 \cos[\theta]^2 - \frac{1}{4} \text{eta01} w1201 \epsilon^2 \omega \cos[\theta]^2 + q1202 \epsilon^2 \cos[2\theta] - qb02 \epsilon^2 \cos[2\theta] - \\
& \frac{1}{2} d w1202 \epsilon^2 \omega \cos[2\theta] - \frac{1}{4} d k uk101 w1201 \epsilon^2 \sin[\theta]^2 + \frac{1}{4} \text{eta01} w1201 \epsilon^2 \omega \sin[\theta]^2 = 0
\end{aligned}$$

eq7new3 =

Replace[Expand@eq7, p_Plus \Rightarrow DeleteCases[p, _? (FreeQ[ϵ])], All] /. $\epsilon^b \rightarrow \theta$ /. $b \geq 4 \rightarrow \theta$ /. $\epsilon^3 \rightarrow a$ /. $\epsilon \rightarrow \theta$ /. $a \rightarrow \epsilon^3$ /. trig

$$\begin{aligned}
& q1201 q12013 \epsilon^3 \cos[\theta] - qb01 qb013 \epsilon^3 \cos[\theta] - \\
& \frac{1}{4} d w1201 w12013 \epsilon^3 \omega \cos[\theta] - \frac{1}{4} d w1201 \epsilon^3 \omega \omega13 \cos[\theta] - \\
& \frac{1}{8} \text{eta01} k uk101 w1201 \epsilon^3 (\cos[\theta] - \cos[3\theta]) - \frac{1}{2} d k uk102 w1201 \epsilon^3 \left(\frac{\cos[\theta]}{2} - \frac{1}{2} \cos[3\theta] \right) - \\
& \frac{1}{4} d k uk101 w1202 \epsilon^3 \left(\frac{\cos[\theta]}{2} - \frac{1}{2} \cos[3\theta] \right) + \frac{1}{2} \text{eta02} w1201 \epsilon^3 \omega \left(\frac{\cos[\theta]}{2} - \frac{1}{2} \cos[3\theta] \right) + \\
& \frac{1}{4} \text{eta01} w1202 \epsilon^3 \omega \left(\frac{\cos[\theta]}{2} - \frac{1}{2} \cos[3\theta] \right) + \frac{1}{4} d k uk102 w1201 \epsilon^3 \left(\frac{\cos[\theta]}{2} + \frac{1}{2} \cos[3\theta] \right) + \\
& \frac{1}{2} d k uk101 w1202 \epsilon^3 \left(\frac{\cos[\theta]}{2} + \frac{1}{2} \cos[3\theta] \right) - \frac{1}{4} \text{eta02} w1201 \epsilon^3 \omega \left(\frac{\cos[\theta]}{2} + \frac{1}{2} \cos[3\theta] \right) - \\
& \frac{1}{2} \text{eta01} w1202 \epsilon^3 \omega \left(\frac{\cos[\theta]}{2} + \frac{1}{2} \cos[3\theta] \right) + q1203 \epsilon^3 \cos[3\theta] - qb03 \epsilon^3 \cos[3\theta] - \\
& \frac{3}{4} d w1203 \epsilon^3 \omega \cos[3\theta] + \frac{1}{16} \text{eta01} k uk101 w1201 \epsilon^3 (3 \cos[\theta] + \cos[3\theta]) = 0
\end{aligned}$$

First order solution - Linear Dispersion Relation

```

s1 = Solve[eq1new1, uk201] // FullSimplify;
s2 = Solve[eq2new1 /. s1[[1]], uk101] // FullSimplify;
s3 = Solve[eq3new1 /. s1[[1]] /. s2[[1]], ws01] // FullSimplify;
s4 = Solve[eq4new1 /. s1[[1]] /. s2[[1]] /. s3[[1]], w1201] // FullSimplify;
s5 = Solve[eq5new1 /. s1[[1]] /. s2[[1]] /. s3[[1]] /. s4[[1]], q1201] // FullSimplify;
s6 = Solve[eq6new1 /. s1[[1]] /. s2[[1]] /. s3[[1]] /. s4[[1]] /. s5[[1]], qb01] //
FullSimplify;
s7 =
Solve[eq7new1 /. s1[[1]] /. s2[[1]] /. s3[[1]] /. s4[[1]] /. s5[[1]] /. s6[[1]], ω] //
FullSimplify;

```

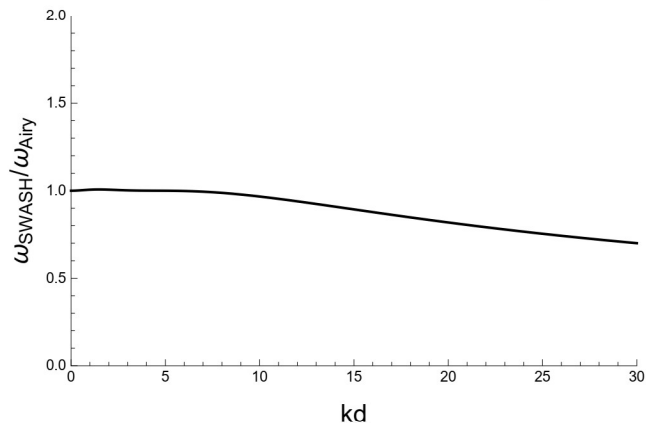
```
Framed[%]
```

$$\left\{ \left\{ \omega \rightarrow -\frac{4\sqrt{d g k^2 (16 + d^2 k^2)}}{\sqrt{256 + 96 d^2 k^2 + d^4 k^4}} \right\}, \left\{ \omega \rightarrow \frac{4\sqrt{d g k^2 (16 + d^2 k^2)}}{\sqrt{256 + 96 d^2 k^2 + d^4 k^4}} \right\} \right\}$$

```
ωex = Sqrt[g k Tanh[d k]] ;
```

```
a1 = Simplify[s7[[2, 1, 2]] / ωex, k * d == kd];
```

```
Plot[a1, {kd, -0, 30}, PlotRange -> {{0, 30.0}, {0.0, 2.0}}, ImageSize -> 400,
Axes -> False, PlotStyle -> {Black}, Frame -> {True, True, False, False},
FrameLabel -> {Style["kd", 16], Style["ωSWASH/ωAiry", 16]}, FrameTicks -> All]
```



Second order solution - wave amplitude

```

s8 = Solve[
eq1new2 /. s1[[1]] /. s2[[1]] /. s3[[1]] /. s4[[1]] /. s5[[1]] /. s6[[1]], uk202];
s9 = Solve[eq2new2 /. s1[[1]] /. s2[[1]] /. s3[[1]] /. s4[[1]] /. s5[[1]] /. s6[[1]] /.
s8[[1]], uk102];
s10 = Solve[eq3new2 /. s1[[1]] /. s2[[1]] /. s3[[1]] /. s4[[1]] /. s5[[1]] /. s6[[1]] /.
s8[[1]] /. s9[[1]], ws02];
s11 = Solve[eq4new2 /. s1[[1]] /. s2[[1]] /. s3[[1]] /. s4[[1]] /. s5[[1]] /. s6[[1]] /.
s8[[1]] /. s9[[1]] /. s10[[1]], w1202];

```

```

s12 = Solve[eq5new2 /. s1[[1]] /. s2[[1]] /. s3[[1]] /. s4[[1]] /. s5[[1]] /. s6[[1]] /.
s8[[1]] /. s9[[1]] /. s10[[1]] /. s11[[1]], q1202];

s13 =
Solve[eq6new2 /. s1[[1]] /. s2[[1]] /. s3[[1]] /. s4[[1]] /. s5[[1]] /. s6[[1]] /. s8[[
1]] /. s9[[1]] /. s10[[1]] /. s11[[1]] /. s12[[1]], qb02];

s14 =
Solve[eq7new2 /. s1[[1]] /. s2[[1]] /. s3[[1]] /. s4[[1]] /. s5[[1]] /. s6[[1]] /. s8[[
1]] /. s9[[1]] /. s10[[1]] /. s11[[1]] /.
s12[[1]] /. s13[[1]] /. s7[[2, 1]], eta02] // FullSimplify;

```

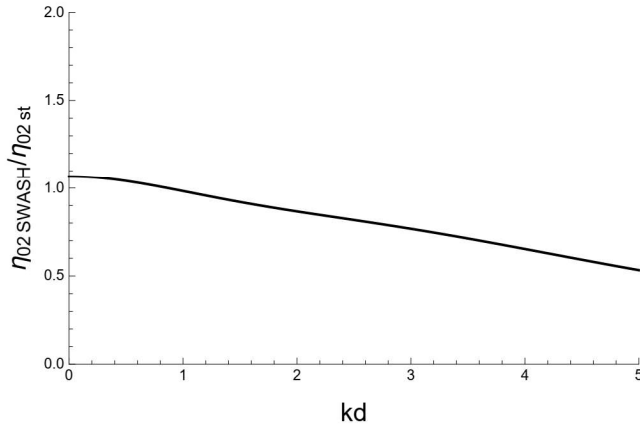
```
Framed[%]
```

$$\left\{ \left\{ \eta_{02} \rightarrow \frac{\eta_{02}^2 \left(49152 + 33792 d^2 k^2 + 9792 d^4 k^4 + 892 d^6 k^6 + 7 d^8 k^8 \right)}{12 d^3 k^2 \left(16 + d^2 k^2 \right) \left(320 + 20 d^2 k^2 + d^4 k^4 \right)} \right\} \right\}$$

```
as =  $\frac{1}{4} \eta_{02}^2 * k * \left( 3 * \left( \text{Coth}[k * d] \right)^3 - \text{Coth}[k * d] \right);$ 
```

```
b = Simplify[s14[[1, 1, 2]] / as, k * d == kd];
```

```
Plot[b, {kd, -0, 5}, PlotRange -> {{0, 5.0}, {0.0, 2.0}}, ImageSize -> 400,
Axes -> False, PlotStyle -> {Black}, Frame -> {True, True, False, False},
FrameLabel -> {Style["kd", 16], Style[" $\eta_{02 \text{ SWASH}} / \eta_{02 \text{ st}}$ ", 16]}, FrameTicks -> All]
```



Third order solution- amplitude dispersion and wave amplitude

```

s15 =
Solve[eq1new3 /. {Cos[3 *  $\theta$ ] -> 0, Sin[3 *  $\theta$ ] -> 0} /. s1[[1]] /. s2[[1]] /. s3[[1]] /.
s4[[1]] /. s5[[1]] /. s6[[1]] /. s8[[1]] /. s9[[1]] /. s10[[1]] /.
s11[[1]] /. s12[[1]] /. s13[[1]] /. s14[[1]], uk2013];

s16 =
Solve[eq2new3 /. {Cos[3 *  $\theta$ ] -> 0, Sin[3 *  $\theta$ ] -> 0} /. s1[[1]] /. s2[[1]] /. s3[[1]] /.
s4[[1]] /. s5[[1]] /. s6[[1]] /. s8[[1]] /. s9[[1]] /. s10[[1]] /.
s11[[1]] /. s12[[1]] /. s13[[1]] /. s14[[1]] /. s15[[1]], uk1013];

s17 =
Solve[eq3new3 /. {Cos[3 *  $\theta$ ] -> 0, Sin[3 *  $\theta$ ] -> 0} /. s1[[1]] /. s2[[1]] /. s3[[1]] /.
s4[[1]] /. s5[[1]] /. s6[[1]] /. s8[[1]] /. s9[[1]] /. s10[[1]] /.
s11[[1]] /. s12[[1]] /. s13[[1]] /. s14[[1]] /. s15[[1]] /. s16[[1]], ws013];

```

```
s18 =
Solve[eq4new3 /. {Cos[3 *  $\theta$ ] -> 0, Sin[3 *  $\theta$ ] -> 0} /. s1[[1]] /. s2[[1]] /. s3[[1]] /.
s4[[1]] /. s5[[1]] /. s6[[1]] /. s8[[1]] /.
s9[[1]] /. s10[[1]] /. s11[[1]] /. s12[[1]] /. s13[[1]] /.
s14[[1]] /. s15[[1]] /. s16[[1]] /. s17[[1]], w12013];
```

```
s19 =
Solve[eq5new3 /. {Cos[3 *  $\theta$ ] -> 0, Sin[3 *  $\theta$ ] -> 0} /. s1[[1]] /. s2[[1]] /. s3[[1]] /.
s4[[1]] /. s5[[1]] /. s6[[1]] /. s8[[1]] /. s9[[1]] /.
s10[[1]] /. s11[[1]] /. s12[[1]] /. s13[[1]] /. s14[[1]] /.
s15[[1]] /. s16[[1]] /. s17[[1]] /. s18[[1]], q12013];
```

```
s20 =
Solve[eq6new3 /. {Cos[3 *  $\theta$ ] -> 0, Sin[3 *  $\theta$ ] -> 0} /. s1[[1]] /. s2[[1]] /. s3[[1]] /.
s4[[1]] /. s5[[1]] /. s6[[1]] /. s8[[1]] /. s9[[1]] /. s10[[1]] /.
s11[[1]] /. s12[[1]] /. s13[[1]] /. s14[[1]] /. s15[[1]] /.
s16[[1]] /. s17[[1]] /. s18[[1]] /. s19[[1]], qb013];
```

```
s21 =
Solve[eq7new3 /. {Cos[3 *  $\theta$ ] -> 0, Sin[3 *  $\theta$ ] -> 0} /. s1[[1]] /. s2[[1]] /. s3[[1]] /.
s4[[1]] /. s5[[1]] /. s6[[1]] /. s8[[1]] /. s9[[1]] /.
s10[[1]] /. s11[[1]] /. s12[[1]] /. s13[[1]] /. s14[[1]] /.
s15[[1]] /. s16[[1]] /. s17[[1]] /. s18[[1]] /. s19[[1]] /.
s20[[1]] /. s7[[2, 1]],  $\omega$ 13] // FullSimplify;
```

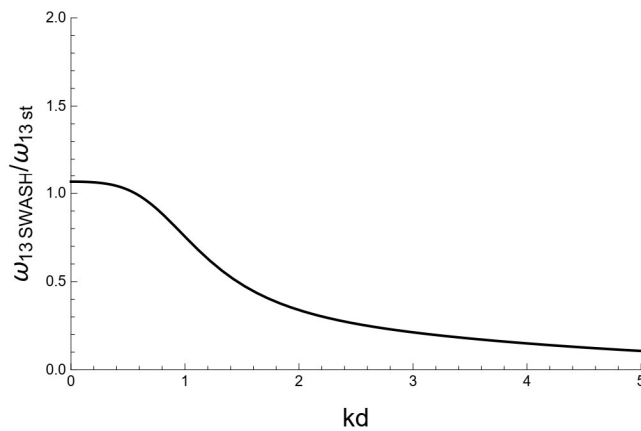
```
Framed[%]
```

$$\left\{ \left\{ \omega_{13} \rightarrow \frac{\left(\eta_{01}^2 \left(1207959552 + d^2 k^2 \left(855638016 + d^2 k^2 \left(687341568 + d^2 k^2 \left(147062784 + 17270784 d^2 k^2 + 1173504 d^4 k^4 + 16568 d^6 k^6 + 89 d^8 k^8 \right) \right) \right) \right) \right) \right) \right) \right\} / \left(96 d^4 k^2 \left(16 + d^2 k^2 \right)^2 \left(320 + 20 d^2 k^2 + d^4 k^4 \right) \left(256 + 96 d^2 k^2 + d^4 k^4 \right) \right) \right\}$$

$$\omega_{13st} = \frac{1}{16} \frac{\eta_{01}^2}{d^2} * k^2 * d^2 * \frac{\left(9 * (\text{Tanh}[k * d])^4 - 10 * (\text{Tanh}[k * d])^2 + 9 \right)}{(\text{Tanh}[k * d])^4};$$

```
b = Simplify[s21[[1, 1, 2]] /  $\omega$ 13st, k * d == kd];
```

```
Plot[b, {kd, -0, 5}, PlotRange -> {{0, 5.0}, {0, 2.0}}, ImageSize -> 400,
Axes -> False, PlotStyle -> {Black}, Frame -> {True, True, False, False},
FrameLabel -> {Style["kd", 16], Style[" $\omega_{13}$  SWASH /  $\omega_{13st}$ ", 16]}, FrameTicks -> All]
```



```
s22 =
Solve[eq1new3 /. s1[[1]] /. s2[[1]] /. s3[[1]] /. s4[[1]] /. s5[[1]] /. s6[[1]] /. s8[[1]] /.
s9[[1]] /. s10[[1]] /. s11[[1]] /. s12[[1]] /.
s13[[1]] /. s14[[1]] /. s15[[1]] /. s16[[1]] /. s17[[1]] /.
s18[[1]] /. s19[[1]] /. s20[[1]], uk203] // Simplify;
```

```

s23 =
  Solve[eq2new3 /. s1[[1]] /. s2[[1]] /. s3[[1]] /. s4[[1]] /. s5[[1]] /. s6[[1]] /. s8[[
    1]] /. s9[[1]] /. s10[[1]] /. s11[[1]] /. s12[[1]] /. s13[[1]] /.
    s14[[1]] /. s15[[1]] /. s16[[1]] /. s17[[1]] /. s18[[1]] /.
    s19[[1]] /. s20[[1]] /. s22[[1]], uk103] // Simplify;

s24 =
  Solve[eq3new3 /. s1[[1]] /. s2[[1]] /. s3[[1]] /. s4[[1]] /. s5[[1]] /. s6[[1]] /. s8[[
    1]] /. s9[[1]] /. s10[[1]] /. s11[[1]] /. s12[[1]] /. s13[[1]] /.
    s14[[1]] /. s15[[1]] /. s16[[1]] /. s17[[1]] /. s18[[1]] /.
    s19[[1]] /. s20[[1]] /. s22[[1]] /. s23[[1]], ws03] // Simplify;

s25 =
  Solve[eq4new3 /. s1[[1]] /. s2[[1]] /. s3[[1]] /. s4[[1]] /. s5[[1]] /. s6[[1]] /. s8[[
    1]] /. s9[[1]] /. s10[[1]] /. s11[[1]] /. s12[[1]] /. s13[[1]] /.
    s14[[1]] /. s15[[1]] /. s16[[1]] /. s17[[1]] /. s18[[1]] /. s19[[1]] /.
    s20[[1]] /. s22[[1]] /. s23[[1]] /. s24[[1]], w1203] // Simplify;

s26 =
  Solve[eq5new3 /. s1[[1]] /. s2[[1]] /. s3[[1]] /. s4[[1]] /. s5[[1]] /. s6[[1]] /. s8[[
    1]] /. s9[[1]] /. s10[[1]] /. s11[[1]] /.
    s12[[1]] /. s13[[1]] /. s14[[1]] /. s15[[1]] /. s16[[1]] /.
    s17[[1]] /. s18[[1]] /. s19[[1]] /. s20[[1]] /. s22[[1]] /.
    s23[[1]] /. s24[[1]] /. s25[[1]], ql203] // Simplify;

s27 =
  Solve[eq6new3 /. s1[[1]] /. s2[[1]] /. s3[[1]] /. s4[[1]] /. s5[[1]] /. s6[[1]] /. s8[[
    1]] /. s9[[1]] /. s10[[1]] /. s11[[1]] /. s12[[1]] /.
    s13[[1]] /. s14[[1]] /. s15[[1]] /. s16[[1]] /. s17[[1]] /.
    s18[[1]] /. s19[[1]] /. s20[[1]] /. s22[[1]] /. s23[[1]] /.
    s24[[1]] /. s25[[1]] /. s26[[1]], qb03] // Simplify;

s28 =
  Solve[eq7new3 /. s1[[1]] /. s2[[1]] /. s3[[1]] /. s4[[1]] /. s5[[1]] /. s6[[1]] /. s8[[
    1]] /. s9[[1]] /. s10[[1]] /. s11[[1]] /. s12[[1]] /.
    s13[[1]] /. s14[[1]] /. s15[[1]] /. s16[[1]] /.
    s17[[1]] /. s18[[1]] /. s19[[1]] /. s20[[1]] /. s22[[1]] /.
    s23[[1]] /. s24[[1]] /. s25[[1]] /. s26[[1]] /. s27[[1]] /.
    s7[[2, 1]] /. s21[[1]], eta03] // FullSimplify;

```

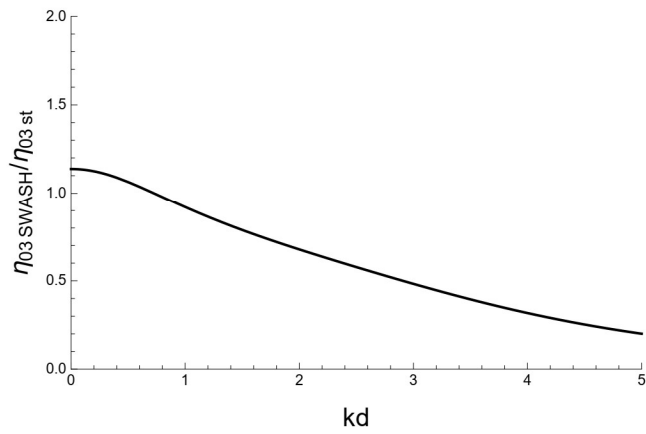
```
Framed[%]
```

$$\left\{ \left\{ \eta_0 \rightarrow \eta_1^3 \right. \right. \\ \left. \left. \frac{(1207959552 + d^2 k^2 (1962934272 + d^2 k^2 (1738014720 + d^2 k^2 (682622976 + 145885184 \\ d^2 k^2 + 14327296 d^4 k^4 + 267928 d^6 k^6 + 2853 d^8 k^8))))}{(384 d^6 k^4 (16 + d^2 k^2) (320 + 20 d^2 k^2 + d^4 k^4) (1280 + 160 d^2 k^2 + 9 d^4 k^4))} \right\} \right\}$$

$$\text{ast3} = \frac{3}{64} \frac{\eta_1^3}{d^2} * k^2 * d^2 * \frac{1 + 8 * (\text{Cosh}[k * d])^6}{(\text{Sinh}[k * d])^6};$$

```
b = Simplify[s28[[1, 1, 2]]/ast3, k * d == kd];
```

```
Plot[b, {kd, -0, 5}, PlotRange -> {{0, 5.0}, {0, 2.0}}, ImageSize -> 400,  
Axes -> False, PlotStyle -> {Black}, Frame -> {True, True, False, False},  
FrameLabel -> {Style["kd", 16], Style[" $\eta_{03 \text{ SWASH}}/\eta_{03 \text{ st}}$ ", 16]}, FrameTicks -> All]
```



```
Quit[]
```

B.2 Second order solutions

Second order amplitude of the surface elevation

\$Assumptions = g > 0 && d > 0 && k > 0;

Exact solution

$$\eta_{2ex} = \frac{1}{4} \eta_{01}^2 * k * \left(3 * (\text{Coth}[k * d])^3 - \text{Coth}[k * d] \right);$$

One layer

$$\eta_{2k1} = \frac{\eta_{01}^2 \left(d^2 + \frac{4}{k^2} \right)}{4 d^3};$$

Two layers

$$\eta_{2k2} = \left(\eta_{01}^2 \left(49 152 + 33 792 d^2 k^2 + 9792 d^4 k^4 + 892 d^6 k^6 + 7 d^8 k^8 \right) \right) / \left(12 d^3 k^2 \left(16 + d^2 k^2 \right) \left(320 + 20 d^2 k^2 + d^4 k^4 \right) \right);$$

Three layers

$$\eta_{2k3} = \left(\eta_{01}^2 \left(44 079 842 304 + 38 773 935 360 d^2 k^2 + 14 751 227 520 d^4 k^4 + 2 589 058 080 d^6 k^6 + 151 553 268 d^8 k^8 + 2 932 065 d^{10} k^{10} + 16 482 d^{12} k^{12} + 25 d^{14} k^{14} \right) \right) / \left(36 d^3 k^2 \left(1 587 237 120 + 411 505 920 d^2 k^2 + 42 620 256 d^4 k^4 + 1 963 440 d^6 k^6 + 32 337 d^8 k^8 + 270 d^{10} k^{10} + d^{12} k^{12} \right) \right);$$

Four layers

$$\eta_{2k4} = \left(\eta_{01}^2 \left(54 043 195 528 445 952 + 53 198 770 598 313 984 d^2 k^2 + 22 935 812 555 407 360 d^4 k^4 + 5 028 960 027 017 216 d^6 k^6 + 466 739 464 765 440 d^8 k^8 + 20 187 671 691 264 d^{10} k^{10} + 420 926 980 096 d^{12} k^{12} + 3 866 914 816 d^{14} k^{14} + 12 686 592 d^{16} k^{16} + 15 504 d^{18} k^{18} + 7 d^{20} k^{20} \right) \right) / \left(12 d^3 k^2 \left(5 910 974 510 923 776 + 2 031 897 488 130 048 d^2 k^2 + 281 406 257 233 920 d^4 k^4 + 19 189 913 878 528 d^6 k^6 + 658 254 069 760 d^8 k^8 + 11 703 681 024 d^{10} k^{10} + 105 091 072 d^{12} k^{12} + 446 208 d^{14} k^{14} + 1008 d^{16} k^{16} + d^{18} k^{18} \right) \right);$$

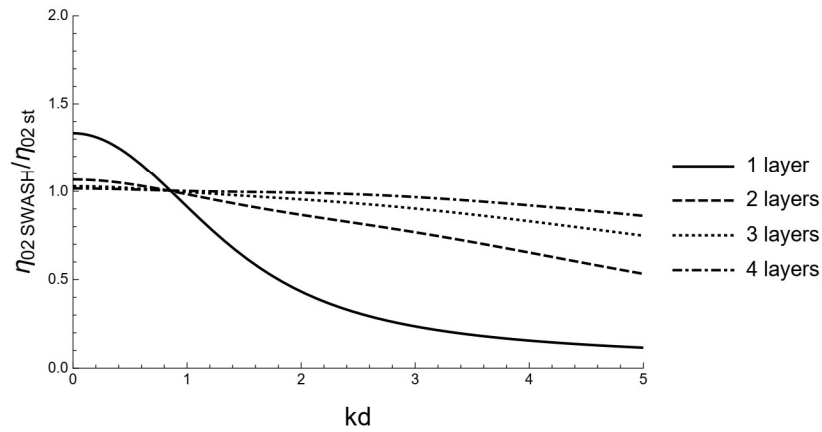
$$b1 = \text{Simplify}[\eta_{2k1} / \eta_{2ex}, k * d == kd];$$

$$b2 = \text{Simplify}[\eta_{2k2} / \eta_{2ex}, k * d == kd];$$

$$b3 = \text{Simplify}[\eta_{2k3} / \eta_{2ex}, k * d == kd];$$

$$b4 = \text{Simplify}[\eta_{2k4} / \eta_{2ex}, k * d == kd];$$

```
p1 = Plot[{b1, b2, b3, b4}, {kd, -0, 5},  
PlotTheme -> "Monochrome", PlotRange -> {{0, 5.0}, {0.0, 2.0}},  
ImageSize -> 400, Axes -> False, Frame -> {True, True, False, False},  
FrameLabel -> {Style["kd", 16], Style[" $\eta_{02 \text{ SWASH}}/\eta_{02 \text{ st}}$ ", 16]}, FrameTicks -> All,  
PlotLegends -> {"1 layer", "2 layers", "3 layers", "4 layers"}]
```



```
Quit[]
```

B.3 Third order solutions

Amplitude dispersion

$$\text{\$Assumptions} = g > 0 \&\& d > 0 \&\& k > 0;$$

Exact solution

$$\omega_{13ex} = \frac{1}{16} \frac{\text{eta}01^2}{d^2} * k^2 * d^2 * \frac{\left(9 * (\text{Tanh}[k * d])^4 - 10 * (\text{Tanh}[k * d])^2 + 9\right)}{(\text{Tanh}[k * d])^4};;$$

One layer

$$\omega_{13k1} = \frac{\text{eta}01^2 (48 + 8 d^2 k^2 + 7 d^4 k^4)}{16 d^4 k^2 (4 + d^2 k^2)};$$

Two layers

$$\omega_{13k2} = \frac{\left(\text{eta}01^2 \left(1207959552 + d^2 k^2 \left(855638016 + d^2 k^2 \left(687341568 + d^2 k^2 \left(147062784 + 17270784 d^2 k^2 + 1173504 d^4 k^4 + 16568 d^6 k^6 + 89 d^8 k^8\right)\right)\right)\right)\right)}{\left(96 d^4 k^2 \left(16 + d^2 k^2\right)^2 \left(320 + 20 d^2 k^2 + d^4 k^4\right) \left(256 + 96 d^2 k^2 + d^4 k^4\right)\right)};$$

Three layers

$$\omega_{13k3} = - \left(\left(\text{eta}01^2 \left(-31088519960728128454656 - 32623755514344332328960 d^2 k^2 - 27579156282033680941056 d^4 k^4 - 10972281381125033558016 d^6 k^6 - 2420679307482659487744 d^8 k^8 - 348224138698867015680 d^{10} k^{10} - 31756215885919764480 d^{12} k^{12} - 1750994668724576256 d^{14} k^{14} - 57638804804902656 d^{16} k^{16} - 1143476054210304 d^{18} k^{18} - 13787606323296 d^{20} k^{20} - 97607671056 d^{22} k^{22} - 367761825 d^{24} k^{24} - 445209 d^{26} k^{26} + 626 d^{28} k^{28} \right) \right) / \left(432 d^4 k^2 \left(12 + d^2 k^2 \right)^3 \left(36 + d^2 k^2 \right) \left(108 + d^2 k^2 \right)^3 \left(1296 + 504 d^2 k^2 + d^4 k^4 \right) \left(1224720 + 204120 d^2 k^2 + 13041 d^4 k^4 + 150 d^6 k^6 + d^8 k^8 \right) \right);$$

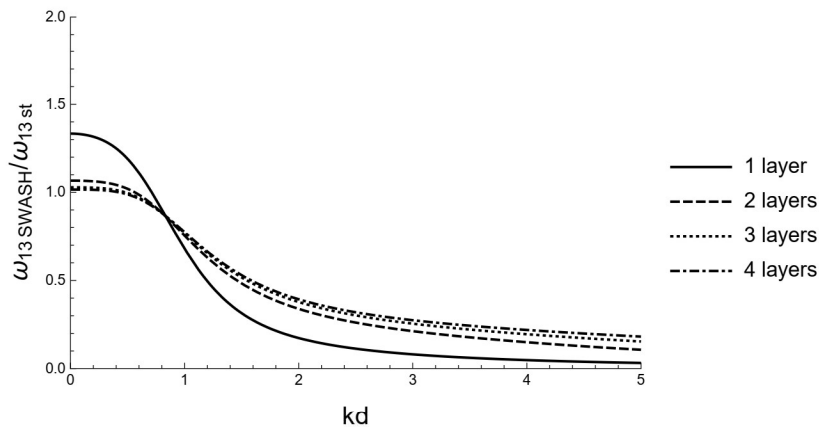
Four layers

$$\omega_{13k4} = - \left(\left(\text{eta}01^2 \left(-5841333965851681082096808370372608 - 6936584084448871284989959939817472 d^2 k^2 - 6107540591899609256411116043501568 d^4 k^4 - 2811807487631241341194874797424640 d^6 k^6 - 740718095542551708026402188034048 d^8 k^8 - 129007865248001098267731091783680 d^{10} k^{10} - 15121698821184752406666024058880 d^{12} k^{12} - 1182971209972508920831774031872 d^{14} k^{14} - 61918427728383418873191333888 d^{16} k^{16} - 2183969829394095665112416256 d^{18} k^{18} - 51945158311296329716858880 d^{20} k^{20} - 822696965193329130078208 d^{22} k^{22} - 8465192998641795596288 d^{24} k^{24} - 5540067723291513344 d^{26} k^{26} - 229760331390386176 d^{28} k^{28} - 588115469139968 d^{30} k^{30} - 802838994944 d^{32} k^{32} - 141118208 d^{34} k^{34} + 1090112 d^{36} k^{36} + 973 d^{38} k^{38} \right) \right) / \left(96 d^4 k^2 \left(64 + d^2 k^2 \right)^2 \left(4096 + 384 d^2 k^2 + d^4 k^4 \right)^3 \left(16777216 + 7340032 d^2 k^2 + 286720 d^4 k^4 + 1792 d^6 k^6 + d^8 k^8 \right) \left(22548578304 + 5284823040 d^2 k^2 + 456916992 d^4 k^4 + 14110720 d^6 k^6 + 166656 d^8 k^8 + 560 d^{10} k^{10} + d^{12} k^{12} \right) \right);$$

```

b1 = Simplify[ $\omega_{13k1} / \omega_{13ex}$ ,  $k * d == kd$ ];
b2 = Simplify[ $\omega_{13k2} / \omega_{13ex}$ ,  $k * d == kd$ ];
b3 = Simplify[ $\omega_{13k3} / \omega_{13ex}$ ,  $k * d == kd$ ];
b4 = Simplify[ $\omega_{13k4} / \omega_{13ex}$ ,  $k * d == kd$ ];
p1 = Plot[{b1, b2, b3, b4}, {kd, -0, 5},
  PlotTheme -> "Monochrome", PlotRange -> {{0, 5.0}, {0.0, 2.0}},
  ImageSize -> 400, Axes -> False, Frame -> {True, True, False, False},
  FrameLabel -> {Style["kd", 16], Style[" $\omega_{13 SWASH} / \omega_{13 st}$ ", 16]}, FrameTicks -> All,
  PlotLegends -> {"1 layer", "2 layers", "3 layers", "4 layers"}]

```



Third order amplitude of the surface elevation

$\$Assumptions = g > 0 \&\& d > 0 \&\& k > 0;$

Exact solution

$$\eta_{3ex} = \frac{3}{64} \frac{\eta_{01}^3}{d^2} * k^2 * d^2 * \frac{1 + 8 * (\text{Cosh}[k * d])^6}{(\text{Sinh}[k * d])^6};$$

One layer

$$\eta_{3k1} = \frac{3 \eta_{01}^3 (4 + d^2 k^2)^2}{64 d^6 k^4};$$

Two layers

$$\eta_{3k2} = \left(\eta_{01}^3 \left(1207959552 + d^2 k^2 \left(1962934272 + d^2 k^2 \left(1738014720 + d^2 k^2 \left(682622976 + 145885184 d^2 k^2 + 14327296 d^4 k^4 + 267928 d^6 k^6 + 2853 d^8 k^8 \right) \right) \right) \right) \right) / \left(384 d^6 k^4 \left(16 + d^2 k^2 \right) \left(320 + 20 d^2 k^2 + d^4 k^4 \right) \left(1280 + 160 d^2 k^2 + 9 d^4 k^4 \right) \right);$$

Three layers

$$\begin{aligned} \text{eta03}_{K3} = & \\ & \left(\text{eta01}^3 \left(31\,984\,074\,033\,670\,914\,048 + 68\,410\,380\,572\,018\,343\,936\,d^2\,k^2 + 75\,778\,453\,868\,355\,256\,320\,d^4\,k^4 + 44\,988\,321\,506\,388\,148\,224\,d^6\,k^6 + 15\,887\,572\,309\,575\,106\,560\,d^8\,k^8 + \right. \right. \\ & 3\,374\,680\,441\,657\,614\,336\,d^{10}\,k^{10} + 398\,745\,233\,417\,594\,880\,d^{12}\,k^{12} + \\ & 24\,406\,435\,566\,273\,024\,d^{14}\,k^{14} + 766\,838\,332\,965\,312\,d^{16}\,k^{16} + 12\,785\,195\,803\,824\,d^{18}\,k^{18} + \\ & \left. 119\,282\,090\,292\,d^{20}\,k^{20} + 656\,990\,169\,d^{22}\,k^{22} + 2\,124\,717\,d^{24}\,k^{24} + 3406\,d^{26}\,k^{26} \right) \Big/ \\ & \left(576\,d^6\,k^4 \left(12 + d^2\,k^2 \right)^2 \left(108 + d^2\,k^2 \right)^2 \left(60\,480 + 15\,120\,d^2\,k^2 + 364\,d^4\,k^4 + 3\,d^6\,k^6 \right) \right. \\ & \left. \left(1\,224\,720 + 204\,120\,d^2\,k^2 + 13\,041\,d^4\,k^4 + 150\,d^6\,k^6 + d^8\,k^8 \right) \right); \end{aligned}$$

Four layers

$$\begin{aligned} \text{eta03}_{K4} = & \left(\text{eta01}^3 \right. \\ & \left(5\,841\,333\,965\,851\,681\,082\,096\,808\,370\,372\,608 + 14\,603\,334\,914\,629\,202\,705\,242\,020\,925\,931\,520\,d^2\,k^2 + 18\,552\,700\,359\,640\,251\,405\,604\,999\,762\,280\,448\,d^4\,k^4 + \right. \\ & 13\,587\,204\,019\,822\,819\,726\,478\,222\,183\,890\,944\,d^6\,k^6 + \\ & 6\,246\,583\,463\,860\,812\,142\,790\,968\,696\,897\,536\,d^8\,k^8 + \\ & 1\,880\,460\,063\,249\,226\,087\,437\,284\,338\,040\,832\,d^{10}\,k^{10} + \\ & 370\,734\,016\,892\,641\,855\,878\,175\,154\,765\,824\,d^{12}\,k^{12} + \\ & 47\,814\,675\,819\,027\,747\,602\,808\,799\,494\,144\,d^{14}\,k^{14} + \\ & 4\,039\,871\,429\,319\,203\,123\,903\,630\,147\,584\,d^{16}\,k^{16} + \\ & 223\,955\,977\,355\,043\,986\,179\,778\,150\,400\,d^{18}\,k^{18} + 8\,120\,400\,182\,063\,760\,474\,963\,443\,712\,d^{20}\,k^{20} + \\ & 190\,062\,489\,558\,855\,972\,764\,516\,352\,d^{22}\,k^{22} + 2\,798\,552\,312\,231\,855\,315\,222\,528\,d^{24}\,k^{24} + \\ & 25\,123\,609\,810\,421\,021\,671\,424\,d^{26}\,k^{26} + 136\,886\,401\,774\,525\,612\,032\,d^{28}\,k^{28} + \\ & 477\,074\,466\,321\,465\,344\,d^{30}\,k^{30} + 1\,120\,560\,391\,806\,976\,d^{32}\,k^{32} + \\ & \left. 1\,801\,813\,503\,744\,d^{34}\,k^{34} + 1\,841\,558\,976\,d^{36}\,k^{36} + 920\,727\,d^{38}\,k^{38} \right) \Big/ \\ & \left(384\,d^6\,k^4 \left(64 + d^2\,k^2 \right) \left(4096 + 384\,d^2\,k^2 + d^4\,k^4 \right)^2 \left(22\,548\,578\,304 + 5\,284\,823\,040\,d^2\,k^2 + \right. \right. \\ & 456\,916\,992\,d^4\,k^4 + 14\,110\,720\,d^6\,k^6 + 166\,656\,d^8\,k^8 + 560\,d^{10}\,k^{10} + d^{12}\,k^{12} \Big) \\ & \left. \left(1\,443\,109\,011\,456 + 676\,457\,349\,120\,d^2\,k^2 + 85\,614\,133\,248\,d^4\,k^4 + \right. \right. \\ & \left. \left. 4\,178\,575\,360\,d^6\,k^6 + 65\,286\,144\,d^8\,k^8 + 362\,880\,d^{10}\,k^{10} + 729\,d^{12}\,k^{12} \right) \right); \end{aligned}$$

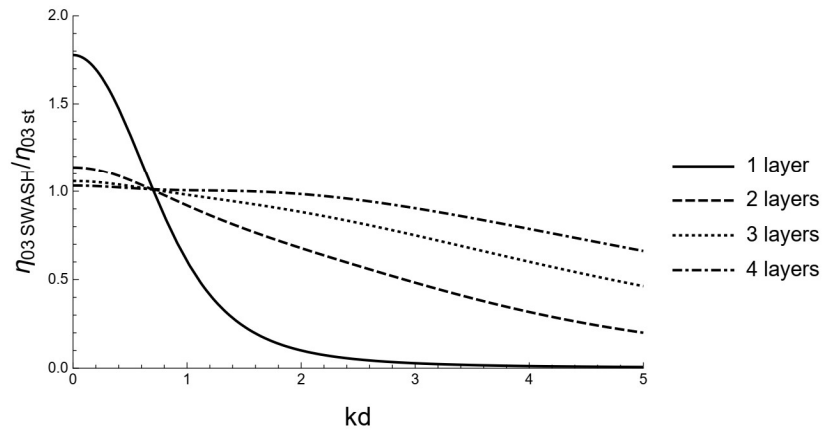
$$\text{b1} = \text{Simplify}[\text{eta03}_{K1} / \text{eta03ex}, k * d == kd];$$

$$\text{b2} = \text{Simplify}[\text{eta03}_{K2} / \text{eta03ex}, k * d == kd];$$

$$\text{b3} = \text{Simplify}[\text{eta03}_{K3} / \text{eta03ex}, k * d == kd];$$

$$\text{b4} = \text{Simplify}[\text{eta03}_{K4} / \text{eta03ex}, k * d == kd];$$

```
p1 = Plot[{b1, b2, b3, b4}, {kd, -0, 5},  
PlotTheme -> "Monochrome", PlotRange -> {{0, 5.0}, {0.0, 2.0}},  
ImageSize -> 400, Axes -> False, Frame -> {True, True, False, False},  
FrameLabel -> {Style["kd", 16], Style[" $\eta_{03 \text{ SWASH}}/\eta_{03 \text{ st}}$ ", 16]}, FrameTicks -> All,  
PlotLegends -> {"1 layer", "2 layers", "3 layers", "4 layers"}]
```



```
Quit[]
```

B.4 Subharmonic transfer functions

Exact solution

Dean-Sharma (1981)

$$\omega_n = (kn * \text{Tanh}[kn * d])^{1/2}; \omega_m = (km * \text{Tanh}[km * d])^{1/2};$$

$$G = \frac{1}{2} * \left(\left(\left(\left(2 * (\omega_m - \omega_n)^2 * (km * kn + \omega_m^2 * \omega_n^2) \right) / \left((\omega_m - \omega_n)^2 - (km - kn) * \text{Tanh}[(km - kn) * d] \right) \right) + \left((\omega_m - \omega_n) * (-\omega_m * (kn^2 - \omega_n^4) + \omega_n * (km^2 - \omega_m^4)) \right) / \left((\omega_m - \omega_n)^2 - (km - kn) * \text{Tanh}[(km - kn) * d] \right) \right) - (km * kn + \omega_m^2 * \omega_n^2) / (\omega_m * \omega_n + \omega_m^2 + \omega_n^2) \right);$$

$$G_{subDe} = G * d /. \{km \rightarrow kdm/d, kn \rightarrow kdn/d\} // \text{Simplify}; (* \text{ multiplied with } d*)$$

Scaffer(1994)

$$\omega_n = (g * kn * \text{Tanh}[kn * d])^{1/2}; \omega_m = (g * km * \text{Tanh}[km * d])^{1/2};$$

$$H = (\omega_m - \omega_n) * \left(-\omega_m * \omega_n - \frac{g^2 * kn * km}{\omega_n * \omega_m} \right) + \frac{\omega_m^3 - \omega_n^3}{2} - \frac{g^2}{2} * \left(\frac{km^2}{\omega_m} - \frac{kn^2}{\omega_n} \right);$$

$$D_s = g * (km - kn) * \text{Tanh}[(km - kn) * d] - (\omega_m - \omega_n)^2;$$

$$L = \frac{1}{2} * \left(\frac{g^2 * km * kn}{\omega_m * \omega_n} + \omega_m * \omega_n - (\omega_m^2 + \omega_n^2) \right);$$

$$G = \frac{1}{g} * \left((\omega_m - \omega_n) * \frac{H}{D_s} - L \right) // \text{Simplify};$$

$$G_{subSc} = G * d /. \{km \rightarrow kdm/d, kn \rightarrow kdn/d\} // \text{Simplify}; (* \text{ multiplied with } d*)$$

All the above expressions are equal

$$\text{Clear}[\omega_m, \omega_n];$$

One solution

$$s1 = \left(\text{eta01m eta01n} (km - kn)^2 \left(4 d g km kn + 8 \omega_m \omega_n + d^2 \left(-kn^2 \omega_m (\omega_m - 2 \omega_n) + km^2 (2 \omega_m - \omega_n) \omega_n - 2 km kn (\omega_m^2 + \omega_n^2) \right) \right) \right) / \left(2 d km kn \left(-4 d g (km - kn)^2 + 4 (\omega_m - \omega_n)^2 + d^2 (km - kn)^2 (\omega_m - \omega_n)^2 \right) \right);$$

$$\omega_m = \frac{2 \sqrt{d g} km}{\sqrt{4 + d^2 km^2}};$$

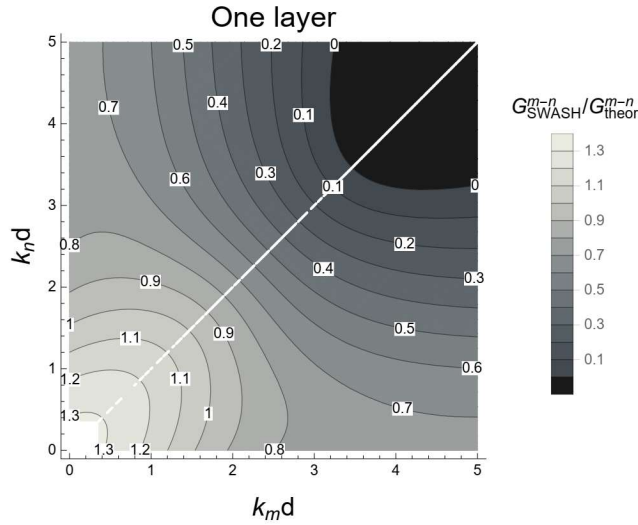
$$\omega_n = \frac{2 \sqrt{d g} kn}{\sqrt{4 + d^2 kn^2}};$$

$$\text{oneSub} = s1 * d / (\text{eta01m eta01n}) /. \{km \rightarrow kdm/d, kn \rightarrow kdn/d\} // \text{FullSimplify} (* \text{ multiplied with } d*);$$

```

p11 = ContourPlot[Quiet[oneSub/GsubDe], {kdm, 0, 5},
  {kdn, 0, 5}, Contours -> Function[{min, max}, Range[0, 1.4, 0.1]],
  ContourLabels -> Function[{x, y, z}, Text[z, {x, y}, Background -> White]],
  ImageSize -> 300, ColorFunction -> "GrayTones",
  PlotLegends -> BarLegend[Automatic, LegendMarkerSize -> 180, LegendFunction -> "Frame",
  LegendMargins -> 5, LegendLabel -> "Gm-nSWASH/Gm-ntheor"], AspectRatio -> Automatic,
  Frame -> {True, True, False, False}, FrameLabel -> {Style["kmd", 16], Style["knd", 16]},
  FrameTicks -> All, PlotLabel -> Style["One layer", FontSize -> 18]]

```



```
Clear[ωm, ωn, s1];
```

Two layers solution

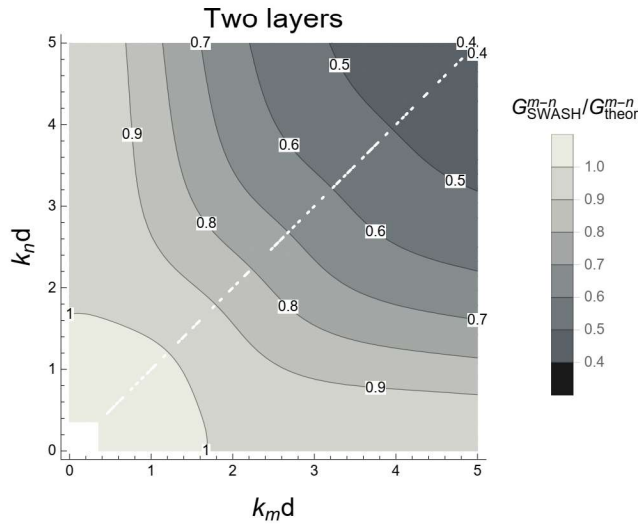
$$\begin{aligned}
s1 = & \left(\text{eta01m eta01n} (km - kn)^2 \left(65536 \omega m \omega n (kn^2 \omega m^2 + 4 km kn \omega m \omega n + km^2 \omega n^2) - \right. \right. \\
& 65536 d g km kn (2 kn^2 \omega m^2 + km kn \omega m \omega n + 2 km^2 \omega n^2) + d^8 km^3 (km - kn)^2 kn^3 \omega m \\
& \omega n (2 km^2 (\omega m - 2 \omega n) \omega n + 2 kn^2 \omega m (-2 \omega m + \omega n) - km kn (\omega m^2 - 6 \omega m \omega n + \omega n^2)) - \\
& 4096 d^3 g km kn (kn^4 \omega m^2 + 2 km kn^3 \omega m (4 \omega m - 3 \omega n) + km^4 \omega n^2 + 2 km^3 kn \omega n (-3 \omega m + 4 \omega n) - \\
& 4 km^2 kn^2 (\omega m^2 - 3 \omega m \omega n + \omega n^2)) + 16 d^7 g km^3 (km - kn)^2 kn^3 \\
& (kn^2 \omega m (3 \omega m + \omega n) + km^2 \omega n (\omega m + 3 \omega n) - km kn (4 \omega m^2 + 5 \omega m \omega n + 4 \omega n^2)) + \\
& 256 d^5 g km kn (kn^6 \omega m^2 + km^6 \omega n^2 - km kn^5 \omega m (6 \omega m + \omega n) - \\
& km^5 kn \omega n (\omega m + 6 \omega n) + km^2 kn^4 (10 \omega m^2 - \omega m \omega n - 10 \omega n^2) - \\
& km^4 kn^2 (10 \omega m^2 + \omega m \omega n - 10 \omega n^2) + km^3 kn^3 (4 \omega m^2 + 5 \omega m \omega n + 4 \omega n^2)) + \\
& 4096 d^2 (32 g^2 km^3 kn^3 + \omega m \omega n (-2 kn^4 \omega m^2 + 6 km^3 kn \omega m \omega n + 6 km kn^3 \omega m \omega n - \\
& 2 km^4 \omega n^2 + km^2 kn^2 (-9 \omega m^2 + 14 \omega m \omega n - 9 \omega n^2))) + 256 d^4 \\
& (16 g^2 km^3 (km - kn)^2 kn^3 + \omega m \omega n (kn^6 \omega m^2 + km^6 \omega n^2 + km^4 kn^2 (-9 \omega m^2 + 28 \omega m \omega n - 15 \omega n^2) + \\
& km^2 kn^4 (-15 \omega m^2 + 28 \omega m \omega n - 9 \omega n^2) + 2 km^3 kn^3 (23 \omega m^2 - 40 \omega m \omega n + 23 \omega n^2))) - \\
& 16 d^6 km kn (16 g^2 km^2 (km - kn)^4 kn^2 - \omega m \omega n (-2 km^6 \omega m \omega n - 2 kn^6 \omega m \omega n + 2 km^4 kn^2 (\omega m^2 + \\
& 2 \omega m \omega n - 21 \omega n^2) + 2 km^3 kn^3 (\omega m^2 - 3 \omega m \omega n + \omega n^2) + 2 km^2 kn^4 (-21 \omega m^2 + 2 \omega m \omega n + \\
& \omega n^2) + km kn^5 (24 \omega m^2 + 14 \omega m \omega n + \omega n^2) + km^5 kn (\omega m^2 + 14 \omega m \omega n + 24 \omega n^2))) \Big) \Big) / \\
& \left(2 d km^2 (-16 + d^2 km^2) kn^2 (-16 + d^2 kn^2) \omega m (-256 d g (km - kn)^2 - 16 d^3 g (km - kn)^4 + \right. \\
& \left. 256 (\omega m - \omega n)^2 + 96 d^2 (km - kn)^2 (\omega m - \omega n)^2 + d^4 (km - kn)^4 (\omega m - \omega n)^2) \omega n \right);
\end{aligned}$$

$$\omega m = \frac{4 \sqrt{d g km^2 (16 + d^2 km^2)}}{\sqrt{256 + 96 d^2 km^2 + d^4 km^4}};$$

$$\omega n = \frac{4 \sqrt{d g k n^2 (16 + d^2 k n^2)}}{\sqrt{256 + 96 d^2 k n^2 + d^4 k n^4}};$$

```
twolsub = s1 * d / (eta01m eta01n) /. {km -> kdm/d, kn -> kdn/d} // Simplify
(* multiplied with d*);
```

```
p21 = ContourPlot[Quiet[twolsub/GsubDe], {kdm, 0, 5},
  {kdn, 0, 5}, Contours -> Function[{min, max}, Range[0, 1.4, 0.1]],
  ContourLabels -> Function[{x, y, z}, Text[z, {x, y}, Background -> White]],
  ImageSize -> 300, ColorFunction -> "GrayTones",
  PlotLegends -> BarLegend[Automatic, LegendMarkerSize -> 180, LegendFunction -> "Frame",
  LegendMargins -> 5, LegendLabel -> "GSWASHm-n/Gtheorm-n"], AspectRatio -> Automatic,
  Frame -> {True, True, False, False}, FrameLabel -> {Style["kmd", 16], Style["knd", 16]},
  FrameTicks -> All, PlotLabel -> Style["Two layers", FontSize -> 18]]
```



```
Clear[ωm, ωn, s1];
```

Three layers solution

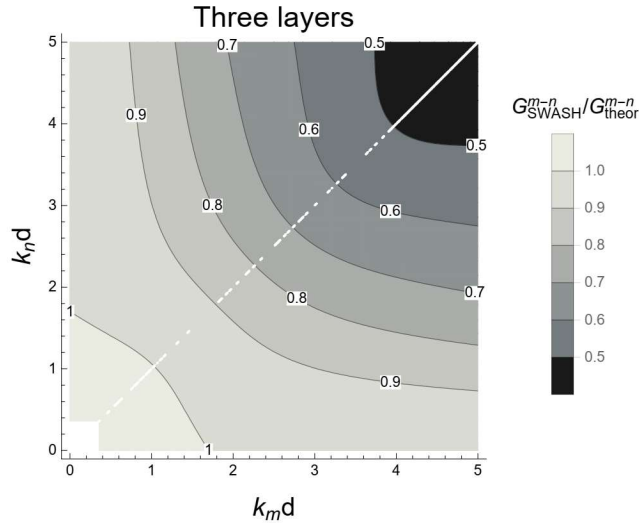
$$\begin{aligned} s1 = & (\text{eta01m eta01n} (km - kn)^2 (78364164096 \omega m \omega n (kn^2 \omega m^2 + 6 km kn \omega m \omega n + km^2 \omega n^2) - \\ & 78364164096 d g km kn (4 kn^2 \omega m^2 + km kn \omega m \omega n + 4 km^2 \omega n^2) + d^{14} km^5 (km - kn)^4 kn^5 \omega m \\ & \omega n (3 km^2 (3 \omega m - 2 \omega n) \omega n + 3 kn^2 \omega m (-2 \omega m + 3 \omega n) - km kn (\omega m^2 + 4 \omega m \omega n + \omega n^2)) - \\ & 12 d^{13} g km^5 (km - kn)^4 kn^5 (km kn (-12 \omega m^2 + 35 \omega m \omega n - 12 \omega n^2) + \\ & 3 kn^2 (2 \omega m^2 - \omega m \omega n + 3 \omega n^2) + km^2 (9 \omega m^2 - 3 \omega m \omega n + 6 \omega n^2)) - \\ & 725594112 d^3 g km kn (6 kn^4 \omega m^2 + 4 km kn^3 \omega m (23 \omega m - 11 \omega n) + 6 km^4 \omega n^2 + \\ & 4 km^3 kn \omega n (-11 \omega m + 23 \omega n) + 3 km^2 kn^2 (7 \omega m^2 + 34 \omega m \omega n + 7 \omega n^2)) + \\ & 559872 d^7 g km kn (6 kn^8 \omega m^2 + 4 km kn^7 \omega m (27 \omega m - 5 \omega n) - 4 km^7 kn (5 \omega m - 27 \omega n) \omega n + \\ & 6 km^8 \omega n^2 + km^6 kn^2 (24 \omega m^2 + 169 \omega m \omega n - 339 \omega n^2) + \\ & km^2 kn^6 (-339 \omega m^2 + 169 \omega m \omega n + 24 \omega n^2) - 2 km^5 kn^3 (94 \omega m^2 + 229 \omega m \omega n + 54 \omega n^2) - \\ & 2 km^3 kn^5 (54 \omega m^2 + 229 \omega m \omega n + 94 \omega n^2) + 4 km^4 kn^4 (111 \omega m^2 + 154 \omega m \omega n + 111 \omega n^2)) + \\ & 20155392 d^5 g km kn (18 kn^6 \omega m^2 + 18 km^6 \omega n^2 - 6 km kn^5 \omega m (26 \omega m + 3 \omega n) - \\ & 6 km^5 kn \omega n (3 \omega m + 26 \omega n) - 3 km^4 kn^2 (10 \omega m^2 + 23 \omega m \omega n - 119 \omega n^2) + \\ & 3 km^2 kn^4 (119 \omega m^2 - 23 \omega m \omega n - 10 \omega n^2) - 2 km^3 kn^3 (196 \omega m^2 - 101 \omega m \omega n + 196 \omega n^2)) - \\ & 432 d^{11} g km^3 (km - kn)^2 kn^3 (3 kn^6 (20 \omega m^2 + \omega m \omega n + \omega n^2) + \\ & 3 km^6 (\omega m^2 + \omega m \omega n + 20 \omega n^2) - 2 km kn^5 (132 \omega m^2 - 2 \omega m \omega n + 21 \omega n^2) - \\ & 2 km^5 kn (21 \omega m^2 - 2 \omega m \omega n + 132 \omega n^2) - 2 km^3 kn^3 (162 \omega m^2 + 29 \omega m \omega n + 162 \omega n^2) + \\ & km^2 kn^4 (372 \omega m^2 + 43 \omega m \omega n + 195 \omega n^2) + km^4 kn^2 (195 \omega m^2 + 43 \omega m \omega n + 372 \omega n^2)) - \\ & 15552 d^9 g km kn (6 kn^{10} \omega m^2 + 3 km^9 kn (\omega m - 20 \omega n) \omega n + 6 km^{10} \omega n^2 + \end{aligned}$$

$$\begin{aligned}
& 3 \text{ km kn}^9 \omega m (-20 \omega m + \omega n) + \text{ km}^2 \text{ kn}^8 (105 \omega m^2 - 5 \omega m \omega n - 42 \omega n^2) + \\
& 6 \text{ km}^3 \text{ kn}^7 (14 \omega m^2 - 19 \omega m \omega n - 24 \omega n^2) - 6 \text{ km}^7 \text{ kn}^3 (24 \omega m^2 + 19 \omega m \omega n - 14 \omega n^2) + \\
& 12 \text{ km}^6 \text{ kn}^4 (62 \omega m^2 + 32 \omega m \omega n - 3 \omega n^2) + 12 \text{ km}^4 \text{ kn}^6 (-3 \omega m^2 + 32 \omega m \omega n + 62 \omega n^2) + \\
& \text{ km}^8 \text{ kn}^2 (-42 \omega m^2 - 5 \omega m \omega n + 105 \omega n^2) - \text{ km}^5 \text{ kn}^5 (660 \omega m^2 + 527 \omega m \omega n + 660 \omega n^2) + \\
& 2176782336 \text{ d}^2 (144 \text{ g}^2 \text{ km}^3 \text{ kn}^3 + \omega m \omega n (-4 \text{ km}^4 \omega m^2 - 4 \text{ km}^4 \omega n^2 + \text{ km}^3 \text{ kn} \omega n (33 \omega m + 2 \omega n) + \\
& \text{ km kn}^3 \omega m (2 \omega m + 33 \omega n) + \text{ km}^2 \text{ kn}^2 (-21 \omega m^2 + 44 \omega m \omega n - 21 \omega n^2))) + \\
& 120932352 \text{ d}^4 (36 \text{ g}^2 \text{ km}^3 \text{ kn}^3 (\text{ km} + \text{ kn})^2 - \omega m \omega n (-3 \text{ kn}^6 \omega m^2 - 3 \text{ km}^6 \omega n^2 + 3 \text{ km}^5 \text{ kn} \\
& \omega n (3 \omega m + \omega n) + 3 \text{ km kn}^5 \omega m (\omega m + 3 \omega n) + \text{ km}^2 \text{ kn}^4 (55 \omega m^2 - 148 \omega m \omega n + 35 \omega n^2) + \\
& \text{ km}^4 \text{ kn}^2 (35 \omega m^2 - 148 \omega m \omega n + 55 \omega n^2) - 2 \text{ km}^3 \text{ kn}^3 (76 \omega m^2 - 81 \omega m \omega n + 76 \omega n^2))) + \\
& 36 \text{ d}^{12} \text{ km}^3 (\text{ km} - \text{ kn})^2 \text{ kn}^3 (72 \text{ g}^2 \text{ km}^2 (\text{ km} - \text{ kn})^4 \text{ kn}^2 + \omega m \omega n \\
& (6 \text{ km}^6 \omega n (2 \omega m + \omega n) + 6 \text{ kn}^6 \omega m (\omega m + 2 \omega n) + 2 \text{ km}^4 \text{ kn}^2 (4 \omega m^2 + 157 \omega m \omega n - 89 \omega n^2) - \\
& \text{ km}^3 \text{ kn}^3 (\omega m^2 + 356 \omega m \omega n + \omega n^2) + \text{ km kn}^5 (103 \omega m^2 - 88 \omega m \omega n + 2 \omega n^2) + \\
& 2 \text{ km}^2 \text{ kn}^4 (-89 \omega m^2 + 157 \omega m \omega n + 4 \omega n^2) + \text{ km}^5 \text{ kn} (2 \omega m^2 - 88 \omega m \omega n + 103 \omega n^2))) - \\
& 46656 \text{ d}^8 (24 \text{ g}^2 \text{ km}^3 (\text{ km} - \text{ kn})^2 \text{ kn}^3 (3 \text{ km}^4 + 4 \text{ km}^3 \text{ kn} - 31 \text{ km}^2 \text{ kn}^2 + 4 \text{ km kn}^3 + 3 \text{ kn}^4) + \\
& \omega m \omega n (-\text{ kn}^{10} \omega m^2 + 2 \text{ km kn}^9 \omega m (\omega m - 6 \omega n) - \text{ km}^{10} \omega n^2 + 2 \text{ km}^9 \text{ kn} \omega n (-6 \omega m + \omega n) + \\
& \text{ km}^6 \text{ kn}^4 (-364 \omega m^2 + 40 \omega m \omega n - 373 \omega n^2) + \text{ km}^4 \text{ kn}^6 (-373 \omega m^2 + 40 \omega m \omega n - 364 \omega n^2) + \\
& \text{ km}^2 \text{ kn}^8 (114 \omega m^2 + 256 \omega m \omega n - 21 \omega n^2) + 2 \text{ km}^7 \text{ kn}^3 (116 \omega m^2 - 374 \omega m \omega n + 13 \omega n^2) + \\
& \text{ km}^8 \text{ kn}^2 (-21 \omega m^2 + 256 \omega m \omega n + 114 \omega n^2) + 2 \text{ km}^3 \text{ kn}^7 (13 \omega m^2 - 374 \omega m \omega n + 116 \omega n^2) + \\
& 2 \text{ km}^5 \text{ kn}^5 (123 \omega m^2 + 575 \omega m \omega n + 123 \omega n^2))) - \\
& 3359232 \text{ d}^6 (12 \text{ g}^2 \text{ km}^3 \text{ kn}^3 (9 \text{ km}^4 - 54 \text{ km}^3 \text{ kn} + 76 \text{ km}^2 \text{ kn}^2 - 54 \text{ km kn}^3 + 9 \text{ kn}^4) + \\
& \omega m \omega n (2 \text{ kn}^8 \omega m^2 - 3 \text{ km kn}^7 \omega m (\omega m - 6 \omega n) + 3 \text{ km}^7 \text{ kn} (6 \omega m - \omega n) \omega n + \\
& 2 \text{ km}^8 \omega n^2 + 2 \text{ km}^4 \text{ kn}^4 (9 \omega m^2 - 224 \omega m \omega n + 9 \omega n^2) + \\
& 2 \text{ km}^3 \text{ kn}^5 (110 \omega m^2 + 59 \omega m \omega n + 18 \omega n^2) - \text{ km}^2 \text{ kn}^6 (132 \omega m^2 + 58 \omega m \omega n + 35 \omega n^2) + \\
& 2 \text{ km}^5 \text{ kn}^3 (18 \omega m^2 + 59 \omega m \omega n + 110 \omega n^2) - \text{ km}^6 \text{ kn}^2 (35 \omega m^2 + 58 \omega m \omega n + 132 \omega n^2))) + \\
& 1296 \text{ d}^{10} \text{ km kn} (24 \text{ g}^2 \text{ km}^2 (\text{ km} - \text{ kn})^4 \text{ kn}^2 (3 \text{ km}^4 - 10 \text{ km}^3 \text{ kn} - 4 \text{ km}^2 \text{ kn}^2 - 10 \text{ km kn}^3 + 3 \text{ kn}^4) - \\
& \omega m \omega n (-3 \text{ km}^{10} \omega m \omega n - 3 \text{ kn}^{10} \omega m \omega n + \text{ km}^8 \text{ kn}^2 (2 \omega m^2 - 103 \omega m \omega n - 156 \omega n^2) + \\
& \text{ km kn}^9 (19 \omega m^2 + 40 \omega m \omega n + \omega n^2) + \text{ km}^2 \text{ kn}^8 (-156 \omega m^2 - 103 \omega m \omega n + 2 \omega n^2) + \\
& 2 \text{ km}^3 \text{ kn}^7 (179 \omega m^2 + 320 \omega m \omega n + 12 \omega n^2) + \text{ km}^9 \text{ kn} (\omega m^2 + 40 \omega m \omega n + 19 \omega n^2) + 2 \text{ km}^7 \text{ kn}^3 \\
& (12 \omega m^2 + 320 \omega m \omega n + 179 \omega n^2) - \text{ km}^4 \text{ kn}^6 (702 \omega m^2 + 1925 \omega m \omega n + 432 \omega n^2) - \text{ km}^6 \text{ kn}^4 \\
& (432 \omega m^2 + 1925 \omega m \omega n + 702 \omega n^2) + \text{ km}^5 \text{ kn}^5 (915 \omega m^2 + 2644 \omega m \omega n + 915 \omega n^2)))))) / \\
& (2 \text{ d km}^2 (-36 + \text{ d}^2 \text{ km}^2)^2 \text{ kn}^2 (-36 + \text{ d}^2 \text{ kn}^2)^2 \omega m (-46656 \text{ d g} (\text{ km} - \text{ kn})^2 - \\
& 4320 \text{ d}^3 \text{ g} (\text{ km} - \text{ kn})^4 - 36 \text{ d}^5 \text{ g} (\text{ km} - \text{ kn})^6 + \\
& 46656 (\omega m - \omega n)^2 + 19440 \text{ d}^2 (\text{ km} - \text{ kn})^2 (\omega m - \omega n)^2 + \\
& 540 \text{ d}^4 (\text{ km} - \text{ kn})^4 (\omega m - \omega n)^2 + \text{ d}^6 (\text{ km} - \text{ kn})^6 (\omega m - \omega n)^2) \omega n); \\
\omega m &= \frac{6 \sqrt{\text{ d g km}^2 (12 + \text{ d}^2 \text{ km}^2) (108 + \text{ d}^2 \text{ km}^2)}}{\sqrt{(36 + \text{ d}^2 \text{ km}^2) (1296 + 504 \text{ d}^2 \text{ km}^2 + \text{ d}^4 \text{ km}^4)}}; \\
\omega n &= \frac{6 \sqrt{\text{ d g kn}^2 (12 + \text{ d}^2 \text{ kn}^2) (108 + \text{ d}^2 \text{ kn}^2)}}{\sqrt{(36 + \text{ d}^2 \text{ kn}^2) (1296 + 504 \text{ d}^2 \text{ kn}^2 + \text{ d}^4 \text{ kn}^4)}}; \\
\text{three} & \text{sub} = \text{s1} * \text{d} / (\text{eta01meta01n}) /. \{ \text{ km} \rightarrow \text{ kdm} / \text{d}, \text{ kn} \rightarrow \text{ kdn} / \text{d} \} // \text{Simplify} \\
& (* \text{ multiplied with } *);
\end{aligned}$$

```

p31 = ContourPlot[Quiet[threeSub/GsubDe], {kmd, 0, 5},
  {knd, 0, 5}, Contours -> Function[{min, max}, Range[0, 1.4, 0.1]],
  ContourLabels -> Function[{x, y, z}, Text[z, {x, y}, Background -> White]],
  ImageSize -> 300, ColorFunction -> "GrayTones",
  PlotLegends -> BarLegend[Automatic, LegendMarkerSize -> 180, LegendFunction -> "Frame",
  LegendMargins -> 5, LegendLabel -> "Gm-nSWASH/Gm-ntheor "], AspectRatio -> Automatic,
  Frame -> {True, True, False, False}, FrameLabel -> {Style["kmd", 16], Style["knd", 16]},
  FrameTicks -> All, PlotLabel -> Style["Three layers", FontSize -> 18]]

```



```
Clear[ωm, ωn, s1];
```

Four layers solution

$$\begin{aligned}
s1 = & \left(\text{eta01m eta01n} (km - kn)^2 \left(1152921504606846976 \omega m \omega n (kn^2 \omega m^2 + 8 km kn \omega m \omega n + km^2 \omega n^2) - \right. \right. \\
& 1152921504606846976 d g km kn (6 kn^2 \omega m^2 + km kn \omega m \omega n + 6 km^2 \omega n^2) + d^{20} km^7 (km - kn)^6 \\
& kn^7 \omega m \omega n (4 km^2 (\omega m - 2 \omega n) \omega n + 4 kn^2 \omega m (-2 \omega m + \omega n) - km kn (\omega m^2 - 10 \omega m \omega n + \omega n^2)) + \\
& 64 d^{19} g km^7 (km - kn)^6 kn^7 (kn^2 (5 \omega m^2 + \omega m \omega n + 2 \omega n^2) + \\
& km^2 (2 \omega m^2 + \omega m \omega n + 5 \omega n^2) - km kn (8 \omega m^2 + 21 \omega m \omega n + 8 \omega n^2)) - \\
& 18014398509481984 d^3 g km kn (11 kn^4 \omega m^2 + 2 km kn^3 \omega m (34 \omega m - 13 \omega n) + \\
& 11 km^4 \omega n^2 + 2 km^3 kn \omega n (-13 \omega m + 34 \omega n) + 2 km^2 kn^2 (29 \omega m^2 + 32 \omega m \omega n + 29 \omega n^2)) + \\
& 281474976710656 d^5 g km kn (27 kn^6 \omega m^2 + km^5 kn (\omega m - 250 \omega n) \omega n + 27 km^6 \omega n^2 + \\
& km kn^5 \omega m (-250 \omega m + \omega n) + km^3 kn^3 (-824 \omega m^2 + 339 \omega m \omega n - 824 \omega n^2) + \\
& km^2 kn^4 (348 \omega m^2 - 157 \omega m \omega n + 42 \omega n^2) + km^4 kn^2 (42 \omega m^2 - 157 \omega m \omega n + 348 \omega n^2)) + \\
& 4096 d^{17} g km^5 (km - kn)^4 kn^5 (km^3 kn^3 (-324 \omega m^2 + 35 \omega m \omega n - 324 \omega n^2) + \\
& kn^6 (57 \omega m^2 - 2 \omega m \omega n + 12 \omega n^2) - km kn^5 (250 \omega m^2 + 11 \omega m \omega n + 56 \omega n^2) + \\
& km^6 (12 \omega m^2 - 2 \omega m \omega n + 57 \omega n^2) + km^2 kn^4 (434 \omega m^2 - 37 \omega m \omega n + 128 \omega n^2) - \\
& km^5 kn (56 \omega m^2 + 11 \omega m \omega n + 250 \omega n^2) + km^4 kn^2 (128 \omega m^2 - 37 \omega m \omega n + 434 \omega n^2)) + \\
& 4398046511104 d^7 g km kn (10 kn^8 \omega m^2 + 4 km kn^7 \omega m (60 \omega m - 13 \omega n) + 10 km^8 \omega n^2 + \\
& 4 km^7 kn \omega n (-13 \omega m + 60 \omega n) + km^6 kn^2 (22 \omega m^2 + 349 \omega m \omega n - 421 \omega n^2) + \\
& km^2 kn^6 (-421 \omega m^2 + 349 \omega m \omega n + 22 \omega n^2) - km^3 kn^5 (1182 \omega m^2 + 777 \omega m \omega n + 380 \omega n^2) + \\
& km^4 kn^4 (853 \omega m^2 + 960 \omega m \omega n + 853 \omega n^2) - km^5 kn^3 (380 \omega m^2 + 777 \omega m \omega n + 1182 \omega n^2)) + \\
& 262144 d^{15} g km^3 (km - kn)^2 kn^3 (km^5 kn^5 (-4752 \omega m^2 + 739 \omega m \omega n - 4752 \omega n^2) + \\
& kn^{10} (63 \omega m^2 + \omega m \omega n + 2 \omega n^2) - km kn^9 (468 \omega m^2 + 15 \omega m \omega n + 32 \omega n^2) + \\
& km^{10} (2 \omega m^2 + \omega m \omega n + 63 \omega n^2) + km^2 kn^8 (1283 \omega m^2 + 49 \omega m \omega n + 357 \omega n^2) - \\
& km^9 kn (32 \omega m^2 + 15 \omega m \omega n + 468 \omega n^2) - 2 km^3 kn^7 (1209 \omega m^2 - 60 \omega m \omega n + 758 \omega n^2) - \\
& 2 km^7 kn^3 (758 \omega m^2 - 60 \omega m \omega n + 1209 \omega n^2) + km^8 kn^2 (357 \omega m^2 + 49 \omega m \omega n + 1283 \omega n^2) + \\
& km^4 kn^6 (4044 \omega m^2 - 539 \omega m \omega n + 3438 \omega n^2) + km^6 kn^4 (3438 \omega m^2 - 539 \omega m \omega n + 4044 \omega n^2)) - \\
& 68719476736 d^9 g km kn (24 kn^{10} \omega m^2 + 24 km^{10} \omega n^2 - km kn^9 \omega m (276 \omega m + \omega n) -
\end{aligned}$$

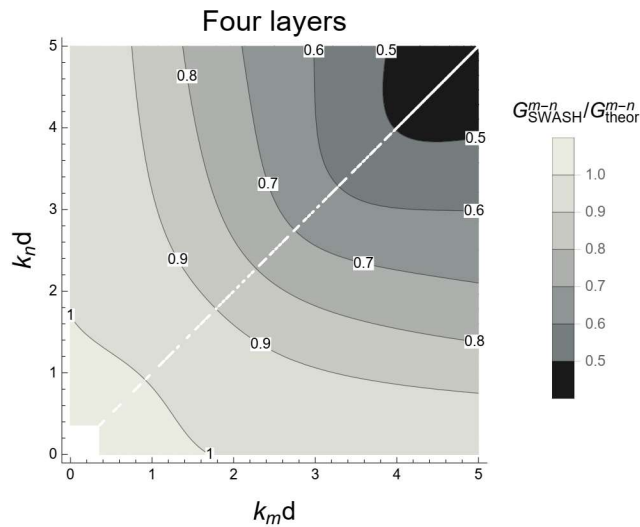
$$\begin{aligned}
& \text{km}^9 \text{kn} \omega n (\omega m + 276 \omega n) - 2 \text{km}^8 \text{kn}^2 (47 \omega m^2 + 35 \omega m \omega n - 430 \omega n^2) + \\
& 2 \text{km}^2 \text{kn}^8 (430 \omega m^2 - 35 \omega m \omega n - 47 \omega n^2) - 2 \text{km}^3 \text{kn}^7 (790 \omega m^2 - 21 \omega m \omega n + 648 \omega n^2) - \\
& 2 \text{km}^7 \text{kn}^3 (648 \omega m^2 - 21 \omega m \omega n + 790 \omega n^2) + 2 \text{km}^6 \text{kn}^4 (2402 \omega m^2 + 242 \omega m \omega n + 1577 \omega n^2) + 2 \\
& \text{km}^4 \text{kn}^6 (1577 \omega m^2 + 242 \omega m \omega n + 2402 \omega n^2) - \text{km}^5 \text{kn}^5 (5252 \omega m^2 + 883 \omega m \omega n + 5252 \omega n^2) + \\
& 1073741824 \text{d}^{11} \text{g km kn} (\text{kn}^{12} \omega m^2 - 26 \text{km kn}^{11} \omega m (6 \omega m - \omega n) + 26 \text{km}^{11} \text{kn} (\omega m - 6 \omega n) \omega n + \\
& \text{km}^{12} \omega n^2 - 2 \text{km}^{10} \text{kn}^2 (47 \omega m^2 + 103 \omega m \omega n - 252 \omega n^2) + \\
& 2 \text{km}^2 \text{kn}^{10} (252 \omega m^2 - 103 \omega m \omega n - 47 \omega n^2) + 4 \text{km}^3 \text{kn}^9 (376 \omega m^2 + 124 \omega m \omega n + 89 \omega n^2) + \\
& 4 \text{km}^9 \text{kn}^3 (89 \omega m^2 + 124 \omega m \omega n + 376 \omega n^2) + 2 \text{km}^5 \text{kn}^7 (4062 \omega m^2 + 953 \omega m \omega n + 458 \omega n^2) - \\
& 8 \text{km}^6 \text{kn}^6 (491 \omega m^2 + 316 \omega m \omega n + 491 \omega n^2) - \text{km}^4 \text{kn}^8 (6775 \omega m^2 + 952 \omega m \omega n + 497 \omega n^2) + \\
& 2 \text{km}^7 \text{kn}^5 (458 \omega m^2 + 953 \omega m \omega n + 4062 \omega n^2) - \text{km}^8 \text{kn}^4 (497 \omega m^2 + 952 \omega m \omega n + 6775 \omega n^2) + \\
& 16777216 \text{d}^{13} \text{g km kn} (3 \text{kn}^{14} \omega m^2 + 3 \text{km}^{14} \omega n^2 - \text{km kn}^{13} \omega m (42 \omega m + \omega n) - \\
& \text{km}^{13} \text{kn} \omega n (\omega m + 42 \omega n) + \text{km}^2 \text{kn}^{12} (168 \omega m^2 + 7 \omega m \omega n - 2 \omega n^2) + \\
& \text{km}^{12} \text{kn}^2 (-2 \omega m^2 + 7 \omega m \omega n + 168 \omega n^2) - \text{km}^3 \text{kn}^{11} (740 \omega m^2 + 25 \omega m \omega n + 344 \omega n^2) - \\
& \text{km}^{11} \text{kn}^3 (344 \omega m^2 + 25 \omega m \omega n + 740 \omega n^2) + \text{km}^4 \text{kn}^{10} (3335 \omega m^2 + 363 \omega m \omega n + 1628 \omega n^2) + \\
& \text{km}^6 \text{kn}^8 (9326 \omega m^2 + 3749 \omega m \omega n + 2015 \omega n^2) - \\
& \text{km}^5 \text{kn}^9 (8074 \omega m^2 + 1665 \omega m \omega n + 2370 \omega n^2) + \text{km}^{10} \text{kn}^4 (1628 \omega m^2 + 363 \omega m \omega n + 3335 \omega n^2) - \\
& \text{km}^7 \text{kn}^7 (4904 \omega m^2 + 4855 \omega m \omega n + 4904 \omega n^2) - \text{km}^9 \text{kn}^5 (2370 \omega m^2 + 1665 \omega m \omega n + 8074 \omega n^2) + \\
& \text{km}^8 \text{kn}^6 (2015 \omega m^2 + 3749 \omega m \omega n + 9326 \omega n^2) + 18014398509481984 \text{d}^2 \\
& (384 \text{g}^2 \text{km}^3 \text{kn}^3 + \omega m \omega n (-6 \text{km}^4 \omega m^2 - 6 \text{km}^4 \omega n^2 + 4 \text{km}^3 \text{kn} \omega n (27 \omega m + \omega n) + \\
& 4 \text{km kn}^3 \omega m (\omega m + 27 \omega n) + \text{km}^2 \text{kn}^2 (-37 \omega m^2 + 90 \omega m \omega n - 37 \omega n^2))) - \\
& 64 \text{d}^{18} \text{km}^5 (\text{km} - \text{kn})^4 \text{kn}^5 (192 \text{g}^2 \text{km}^2 (\text{km} - \text{kn})^4 \text{kn}^2 - \omega m \omega n (4 \text{kn}^6 \omega m (4 \omega m - 19 \omega n) + \\
& 4 \text{km}^6 \omega n (-19 \omega m + 4 \omega n) + 2 \text{km}^4 \text{kn}^2 (9 \omega m^2 - 170 \omega m \omega n - 259 \omega n^2) - \\
& 2 \text{km}^2 \text{kn}^4 (259 \omega m^2 + 170 \omega m \omega n - 9 \omega n^2) + \text{km kn}^5 (322 \omega m^2 + 314 \omega m \omega n + 3 \omega n^2) - \\
& 2 \text{km}^3 \text{kn}^3 (4 \omega m^2 - 269 \omega m \omega n + 4 \omega n^2) + \text{km}^5 \text{kn} (3 \omega m^2 + 314 \omega m \omega n + 322 \omega n^2))) + \\
& 281474976710656 \text{d}^4 (64 \text{g}^2 \text{km}^3 \text{kn}^3 (11 \text{km}^2 + 18 \text{km kn} + 11 \text{kn}^2) - \\
& \omega m \omega n (-15 \text{kn}^6 \omega m^2 - 15 \text{km}^6 \omega n^2 + 4 \text{km}^5 \text{kn} \omega n (16 \omega m + 5 \omega n) + 4 \text{km kn}^5 \omega m (5 \omega m + 16 \omega n) + \\
& \text{km}^2 \text{kn}^4 (417 \omega m^2 - 1328 \omega m \omega n + 279 \omega n^2) + \text{km}^4 \text{kn}^2 (279 \omega m^2 - 1328 \omega m \omega n + 417 \omega n^2) - \\
& 2 \text{km}^3 \text{kn}^3 (533 \omega m^2 - 34 \omega m \omega n + 533 \omega n^2))) - 4398046511104 \\
& \text{d}^6 (64 \text{g}^2 \text{km}^3 \text{kn}^3 (27 \text{km}^4 - 152 \text{km}^3 \text{kn} + 134 \text{km}^2 \text{kn}^2 - 152 \text{km kn}^3 + 27 \text{kn}^4) + \\
& \omega m \omega n (20 \text{kn}^8 \omega m^2 + 20 \text{km}^7 \text{kn} (11 \omega m - 2 \omega n) \omega n + 20 \text{km}^8 \omega n^2 + \\
& 20 \text{km kn}^7 \omega m (-2 \omega m + 11 \omega n) + 2 \text{km}^3 \text{kn}^5 (681 \omega m^2 + 1658 \omega m \omega n - 89 \omega n^2) + 6 \text{km}^4 \text{kn}^4 \\
& (213 \omega m^2 - 2239 \omega m \omega n + 213 \omega n^2) - \text{km}^2 \text{kn}^6 (1108 \omega m^2 + 970 \omega m \omega n + 315 \omega n^2) + 2 \text{km}^5 \\
& \text{kn}^3 (-89 \omega m^2 + 1658 \omega m \omega n + 681 \omega n^2) - \text{km}^6 \text{kn}^2 (315 \omega m^2 + 970 \omega m \omega n + 1108 \omega n^2))) - \\
& 16777216 \text{d}^{12} (64 \text{g}^2 \text{km}^3 (\text{km} - \text{kn})^2 \text{kn}^3 (\text{km}^8 - 48 \text{km}^7 \text{kn} + 168 \text{km}^6 \text{kn}^2 - 36 \text{km}^5 \text{kn}^3 - \\
& 217 \text{km}^4 \text{kn}^4 - 36 \text{km}^3 \text{kn}^5 + 168 \text{km}^2 \text{kn}^6 - 48 \text{km kn}^7 + \text{kn}^8) + \\
& \omega m \omega n (-\text{kn}^{14} \omega m^2 - \text{km}^{14} \omega n^2 + 4 \text{km}^{13} \text{kn} \omega n (12 \omega m + \omega n) + 4 \text{km kn}^{13} \omega m (\omega m + 12 \omega n) + \\
& \text{km}^8 \text{kn}^6 (173 \omega m^2 - 19896 \omega m \omega n - 12705 \omega n^2) + \text{km}^{10} \text{kn}^4 \\
& (1875 \omega m^2 + 388 \omega m \omega n - 1509 \omega n^2) - 8 \text{km}^9 \text{kn}^5 (137 \omega m^2 + 555 \omega m \omega n - 1210 \omega n^2) + \\
& 8 \text{km}^5 \text{kn}^9 (1210 \omega m^2 - 555 \omega m \omega n - 137 \omega n^2) + \text{km}^{12} \text{kn}^2 (37 \omega m^2 - 1056 \omega m \omega n - 83 \omega n^2) + \\
& \text{km}^2 \text{kn}^{12} (-83 \omega m^2 - 1056 \omega m \omega n + 37 \omega n^2) - 2 \text{km}^{11} \text{kn}^3 (345 \omega m^2 - 1534 \omega m \omega n + \\
& 81 \omega n^2) + \text{km}^6 \text{kn}^8 (-12705 \omega m^2 - 19896 \omega m \omega n + 173 \omega n^2) + 22 \text{km}^7 \text{kn}^7 \\
& (189 \omega m^2 + 2014 \omega m \omega n + 189 \omega n^2) - 2 \text{km}^3 \text{kn}^{11} (81 \omega m^2 - 1534 \omega m \omega n + 345 \omega n^2) + \\
& \text{km}^4 \text{kn}^{10} (-1509 \omega m^2 + 388 \omega m \omega n + 1875 \omega n^2))) - 68719476736 \text{d}^8 \\
& (128 \text{g}^2 \text{km}^3 \text{kn}^3 (5 \text{km}^6 + 10 \text{km}^5 \text{kn} - 72 \text{km}^4 \text{kn}^2 + 78 \text{km}^3 \text{kn}^3 - 72 \text{km}^2 \text{kn}^4 + 10 \text{km kn}^5 + 5 \text{kn}^6) + \\
& \omega m \omega n (-15 \text{kn}^{10} \omega m^2 + 8 \text{km kn}^9 \omega m (5 \omega m - 13 \omega n) - 8 \text{km}^9 \text{kn} (13 \omega m - 5 \omega n) \omega n - \\
& 15 \text{km}^{10} \omega n^2 + \text{km}^4 \text{kn}^6 (-5322 \omega m^2 + 3682 \omega m \omega n - 5431 \omega n^2) + \\
& \text{km}^6 \text{kn}^4 (-5431 \omega m^2 + 3682 \omega m \omega n - 5322 \omega n^2) + \text{km}^2 \text{kn}^8 \\
& (546 \omega m^2 + 3280 \omega m \omega n - 315 \omega n^2) + 4 \text{km}^7 \text{kn}^3 (783 \omega m^2 - 2445 \omega m \omega n + 409 \omega n^2) + \text{km}^8 \\
& \text{kn}^2 (-315 \omega m^2 + 3280 \omega m \omega n + 546 \omega n^2) + 4 \text{km}^3 \text{kn}^7 (409 \omega m^2 - 2445 \omega m \omega n + 783 \omega n^2) + \\
& 2 \text{km}^5 \text{kn}^5 (2215 \omega m^2 + 1362 \omega m \omega n + 2215 \omega n^2))) - 4096 \text{d}^{16} \text{km}^3 (\text{km} - \text{kn})^2 \text{kn}^3 \\
& (64 \text{g}^2 \text{km}^2 (\text{km} - \text{kn})^4 \text{kn}^2 (10 \text{km}^4 - 28 \text{km}^3 \text{kn} + 19 \text{km}^2 \text{kn}^2 - 28 \text{km kn}^3 + 10 \text{kn}^4) + \\
& \omega m \omega n (4 \text{km}^{10} \omega n (13 \omega m + 2 \omega n) + 4 \text{kn}^{10} \omega m (2 \omega m + 13 \omega n) + \\
& 2 \text{km}^8 \text{kn}^2 (6 \omega m^2 + 1682 \omega m \omega n - 315 \omega n^2) + \text{km kn}^9 (32 \omega m^2 - 494 \omega m \omega n + 3 \omega n^2) + \\
& 2 \text{km}^2 \text{kn}^8 (-315 \omega m^2 + 1682 \omega m \omega n + 6 \omega n^2) + \text{km}^9 \text{kn} (3 \omega m^2 - 494 \omega m \omega n + 32 \omega n^2) + \text{km}^3 \\
& \text{kn}^7 (1432 \omega m^2 - 11636 \omega m \omega n + 33 \omega n^2) - 4 \text{km}^4 \text{kn}^6 (713 \omega m^2 - 6066 \omega m \omega n + 429 \omega n^2) -
\end{aligned}$$

$$\begin{aligned}
& 4 \text{ km}^6 \text{ kn}^4 (429 \omega m^2 - 6066 \omega m \omega n + 713 \omega n^2) + \text{ km}^7 \text{ kn}^3 (33 \omega m^2 - 11636 \omega m \omega n + \\
& 1432 \omega n^2) + \text{ km}^5 \text{ kn}^5 (3957 \omega m^2 - 31658 \omega m \omega n + 3957 \omega n^2) \Big) - \\
& 262144 \text{ d}^{14} \text{ km kn} (64 \text{ g}^2 \text{ km}^2 (\text{ km} - \text{ kn})^4 \text{ kn}^2 (3 \text{ km}^8 - 20 \text{ km}^7 \text{ kn} + 24 \text{ km}^6 \text{ kn}^2 - \\
& 88 \text{ km}^5 \text{ kn}^3 + 213 \text{ km}^4 \text{ kn}^4 - 88 \text{ km}^3 \text{ kn}^5 + 24 \text{ km}^2 \text{ kn}^6 - 20 \text{ km kn}^7 + 3 \text{ kn}^8) - \\
& \omega m \omega n (-4 \text{ km}^{14} \omega m \omega n - 4 \text{ kn}^{14} \omega m \omega n + 2 \text{ km}^4 \text{ kn}^{10} (871 \omega m^2 - 15542 \omega m \omega n - 985 \omega n^2) - 2 \\
& \text{ km}^{10} \text{ kn}^4 (985 \omega m^2 + 15542 \omega m \omega n - 871 \omega n^2) + 2 \text{ km}^{12} \text{ kn}^2 (\omega m^2 - 462 \omega m \omega n - 325 \omega n^2) + \\
& 2 \text{ km}^2 \text{ kn}^{12} (-325 \omega m^2 - 462 \omega m \omega n + \omega n^2) + \text{ km kn}^{13} (94 \omega m^2 + 78 \omega m \omega n + \omega n^2) + \\
& 6 \text{ km}^3 \text{ kn}^{11} (39 \omega m^2 + 1347 \omega m \omega n + 13 \omega n^2) + 6 \text{ km}^{11} \text{ kn}^3 (13 \omega m^2 + 1347 \omega m \omega n + 39 \omega n^2) + \\
& \text{ km}^{13} \text{ kn} (\omega m^2 + 78 \omega m \omega n + 94 \omega n^2) + 2 \text{ km}^9 \text{ kn}^5 (3577 \omega m^2 + 30645 \omega m \omega n + 124 \omega n^2) - \\
& 2 \text{ km}^8 \text{ kn}^6 (5163 \omega m^2 + 38446 \omega m \omega n + 2783 \omega n^2) + \\
& 2 \text{ km}^5 \text{ kn}^9 (124 \omega m^2 + 30645 \omega m \omega n + 3577 \omega n^2) + 2 \text{ km}^7 \text{ kn}^7 (4451 \omega m^2 + \\
& 39511 \omega m \omega n + 4451 \omega n^2) - 2 \text{ km}^6 \text{ kn}^8 (2783 \omega m^2 + 38446 \omega m \omega n + 5163 \omega n^2) \Big) + \\
& 1073741824 \text{ d}^{10} (128 \text{ g}^2 \text{ km}^3 \text{ kn}^3 (12 \text{ km}^8 - 116 \text{ km}^7 \text{ kn} + 316 \text{ km}^6 \text{ kn}^2 - 410 \text{ km}^5 \text{ kn}^3 + \\
& 407 \text{ km}^4 \text{ kn}^4 - 410 \text{ km}^3 \text{ kn}^5 + 316 \text{ km}^2 \text{ kn}^6 - 116 \text{ km kn}^7 + 12 \text{ kn}^8) - \\
& \omega m \omega n (6 \text{ kn}^{12} \omega m^2 + 6 \text{ km}^{12} \omega n^2 - 4 \text{ km}^{11} \text{ kn} \omega n (29 \omega m + 5 \omega n) - 4 \text{ km kn}^{11} \omega m (5 \omega m + 29 \omega n) + \\
& \text{ km}^2 \text{ kn}^{10} (285 \omega m^2 + 242 \omega m \omega n + 279 \omega n^2) + \text{ km}^{10} \text{ kn}^2 (279 \omega m^2 + 242 \omega m \omega n + 285 \omega n^2) - \\
& 4 \text{ km}^3 \text{ kn}^9 (607 \omega m^2 - 103 \omega m \omega n + 298 \omega n^2) - 4 \text{ km}^9 \text{ kn}^3 (298 \omega m^2 - 103 \omega m \omega n + 607 \omega n^2) + \\
& 2 \text{ km}^4 \text{ kn}^8 (2746 \omega m^2 + 8662 \omega m \omega n + 965 \omega n^2) - 4 \text{ km}^5 \text{ kn}^7 (2872 \omega m^2 + 16027 \omega m \omega n + \\
& 2057 \omega n^2) + 2 \text{ km}^8 \text{ kn}^4 (965 \omega m^2 + 8662 \omega m \omega n + 2746 \omega n^2) - 4 \text{ km}^7 \text{ kn}^5 (2057 \omega m^2 + \\
& 16027 \omega m \omega n + 2872 \omega n^2) + 3 \text{ km}^6 \text{ kn}^6 (5411 \omega m^2 + 29962 \omega m \omega n + 5411 \omega n^2) \Big) \Big) / \\
& (2 \text{ d km}^2 (-64 + \text{ d}^2 \text{ km}^2)^3 \text{ kn}^2 (-64 + \text{ d}^2 \text{ kn}^2)^3 \omega m (-16777216 \text{ d g} (\text{ km} - \text{ kn})^2 - \\
& 1835008 \text{ d}^3 \text{ g} (\text{ km} - \text{ kn})^4 - \\
& 28672 \text{ d}^5 \text{ g} (\text{ km} - \text{ kn})^6 - \\
& 64 \text{ d}^7 \text{ g} (\text{ km} - \text{ kn})^8 + 16777216 (\omega m - \omega n)^2 + \\
& 7340032 \text{ d}^2 (\text{ km} - \text{ kn})^2 (\omega m - \omega n)^2 + \\
& 286720 \text{ d}^4 (\text{ km} - \text{ kn})^4 (\omega m - \omega n)^2 + \\
& 1792 \text{ d}^6 (\text{ km} - \text{ kn})^6 (\omega m - \omega n)^2 + \\
& \text{ d}^8 (\text{ km} - \text{ kn})^8 (\omega m - \omega n)^2 \omega n) ; \\
& \omega m = 8 \text{ km} \sqrt{((\text{ d g} (64 + \text{ d}^2 \text{ km}^2) (4096 + 384 \text{ d}^2 \text{ km}^2 + \text{ d}^4 \text{ km}^4)) / \\
& (16777216 + 7340032 \text{ d}^2 \text{ km}^2 + 286720 \text{ d}^4 \text{ km}^4 + 1792 \text{ d}^6 \text{ km}^6 + \text{ d}^8 \text{ km}^8))} ; \\
& \omega n = 8 \text{ kn} \sqrt{((\text{ d g} (64 + \text{ d}^2 \text{ kn}^2) (4096 + 384 \text{ d}^2 \text{ kn}^2 + \text{ d}^4 \text{ kn}^4)) / \\
& (16777216 + 7340032 \text{ d}^2 \text{ kn}^2 + 286720 \text{ d}^4 \text{ kn}^4 + 1792 \text{ d}^6 \text{ kn}^6 + \text{ d}^8 \text{ kn}^8))} ; \\
& \text{fourlsub} = \text{s1} * \text{d} / (\text{eta01m eta01n}) /. \{ \text{ km} \rightarrow \text{ kdm} / \text{ d}, \text{ kn} \rightarrow \text{ kdn} / \text{ d} \} // \text{Simplify} \\
& (* \text{ multiplied with d*});
\end{aligned}$$

```

p41 = ContourPlot[Quiet[fourlsub/GsubDe], {kdm, 0, 5},
  {kdn, 0, 5}, Contours -> Function[{min, max}, Range[0, 1.4, 0.1]],
  ContourLabels -> Function[{x, y, z}, Text[z, {x, y}, Background -> White]],
  ImageSize -> 300, ColorFunction -> "GrayTones",
  PlotLegends -> BarLegend[Automatic, LegendMarkerSize -> 180, LegendFunction -> "Frame",
  LegendMargins -> 5, LegendLabel -> " $G_{SWASH}^{m-n}/G_{theor}^{m-n}$ "], AspectRatio -> Automatic,
  Frame -> {True, True, False, False}, FrameLabel -> {Style["kmd", 16], Style["knd", 16]},
  FrameTicks -> All, PlotLabel -> Style["Four layers", FontSize -> 18]]

```



```
Quit[]
```

B.5 Superharmonic transfer functions

Exact solution

Schaffer (1994)

$$\omega_n = (g * kn * \text{Tanh}[kn * d])^{1/2};$$

$$\omega_m = (g * km * \text{Tanh}[km * d])^{1/2};$$

$$H = (\omega_m + \omega_n) * \left(\omega_m * \omega_n - \frac{g^2 * kn * km}{\omega_n * \omega_m} \right) + \frac{\omega_m^3 + \omega_n^3}{2} - \frac{g^2}{2} * \left(\frac{km^2}{\omega_m} + \frac{kn^2}{\omega_n} \right);$$

$$D_s = g * (km + kn) * \text{Tanh}[(km + kn) * d] - (\omega_m + \omega_n)^2;$$

$$L = \frac{1}{2} * \left(\frac{g^2 * km * kn}{\omega_m * \omega_n} - \omega_m * \omega_n - (\omega_m^2 + \omega_n^2) \right);$$

$$G = \frac{1}{g} * \left((\omega_m + \omega_n) * \frac{H}{D_s} - L \right) // \text{Simplify};$$

$$G_{supSc} = G * d /. \{km \rightarrow kdm/d, kn \rightarrow kdn/d\} // \text{Simplify}; (* \text{ multiplied with } d*)$$

Sand (1986)

$$a_m = \left(\frac{d * \omega_m^2}{g * 2 * \pi} \right)^{1/2};$$

$$a_n = \left(\frac{d * \omega_n^2}{g * 2 * \pi} \right)^{1/2};$$

$$G = \left(\left(2 * (a_n + a_m)^2 * \left(\frac{kn * d * km * d}{a_n * a_m} - 4 * \pi^2 * a_n * a_m \right) + \right. \right. \\ \left. \left. (a_n + a_m) * \left(\frac{km^2 * d^2}{a_m} + \frac{kn^2 * d^2}{a_n} - 4 * \pi^2 * (a_n^3 + a_m^3) \right) \right) \right) / \\ \left((4 * \pi * (a_n + a_m)^2) - 2 * (km + kn) * d * \text{Tanh}[(km + kn) * d] \right) + \\ \left((4 * \pi^2 * a_n^2 * a_m^2 * \left(1 + \frac{a_n}{a_m} + \frac{a_m}{a_n} \right) - kn * d * km * d) \right) / (4 * \pi * a_n * a_m);$$

$$G_{supSa} = G /. \{km \rightarrow kdm/d, kn \rightarrow kdn/d\} // \text{Simplify}; (* \text{ multiplied with } d*)$$

Dean-Sharma (1981)

$$\omega_n = (kn * \text{Tanh}[kn * d])^{1/2};$$

$$\omega_m = (km * \text{Tanh}[km * d])^{1/2};$$

$$G = \frac{1}{2} * \\ \left(\left(\left((2 * (\omega_m + \omega_n)^2 * (km * kn - \omega_m^2 * \omega_n^2)) / ((\omega_m + \omega_n)^2 - (km + kn) * \text{Tanh}[(km + kn) * d]) \right) + \right. \right. \\ \left. \left((\omega_m + \omega_n) * (\omega_m * (kn^2 - \omega_n^4) + \omega_n * (km^2 - \omega_m^4)) \right) / ((\omega_m + \omega_n)^2 - (km + kn) * \text{Tanh}[(km + kn) * d]) \right) \right) - (km * kn - \omega_m^2 * \omega_n^2) / (\omega_m * \omega_n + \omega_m^2 + \omega_n^2);$$

$$G_{supDe} = G * d /. \{km \rightarrow kdm/d, kn \rightarrow kdn/d\} // \text{Simplify}; (* \text{ multiplied with } d*)$$

All the above expressions are equal

Clear[\omega_m, \omega_n];

One layer solution

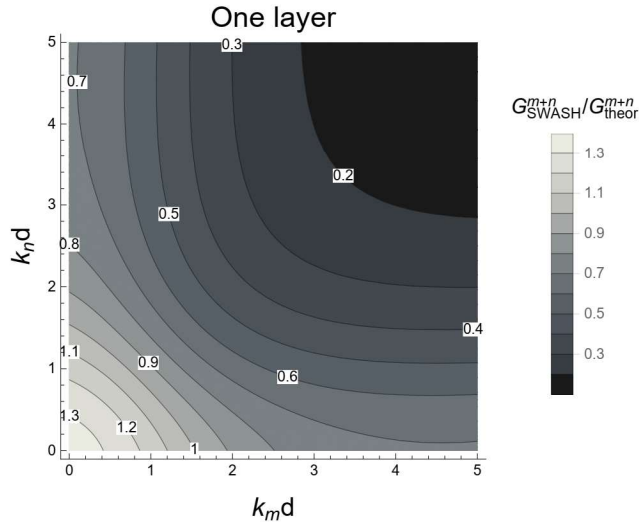
$$s1 = \left(\text{eta01m eta01n (km + kn)}^2 \right. \\ \left. \left(4 d g km kn + 8 \omega m \omega n + d^2 (km^2 \omega n (2 \omega m + \omega n) + kn^2 \omega m (\omega m + 2 \omega n) - 2 km kn (\omega m^2 + \omega n^2)) \right) \right) / \\ \left(2 d km kn (-4 d g (km + kn)^2 + 4 (\omega m + \omega n)^2 + d^2 (km + kn)^2 (\omega m + \omega n)^2) \right);$$

$$\omega m = \frac{2 \sqrt{d g km}}{\sqrt{4 + d^2 km^2}};$$

$$\omega n = \frac{2 \sqrt{d g kn}}{\sqrt{4 + d^2 kn^2}};$$

```
oneIsup = s1 * d / (eta01m eta01n) /. {km -> kdm/d, kn -> kdn/d} // Simplify
(* multiplied with d*);
```

```
p11 = ContourPlot[oneIsup/GsupSa, {kdm, 0, 5},
  {kdn, 0, 5}, Contours -> Function[{min, max}, Range[0, 1.4, 0.1]],
  ContourLabels -> Function[{x, y, z}, Text[z, {x, y}, Background -> White]],
  ImageSize -> 300, ColorFunction -> "GrayTones",
  PlotLegends -> BarLegend[Automatic, LegendMarkerSize -> 180, LegendFunction -> "Frame",
  LegendMargins -> 5, LegendLabel -> "Gm+nSWASH/Gm+ntheor"], AspectRatio -> Automatic,
  Frame -> {True, True, False, False}, FrameLabel -> {Style["kmd", 16], Style["knd", 16]},
  FrameTicks -> All, PlotLabel -> Style["One layer", FontSize -> 18]]
```



```
Clear[ωm, ωn];
```

Two layers solution

$$\begin{aligned}
 s1 = & \left(\text{eta01m eta01n} (km + kn)^2 \left(65536 \omega m \omega n (kn^2 \omega m^2 + 4 km kn \omega m \omega n + km^2 \omega n^2) - \right. \right. \\
 & 65536 d g km kn (2 kn^2 \omega m^2 + km kn \omega m \omega n + 2 km^2 \omega n^2) - 16 d^7 g km^3 kn^3 (km + kn)^2 \\
 & (km^2 (\omega m - 3 \omega n) \omega n + kn^2 \omega m (-3 \omega m + \omega n) + km kn (-4 \omega m^2 + 5 \omega m \omega n - 4 \omega n^2)) - \\
 & 4096 d^3 g km kn (kn^4 \omega m^2 + km^4 \omega n^2 - 2 km kn^3 \omega m (4 \omega m + 3 \omega n) - 2 km^3 kn \omega n (3 \omega m + 4 \omega n) - \\
 & 4 km^2 kn^2 (\omega m^2 + 3 \omega m \omega n + \omega n^2)) + d^8 km^3 kn^3 (km + kn)^2 \omega m \omega n \\
 & (2 kn^2 \omega m (2 \omega m + \omega n) + 2 km^2 \omega n (\omega m + 2 \omega n) - km kn (\omega m^2 + 6 \omega m \omega n + \omega n^2)) + \\
 & 256 d^5 g km kn (kn^6 \omega m^2 + km kn^5 \omega m (6 \omega m - \omega n) + km^6 \omega n^2 + \\
 & km^5 kn \omega n (-\omega m + 6 \omega n) + km^2 kn^4 (10 \omega m^2 + \omega m \omega n - 10 \omega n^2) + \\
 & km^3 kn^3 (-4 \omega m^2 + 5 \omega m \omega n - 4 \omega n^2) + km^4 kn^2 (-10 \omega m^2 + \omega m \omega n + 10 \omega n^2)) + \\
 & 4096 d^2 (32 g^2 km^3 kn^3 - \omega m \omega n (2 kn^4 \omega m^2 - 6 km^3 kn \omega m \omega n - 6 km kn^3 \omega m \omega n + \\
 & 2 km^4 \omega n^2 + km^2 kn^2 (9 \omega m^2 + 14 \omega m \omega n + 9 \omega n^2))) + 256 d^4 \\
 & (16 g^2 km^3 kn^3 (km + kn)^2 - \omega m \omega n (-kn^6 \omega m^2 - km^6 \omega n^2 + km^2 kn^4 (15 \omega m^2 + 28 \omega m \omega n + 9 \omega n^2) + \\
 & km^4 kn^2 (9 \omega m^2 + 28 \omega m \omega n + 15 \omega n^2) + 2 km^3 kn^3 (23 \omega m^2 + 40 \omega m \omega n + 23 \omega n^2))) - \\
 & 16 d^6 km kn (16 g^2 km^2 kn^2 (km + kn)^4 - \omega m \omega n (-2 km^6 \omega m \omega n - 2 kn^6 \omega m \omega n - 2 km^4 kn^2 (\omega m^2 - \\
 & 2 \omega m \omega n - 21 \omega n^2) + 2 km^2 kn^4 (21 \omega m^2 + 2 \omega m \omega n - \omega n^2) + km kn^5 (24 \omega m^2 - 14 \omega m \omega n + \\
 & \omega n^2) + 2 km^3 kn^3 (\omega m^2 + 3 \omega m \omega n + \omega n^2) + km^5 kn (\omega m^2 - 14 \omega m \omega n + 24 \omega n^2))) \Big) \Big) / \\
 & \left(2 d km^2 (-16 + d^2 km^2) kn^2 (-16 + d^2 kn^2) \omega m \omega n (-256 d g (km + kn)^2 - 16 d^3 g (km + kn)^4 + \right. \\
 & \left. 256 (\omega m + \omega n)^2 + 96 d^2 (km + kn)^2 (\omega m + \omega n)^2 + d^4 (km + kn)^4 (\omega m + \omega n)^2 \right) \Big);
 \end{aligned}$$

$$\omega m = \frac{4 \sqrt{d g km^2 (16 + d^2 km^2)}}{\sqrt{256 + 96 d^2 km^2 + d^4 km^4}};$$

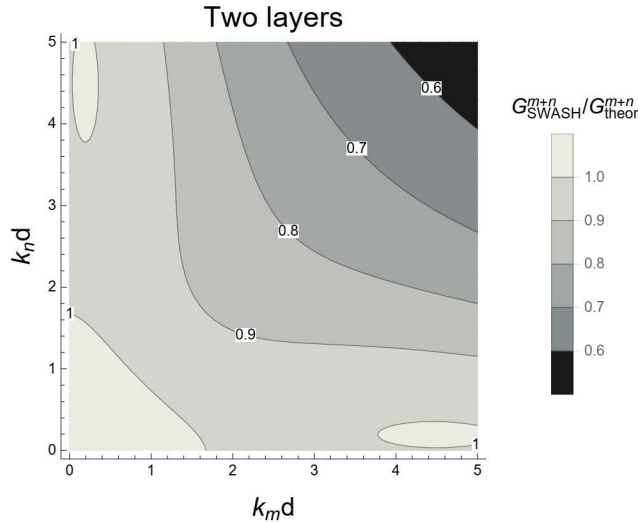
$$\omega n = \frac{4 \sqrt{d g kn^2 (16 + d^2 kn^2)}}{\sqrt{256 + 96 d^2 kn^2 + d^4 kn^4}};$$

twolsup = s1 * d / (eta01m eta01n) /. {km -> kdm/d, kn -> kdn/d} // Simplify
 (* multiplied with d*);

```

p21 = ContourPlot[twosup/GsupSa, {kdm, 0, 5},
  {kdn, 0, 5}, Contours -> Function[{min, max}, Range[0, 1.4, 0.1]],
  ContourLabels -> Function[{x, y, z}, Text[z, {x, y}, Background -> White]],
  ImageSize -> 300, ColorFunction -> "GrayTones",
  PlotLegends -> BarLegend[Automatic, LegendMarkerSize -> 180, LegendFunction -> "Frame",
  LegendMargins -> 5, LegendLabel -> "Gm+nSWASH/Gm+ntheor"], AspectRatio -> Automatic,
  Frame -> {True, True, False, False}, FrameLabel -> {Style["kmd", 16], Style["knd", 16]},
  FrameTicks -> All, PlotLabel -> Style["Two layers", FontSize -> 18]]

```



```
Clear[ωm, ωn];
```

Three layers solution

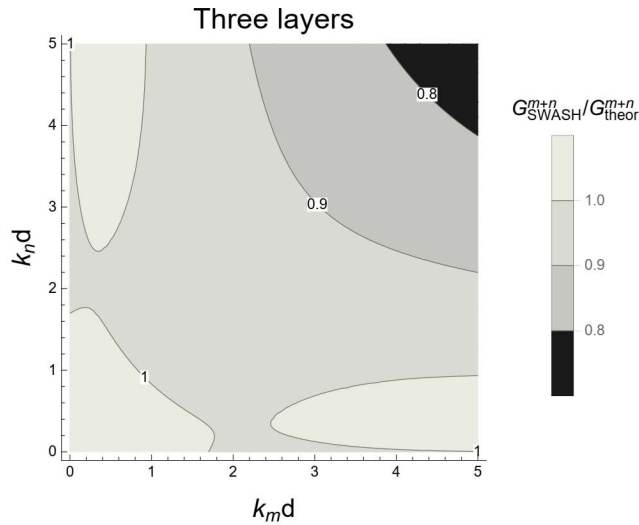
$$\begin{aligned}
s1 = & \left(\text{eta01m eta01n} (km + kn)^2 \left(78364164096 \omega m \omega n (kn^2 \omega m^2 + 6 km kn \omega m \omega n + km^2 \omega n^2) - \right. \right. \\
& 78364164096 d g km kn (4 kn^2 \omega m^2 + km kn \omega m \omega n + 4 km^2 \omega n^2) + d^{14} km^5 kn^5 (km + kn)^4 \\
& \left. \omega m \omega n (3 km^2 \omega n (3 \omega m + 2 \omega n) + 3 kn^2 \omega m (2 \omega m + 3 \omega n) - km kn (\omega m^2 - 4 \omega m \omega n + \omega n^2)) - \right. \\
& 725594112 d^3 g km kn (6 kn^4 \omega m^2 + 6 km^4 \omega n^2 - 4 km kn^3 \omega m (23 \omega m + 11 \omega n) - \\
& \left. 4 km^3 kn \omega n (11 \omega m + 23 \omega n) + 3 km^2 kn^2 (7 \omega m^2 - 34 \omega m \omega n + 7 \omega n^2)) - \right. \\
& 12 d^{13} g km^5 kn^5 (km + kn)^4 (3 km^2 (3 \omega m^2 + \omega m \omega n + 2 \omega n^2) + \\
& \left. 3 kn^2 (2 \omega m^2 + \omega m \omega n + 3 \omega n^2) + km kn (12 \omega m^2 + 35 \omega m \omega n + 12 \omega n^2)) + \right. \\
& 559872 d^7 g km kn (6 kn^8 \omega m^2 + 6 km^8 \omega n^2 - 4 km kn^7 \omega m (27 \omega m + 5 \omega n) - \\
& \left. 4 km^7 kn \omega n (5 \omega m + 27 \omega n) + km^6 kn^2 (24 \omega m^2 - 169 \omega m \omega n - 339 \omega n^2) + \right. \\
& \left. km^2 kn^6 (-339 \omega m^2 - 169 \omega m \omega n + 24 \omega n^2) + 2 km^5 kn^3 (94 \omega m^2 - 229 \omega m \omega n + 54 \omega n^2) + \right. \\
& \left. 2 km^3 kn^5 (54 \omega m^2 - 229 \omega m \omega n + 94 \omega n^2) + 4 km^4 kn^4 (111 \omega m^2 - 154 \omega m \omega n + 111 \omega n^2) \right) + \\
& 20155392 d^5 g km kn (18 kn^6 \omega m^2 + 6 km kn^5 \omega m (26 \omega m - 3 \omega n) - \\
& \left. 6 km^5 kn (3 \omega m - 26 \omega n) \omega n + 18 km^6 \omega n^2 + 3 km^2 kn^4 (119 \omega m^2 + 23 \omega m \omega n - 10 \omega n^2) + \right. \\
& \left. 3 km^4 kn^2 (-10 \omega m^2 + 23 \omega m \omega n + 119 \omega n^2) + 2 km^3 kn^3 (196 \omega m^2 + 101 \omega m \omega n + 196 \omega n^2) \right) - \\
& 432 d^{11} g km^3 kn^3 (km + kn)^2 (3 kn^6 (20 \omega m^2 - \omega m \omega n + \omega n^2) + \\
& \left. 3 km^6 (\omega m^2 - \omega m \omega n + 20 \omega n^2) + 2 km kn^5 (132 \omega m^2 + 2 \omega m \omega n + 21 \omega n^2) + \right. \\
& \left. 2 km^5 kn (21 \omega m^2 + 2 \omega m \omega n + 132 \omega n^2) + 2 km^3 kn^3 (162 \omega m^2 - 29 \omega m \omega n + 162 \omega n^2) + \right. \\
& \left. km^2 kn^4 (372 \omega m^2 - 43 \omega m \omega n + 195 \omega n^2) + km^4 kn^2 (195 \omega m^2 - 43 \omega m \omega n + 372 \omega n^2) \right) - \\
& 15552 d^9 g km kn (6 kn^{10} \omega m^2 + 6 km^{10} \omega n^2 + 3 km kn^9 \omega m (20 \omega m + \omega n) + \\
& \left. 3 km^9 kn \omega n (\omega m + 20 \omega n) - 12 km^4 kn^6 (3 \omega m^2 + 32 \omega m \omega n - 62 \omega n^2) + \right. \\
& \left. km^2 kn^8 (105 \omega m^2 + 5 \omega m \omega n - 42 \omega n^2) - 6 km^3 kn^7 (14 \omega m^2 + 19 \omega m \omega n - 24 \omega n^2) + \right. \\
& \left. 6 km^7 kn^3 (24 \omega m^2 - 19 \omega m \omega n - 14 \omega n^2) + 12 km^6 kn^4 (62 \omega m^2 - 32 \omega m \omega n - 3 \omega n^2) + \right. \\
& \left. km^8 kn^2 (-42 \omega m^2 + 5 \omega m \omega n + 105 \omega n^2) + km^5 kn^5 (660 \omega m^2 - 527 \omega m \omega n + 660 \omega n^2) \right) + \\
& 2176782336 d^2 (144 g^2 km^3 kn^3 - \omega m \omega n (4 kn^4 \omega m^2 + km kn^3 \omega m (2 \omega m - 33 \omega n) + \\
& \left. 4 km^4 \omega n^2 + km^3 kn \omega n (-33 \omega m + 2 \omega n) + km^2 kn^2 (21 \omega m^2 + 44 \omega m \omega n + 21 \omega n^2) \right) +
\end{aligned}$$

$$\begin{aligned}
& 120932352 d^4 \left(36 g^2 km^3 (km - kn)^2 kn^3 - \omega m \omega n (-3 kn^6 \omega m^2 - 3 km kn^5 \omega m (\omega m - 3 \omega n) + \right. \\
& \quad \left. 3 km^5 kn (3 \omega m - \omega n) \omega n - 3 km^6 \omega n^2 + km^2 kn^4 (55 \omega m^2 + 148 \omega m \omega n + 35 \omega n^2) + \right. \\
& \quad \left. km^4 kn^2 (35 \omega m^2 + 148 \omega m \omega n + 55 \omega n^2) + 2 km^3 kn^3 (76 \omega m^2 + 81 \omega m \omega n + 76 \omega n^2) \right) + \\
& 36 d^{12} km^3 kn^3 (km + kn)^2 \left(72 g^2 km^2 kn^2 (km + kn)^4 + \omega m \omega n \right. \\
& \quad \left(-6 kn^6 \omega m (\omega m - 2 \omega n) + 6 km^6 (2 \omega m - \omega n) \omega n + 2 km^2 kn^4 (89 \omega m^2 + 157 \omega m \omega n - 4 \omega n^2) - \right. \\
& \quad \left. km^3 kn^3 (\omega m^2 - 356 \omega m \omega n + \omega n^2) + km kn^5 (103 \omega m^2 + 88 \omega m \omega n + 2 \omega n^2) + \right. \\
& \quad \left. 2 km^4 kn^2 (-4 \omega m^2 + 157 \omega m \omega n + 89 \omega n^2) + km^5 kn (2 \omega m^2 + 88 \omega m \omega n + 103 \omega n^2) \right) - \\
& 3359232 d^6 \left(12 g^2 km^3 kn^3 (9 km^4 + 54 km^3 kn + 76 km^2 kn^2 + 54 km kn^3 + 9 kn^4) + \right. \\
& \quad \omega m \omega n (2 kn^8 \omega m^2 + 2 km^8 \omega n^2 + 3 km^7 kn \omega n (6 \omega m + \omega n) + \\
& \quad 3 km kn^7 \omega m (\omega m + 6 \omega n) + km^6 kn^2 (-35 \omega m^2 + 58 \omega m \omega n - 132 \omega n^2) + \\
& \quad km^2 kn^6 (-132 \omega m^2 + 58 \omega m \omega n - 35 \omega n^2) + 2 km^4 kn^4 (9 \omega m^2 + 224 \omega m \omega n + 9 \omega n^2) - \\
& \quad \left. 2 km^3 kn^5 (110 \omega m^2 - 59 \omega m \omega n + 18 \omega n^2) - 2 km^5 kn^3 (18 \omega m^2 - 59 \omega m \omega n + 110 \omega n^2) \right) - \\
& 46656 d^8 \left(24 g^2 km^3 kn^3 (km + kn)^2 (3 km^4 - 4 km^3 kn - 31 km^2 kn^2 - 4 km kn^3 + 3 kn^4) - \right. \\
& \quad \omega m \omega n (kn^{10} \omega m^2 + km^{10} \omega n^2 + 2 km^9 kn \omega n (6 \omega m + \omega n) + \\
& \quad 2 km kn^9 \omega m (\omega m + 6 \omega n) + km^8 kn^2 (21 \omega m^2 + 256 \omega m \omega n - 114 \omega n^2) + \\
& \quad 2 km^7 kn^3 (116 \omega m^2 + 374 \omega m \omega n + 13 \omega n^2) + km^2 kn^8 (-114 \omega m^2 + 256 \omega m \omega n + 21 \omega n^2) + \\
& \quad 2 km^3 kn^7 (13 \omega m^2 + 374 \omega m \omega n + 116 \omega n^2) + 2 km^5 kn^5 (123 \omega m^2 - 575 \omega m \omega n + 123 \omega n^2) + \\
& \quad \left. km^4 kn^6 (373 \omega m^2 + 40 \omega m \omega n + 364 \omega n^2) + km^6 kn^4 (364 \omega m^2 + 40 \omega m \omega n + 373 \omega n^2) \right) + \\
& 1296 d^{10} km kn \left(24 g^2 km^2 kn^2 (km + kn)^4 (3 km^4 + 10 km^3 kn - 4 km^2 kn^2 + 10 km kn^3 + 3 kn^4) - \right. \\
& \quad \omega m \omega n (-3 km^{10} \omega m \omega n - 3 kn^{10} \omega m \omega n + km^2 kn^8 (156 \omega m^2 - 103 \omega m \omega n - 2 \omega n^2) + \\
& \quad km kn^9 (19 \omega m^2 - 40 \omega m \omega n + \omega n^2) + 2 km^3 kn^7 (179 \omega m^2 - 320 \omega m \omega n + 12 \omega n^2) + \\
& \quad km^9 kn (\omega m^2 - 40 \omega m \omega n + 19 \omega n^2) + km^8 kn^2 (-2 \omega m^2 - 103 \omega m \omega n + 156 \omega n^2) + 2 km^7 kn^3 \\
& \quad (12 \omega m^2 - 320 \omega m \omega n + 179 \omega n^2) + km^4 kn^6 (702 \omega m^2 - 1925 \omega m \omega n + 432 \omega n^2) + km^6 kn^4 \\
& \quad \left. (432 \omega m^2 - 1925 \omega m \omega n + 702 \omega n^2) + km^5 kn^5 (915 \omega m^2 - 2644 \omega m \omega n + 915 \omega n^2) \right) \Big) / \\
& \left(2 d km^2 (-36 + d^2 km^2)^2 kn^2 (-36 + d^2 kn^2)^2 \omega m \omega n (-46656 d g (km + kn)^2 - \right. \\
& \quad 4320 d^3 g (km + kn)^4 - 36 d^5 g (km + kn)^6 + \\
& \quad 46656 (\omega m + \omega n)^2 + 19440 d^2 (km + kn)^2 (\omega m + \omega n)^2 + \\
& \quad \left. 540 d^4 (km + kn)^4 (\omega m + \omega n)^2 + d^6 (km + kn)^6 (\omega m + \omega n)^2 \right) \Big); \\
\omega m &= \frac{6 \sqrt{d g km^2 (12 + d^2 km^2) (108 + d^2 km^2)}}{\sqrt{(36 + d^2 km^2) (1296 + 504 d^2 km^2 + d^4 km^4)}}; \\
\omega n &= \frac{6 \sqrt{d g kn^2 (12 + d^2 kn^2) (108 + d^2 kn^2)}}{\sqrt{(36 + d^2 kn^2) (1296 + 504 d^2 kn^2 + d^4 kn^4)}}; \\
\text{threeIsup} &= s1 * d / (\text{eta01meta01n}) /. \{km \rightarrow kdm/d, kn \rightarrow kdn/d\} // \text{Simplify} \\
& (* \text{ multiplied with } d*);
\end{aligned}$$

```

p31 = ContourPlot[threeIsup/GsupSa, {kdm, 0, 5},
  {kdn, 0, 5}, Contours -> Function[{min, max}, Range[0, 1.4, 0.1]],
  ContourLabels -> Function[{x, y, z}, Text[z, {x, y}, Background -> White]],
  ImageSize -> 300, ColorFunction -> "GrayTones",
  PlotLegends -> BarLegend[Automatic, LegendMarkerSize -> 180, LegendFunction -> "Frame",
  LegendMargins -> 5, LegendLabel -> "Gm+nSWASH/Gm+ntheor"], AspectRatio -> Automatic,
  Frame -> {True, True, False, False}, FrameLabel -> {Style["kmd", 16], Style["knd", 16]},
  FrameTicks -> All, PlotLabel -> Style["Three layers", FontSize -> 18]]

```



```
Clear[ωm, ωn];
```

Four layers solution

$$\begin{aligned}
s1 = & (\text{eta01m eta01n} (km + kn))^2 \\
& (1152921504606846976 \omega m \omega n (kn^2 \omega m^2 + 8 km kn \omega m \omega n + km^2 \omega n^2) - 1152921504606846976 \\
& d g km kn (6 kn^2 \omega m^2 + km kn \omega m \omega n + 6 km^2 \omega n^2) + d^{20} km^7 kn^7 (km + kn)^6 \omega m \omega n \\
& (4 kn^2 \omega m (2 \omega m + \omega n) + 4 km^2 \omega n (\omega m + 2 \omega n) - km kn (\omega m^2 + 10 \omega m \omega n + \omega n^2)) + \\
& 64 d^{19} g km^7 kn^7 (km + kn)^6 (kn^2 (5 \omega m^2 - \omega m \omega n + 2 \omega n^2) + \\
& km^2 (2 \omega m^2 - \omega m \omega n + 5 \omega n^2) + km kn (8 \omega m^2 - 21 \omega m \omega n + 8 \omega n^2)) - \\
& 18014398509481984 d^3 g km kn (11 kn^4 \omega m^2 + 11 km^4 \omega n^2 - 2 km kn^3 \omega m (34 \omega m + 13 \omega n) - \\
& 2 km^3 kn \omega n (13 \omega m + 34 \omega n) + 2 km^2 kn^2 (29 \omega m^2 - 32 \omega m \omega n + 29 \omega n^2)) + \\
& 4096 d^{17} g km^5 kn^5 (km + kn)^4 (kn^6 (57 \omega m^2 + 2 \omega m \omega n + 12 \omega n^2) + \\
& km kn^5 (250 \omega m^2 - 11 \omega m \omega n + 56 \omega n^2) + km^6 (12 \omega m^2 + 2 \omega m \omega n + 57 \omega n^2) + \\
& km^2 kn^4 (434 \omega m^2 + 37 \omega m \omega n + 128 \omega n^2) + km^5 kn (56 \omega m^2 - 11 \omega m \omega n + 250 \omega n^2) + \\
& km^3 kn^3 (324 \omega m^2 + 35 \omega m \omega n + 324 \omega n^2) + km^4 kn^2 (128 \omega m^2 + 37 \omega m \omega n + 434 \omega n^2)) + \\
& 281474976710656 d^5 g km kn (27 kn^6 \omega m^2 + 27 km^6 \omega n^2 + km kn^5 \omega m (250 \omega m + \omega n) + \\
& km^5 kn \omega n (\omega m + 250 \omega n) + km^2 kn^4 (348 \omega m^2 + 157 \omega m \omega n + 42 \omega n^2) + \\
& km^4 kn^2 (42 \omega m^2 + 157 \omega m \omega n + 348 \omega n^2) + km^3 kn^3 (824 \omega m^2 + 339 \omega m \omega n + 824 \omega n^2)) + \\
& 4398046511104 d^7 g km kn (10 kn^8 \omega m^2 + 10 km^8 \omega n^2 - 4 km kn^7 \omega m (60 \omega m + 13 \omega n) - \\
& 4 km^7 kn \omega n (13 \omega m + 60 \omega n) + km^6 kn^2 (22 \omega m^2 - 349 \omega m \omega n - 421 \omega n^2) + \\
& km^2 kn^6 (-421 \omega m^2 - 349 \omega m \omega n + 22 \omega n^2) + km^3 kn^5 (1182 \omega m^2 - 777 \omega m \omega n + 380 \omega n^2) + \\
& km^4 kn^4 (853 \omega m^2 - 960 \omega m \omega n + 853 \omega n^2) + km^5 kn^3 (380 \omega m^2 - 777 \omega m \omega n + 1182 \omega n^2)) + \\
& 1073741824 d^{11} g km kn (kn^{12} \omega m^2 + km^{12} \omega n^2 + 26 km kn^{11} \omega m (6 \omega m + \omega n) + \\
& 26 km^{11} kn \omega n (\omega m + 6 \omega n) + km^8 kn^4 (-497 \omega m^2 + 952 \omega m \omega n - 6775 \omega n^2) + \\
& km^4 kn^8 (-6775 \omega m^2 + 952 \omega m \omega n - 497 \omega n^2) + 2 km^2 kn^{10} (252 \omega m^2 + 103 \omega m \omega n - 47 \omega n^2) - \\
& 4 km^3 kn^9 (376 \omega m^2 - 124 \omega m \omega n + 89 \omega n^2) + 2 km^{10} kn^2 (-47 \omega m^2 + 103 \omega m \omega n + 252 \omega n^2) - \\
& 4 km^9 kn^3 (89 \omega m^2 - 124 \omega m \omega n + 376 \omega n^2) - 2 km^5 kn^7 (4062 \omega m^2 - 953 \omega m \omega n + 458 \omega n^2) -
\end{aligned}$$

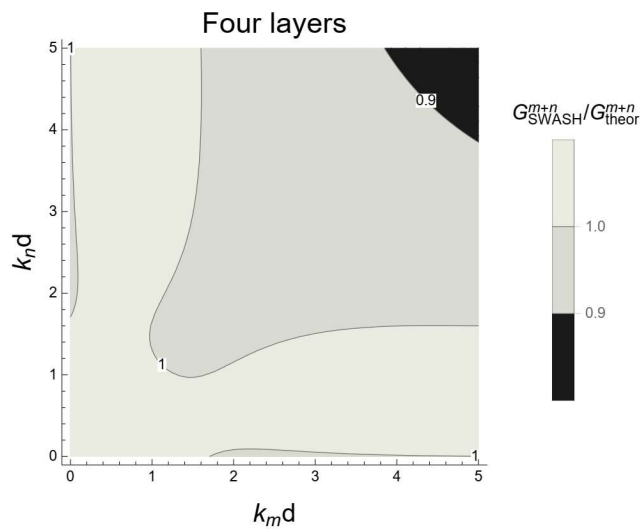
$$\begin{aligned}
& 8 \text{ km}^6 \text{ kn}^6 (491 \omega m^2 - 316 \omega m \omega n + 491 \omega n^2) - 2 \text{ km}^7 \text{ kn}^5 (458 \omega m^2 - 953 \omega m \omega n + 4062 \omega n^2) + \\
& 262 \text{ 144 d}^{15} \text{ g km}^3 \text{ kn}^3 (\text{km} + \text{kn})^2 (\text{kn}^{10} (63 \omega m^2 - \omega m \omega n + 2 \omega n^2) + \\
& \text{km kn}^9 (468 \omega m^2 - 15 \omega m \omega n + 32 \omega n^2) + \text{km}^{10} (2 \omega m^2 - \omega m \omega n + 63 \omega n^2) + \\
& \text{km}^2 \text{ kn}^8 (1283 \omega m^2 - 49 \omega m \omega n + 357 \omega n^2) + \text{km}^9 \text{ kn} (32 \omega m^2 - 15 \omega m \omega n + 468 \omega n^2) + \\
& 2 \text{ km}^3 \text{ kn}^7 (1209 \omega m^2 + 60 \omega m \omega n + 758 \omega n^2) + 2 \text{ km}^7 \text{ kn}^3 (758 \omega m^2 + 60 \omega m \omega n + 1209 \omega n^2) + \\
& \text{km}^8 \text{ kn}^2 (357 \omega m^2 - 49 \omega m \omega n + 1283 \omega n^2) + \text{km}^4 \text{ kn}^6 (4044 \omega m^2 + 539 \omega m \omega n + 3438 \omega n^2) + \\
& \text{km}^6 \text{ kn}^4 (3438 \omega m^2 + 539 \omega m \omega n + 4044 \omega n^2) + \text{km}^5 \text{ kn}^5 (4752 \omega m^2 + 739 \omega m \omega n + 4752 \omega n^2) - \\
& 68 \text{ 719 476 736 d}^9 \text{ g km kn} (24 \text{ kn}^{10} \omega m^2 + \text{km kn}^9 \omega m (276 \omega m - \omega n) + 24 \text{ km}^{10} \omega n^2 + \\
& \text{km}^9 \text{ kn} \omega n (-\omega m + 276 \omega n) + 2 \text{ km}^2 \text{ kn}^8 (430 \omega m^2 + 35 \omega m \omega n - 47 \omega n^2) + \\
& 2 \text{ km}^8 \text{ kn}^2 (-47 \omega m^2 + 35 \omega m \omega n + 430 \omega n^2) + 2 \text{ km}^3 \text{ kn}^7 (790 \omega m^2 + 21 \omega m \omega n + 648 \omega n^2) + \\
& 2 \text{ km}^7 \text{ kn}^3 (648 \omega m^2 + 21 \omega m \omega n + 790 \omega n^2) + 2 \text{ km}^6 \text{ kn}^4 (2402 \omega m^2 - 242 \omega m \omega n + 1577 \omega n^2) + \\
& 2 \text{ km}^4 \text{ kn}^6 (1577 \omega m^2 - 242 \omega m \omega n + 2402 \omega n^2) + \\
& \text{km}^5 \text{ kn}^5 (5252 \omega m^2 - 883 \omega m \omega n + 5252 \omega n^2) + 16 \text{ 777 216 d}^{13} \text{ g km kn} \\
& (3 \text{ km}^{14} \omega m^2 + \text{km kn}^{13} \omega m (42 \omega m - \omega n) + 3 \text{ km}^{14} \omega n^2 + \text{km}^{13} \text{ kn} \omega n (-\omega m + 42 \omega n) + \\
& \text{km}^2 \text{ kn}^{12} (168 \omega m^2 - 7 \omega m \omega n - 2 \omega n^2) + \text{km}^{12} \text{ kn}^2 (-2 \omega m^2 - 7 \omega m \omega n + 168 \omega n^2) + \\
& \text{km}^3 \text{ kn}^{11} (740 \omega m^2 - 25 \omega m \omega n + 344 \omega n^2) + \text{km}^{11} \text{ kn}^3 (344 \omega m^2 - 25 \omega m \omega n + 740 \omega n^2) + \\
& \text{km}^4 \text{ kn}^{10} (3335 \omega m^2 - 363 \omega m \omega n + 1628 \omega n^2) + \text{km}^6 \text{ kn}^8 (9326 \omega m^2 - 3749 \omega m \omega n + 2015 \omega n^2) + \\
& \text{km}^5 \text{ kn}^9 (8074 \omega m^2 - 1665 \omega m \omega n + 2370 \omega n^2) + \text{km}^{10} \text{ kn}^4 (1628 \omega m^2 - 363 \omega m \omega n + 3335 \omega n^2) + \\
& \text{km}^7 \text{ kn}^7 (4904 \omega m^2 - 4855 \omega m \omega n + 4904 \omega n^2) + \text{km}^9 \text{ kn}^5 (2370 \omega m^2 - 1665 \omega m \omega n + 8074 \omega n^2) + \\
& \text{km}^8 \text{ kn}^6 (2015 \omega m^2 - 3749 \omega m \omega n + 9326 \omega n^2) - \\
& 64 \text{ d}^{18} \text{ km}^5 \text{ kn}^5 (\text{km} + \text{kn})^4 (192 \text{ g}^2 \text{ km}^2 \text{ kn}^2 (\text{km} + \text{kn})^4 + \omega m \omega n (4 \text{ km}^6 \omega n (19 \omega m + 4 \omega n) + \\
& 4 \text{ kn}^6 \omega m (4 \omega m + 19 \omega n) + \text{km}^5 \text{ kn} (-3 \omega m^2 + 314 \omega m \omega n - 322 \omega n^2) + \\
& 2 \text{ km}^4 \text{ kn}^2 (9 \omega m^2 + 170 \omega m \omega n - 259 \omega n^2) + \text{km kn}^5 (-322 \omega m^2 + 314 \omega m \omega n - 3 \omega n^2) + \\
& 2 \text{ km}^3 \text{ kn}^3 (4 \omega m^2 + 269 \omega m \omega n + 4 \omega n^2) + 2 \text{ km}^2 \text{ kn}^4 (-259 \omega m^2 + 170 \omega m \omega n + 9 \omega n^2)) + \\
& 18 \text{ 014 398 509 481 984 d}^2 (384 \text{ g}^2 \text{ km}^3 \text{ kn}^3 - \omega m \omega n (6 \text{ kn}^4 \omega m^2 + 4 \text{ km kn}^3 \omega m (\omega m - 27 \omega n) + \\
& 6 \text{ km}^4 \omega n^2 + 4 \text{ km}^3 \text{ kn} \omega n (-27 \omega m + \omega n) + \text{km}^2 \text{ kn}^2 (37 \omega m^2 + 90 \omega m \omega n + 37 \omega n^2))) - \\
& 4 \text{ 398 046 511 104 d}^6 (64 \text{ g}^2 \text{ km}^3 \text{ kn}^3 (27 \text{ km}^4 + 152 \text{ km}^3 \text{ kn} + 134 \text{ km}^2 \text{ kn}^2 + 152 \text{ km kn}^3 + 27 \text{ kn}^4) + \\
& \omega m \omega n (20 \text{ kn}^8 \omega m^2 + 20 \text{ km}^8 \omega n^2 + 20 \text{ km}^7 \text{ kn} \omega n (11 \omega m + 2 \omega n) + 20 \text{ km kn}^7 \omega m \\
& (2 \omega m + 11 \omega n) + \text{km}^6 \text{ kn}^2 (-315 \omega m^2 + 970 \omega m \omega n - 1108 \omega n^2) + 2 \text{ km}^5 \text{ kn}^3 (89 \omega m^2 + \\
& 1658 \omega m \omega n - 681 \omega n^2) + \text{km}^2 \text{ kn}^6 (-1108 \omega m^2 + 970 \omega m \omega n - 315 \omega n^2) + 2 \text{ km}^3 \text{ kn}^5 \\
& (-681 \omega m^2 + 1658 \omega m \omega n + 89 \omega n^2) + 6 \text{ km}^4 \text{ kn}^4 (213 \omega m^2 + 2239 \omega m \omega n + 213 \omega n^2))) + \\
& 281 \text{ 474 976 710 656 d}^4 (64 \text{ g}^2 \text{ km}^3 \text{ kn}^3 (11 \text{ km}^2 - 18 \text{ km kn} + 11 \text{ kn}^2) - \\
& \omega m \omega n (-15 \text{ kn}^6 \omega m^2 + 4 \text{ km}^5 \text{ kn} (16 \omega m - 5 \omega n) \omega n - 15 \text{ km}^6 \omega n^2 + \\
& 4 \text{ km kn}^5 \omega m (-5 \omega m + 16 \omega n) + \text{km}^2 \text{ kn}^4 (417 \omega m^2 + 1328 \omega m \omega n + 279 \omega n^2) + \text{km}^4 \text{ kn}^2 \\
& (279 \omega m^2 + 1328 \omega m \omega n + 417 \omega n^2) + 2 \text{ km}^3 \text{ kn}^3 (533 \omega m^2 + 34 \omega m \omega n + 533 \omega n^2))) - \\
& 16 \text{ 777 216 d}^{12} (64 \text{ g}^2 \text{ km}^3 \text{ kn}^3 (\text{km} + \text{kn})^2 (\text{km}^8 + 48 \text{ km}^7 \text{ kn} + 168 \text{ km}^6 \text{ kn}^2 + 36 \text{ km}^5 \text{ kn}^3 - \\
& 217 \text{ km}^4 \text{ kn}^4 + 36 \text{ km}^3 \text{ kn}^5 + 168 \text{ km}^2 \text{ kn}^6 + 48 \text{ km kn}^7 + \text{kn}^8) + \\
& \omega m \omega n (-\text{kn}^{14} \omega m^2 - 4 \text{ km kn}^{13} \omega m (\omega m - 12 \omega n) + 4 \text{ km}^{13} \text{ kn} (12 \omega m - \omega n) \omega n - \\
& \text{km}^{14} \omega n^2 + \text{km}^8 \text{ kn}^6 (173 \omega m^2 + 19896 \omega m \omega n - 12705 \omega n^2) + \text{km}^{10} \text{ kn}^4 \\
& (1875 \omega m^2 - 388 \omega m \omega n - 1509 \omega n^2) + 8 \text{ km}^9 \text{ kn}^5 (137 \omega m^2 - 555 \omega m \omega n - 1210 \omega n^2) - \\
& 8 \text{ km}^5 \text{ kn}^9 (1210 \omega m^2 + 555 \omega m \omega n - 137 \omega n^2) + \text{km}^{12} \text{ kn}^2 (37 \omega m^2 + 1056 \omega m \omega n - 83 \omega n^2) + \\
& \text{km}^2 \text{ kn}^{12} (-83 \omega m^2 + 1056 \omega m \omega n + 37 \omega n^2) + 2 \text{ km}^{11} \text{ kn}^3 (345 \omega m^2 + 1534 \omega m \omega n + \\
& 81 \omega n^2) + \text{km}^6 \text{ kn}^8 (-12705 \omega m^2 + 19896 \omega m \omega n + 173 \omega n^2) - 22 \text{ km}^7 \text{ kn}^7 \\
& (189 \omega m^2 - 2014 \omega m \omega n + 189 \omega n^2) + 2 \text{ km}^3 \text{ kn}^{11} (81 \omega m^2 + 1534 \omega m \omega n + 345 \omega n^2) + \\
& \text{km}^4 \text{ kn}^{10} (-1509 \omega m^2 - 388 \omega m \omega n + 1875 \omega n^2))) - 4096 \text{ d}^{16} \text{ km}^3 \text{ kn}^3 (\text{km} + \text{kn})^2 \\
& (64 \text{ g}^2 \text{ km}^2 \text{ kn}^2 (\text{km} + \text{kn})^4 (10 \text{ km}^4 + 28 \text{ km}^3 \text{ kn} + 19 \text{ km}^2 \text{ kn}^2 + 28 \text{ km kn}^3 + 10 \text{ kn}^4) + \\
& \omega m \omega n (4 \text{ km}^{10} (13 \omega m - 2 \omega n) \omega n + 4 \text{ km}^{10} \omega m (-2 \omega m + 13 \omega n) + \\
& 2 \text{ km}^2 \text{ kn}^8 (315 \omega m^2 + 1682 \omega m \omega n - 6 \omega n^2) + \text{km kn}^9 (32 \omega m^2 + 494 \omega m \omega n + 3 \omega n^2) + \\
& \text{km}^9 \text{ kn} (3 \omega m^2 + 494 \omega m \omega n + 32 \omega n^2) + \text{km}^3 \text{ kn}^7 (1432 \omega m^2 + 11636 \omega m \omega n + 33 \omega n^2) + \\
& 2 \text{ km}^8 \text{ kn}^2 (-6 \omega m^2 + 1682 \omega m \omega n + 315 \omega n^2) + 4 \text{ km}^4 \text{ kn}^6 (713 \omega m^2 + 6066 \omega m \omega n + \\
& 429 \omega n^2) + 4 \text{ km}^6 \text{ kn}^4 (429 \omega m^2 + 6066 \omega m \omega n + 713 \omega n^2) + \text{km}^7 \text{ kn}^3 (33 \omega m^2 + \\
& 11636 \omega m \omega n + 1432 \omega n^2) + \text{km}^5 \text{ kn}^5 (3957 \omega m^2 + 31658 \omega m \omega n + 3957 \omega n^2))) - \\
& 262 \text{ 144 d}^{14} \text{ km kn} (64 \text{ g}^2 \text{ km}^2 \text{ kn}^2 (\text{km} + \text{kn})^4 (3 \text{ km}^8 + 20 \text{ km}^7 \text{ kn} + 24 \text{ km}^6 \text{ kn}^2 + \\
& 88 \text{ km}^5 \text{ kn}^3 + 213 \text{ km}^4 \text{ kn}^4 + 88 \text{ km}^3 \text{ kn}^5 + 24 \text{ km}^2 \text{ kn}^6 + 20 \text{ km kn}^7 + 3 \text{ kn}^8) -
\end{aligned}$$

$$\begin{aligned}
& \omega m \omega n \left(-4 \text{ km}^{14} \omega m \omega n - 4 \text{ kn}^{14} \omega m \omega n - 2 \text{ km}^4 \text{ kn}^{10} \left(871 \omega m^2 + 15\,542 \omega m \omega n - 985 \omega n^2 \right) + 2 \right. \\
& \quad \left. \text{km}^{10} \text{ kn}^4 \left(985 \omega m^2 - 15\,542 \omega m \omega n - 871 \omega n^2 \right) - 2 \text{ km}^{12} \text{ kn}^2 \left(\omega m^2 + 462 \omega m \omega n - 325 \omega n^2 \right) + \right. \\
& \quad 2 \text{ km}^2 \text{ kn}^{12} \left(325 \omega m^2 - 462 \omega m \omega n - \omega n^2 \right) + \text{ km kn}^{13} \left(94 \omega m^2 - 78 \omega m \omega n + \omega n^2 \right) + \\
& \quad 6 \text{ km}^3 \text{ kn}^{11} \left(39 \omega m^2 - 1347 \omega m \omega n + 13 \omega n^2 \right) + 6 \text{ km}^{11} \text{ kn}^3 \left(13 \omega m^2 - 1347 \omega m \omega n + 39 \omega n^2 \right) + \\
& \quad \text{km}^{13} \text{ kn} \left(\omega m^2 - 78 \omega m \omega n + 94 \omega n^2 \right) + 2 \text{ km}^9 \text{ kn}^5 \left(3577 \omega m^2 - 30\,645 \omega m \omega n + 124 \omega n^2 \right) + \\
& \quad 2 \text{ km}^8 \text{ kn}^6 \left(5163 \omega m^2 - 38\,446 \omega m \omega n + 2783 \omega n^2 \right) + \\
& \quad 2 \text{ km}^5 \text{ kn}^9 \left(124 \omega m^2 - 30\,645 \omega m \omega n + 3577 \omega n^2 \right) + 2 \text{ km}^7 \text{ kn}^7 \left(4451 \omega m^2 - \right. \\
& \quad \left. 39\,511 \omega m \omega n + 4451 \omega n^2 \right) + 2 \text{ km}^6 \text{ kn}^8 \left(2783 \omega m^2 - 38\,446 \omega m \omega n + 5163 \omega n^2 \right) \left. \right) + \\
& 1\,073\,741\,824 \text{ d}^{10} \left(128 \text{ g}^2 \text{ km}^3 \text{ kn}^3 \left(12 \text{ km}^8 + 116 \text{ km}^7 \text{ kn} + 316 \text{ km}^6 \text{ kn}^2 + 410 \text{ km}^5 \text{ kn}^3 + \right. \right. \\
& \quad \left. \left. 407 \text{ km}^4 \text{ kn}^4 + 410 \text{ km}^3 \text{ kn}^5 + 316 \text{ km}^2 \text{ kn}^6 + 116 \text{ km kn}^7 + 12 \text{ kn}^8 \right) - \right. \\
& \quad \omega m \omega n \left(6 \text{ km}^{12} \omega m^2 + 4 \text{ km kn}^{11} \omega m \left(5 \omega m - 29 \omega n \right) - 4 \text{ km}^{11} \text{ kn} \left(29 \omega m - 5 \omega n \right) \omega n + 6 \text{ km}^{12} \omega n^2 + \right. \\
& \quad \left. \text{km}^2 \text{ kn}^{10} \left(285 \omega m^2 - 242 \omega m \omega n + 279 \omega n^2 \right) + \text{ km}^{10} \text{ kn}^2 \left(279 \omega m^2 - 242 \omega m \omega n + 285 \omega n^2 \right) + \right. \\
& \quad 4 \text{ km}^3 \text{ kn}^9 \left(607 \omega m^2 + 103 \omega m \omega n + 298 \omega n^2 \right) + 4 \text{ km}^9 \text{ kn}^3 \left(298 \omega m^2 + 103 \omega m \omega n + 607 \omega n^2 \right) + \\
& \quad 2 \text{ km}^4 \text{ kn}^8 \left(2746 \omega m^2 - 8662 \omega m \omega n + 965 \omega n^2 \right) + \\
& \quad 4 \text{ km}^5 \text{ kn}^7 \left(2872 \omega m^2 - 16\,027 \omega m \omega n + 2057 \omega n^2 \right) + 2 \text{ km}^8 \text{ kn}^4 \\
& \quad \left. \left(965 \omega m^2 - 8662 \omega m \omega n + 2746 \omega n^2 \right) + 4 \text{ km}^7 \text{ kn}^5 \left(2057 \omega m^2 - 16\,027 \omega m \omega n + 2872 \omega n^2 \right) + \right. \\
& \quad \left. 3 \text{ km}^6 \text{ kn}^6 \left(5411 \omega m^2 - 29\,962 \omega m \omega n + 5411 \omega n^2 \right) \right) - 68\,719\,476\,736 \text{ d}^8 \\
& \left(128 \text{ g}^2 \text{ km}^3 \text{ kn}^3 \left(5 \text{ km}^6 - 10 \text{ km}^5 \text{ kn} - 72 \text{ km}^4 \text{ kn}^2 - 78 \text{ km}^3 \text{ kn}^3 - 72 \text{ km}^2 \text{ kn}^4 - 10 \text{ km kn}^5 + 5 \text{ kn}^6 \right) - \right. \\
& \quad \omega m \omega n \left(15 \text{ km}^{10} \omega m^2 + 15 \text{ km}^{10} \omega n^2 + 8 \text{ km}^9 \text{ kn} \omega n \left(13 \omega m + 5 \omega n \right) + \right. \\
& \quad 8 \text{ km kn}^9 \omega m \left(5 \omega m + 13 \omega n \right) + \text{ km}^8 \text{ kn}^2 \left(315 \omega m^2 + 3280 \omega m \omega n - 546 \omega n^2 \right) + \\
& \quad \left. \text{km}^2 \text{ kn}^8 \left(-546 \omega m^2 + 3280 \omega m \omega n + 315 \omega n^2 \right) + 4 \text{ km}^7 \text{ kn}^3 \right. \\
& \quad \left. \left(783 \omega m^2 + 2445 \omega m \omega n + 409 \omega n^2 \right) + 4 \text{ km}^3 \text{ kn}^7 \left(409 \omega m^2 + 2445 \omega m \omega n + 783 \omega n^2 \right) + \right. \\
& \quad \left. 2 \text{ km}^5 \text{ kn}^5 \left(2215 \omega m^2 - 1362 \omega m \omega n + 2215 \omega n^2 \right) + \text{ km}^6 \text{ kn}^4 \left(5431 \omega m^2 + \right. \right. \\
& \quad \left. \left. 3682 \omega m \omega n + 5322 \omega n^2 \right) + \text{ km}^4 \text{ kn}^6 \left(5322 \omega m^2 + 3682 \omega m \omega n + 5431 \omega n^2 \right) \left. \right) \right) / \\
& \left(2 \text{ d km}^2 \left(-8 + \text{ d km} \right)^3 \left(8 + \text{ d km} \right)^3 \text{ kn}^2 \left(-8 + \text{ d kn} \right)^3 \left(8 + \text{ d kn} \right)^3 \right. \\
& \quad \omega m \\
& \quad \omega n \\
& \quad \left. \left(-16\,777\,216 \text{ d g} \left(\text{ km} + \text{ kn} \right)^2 - \right. \right. \\
& \quad 1\,835\,008 \text{ d}^3 \text{ g} \left(\text{ km} + \text{ kn} \right)^4 - 28\,672 \text{ d}^5 \text{ g} \left(\text{ km} + \text{ kn} \right)^6 - \\
& \quad 64 \text{ d}^7 \text{ g} \left(\text{ km} + \text{ kn} \right)^8 + 16\,777\,216 \left(\omega m + \omega n \right)^2 + \\
& \quad 7\,340\,032 \text{ d}^2 \left(\text{ km} + \text{ kn} \right)^2 \left(\omega m + \omega n \right)^2 + \\
& \quad 286\,720 \text{ d}^4 \left(\text{ km} + \text{ kn} \right)^4 \left(\omega m + \omega n \right)^2 + \\
& \quad 1792 \text{ d}^6 \left(\text{ km} + \text{ kn} \right)^6 \left(\omega m + \omega n \right)^2 + \\
& \quad \left. \left. \text{d}^8 \left(\text{ km} + \text{ kn} \right)^8 \left(\omega m + \omega n \right)^2 \right) \right); \\
& \omega m = 8 \text{ km} \sqrt{\left(\left(\text{ d g} \left(64 + \text{ d}^2 \text{ km}^2 \right) \left(4096 + 384 \text{ d}^2 \text{ km}^2 + \text{ d}^4 \text{ km}^4 \right) \right) / \right.} \\
& \quad \left. \left(16\,777\,216 + 7\,340\,032 \text{ d}^2 \text{ km}^2 + 286\,720 \text{ d}^4 \text{ km}^4 + 1792 \text{ d}^6 \text{ km}^6 + \text{ d}^8 \text{ km}^8 \right) \right); \\
& \omega n = 8 \text{ kn} \sqrt{\left(\left(\text{ d g} \left(64 + \text{ d}^2 \text{ kn}^2 \right) \left(4096 + 384 \text{ d}^2 \text{ kn}^2 + \text{ d}^4 \text{ kn}^4 \right) \right) / \right.} \\
& \quad \left. \left(16\,777\,216 + 7\,340\,032 \text{ d}^2 \text{ kn}^2 + 286\,720 \text{ d}^4 \text{ kn}^4 + 1792 \text{ d}^6 \text{ kn}^6 + \text{ d}^8 \text{ kn}^8 \right) \right); \\
& \text{fourlsup} = \text{s1} * \text{d} / \left(\text{eta01m eta01n} \right) /. \{ \text{ km} \rightarrow \text{ kdm} / \text{ d}, \text{ kn} \rightarrow \text{ kdn} / \text{ d} \} // \text{Simplify} // \text{Refine} \\
& \quad (* \text{ multiplied with d*});
\end{aligned}$$

```

p41 = ContourPlot[fourlsup/GsupSa, {kdm, 0, 5},
  {kdn, 0, 5}, Contours -> Function[{min, max}, Range[0, 1.4, 0.1]],
  ContourLabels -> Function[{x, y, z}, Text[z, {x, y}, Background -> White]],
  ImageSize -> 300, ColorFunction -> "GrayTones",
  PlotLegends -> BarLegend[Automatic, LegendMarkerSize -> 180, LegendFunction -> "Frame",
    LegendMargins -> 5, LegendLabel -> " $G_{\text{SWASH}}^{m+n}/G_{\text{theor}}^{m+n}$ "], AspectRatio -> Automatic,
  Frame -> {True, True, False, False}, FrameLabel -> {Style["kmd", 16], Style["knd", 16]},
  FrameTicks -> All, PlotLabel -> Style["Four layers", FontSize -> 18]]

```



Quit[]

Appendix C

Source code of the implemented internal wave generation method in SWASH

This Appendix chapter provides the reader with the main source code of the internal wave generation method which has been made freely available through SWASH 6.01 (<http://swash.sourceforge.net>).

C.1 New subroutine SwashIntWavgen.ftn90

In this subroutine the source function amplitude and the shape factor of the source area are calculated.

```
subroutine SwashIntWavgen ( igser, nfreq, wdir, shape )
!
!  --|-----|--
!  | Delft University of Technology |
!  | Faculty of Civil Engineering |
!  | Environmental Fluid Mechanics Section |
!  | P.O. Box 5048, 2600 GA Delft, The Netherlands |
!  | |
!  | Programmers: The SWASH team |
!  --|-----|--
!
!
!  SWASH (Simulating WAVes till SHore); a non-hydrostatic wave-flow model
!  Copyright (C) 2010-2020 Delft University of Technology
!
!  This program is free software; you can redistribute it and/or
```

```

! modify it under the terms of the GNU General Public License as
! published by the Free Software Foundation; either version 2 of
! the License, or (at your option) any later version.
!
! This program is distributed in the hope that it will be useful,
! but WITHOUT ANY WARRANTY; without even the implied warranty of
! MERCHANTABILITY or FITNESS FOR A PARTICULAR PURPOSE. See the
! GNU General Public License for more details.
!
! A copy of the GNU General Public License is available at
! http://www.gnu.org/copyleft/gpl.html#SEC3
! or by writing to the Free Software Foundation, Inc.,
! 59 Temple Place, Suite 330, Boston, MA 02111-1307 USA
!
!
! Authors
!
! 1.00: Panagiotis Vasarmidis
!
! Updates
!
! 1.00, June 2019: New subroutine
!
! Purpose
!
! Computes the source function amplitude and shape factor of source area
!
! Modules used
!
!   use ocpcomm4
!   use SwashCommdata3
!   use m_bndspec
!
!   implicit none
!
! Argument variables
!
!   integer, intent(in) :: nfreq ! number of frequencies
!   integer, intent(in) :: shape ! spectral shape
!                                   ! = 1; Pierson Moskowitz
!                                   ! = 2; Jonswap
!                                   ! = 3; TMA
!
!   real, intent(in) :: wdir ! incident or peak wave direction with
!                             respect to problem coordinates
!
!
!   type(bfsdat), intent(inout) :: igser ! list containing parameters
!                                       for internal-generated series of wave components
!
!

```

182C. Source code of the implemented internal wave generation method in SWASH

```
! Local variables
!
integer :: icemds ! counter for number of evanescent modes
integer, save :: ient = 0 ! number of entries in this subroutine
integer :: j ! loop counter
!
real :: ampl ! amplitude of an internal-generated wave component
real :: beta ! shape factor beta of the source area
real :: cdn ! part of formula for computing energy velocity (
denominator)
real :: cen ! energy velocity
real :: cnu ! part of formula for computing energy velocity (
numerator)
real :: fac1 ! auxiliary factor
real :: fac2 ! auxiliary factor
real :: ishap ! shape factor I of the source area
real :: kwav ! wave number of an internal-generated wave component
real :: n ! ratio of group and phase velocity
real :: omega ! angular frequency of an internal-generated wave
component
real :: omegcf ! cut-off frequency
real :: rval ! auxiliary real
real :: swd ! still water depth
real :: theta ! wave direction of an internal-generated component
with respect to computational coordinates
real :: urmax ! maximum Ursell number
!
logical, save :: nowarn = .false. ! give no warning again
logical, save :: nowarn2 = .false. ! give no other warning again
!
character(120) :: msgstr ! string to pass message
!
! Structure
!
! Description of the pseudo code
!
! Source text
!
if (ltrace) call strace (ient, 'SwashIntWavgen')
!
! get still water depth
!
swd = piwg(3)
!
! determine the cut-off frequency above which are the evanescent
modes to be filtered out
! (based on numerical dispersion relation; to be saved a slightly
smaller cut-off is chosen)
!
omegcf = 0.9 * 2. * real(kmax) * sqrt(grav/swd)
```

```

!
allocate(igser%kwave(nfreq,1))
allocate(igser%sfamp(nfreq))
allocate(igser%bshap(nfreq))
!
igser%kwave = 0.
igser%sfamp = 0.
igser%bshap = 0.
!
urmax = -999.
icemds = 0
!
do j = 1, nfreq
!
  ampl = igser%ampl (j)
  omega = igser%omega(j)
!
  theta = wdir - alpc + igser%theta(j)
!
  ! filter out the evanescent modes, if appropriate
!
  if ( numdisp ) then
!
    if ( omega > omegcf ) then
      icemds = icemds + 1
      ampl = 0.
      igser%ampl(j) = 0.
    endif
!
  endif
!
  ! calculate wave number and store it
!
  call disprel ( swd, omega, kwav, rval, n )
!
  igser%kwave(j,1) = kwav
!
  ! correct amplitude in case of TMA spectrum for shallow water
!
  if ( shape == 3 ) ampl = ampl * omega * omega / ( grav * kwav *
    sqrt(2.*n) )
!
  ! compute the maximum Ursell number
!
  if ( ampl /= 0. .and. kwav /= 0. ) then
!
    ! this is the classical definition of the Ursell number
    !rval = ampl / swd / swd / swd / kwav / kwav
    ! this is another variant of the Ursell number more appropriate
    for large kd > 1 or intermediate depths (see Beji, 1995)

```

184C. *Source code of the implemented internal wave generation method in SWASH*

```
    rval = ampl * kwav / ( tanh(kwav*swd)*tanh(kwav*swd)*tanh(kwav*
      swd) )
    if ( rval > urmax ) urmax = rval
    !
endif
!
! in case of periodicity, wave direction must be corrected so
  that wave number is an integer multiple of 2pi/length with
  length the periodicity length
!
if ( bcperx ) then
  !
  rval = nint( kwav*cos(theta) / ( pi2/xclen ) ) * pi2/xclen /
    kwav
  if ( rval > 1. ) then
    theta = acos ( rval - pi2/xclen / kwav )
  else if ( rval < -1. ) then
    theta = acos ( rval + pi2/xclen / kwav )
  else
    theta = acos ( rval )
  endif
!
else if ( bcpery ) then
  !
  rval = nint( kwav*sin(theta) / ( pi2/yclen ) ) * pi2/yclen /
    kwav
  if ( rval > 1. ) then
    theta = asin ( rval - pi2/yclen / kwav )
  else if ( rval < -1. ) then
    theta = asin ( rval + pi2/yclen / kwav )
  else
    theta = asin ( rval )
  endif
!
endif
!
! calculate shape factor beta
!
beta = 80. / piwg(4) ** 2 / ( pi2/kwav ) ** 2
!
! calculate energy velocity
!
fac1 = kwav * swd
fac2 = sqrt( grav * swd )
!
if ( kpmax == 1 ) then
  !
  cnu = 8. * fac2
  cdn = (4. + fac1 ** 2.) ** 1.5
  !
endif
```

```

else if ( kpmx == 2 ) then
  !
  cnu = 64. * fac2 * (256. + 32. * fac1 ** 2. + 5. * fac1 ** 4.)
  cdn = sqrt((16. + fac1 ** 2.) * (256. + 96. * fac1 ** 2. + fac1
    ** 4.) ** 3.)
  !
else if ( kpmx == 3 ) then
  !
  cnu = 72. * fac2 * (5038848. + 933120. * fac1 ** 2. + 147744. *
    fac1 ** 4. + 3024. * fac1 ** 6. + 35. * fac1 ** 8.)
  cdn = sqrt((1296. + 120. * fac1 ** 2. + fac1 ** 4.) * (46656. +
    19440. * fac1 ** 2. + 540. * fac1 ** 4. + fac1 ** 6.) **
    3.)
  !
else
  !
  cnu = (0.5 + fac1 / sinh( 2. * fac1 )) * (omega / kwav)
  cdn = 1.
  !
endif
cen = cnu / cdn
! calculate shape factor I
!
if ( optg /= 5 ) then
  !
  if ( lsrcfy ) then
    !
    ishap = sqrt( pi/beta ) * exp( -( kwav * cos(theta) ) ** 2 /
      4. / beta ) / cos(theta)
    !
  else if ( lsrcfx ) then
    !
    ishap = sqrt( pi/beta ) * exp( -( kwav * sin(theta) ) ** 2 /
      4. / beta ) / sin(theta)
    !
  endif
else
  !
  ishap = sqrt( pi/beta ) * exp( -( kwav ) ** 2 / 4. / beta )
  !
endif
!
! store parameters for internal wave generation
!
igser%theta(j) = theta
igser%bshap(j) = beta
igser%sfamp(j) = 2. * ampl * cen / ishap

```

```
!
enddo
!
! give warning if maximum Ursell number > 0.2
!
if ( urmax > 0.2 .and. .not.nowarn2 ) then
!
write (msgstr,'(a,f5.2,a)') 'the Ursell number associated with
the internal-generated wave field = ',urmax, ' > 0.2'
call msgerr (1, trim(msgstr) )
write (PRINTF,'(a)') ' (linear wave theory and possible second
order bound long waves not valid)'
!
nowarn2 = .true.
!
endif
!
! give warning for filtering out the evanescent modes
!
if ( icemds > 0 .and. .not.nowarn ) then
!
rval = 100.*real(icemds)/real(nfreq)
!
if ( .not. rval < 10. ) then
write (msgstr,'(a,f5.1,a,f5.2,a)') 'percentage of internal-
generated components that have been filtered out (
evanescent modes) = ',rval, ' (cut-off = ',omegcf/pi2,' Hz)
,
call msgerr (1, trim(msgstr) )
endif
!
nowarn = .true.
!
endif
!
end subroutine SwashIntWavgen
```

C.2 Extension of subroutine SwashUpdateData.ftn90

The subroutine "SwashUpdateData" has been extended to account for internal wave generation. More precisely, in the following section of the code, the spatially distributed mass that has to be added in the free surface equation to generate waves is calculated at each time step.

```

subroutine SwashUpdateData ( it )
!
! update source function by means of internal wave generation
!
if ( iwvgen /= 0 ) then
!
  curbfs => fbfs
  do
    nfreq = curbfs%nfreq
    wdir = curbfs%spparm(3)
    !
    if ( wdir == -999. ) then
      ! incident or peak wave direction normal to the boundary
      if ( lsrcfy ) then
        wdir = alpc
      else if ( lsrcfx ) then
        wdir = 0.5*pi + alpc
      endif
    endif
    !
    ! if appropriate, ramp function is applied to prevent initially
    ! short large waves
    !
    tsmo = piwg(5)
    if ( lrampf .and. tsmo /= 0. ) then
      !
      fsmo = .5 * ( 1. + tanh( timco/tsmo - 3. ) )
      !
    else
      !
      fsmo = 1.
      !
    endif
    !
    shape = abs(spshape(2))
    !
    ! compute the source function amplitude and shape factor of
    ! source area
    !
    if ( it == 0 ) call SwashIntWavgen (curbfs, nfreq, wdir, shape)
    !
  
```

```

! compute source function
!
if ( oned ) then
!
cgsrc = piwg(1) - dble(xoffs)
hwidt = 0.5 * piwg(2)
!
isrcb = nint(cgsrc/dx - hwidt/dx - real(MXF) + 101.) - 99
isrce = nint(cgsrc/dx + hwidt/dx - real(MXF) + 101.) - 99
!
do i = 2, mxc-1
!
indx = kgrpnt(i,1)
!
if ( .not. i < isrcb .and. .not. i > isrce ) then
!
xp = real(i-isrcb) * dx - hwidt
!
sfval = 0.
!
do jj = 1, nfreq
!
ampl = curbfs%sfamp(jj)
beta = curbfs%bshap(jj)
!
omega = curbfs%omega(jj)
phase = curbfs%phase(jj)
!
sfval = sfval + ampl * exp( -beta * xp**2 ) * cos(
omega * timco + phase )
!
enddo
!
srcm(indx) = fsmo * sfval
!
endif
!
enddo
!
else
!
if ( lsrcfy ) then
!
cgsrc = piwg(1) - dble(xoffs)
hwidt = 0.5 * piwg(2)
!
isrcb = nint(cgsrc/dx - hwidt/dx - real(MXF) + 101.) - 99
isrce = nint(cgsrc/dx + hwidt/dx - real(MXF) + 101.) - 99
!
do j = 2, myc-1

```

```

do i = 2, mxc-1
  !
  indx = kgrpnt(i,j)
  !
  if ( .not. i < isrcb .and. .not. i > isrce ) then
    !
    xp = real(i-isrcb) * dx - hwidt
    yp = real(j+MYF-2) * dy
    !
    sfval = 0.
    !
    do jj = 1, nfreq
      !
      ampl = curbfs%sfamp(jj)
      beta = curbfs%bshap(jj)
      !
      omega = curbfs%omega(jj)
      theta = curbfs%theta(jj)
      kwav = curbfs%kwave(jj,1)
      phase = curbfs%phase(jj)
      !
      sfval = sfval + ampl * exp( -beta * xp**2 ) *
        cos( kwav * yp * sin(theta) + omega *
          timco + phase )
      !
    enddo
    !
    srcm(indx) = fsmo * sfval
    !
  endif
  !
enddo
enddo
!
else if ( lsrcfx ) then
  !
  cgsrc = piwg(1) - dble(yoffs)
  hwidt = 0.5 * piwg(2)
  !
  isrcb = nint(cgsrc/dy - hwidt/dy - real(MYF) + 101.) - 99
  isrce = nint(cgsrc/dy + hwidt/dy - real(MYF) + 101.) - 99
  !
  do i = 2, mxc-1
    do j = 2, myc-1
      !
      indx = kgrpnt(i,j)
      !
      if ( .not. j < isrcb .and. .not. j > isrce ) then
        !
        yp = real(j-isrcb) * dy - hwidt

```

190C. Source code of the implemented internal wave generation method in SWASH

```
        xp = real(i+MXF-2) * dx
        !
        sfval = 0.
        !
        do jj = 1, nfreq
            !
            ampl = curbfs%sfamp(jj)
            beta = curbfs%bshap(jj)
            !
            omega = curbfs%omega(jj)
            theta = curbfs%theta(jj)
            kwav = curbfs%kwave(jj,1)
            phase = curbfs%phase(jj)
            !
            sfval = sfval + ampl * exp( -beta * yp**2 ) *
                cos( kwav * xp * cos(theta) + omega *
                    timco + phase )
            !
        enddo
        !
        srcm(indx) = fsmo * sfval
        !
    endif
    !
    enddo
    enddo
    !
    endif
    !
    if ( .not.associated(curbfs%nextbfs) ) exit
    curbfs => curbfs%nextbfs
    !
enddo
!
endif
!
end subroutine SwashUpdateData
```

References

- Airy, G. (1845). On Tides and Waves. *Encyclopedia Metropolitana, London*, pages 241–396.
- Altomare, C., Crespo, A. J., Domínguez, J. M., Gómez-Gesteira, M., Suzuki, T., and Verwaest, T. (2015). Applicability of Smoothed Particle Hydrodynamics for estimation of sea wave impact on coastal structures. *Coastal Engineering*, 96:1–12.
- Altomare, C., Domínguez, J., Crespo, A., González-Cao, J., Suzuki, T., Gómez-Gesteira, M., and Troch, P. (2017). Long-crested wave generation and absorption for SPH-based DualSPHysics model. *Coastal Engineering*, 127(June):37–54.
- Altomare, C., Tagliaferro, B., Dominguez, J. M., Suzuki, T., and Viccione, G. (2018). Improved relaxation zone method in SPH-based model for coastal engineering applications. *Applied Ocean Research*, 81(September):15–33.
- Bai, Y. and Cheung, K. F. (2012). Depth-integrated free-surface flow with a two-layer non-hydrostatic formulation. *International Journal for Numerical Methods in Fluids*, 69(2):411–429.
- Bai, Y. and Cheung, K. F. (2013). Dispersion and nonlinearity of multi-layer non-hydrostatic free-surface flow. *Journal of Fluid Mechanics*, 726:226–260.
- Balitsky, P., Fernandez, G. V., Stratigaki, V., and Troch, P. (2018). Assessment of the power output of a two-array clustered WEC farm using a bem solver coupling and a wave-propagation model. *Energies*, 11(11):2907.
- Balitsky, P., Quartier, N., Stratigaki, V., Verao Fernandez, G., Vasarmidis, P., and Troch, P. (2019). Analysing the Near-Field Effects and the Power Production of Near-Shore WEC Array Using a New Wave-to-Wire Model. *Water*, 11(6):1137.
- Beels, C., Troch, P., De Backer, G., Vantorre, M., and De Rouck, J. (2010). Numerical implementation and sensitivity analysis of a wave energy converter in a time-dependent mild-slope equation model. *Coastal Engineering*, 57(5):471–492.
- Benoit, M., Marcos, F., and Becq, F. (1997). Development of a Third Generation Shallow-Water Wave Model with Unstructured Spatial Meshing. In *Coastal*

- Engineering 1996*, pages 465–478, New York, NY. American Society of Civil Engineers.
- Berkhoff, J. (1972). Computation of combined refraction-diffraction. *13th International Conference on Coastal Engineering*, pages 471–490.
- Berkhoff, J., Booy, N., and Radder, A. C. (1982). Verification of Numerical Wave Propagation Models for Simple Harmonic Linear Water Waves. *Coastal Engineering*, 6:255–279.
- Blayo, E. and Debreu, L. (2005). Revisiting open boundary conditions from the point of view of characteristic variables. *Ocean Modelling*, 9(3):231–252.
- Booij, N. (1983). A note on the accuracy of the mild-slope equation. *Coastal Engineering*, 7(3):191–203.
- Booij, N., Ris, R. C., and Holthuijsen, L. H. (1999). A third-generation wave model for coastal regions: 1. Model description and validation. *Journal of Geophysical Research: Oceans*, 104(C4):7649–7666.
- Borgman, L. E. and Panicker, N. N. (1970). Design Study for a Suggested Wave Gauge Array off Point Mugu, California.
- Bouws, E., Günther, H., Rosenthal, W., and Vincent, C. L. (1985). Similarity of the wind wave spectrum in finite depth water: 1. Spectral form. *Journal of Geophysical Research*, 90(C1):975.
- Briggs, M. J., Thompson, E. F., and Vincent, C. L. (1995). Wave Diffraction around Breakwater. *Journal of Waterway, Port, Coastal, and Ocean Engineering*, 121(1):23–35.
- Brocchini, M. (2013). A reasoned overview on Boussinesq-type models: the interplay between physics, mathematics and numerics. *Proceedings of the Royal Society A: Mathematical, Physical and Engineering Sciences*, 469(2160):20130496.
- Brorsen, M. and Helm-Petersen, J. (1998). On the Reflection of Short-Crested Waves in Numerical Models. *International Conference on Coastal Engineering*, pages 394–407.
- Casulli, V. and Stelling, G. S. (1998). Numerical Simulation of 3D Quasi-Hydrostatic, Free-Surface Flows. *Journal of Hydraulic Engineering*, 124(7):678–686.
- Choi, J., Lim, C. H., Lee, J. I., and Yoon, S. B. (2009). Evolution of waves and currents over a submerged laboratory shoal. *Coastal Engineering*, 56(3):297–312.
- Choi, J. and Yoon, S. B. (2009). Numerical simulations using momentum source wave-maker applied to RANS equation model. *Coastal Engineering*, 56(10):1043–1060.
- Copeland, G. J. (1985). A practical alternative to the "mild-slope" wave equation. *Coastal Engineering*, 9(2):125–149.

- Dalrymple, R. and Rogers, B. (2006). Numerical modeling of water waves with the SPH method. *Coastal Engineering*, 53(2-3):141–147.
- Dangendorf, S., Hay, C., Calafat, F. M., Marcos, M., Piecuch, C. G., Berk, K., and Jensen, J. (2019). Persistent acceleration in global sea-level rise since the 1960s. *Nature Climate Change*, 9(9):705–710.
- Dimakopoulos, A. S. and Dimas, A. A. (2011). Large-wave simulation of three-dimensional, cross-shore and oblique, spilling breaking on constant slope beach. *Coastal Engineering*, 58(8):790–801.
- Frigaard, P., Helm-Petersen, J., Klopman, G., Stansberg, C. T., Benoit, M., Briggs, M. J., Miles, M., Santas, J., Schäffer, H. A., and Hawkes, P. J. (1997). IAHR List of Sea Parameteres: an update for multidirectional waves. In *Proc. IAHR Seminar Multidirectional Waves and their Interaction with Structures. 27th IAHR Congress*, San Francisco.
- Gobbi, M. F., Kirby, J. T., and Wei, G. (2000). A fully nonlinear Boussinesq model for surface waves. Part 2. Extension to $O(kh)^4$. *Journal of Fluid Mechanics*, 405:181–210.
- Grilli, S. T. and Horrillo, J. (1997). Numerical generation and absorption of fully nonlinear periodic waves. *Journal of Engineering Mechanics*, 123(10):1060–1069.
- Grilli, S. T., Vogelmann, S., and Watts, P. (2002). Development of a 3D numerical wave tank for modeling tsunami generation by underwater landslides. *Engineering Analysis with Boundary Elements*, 26(4):301–313.
- Gruwez, V., Altomare, C., Suzuki, T., Streicher, M., Cappietti, L., Kortenhuis, A., and Troch, P. (2020). An Inter-Model Comparison for Wave Interactions with Sea Dikes on Shallow Foreshores. *Journal of Marine Science and Engineering*, 8(12):985.
- Ha, T., Lin, P., and Cho, Y. S. (2013). Generation of 3D regular and irregular waves using Navier-Stokes equations model with an internal wave maker. *Coastal Engineering*, 76:55–67.
- Hansen, E. O. (1978). Long period waves in natural wave trains. Technical report, Institute of Hydrodynamics and Hydraulic Engineering, Technical University of Denmark.
- Higdon, R. L. (1987). Numerical Absorbing Boundary Conditions for the Wave Equation. *Mathematics of Computation*, 49(179):65.
- Higuera, P., Lara, J. L., and Losada, I. J. (2013a). Realistic wave generation and active wave absorption for Navier–Stokes models. *Coastal Engineering*, 71:102–118.
- Higuera, P., Lara, J. L., and Losada, I. J. (2013b). Simulating coastal engineering processes with OpenFOAM®. *Coastal Engineering*, 71:119–134.

- Higuera, P., Losada, I. J., and Lara, J. L. (2015). Three-dimensional numerical wave generation with moving boundaries. *Coastal Engineering*, 101:35–47.
- Jacobsen, N. G., Fuhrman, D. R., and Fredsøe, J. (2012). A wave generation toolbox for the open-source CFD library: OpenFoam®. *International Journal for Numerical Methods in Fluids*, 70(9):1073–1088.
- Johnson, D. and Pattiaratchi, C. (2006). Boussinesq modelling of transient rip currents. *Coastal Engineering*, 53(5-6):419–439.
- Kennedy, A. B., Kirby, J. T., Chen, Q., and Dalrymple, R. A. (2001). Boussinesq-type equations with improved nonlinear performance. *Wave Motion*, 33(3):225–243.
- Kim, G. and Lee, C. (2013). Internal generation of waves on an arced band. *Ocean Engineering*, 67(17-18):77–88.
- Kirby, J. T. (2016). Boussinesq models and their application to coastal processes across a wide range of scales. *Journal of Waterway, Port, Coastal and Ocean Engineering*, 142(6):1–29.
- Klonaris, G. T., Memos, C. D., and Drønen, N. K. (2016). High-Order Boussinesq-Type Model for Integrated Nearshore Dynamics. *Journal of Waterway, Port, Coastal, and Ocean Engineering*, 142(6):04016010.
- Kuik, A. J., van Vledder, G. P., and Holthuijsen, L. H. (1988). A Method for the Routine Analysis of Pitch-and-Roll Buoy Wave Data.
- Larsen, J. and Dancy, H. (1983). Open boundaries in short wave simulations—A new approach. *Coastal Engineering*, 7:285–297.
- Lee, C., Cho, Y. S., and Yum, K. (2001). Internal generation of waves for extended Boussinesq equations. *Coastal Engineering*, 42(2):155–162.
- Lee, C. and Suh, K. D. (1998). Internal generation of waves for time-dependent mild-slope equations. *Coastal Engineering*, 34(1-2):35–57.
- Lee, C. and Yoon, S. B. (2007). Internal generation of waves on an arc in a rectangular grid system. *Coastal Engineering*, 54(4):357–368.
- Lin, P. and Liu, P. L. (1998). A numerical study of breaking waves in the surf zone. *Journal of Fluid Mechanics*, 359:239–264.
- Lin, X. and Yu, X. (2015). A finite difference method for effective treatment of mild-slope wave equation subject to non-reflecting boundary conditions. *Applied Ocean Research*, 53:179–189.
- Lynett, P. and Liu, P. L. (2004a). A two-layer approach to wave modelling. *Proceedings of the Royal Society of London. Series A: Mathematical, Physical and Engineering Sciences*, 460(2049):2637–2669.

- Lynett, P. J. and Liu, P. L. (2002). A two-dimensional, depth-integrated model for internal wave propagation over variable bathymetry. *Wave Motion*, 36(3):221–240.
- Lynett, P. J. and Liu, P. L. (2004b). Linear analysis of the multi-layer model. *Coastal Engineering*, 51(5-6):439–454.
- Ma, G., Shi, F., and Kirby, J. T. (2012). Shock-capturing non-hydrostatic model for fully dispersive surface wave processes. *Ocean Modelling*, 43-44:22–35.
- Madsen, P. and Sørensen, O. (1993). Bound waves and triad interactions in shallow water. *Ocean Engineering*, 20(4):359–388.
- Madsen, P. A., Bingham, H. B., and Schäffer, H. A. (2003). Boussinesq-type formulations for fully nonlinear and extremely dispersive water waves: derivation and analysis. *Proceedings of the Royal Society of London. Series A: Mathematical, Physical and Engineering Sciences*, 459(2033):1075–1104.
- Madsen, P. A., Murray, R., and Sørensen, O. R. (1991). A new form of the Boussinesq equations with improved linear dispersion characteristics. *Coastal Engineering*, 15(4):371–388.
- Madsen, P. A. and Schäffer, H. A. (1998). Higher-order Boussinesq-type equations for surface gravity waves: derivation and analysis. *Philosophical Transactions of the Royal Society of London. Series A: Mathematical, Physical and Engineering Sciences*, 356(1749):3123–3181.
- Madsen, P. A. and Sørensen, O. R. (1992). A new form of the Boussinesq equations with improved linear dispersion characteristics. Part 2. A slowly-varying bathymetry. *Coastal Engineering*, 18(3-4):183–204.
- Mayer, S., Garapon, A., and Sørensen, L. S. (1998). A fractional step method for unsteady free-surface flow with applications to non-linear wave dynamics. *International Journal for Numerical Methods in Fluids*, 28(2):293–315.
- Memos, C. D., Klonaris, G. T., and Chondros, M. K. (2016). On Higher-Order Boussinesq-Type Wave Models. *Journal of Waterway, Port, Coastal, and Ocean Engineering*, 142(1):04015011.
- Miles, M. D. (1989). A Note on Directional Random Wave Synthesis by the Single Summation Method. In *Proc. 23rd IAHR Congress*, pages C:243–250, Ottawa, Canada.
- Mitsuyasu, H., Tasai, F., Suhara, T., Mizuno, S., Ohkusu, M., Honda, T., and Rikishi, K. (1975). Observations of the Directional Spectrum of Ocean Waves Using a Cloverleaf Buoy.
- Neumann, B., Vafeidis, A. T., Zimmermann, J., and Nicholls, R. J. (2015). Future Coastal Population Growth and Exposure to Sea-Level Rise and Coastal Flooding - A Global Assessment. *PLOS ONE*, 10(3):e0118571.

- Nicolae Lerma, A., Pedreros, R., Robinet, A., and Sénéchal, N. (2017). Simulating wave setup and runup during storm conditions on a complex barred beach. *Coastal Engineering*, 123(July 2016):29–41.
- Nwogu, O. (1993). Alternative Form of Boussinesq Equations for Nearshore Wave Propagation. *Journal of Waterway, Port, Coastal, and Ocean Engineering*, 119(6):618–638.
- Orszaghova, J., Borthwick, A. G., and Taylor, P. H. (2012). From the paddle to the beach - A Boussinesq shallow water numerical wave tank based on Madsen and Sørensen's equations. *Journal of Computational Physics*, 231(2):328–344.
- Peregrine, D. H. (1967). Long waves on a beach. *Journal of Fluid Mechanics*, 27(4):815–827.
- Radder, A. and Dingemans, M. (1985). Canonical equations for almost periodic, weakly nonlinear gravity waves. *Wave Motion*, 7(5):473–485.
- Radder, A. C. (1979). On the parabolic equation method for water-wave propagation. *Journal of Fluid Mechanics*, 95(1):159–176.
- Reniers, A., Groenewegen, M., Ewans, K., Masterton, S., Stelling, G., and Meek, J. (2010). Estimation of infragravity waves at intermediate water depth. *Coastal Engineering*, 57(1):52–61.
- Rijnsdorp, D. P., Hansen, J. E., and Lowe, R. J. (2018). Simulating the wave-induced response of a submerged wave-energy converter using a non-hydrostatic wave-flow model. *Coastal Engineering*, 140(May):189–204.
- Rijnsdorp, D. P., Ruessink, G., and Zijlema, M. (2015). Infragravity-wave dynamics in a barred coastal region, a numerical study. *Journal of Geophysical Research: Oceans*, 120(6):4068–4089.
- Rijnsdorp, D. P., Smit, P. B., and Zijlema, M. (2014). Non-hydrostatic modelling of infragravity waves under laboratory conditions. *Coastal Engineering*, 85:30–42.
- Rijnsdorp, D. P., Smit, P. B., Zijlema, M., and Reniers, A. J. (2017). Efficient non-hydrostatic modelling of 3D wave-induced currents using a subgrid approach. *Ocean Modelling*, 116:118–133.
- Rusu, E. and Guedes Soares, C. (2013). Coastal impact induced by a Pelamis wave farm operating in the Portuguese nearshore. *Renewable Energy*, 58:34–49.
- Sand, S. E. and Mansard, E. (1986). Reproduction of higher harmonics in irregular waves. *Ocean Engineering*, 13(1):57–83.
- Sand, S. E. and Mynett, A. E. (1987). Directional Wave Generation and Analysis. In *IAHR Seminar on Wave Analysis and Generation in Laboratory Basins*, pages 363–376, Lausanne, Switzerland.
- Schäffer, H. A. (1996). Second-order wavemaker theory for irregular waves. *Ocean Engineering*, 23(1):47–88.

- Schäffer, H. A. and Sørensen, O. R. (2006). On the internal wave generation in Boussinesq and mild-slope equations. *Coastal Engineering*, 53(4):319–323.
- Sharma, J. and Dean, R. (1981). Second-Order Directional Seas and Associated Wave Forces. *Society of Petroleum Engineers Journal*, 21(01):129–140.
- Shi, F., Kirby, J. T., Harris, J. C., Geiman, J. D., and Grilli, S. T. (2012). A high-order adaptive time-stepping TVD solver for Boussinesq modeling of breaking waves and coastal inundation. *Ocean Modelling*, 43-44:36–51.
- Skjelbreia, L. (1959). *Gravity waves: Stokes' third order approximation tables of functions*. Council on Wave Research, the Engineering Foundation.
- Smit, P., Janssen, T., Holthuijsen, L., and Smith, J. (2014). Non-hydrostatic modeling of surf zone wave dynamics. *Coastal Engineering*, 83:36–48.
- Smit, P., Zijlema, M., and Stelling, G. (2013). Depth-induced wave breaking in a non-hydrostatic, near-shore wave model. *Coastal Engineering*, 76:1–16.
- Sørensen, O. R., Schäffer, H. A., and Sørensen, L. S. (2004). Boussinesq-type modelling using an unstructured finite element technique. *Coastal Engineering*, 50(4):181–198.
- Stelling, G. and Zijlema, M. (2003). An accurate and efficient finite-difference algorithm for non-hydrostatic free-surface flow with application to wave propagation. *International Journal for Numerical Methods in Fluids*, 43(1):1–23.
- Stokes, G. G. (1847). On the Theory of Oscillatory Waves. *Transactions of the Cambridge Philosophical Society*, 8:441–455.
- Stratigaki, V., Vanneste, D., Troch, P., Gysens, S., and Willems, M. (2011). Numerical modeling of wave penetration in Ostend harbour. *Coastal Engineering Proceedings*, 1(32):42.
- Suh, K. D., Lee, C., and Park, W. S. (1997). Time-dependent equations for wave propagation on rapidly varying topography. *Coastal Engineering*, 32(2-3):91–117.
- Suzuki, T., Altomare, C., Veale, W., Verwaest, T., Trouw, K., Troch, P., and Zijlema, M. (2017). Efficient and robust wave overtopping estimation for impermeable coastal structures in shallow foreshores using SWASH. *Coastal Engineering*, 122(January):108–123.
- Suzuki, T., Hu, Z., Kumada, K., Phan, L., and Zijlema, M. (2019). Non-hydrostatic modeling of drag, inertia and porous effects in wave propagation over dense vegetation fields. *Coastal Engineering*, 149:49–64.
- The Wamdi Group (1988). The WAM Model—A Third Generation Ocean Wave Prediction Model. *Journal of Physical Oceanography*, 18(12):1775–1810.

- Tolman, H. L. (1991). A Third-Generation Model for Wind Waves on Slowly Varying, Unsteady, and Inhomogeneous Depths and Currents. *Journal of Physical Oceanography*, 21(6):782–797.
- Troch, P. (1998). MILDwave – A numerical model for propagation and transformation of linear water waves. Technical report, Internal Report, Department of Civil Engineering, Ghent University, Department of Civil Engineering, Ghent University: Ghent.
- Troch, P. and Stratigaki, V. (2016). Phase-Resolving Wave Propagation Array Models. In Folley, M. E., editor, *Numerical Modelling of Wave Energy Converters*, chapter 10, pages 191–216. Elsevier, elsevier edition.
- Vasarmidis, P., Stratigaki, V., Suzuki, T., Zijlema, M., and Troch, P. (2019a). Internal Wave Generation in a Non-Hydrostatic Wave Model. *Water*, 11(5):986.
- Vasarmidis, P., Stratigaki, V., Suzuki, T., Zijlema, M., and Troch, P. (2020). An internal wave generation method for the non-hydrostatic model SWASH. In *Coastal Engineering Proceedings*, number 36v, page 16.
- Vasarmidis, P., Stratigaki, V., Suzuki, T., Zijlema, M., and Troch, P. (2021). On the accuracy of internal wave generation method in a non-hydrostatic wave model to generate and absorb dispersive and directional waves. *Ocean Engineering*, 219:108303.
- Vasarmidis, P., Stratigaki, V., and Troch, P. (2019b). Accurate and Fast Generation of Irregular Short Crested Waves by Using Periodic Boundaries in a Mild-Slope Wave Model. *Energies*, 12(5):785.
- Verao Fernandez, G. (2019). *A numerical study of the far field effects of wave energy converters in short and long-crested waves utilizing a coupled model suite*. PhD thesis, Ghent University.
- Verao Fernandez, G., Balitsky, P., Stratigaki, V., and Troch, P. (2018). Coupling Methodology for Studying the Far Field Effects of Wave Energy Converter Arrays over a Varying Bathymetry. *Energies*, 11(11):2899.
- Verao Fernandez, G., Stratigaki, V., Vasarmidis, P., Balitsky, P., and Troch, P. (2019). Wake Effect Assessment in Long- and Short-Crested Seas of Heaving-Point Absorber and Oscillating Wave Surge WEC Arrays. *Water*, 11(6):1126.
- Vincent, C. L. and Briggs, M. J. (1989). Refraction—Diffraction of Irregular Waves over a Mound. *Journal of Waterway, Port, Coastal, and Ocean Engineering*, 115(2):269–284.
- Wei, G. and Kirby, J. T. (1995). Time-Dependent Numerical Code for Extended Boussinesq Equations. *Journal of Waterway, Port, Coastal, and Ocean Engineering*, 121(5):251–261.
- Wei, G., Kirby, J. T., and Sinha, A. (1999). Generation of waves in Boussinesq models using a source function method. *Coastal Engineering*, 36(4):271–299.

- Wellens, P. and Borsboom, M. (2020). A generating and absorbing boundary condition for dispersive waves in detailed simulations of free-surface flow interaction with marine structures. *Computers and Fluids*, 200:104387.
- Wellens, R. (2012). *Wave Simulation in Truncated Domains for Offshore Applications*. Doctoral thesis, Delft University of Technology.
- Whitham, G. B. (1999). *Linear and Nonlinear Waves*. John Wiley & Sons, Inc., Hoboken, NJ, USA.
- Yamazaki, Y., Cheung, K. F., and Kowalik, Z. (2011). Depth-integrated, non-hydrostatic model with grid nesting for tsunami generation, propagation, and run-up. *International Journal for Numerical Methods in Fluids*, 67(12):2081–2107.
- Zijlema, M., Stelling, G., and Smit, P. (2011). SWASH: An operational public domain code for simulating wave fields and rapidly varied flows in coastal waters. *Coastal Engineering*, 58(10):992–1012.
- Zijlema, M. and Stelling, G. S. (2005). Further experiences with computing non-hydrostatic free-surface flows involving water waves. *International Journal for Numerical Methods in Fluids*, 48(2):169–197.
- Zijlema, M. and Stelling, G. S. (2008). Efficient computation of surf zone waves using the nonlinear shallow water equations with non-hydrostatic pressure. *Coastal Engineering*, 55(10):780–790.



Discretization of water surface of a short-crested wave field.